

Anomalous Broadening of Jet-Peak Shapes in Pb–Pb Collisions and Characterization of Monolithic Active Pixel Sensors for the ALICE Inner Tracking System Upgrade

CERN-THESIS-2017-339
19/02/2018



Mónika Varga-Kőfaragó

A catalogue record is available from the Utrecht University Library.

ISBN: 978-90-393-6940-1

Copyright © 2018 by M. Varga-Kófaragó

All rights reserved. No part of this book may be reproduced, stored in a database or retrieval system, or published in any form or any way, electronically, mechanically, by print, photoprint, microfilm or any other means without prior written permission of the author.

Typeset using L^AT_EX

Printed by: ProefschriftMaken || www.proefschriftmaken.nl

Cover design by: Bence Varga

Anomalous Broadening of Jet-Peak Shapes in Pb–Pb Collisions and Characterization of Monolithic Active Pixel Sensors for the ALICE Inner Tracking System Upgrade

Een Afwijkende Verbreding van Jetpiekvormen in
Lood-Lood botsingen en de Karakterisering van
Monolithische Actieve Pixelsensoren voor de Upgrade van
het Binnenste Trackingsysteem van ALICE

(met een samenvatting in het Nederlands)

Proefschrift

ter verkrijging van de graad van doctor aan de Universiteit Utrecht op
gezag van de rector magnificus, prof.dr. G.J. van der Zwaan, ingevolge
het besluit van het college voor promoties in het openbaar te verdedigen
op woensdag 19 februari 2018 des middags te 2.30 uur
door

Mónika Varga-Kőfaragó

geboren op 29 september 1988.
te Budapest, Hongarije

Promotor: Prof.dr. R.J.M. Snellings

Copromotor: Dr. J.F. Grosse-Oetringhaus

Contents

Outline	1
I INTRODUCTION	3
1 Heavy-ion physics	5
1.1 The Quark-Gluon Plasma	5
1.2 Colliding systems	6
1.3 Centrality: definition and determination	7
1.4 Jet physics	8
1.5 The QGP as an almost ideal liquid	10
1.6 Heavy quarks	12
2 The LHC and the ALICE experiment	15
2.1 The Large Hadron Collider	15
2.2 The ALICE experiment	15
2.3 Upgrade of ALICE in 2019–2020	19
II INNER TRACKING SYSTEM UPGRADE	21
3 Motivation and technology	23
3.1 Motivation and requirements of the upgrade	23
3.2 Monolithic Active Pixel Sensors	26
3.2.1 Technology aspects	28
3.2.2 Radiation effects	29
3.3 The ALPIDE family	30
3.3.1 Small-scale prototypes	31
3.3.2 The pALPIDE-1 sensor	33
3.3.3 The pALPIDE-2 and pALPIDE-3 sensors	39
3.3.4 The ALPIDE sensor	41

4	Sensor prototype characterization tools	43
4.1	Measurement methods	43
4.2	The EU Telescope framework	45
4.2.1	Tracking models	49
4.3	Optimization of the telescope setup	51
4.3.1	Default parameters of the simulations	52
4.3.2	Study of the effect of the parameters	53
4.3.3	The final telescope setup	60
5	Characterization of the pALPIDE-1 prototype	63
5.1	Charge threshold and temporal noise	63
5.2	Detection efficiency	66
5.3	Cluster size	74
5.4	Position resolution	80
5.5	Noise occupancy	88
5.6	The operating range	94
5.7	Cluster shape	95
5.8	Outlook on later prototypes	99
5.8.1	pALPIDE-2	99
5.8.2	pALPIDE-3	103
5.8.3	ALPIDE	104
5.9	Summary	104
III	NEAR-SIDE JET PEAK SHAPE ANALYSIS	107
6	Motivation and datasets	109
6.1	Motivation	109
6.2	Data sets and physics selection	112
6.3	Track and collision vertex reconstruction	114
6.4	Monte Carlo event generators	116
6.4.1	PYTHIA	117
6.4.2	HIJING	118
6.4.3	AMPT	118
7	Analysis technique	121
7.1	Two-particle correlations	121
7.1.1	Analysis method	122
7.1.2	Fitting procedure of the near-side peak	128
7.1.3	Validation of the method with HIJING	145
7.2	Systematic studies and uncertainties	146

8	Results	157
8.1	Width of the near-side peak	157
8.2	Depletion yield	160
8.3	Comparison to results from other experiments	161
8.4	Comparison to models	163
8.4.1	Width of the near-side peak	163
8.4.2	Depletion yield	166
8.4.3	Flow	168
8.5	Interplay of jets and flow	170
8.6	Summary	171
8.7	Physics outlook	172
	Appendices	175
A	Test-beam measurement campaigns	175
A.1	Measurements at the PS	175
A.1.1	July 2014	175
A.1.2	September–November 2014	177
A.1.3	December 2014	178
A.2	Measurements at the SPS	178
A.3	Measurements at DESY	178
B	Technical details of the analysis of the pALPIDE-1	181
B.1	Integration of the chip in the EUTelescope framework	181
B.2	Default parameters of the analysis	182
C	Datasets of the $\Delta\varphi$–$\Delta\eta$ analysis	185
C.1	2010 Pb–Pb	185
C.2	2011 Pb–Pb	185
C.3	2011 pp	186
	Acronyms	187
	Bibliography	191
	Summary in English	203
	Samenvatting in het Nederlands	205
	Acknowledgments	207
	Curriculum Vitae	209

Outline

The Thesis is organized around two main topics. Firstly, the upgrade of the innermost detector, the Inner Tracking System, of the ALICE experiment at the Large Hadron Collider (LHC) is presented. The upgrade will allow measuring heavy-flavor particles with much larger precision than the current detector and certain decay channels will be accessible for the first time. This will be achieved by collecting a factor of 100 more data after the upgrade during the Second Long Shutdown (2019–2020) of the LHC and by a much more precise tracking and better transverse momentum resolution. The Thesis details my contribution to the upgrade in the testing of the prototypes of the detector. I focused on the measurements at the test-beam facilities, I optimized the test setup by simulations and I took part in the data taking. My main contribution, however, was the preparation of the software used for the data analysis from test-beam measurements and the analysis of the data from the first full-scale prototype.

The second topic of the Thesis is an analysis of Pb–Pb and pp collisions taken by the ALICE detector at $\sqrt{s_{\text{NN}}} = 2.76$ TeV. Two-particle angular correlation measurements are presented as a function of transverse momentum and the centrality of the collisions in the case of the Pb–Pb data. The data is compared to simulations with the AMPT and the PYTHIA Monte Carlo generators for Pb–Pb and pp collisions, respectively. With these comparisons the interaction of jets with the flowing medium created in heavy-ion collisions can be studied. I contributed to this analysis with the characterization of the near-side jet peak and I carried out the systematic uncertainty studies and the comparison to the Monte Carlo generators. The analysis was published in Refs. [1, 2]

The Thesis is organized as the following: Part I contains an introduction to both topics with Chapter 1 introducing the theory and Chapter 2 the ALICE experiment at the LHC. Part II presents the upgrade of the Inner Tracking System of ALICE. This part is subdivided into three chapters: Chapter 3 introduces and motivates the upgrade and gives an overview of the detector prototypes. Chapter 4 describes the tools used for the characterization of the prototypes and the simulation of the measurement setup. In Chapter 5, the results of the characterization are discussed.

Part III presents the angular correlation measurements in three chapters. Chapter 6 describes the motivations of the analysis and the used datasets and Monte Carlo generators. Chapter 7 presents the details of the analysis technique and the studies of the systematic uncertainties. Finally in Chapter 8, the results of the analysis and the comparisons to the Monte Carlo generators are given.

Part I

INTRODUCTION

1. Heavy-ion physics

1.1 The Quark-Gluon Plasma

The Universe started with the Big Bang 13.77 billion years ago [3]. In heavy-ion colliders, a similar state to what filled the Universe about 10 microseconds after the Big Bang can be formed [4]. The produced state, the so-called Quark-Gluon Plasma (QGP), is created when ordinary matter is put under extreme pressure and/or is heated to extreme temperature [5–7]. These extreme conditions can be achieved when two heavy-ions, e.g. lead (Pb) or gold (Au) ions, collide at ultrarelativistic energies. In these collisions, the QGP exists for a very short time (few fm/c) [8], and thus it can only be studied indirectly. Large-scale detectors are built around the collision points of the accelerators to study the particles formed in these collisions, and from these studies, the nature of the interaction can be established. Today, two such circular heavy-ion accelerators are operational, the Large Hadron Collider (LHC) at the European Organization for Nuclear Research (CERN) [9] and the Relativistic Heavy Ion Collider (RHIC) at the Brookhaven National Laboratory [10].

The QGP acts as a strongly interacting almost ideal liquid [11], and its physics is described by Quantum Chromodynamics (QCD). Its phase diagram is presented in Fig. 1.1. At low temperature and low baryon density, ordinary matter, i.e. the matter that is surrounding us, is present. At higher temperature or baryon density a phase transition to the QGP occurs. It is thought to be a first order transition at high baryon density with a critical endpoint and cross-over type at lower baryon densities [5]. Fig. 1.1 does not contain scales for the two axes, because the exact place and shape of this phase transition line is not yet known.

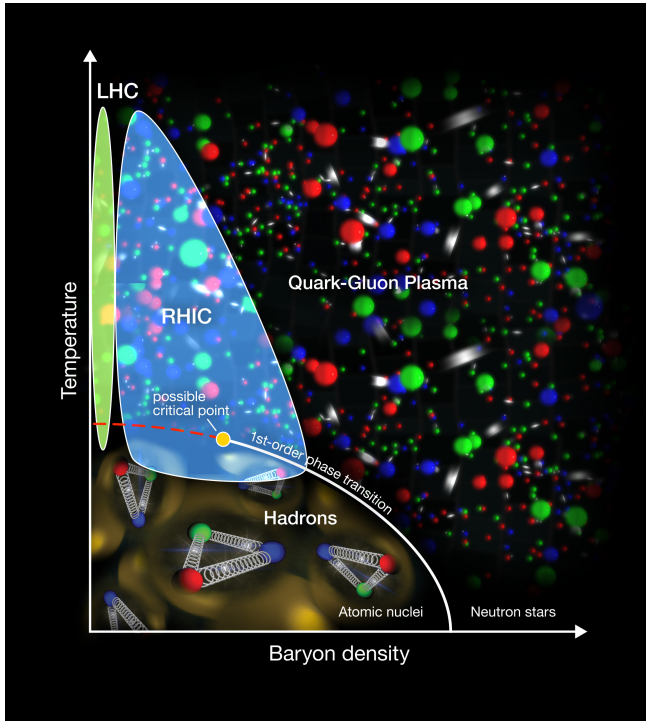


Figure 1.1: The phase diagram of QCD [10].

1.2 Colliding systems

In heavy-ion physics, the nature of the QGP produced in the collisions of heavy ions is investigated. In many of the studies, the properties of the QGP can be inferred only indirectly from comparisons with measurements of a system where the QGP is not present. For these comparisons, proton-proton (pp) collisions are used, where similar hard processes as in heavy-ion (AA) collisions occur; however, the QGP is believed to be not produced.

Differences between heavy-ion collisions and pp collisions can occur for two reasons. One is the presence of the QGP; however, the presence of the so-called cold nuclear effects can result in modifications as well. This term refers to all effects arising from a different structure in the initial state of the collision depending on whether protons or heavier ions are colliding. These differences include e.g. a difference in the wave function of the colliding nuclei or a change in the parton distribution function (the distribution function of quarks and gluons) in heavy-ions compared to protons. These cold nuclear effects can be studied by comparing pp collisions to collisions of protons with heavy-ions (pA collisions).

1.3 Centrality: definition and determination

Heavy-ion collisions can be categorized according to their impact parameter (b), which is defined as the distance of the centers of the colliding nuclei in the plane perpendicular to the direction of the beam. The impact parameter also defines the overlap area of the two colliding nuclei, which is the region where the QGP is produced. Therefore studying the properties of the collisions as a function of the size of the overlap area can give insight into the properties of the QGP. In heavy-ion physics, instead of the impact parameter, the collisions are categorized by their centrality, which is stated as a percentage of the total nuclear interaction cross-section. Low percentiles mean head-on collision (Fig. 1.2a), called central events, while high percentiles are called peripheral collisions (Fig. 1.2b). This means that the impact parameter was large, therefore the centers of the nuclei were far from each other.



Figure 1.2: Panel (a) shows the position of the two colliding nuclei in a central collision in the plane perpendicular to the direction of the beam, while panel (b) shows it in a peripheral case.

The impact parameter of the collisions cannot be measured directly, therefore the centrality has to be determined by other means. It is possible to determine it by measuring a property of the event which has a monotonic dependence on the impact parameter. Typical examples are the multiplicity of the event or the energy deposited in a certain detector. Comparing these with model calculations, one can infer the connection of the measurable quantities and the centrality percentiles. For these comparisons the Glauber model [12] is used, and the details of such a calculation can be found in Ref. [13]. In Fig. 1.3, as an example, the number of recorded events is shown as a function of the summed amplitude of one of the forward detectors used in ALICE for the centrality determination. The data is overlaid with a Glauber model simulation, from which the centrality percentiles are calculated.

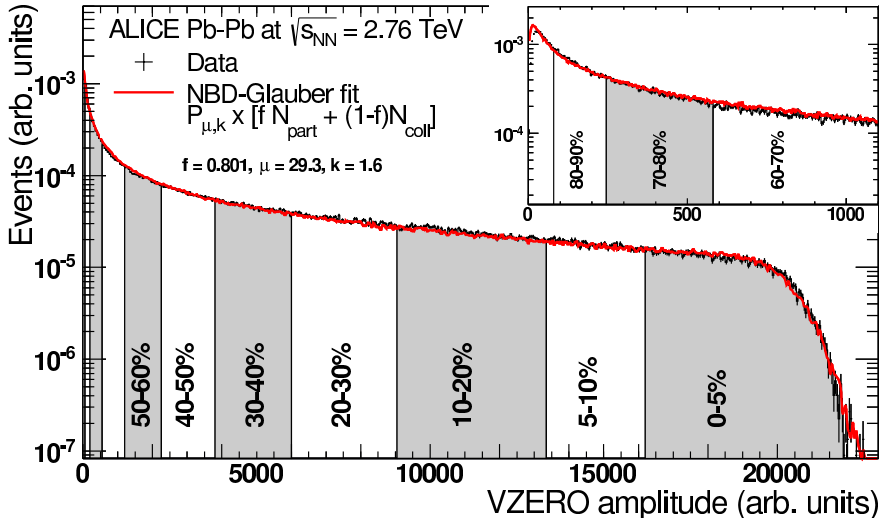


Figure 1.3: The number of recorded events as a function of the summed amplitude of one of the forward detectors used in ALICE for the centrality determination. The data is overlaid with a Glauber model simulation to extract the centrality percentiles [13].

1.4 Jet physics

In pp, pA or AA collisions, partons from the nucleon or nucleus collide at high energies. In these parton-parton collisions, in leading order QCD, quark-antiquark, gluon-gluon or (anti)quark-gluon pairs are created, which fly back-to-back in the rest frame of the colliding partons. These quarks and gluons are colored objects created at high virtuality, therefore they cannot exist freely. They lose virtuality by radiating gluons, and finally they hadronize into many collinear particles, which are spatially correlated and referred to as jets.

Jets are created in both pp and AA collisions, therefore studying their structure can give insight into the interactions of the fragmenting parton with the QGP. In pp collisions, the back-to-back jets appear with the same energy, while it was seen at RHIC and at the LHC that in central heavy-ion collisions, the energy of the two jets is highly asymmetric [14,15]. This phenomena is generally referred to as jet quenching, and it is caused by the partons losing energy while traversing the QGP. The energy is lost by elastic and inelastic scattering in the medium, including induced gluon radiation. A similar phenomena was seen at RHIC, where two-particle angular correlations were studied. In this study, the back-to-back correlations seen in pp collisions were found to be reduced in central Au-Au collisions [16].

The energy loss of partons with high momentum in the plane perpen-

pendicular to the direction of the beam (transverse momentum – p_T) can also be studied without the direct reconstruction of jets through the comparison of the hadron p_T spectra. This is dominated by the leading (most energetic) particles of the jets both in heavy-ion collisions and in pp collisions. In Fig. 1.4, the so-called nuclear modification factor (R_{AA}) for unidentified charged hadrons is shown, which is the ratio of the p_T spectrum in heavy-ion collisions and the one in pp collisions, normalized by the number of binary collisions:

$$R_{AA}(p_T) = \frac{(1/N_{evt}^{AA})d^2N_{ch}^{AA}/d\eta dp_T}{\langle N_{coll} \rangle (1/N_{evt}^{pp})d^2N_{ch}^{pp}/d\eta dp_T}. \quad (1.1)$$

The superscript AA or pp stands for the heavy-ion and the pp collision, respectively, N_{evt} represents the number of events, N_{ch} is the number charged tracks and $\langle N_{coll} \rangle$ is the number of binary nucleon–nucleon collisions in the heavy-ion case. In Pb–Pb collisions, a suppression with respect to pp collisions of around a factor of 7 is present at $\sqrt{s_{NN}} = 2.76$ TeV around $p_T = 6 - 7$ GeV/c [17]. In Au–Au collisions at $\sqrt{s_{NN}} = 200$ GeV, the suppression is less, it is around a factor 4 – 5 [18, 19]. These measurements indicate the formation of a dense QGP in these collisions.

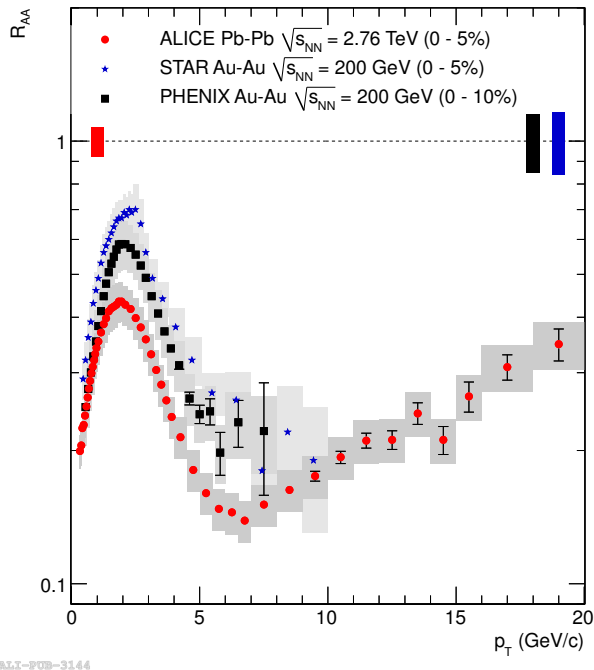


Figure 1.4: Nuclear modification factor for unidentified charged hadrons from Pb–Pb and Au–Au collisions [17].

1.5 The QGP as an almost ideal liquid

In an ideal liquid, the shear viscosity over entropy density ratio is zero ($\eta/s = 0$). The QGP is believed to act as an almost ideal fluid with almost zero shear viscosity over entropy density, and its evolution can be described by relativistic hydrodynamics [11]. It is expanding, and its radial expansion is characterized by the radial flow velocity (β_T), which can be extracted from the transverse momentum spectra of the measured hadrons [20, 21]. The medium is also expanding longitudinally, which is due to the direction of the momenta of the colliding particles before the collision [22].

When the two colliding ions do not overlap completely, the created medium has an anisotropic shape. This spatial asymmetry results in asymmetric pressure gradients in the plane perpendicular to the beam direction (transverse plane). This is translated into an asymmetry in the transverse momentum of the particles if the medium is an interacting liquid (see Fig. 1.5). The stronger the interaction is, the larger the magnitude of the asymmetry becomes, therefore this can be used to determine the strength of the interaction. The asymmetry can be described by the Fourier moments of the azimuthal angle distribution of the created particles [24]:

$$E \frac{d^3 N}{d^3 \mathbf{p}} = \frac{1}{2\pi} \frac{d^2 N}{p_T dp_T dy} \left(1 + 2 \sum_{n=1}^{\infty} v_n \cos[n(\varphi - \Psi_n)] \right) \quad (1.2)$$

In the equation, E is the energy, \mathbf{p} and p_T are the momentum and the transverse momentum, φ is the azimuthal angle measured in the transverse plane and y is the rapidity of the particle. N represents the number of particles. Ψ_n represents the n^{th} symmetry plane, which is the plane given by the direction of the beam and the symmetry axis of the n^{th} harmonic. For $n = 2$, the symmetry plane is highly correlated to the reaction plane,

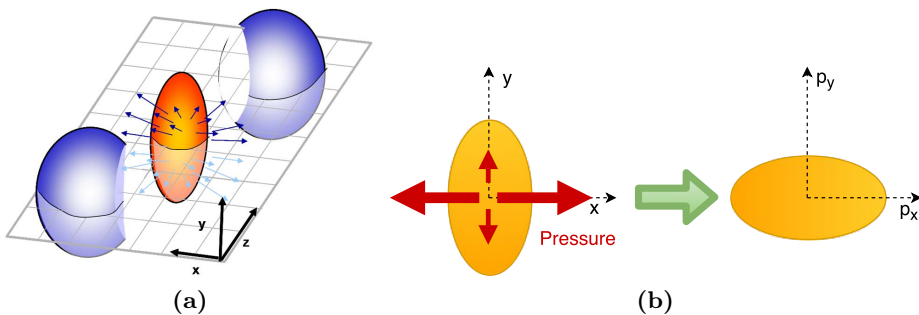


Figure 1.5: Illustration of how the spatial anisotropy (a) [23] is translated into momentum space anisotropy (b).

which is the plane given by the vector connecting the centers of the colliding nuclei and the direction of the beam. The v_n parameters are the parameters describing the anisotropy in the transverse plane. The dominating parameter is v_2 , which is referred to as the elliptic flow parameter, while v_3 is smaller and is called the triangular flow. The anisotropy can be studied statistically from many collisions, but it can even be visible event-by-event as is shown in Fig. 1.6. The parameter v_2 was already measured at the AGS (Alternating Gradient Synchrotron) [25, 26] and the SPS (Super Proton Synchrotron) [27–30], and it was first found to be compatible with hydrodynamical calculations at RHIC [31]. The parameter v_3 , which originates from the spatial fluctuations of the colliding partons in the ions, was determined first at RHIC [32] and then at the LHC by the ALICE collaboration [33].

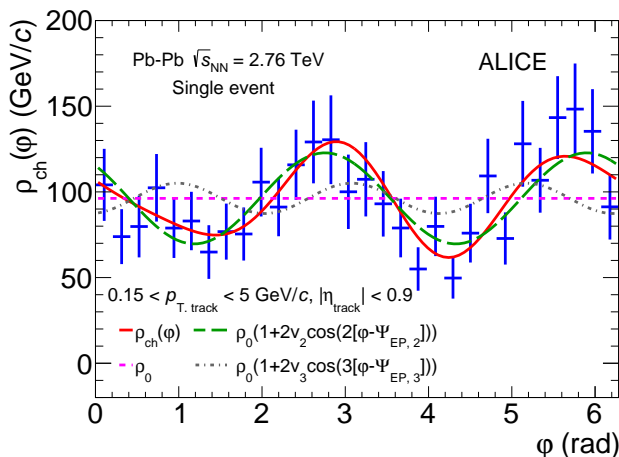


Figure 1.6: Anisotropy of charged particles measured from one event [34].

1.6 Heavy quarks

The six quarks of the Standard Model have very different masses (ranging from $2.2 \text{ MeV}/c^2$ to $173.1 \text{ GeV}/c^2$) [35]. The heavier three (c , b and t quarks) are referred to as heavy quarks and because of their large mass, they might act differently in the medium compared to light quarks. They are mostly produced in scatterings with high momentum transfer, which happens only at the beginning of the collision. This means that their production is less affected by the medium, which allows for an easier theoretical description. Since heavy quarks are only produced at the beginning of the collision and their annihilation cross section is negligible, the finally detected particles with heavy-quark content can be traced back to the heavy quarks produced in the original collisions. This allows for the determination of their interaction with the medium from their measured spatial and momentum distributions.

In heavy-ion collisions, from the three heavy quarks, only c and b are usually studied. This is due to their high enough production cross section and the fact that the particles which contain them live long enough to be reconstructable. The production cross section of the t quark is much lower and they decay before hadronization, therefore most of them are detected as particles with b -quark content instead.

The quarks produced in scatterings with high-momentum transfer can fragment differently depending on their masses. In the case of heavy quarks, gluon radiation is suppressed at angles smaller than the ratio of their mass and their energy [36]. This suppression is referred to as the dead-cone effect. Because of this, if jets lose energy dominantly by gluon radiation, jets with heavy-quark contents are expected to suffer less quenching than jets with light quarks. The comparison of jets with or without heavy quarks can therefore yield information on the energy loss mechanisms of jets propagating through the QGP.

Apart from being produced at the beginning of the collision, c quarks can also be produced via gluon splitting. The energy loss of these quarks is expected to depend on the lifetime of the parent gluon and on the separation of the quark and the antiquark, therefore they may lose energy differently than the quarks which were produced directly in the hard scatterings. These quarks mainly contribute to the production of heavy-flavor hadrons carrying a low fraction of the momentum of the jets. [37]

The large mass of heavy quarks makes full thermalization in the medium unlikely, which can be tested by measuring the anisotropic flow of particles containing heavy quarks. The elliptic flow of particles with heavy-quark content has been measured for several particle types [38–41], and it was found to be significant and to have a similar magnitude as in the case of light quarks. Because of the dead cone effect, the nuclear modification

was also expected to be weaker in the case of particles with heavy quarks; however, it was also measured to be of similar magnitude at high p_T for D mesons as in the case of light quarks [42]. These observations put strong constraints on theoretical models; however, the precision of these measurements is much lower than the precision in the case of light quarks. This comes from two effects, firstly, heavy quarks are less frequently produced than light quarks, therefore the available statistics is much smaller. Secondly, the identification of particles with heavy quarks is more complicated than the identification of the more abundantly produced particles. The identification of particles with heavy quarks can greatly benefit from the reconstruction of their decay vertex, which requires more precise tracking in the vicinity of the collision vertex than what is needed for light quarks. Further studies are therefore required for the full understanding of the interactions of heavy quarks with the medium.

2. The LHC and the ALICE experiment

2.1 The Large Hadron Collider

The Large Hadron Collider (LHC) is located at the European Organization for Nuclear Research (CERN) on the border of France and Switzerland [9]. It is a circular collider with two beams of particles circulating in opposite directions, and currently, it provides proton and nucleus collisions with the highest artificially produced energy in the world. It currently collides protons at a maximum center-of-mass energy of $\sqrt{s} = 13$ TeV and heavy ions (Pb) at a maximum center-of-mass energy per nucleon of $\sqrt{s_{\text{NN}}} = 5.02$ TeV. It can also provide asymmetric collisions, where a proton is collided with a Pb-ion. The collisions happen at four interaction points, which are surrounded by four large detector systems. The four experiments are specialized for different studies, CMS (Compact Muon Solenoid) and ATLAS (A Toroidal LHC ApparatuS) are general purpose detectors, which focus on pp collisions, especially on measuring the properties of the Higgs boson and on searches for physics beyond the Standard Model. LHCb (Large Hadron Collider beauty) is also focusing on pp collisions, but its main purpose is to study CP violation in physics related to heavy quarks. All four experiments record and study heavy-ion collisions as well; however, ALICE (A Large Ion Collider Experiment) is the one which was built specifically to study Pb–Pb collisions.

2.2 The ALICE experiment

ALICE was designed to study the QGP produced in heavy-ion collisions. It recorded its first pp collisions in 2009 and the first Pb–Pb collision in 2010. The detector system is organized as a typical detector built for high-energy collisions, with its different subsystems arranged into concentric layers surrounding the collisions point. The detectors close to the interaction point are used for charged particle tracking, while the outermost detectors are calorimeters used for measuring the energy of the

particles. Between these, detectors used for particle identification (PID) are placed. In the following, a short summary of the different subsystems is given, but the interested reader is referred to Ref. [43], where a complete description of the detector system of ALICE is given. The detector with its subsystems is shown in Fig. 2.1.

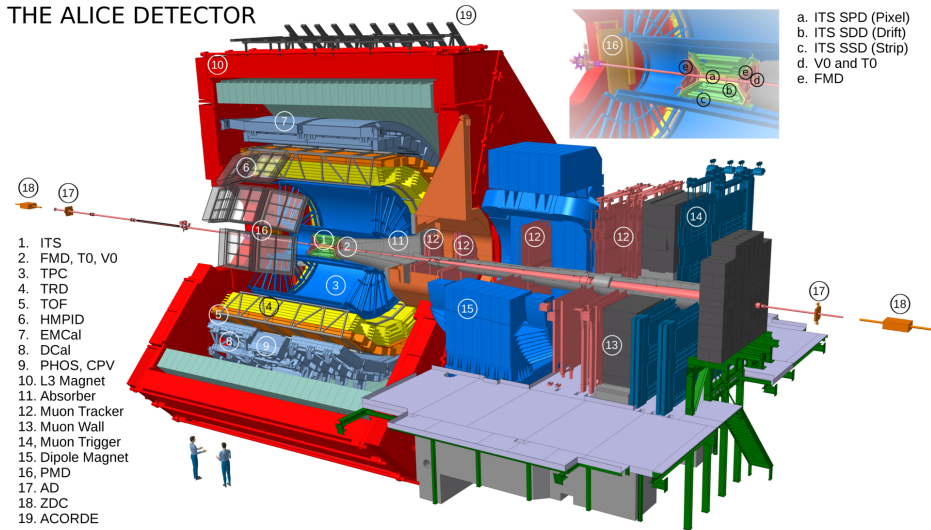


Figure 2.1: Schematic drawing of the ALICE detector [44].

Tracking detectors

The main tracking detectors of ALICE are the Inner Tracking System (ITS) and the Time-Projection Chamber (TPC). The ITS is the innermost detector, which is closest to the interaction point, and it consists of six layers of silicon detector. The two inner layers are pixel detectors (Silicon Pixel Detector – SPD), the two middle layers are drift detectors (Silicon Drift Detector – SDD) and the two outer layers are strip detectors. (Silicon Strip Detector – SSD). The innermost layer is at a distance of 3.9 cm from the interaction point, while the outermost layer is at 43 cm. The detector covers a pseudorapidity range of $|\eta| < 0.9$. The main purpose of the ITS is the tracking of charged particles and from these the reconstruction of the primary vertex, but it takes part in the PID and the triggering as well.

The next detector moving outwards from the interaction point is the TPC. It is a cylindrical gaseous detector, and its sensitive volume has an inner radius of 85 cm and an outer radius of 250 cm. It is the main tracking detector of ALICE, and it also has an important role in PID.

Particle identification

Outside the TPC, the dedicated PID detectors can be found. The Transition Radiation Detector (TRD) is used mainly for the identification of electrons above $p_T = 1 \text{ GeV}/c$ based on their radiation in a specifically designed radiator, but it can also contribute to the tracking of particles. The Time Of Flight (TOF) detector identifies particles based on measuring the time needed for them to reach the detector from the interaction point. For this, the time of the collision needs to be determined, which is done by the T0 (Time 0) detector. The T0 is placed close to the interaction point in the transverse plane, but further (-72.7 cm and 375 cm) along the beam direction. The TOF itself can also be used to determine the time of the collision in high multiplicity events.

The High-Momentum Particle Identification Detector (HMPID) is also used for identifying particles above $p_T = 1 \text{ GeV}/c$, but its working principle is based on the detection of Cherenkov radiation. The HMPID covers only around 5% of the central barrel phase space, while the other detectors used for PID cover the full area.

Calorimeters

Outside the PID detectors, the calorimeters of ALICE can be found. The ElectroMagnetic CALorimeter (EMCal) is a large Pb-scintillator sampling calorimeter, which is meant to help ALICE in studying jet-quenching in heavy-ion collisions. It measures the energy of charged particles, certain neutral hadrons (e.g. π^0 and η) and photons, and it can also be used as a trigger for high p_T jets. The Di-Jet Calorimeter (DCAL) uses the same technology as the EMCal, but it covers the phase space opposite of the EMCal, therefore it extends its measurements to dijets.

The spectrum of photons can also be measured with the PHOTon Spectrometer (PHOS). It is a high-resolution electromagnetic spectrometer used for studying the thermal and dynamical properties of the initial phase and for studying jet-quenching by measuring photons. In front of PHOS, the Charged-Particle Veto (CPV) detector is installed, which is a gaseous detector used to reject signals in PHOS originating from charged particles.

Magnets

All the detectors described above are embedded in a 0.5 T magnetic field used for the measurement of the transverse momentum of charged particles. This field is provided by a solenoid magnet, which is operated at room temperature. ALICE has a dipole magnet as well, which is placed at a distance of 7 m from the collision point and which has a magnetic field

around 0.7 T at its center. The dipole is used for the measurement of the momentum of muons, which will be further discussed below.

Muon detectors

In ALICE, the muon detectors are placed in the forward direction, where an absorber shields these detectors from hadrons and photons produced in the collisions. Behind the absorber, tracking and triggering detectors are placed to measure muons at large negative pseudorapidity ($-4.0 \lesssim \eta \lesssim -2.5$).

There is an additional muon detector placed outside of the solenoid of ALICE, which has a different task compared to the ones described above. The ALICE COsmic Ray DETector (ACORDE) is used for providing trigger for commissioning, calibration and alignment of some of the tracking detectors, and it is also used to study cosmic muons, when there are no collisions in the LHC. It is an array of plastic scintillator counters, which are placed on the top part of the solenoid.

Forward detectors

The forward detectors of ALICE are used for triggering and event characterization purposes. The T0 (Time 0), V0 (Vertex 0), the Forward Multiplicity Detector (FMD) and the Photon Multiplicity Detector (PMD) are located in the central barrel, close to the beam pipe, while the Zero Degree Calorimeter (ZDC) is located further from the interaction region in the forward and backward direction (at ± 116 m). The V0 detector consists of two arrays of scintillator counters (one on the forward and one on the backward side of the interaction region), which are used for triggering and for centrality determination. The T0 consists of two Cherenkov counters, and it is used for triggering, for measuring the vertex position and for providing the interaction time for the TOF detector.

The purpose of the ZDC is to measure the spectator nucleons (the nucleons that did not take part in the collision), which give important information on the centrality of the collision and can also be used for triggering purposes. The ZDC has a segmentation in the transverse plane, therefore it can provide information also on the orientation of the reaction plane. It measures both the spectator protons and neutrons in two separate detectors.

The FMD and the PMD provide in the forward direction the determination of the multiplicity of charged particles and photons, respectively. The FMD uses rings of Silicon strip detectors, while the PMD consists of converters for photons, and it measures the converted charged particles in

gas proportional counters. Both detectors can be used also to measure the orientation of the reaction plane.

Coordinate system used in ALICE

ALICE is using a right handed coordinate system with its origin at the nominal interaction point. The x -axis is pointing towards the center of the collider and the y -axis is pointing upwards. The x - y plane is referred to as the transverse plane, while the beam direction (z) as the longitudinal direction. The azimuthal angle (φ) is measured in the x - y plane from the x -axis. The polar angle (θ) is measured from the z -axis, and it is defined such that $\theta = 0$ is the axis itself, and it varies from 0 to π . Often instead of the polar angle the pseudorapidity is used, which is defined as

$$\eta = -\ln \left[\tan \left(\frac{\theta}{2} \right) \right]. \quad (2.1)$$

It varies from 0 in the x - y plane to $\pm\infty$ parallel to the z -axis. It is related to the momentum (\mathbf{p}) of the particle by the following formula:

$$\eta = \frac{1}{2} \ln \left(\frac{|\mathbf{p}| + p_z}{|\mathbf{p}| - p_z} \right) \quad (2.2)$$

where p_z is the z component of the momentum.

2.3 Upgrade of ALICE in 2019–2020

ALICE will be upgraded in the Second Long Shutdown of the LHC to be able to accomplish the physics program planned for Run 3 and 4 of the LHC. The main physics goals after the upgrade will be the following [37]:

- Study of the thermalization of partons in the QGP, focusing on heavy-flavor quarks.
- Study of quarkonium dissociation, especially at low transverse momentum.
- Study of the initial temperature and the equation of state of the medium by low-mass dileptons.
- Further study of jet-quenching mechanisms.
- Search for the existence of heavier nuclear states and study their decay properties.

Many of these probes cannot be efficiently selected by a hardware trigger because of the large combinatorial background at low transverse momentum, therefore it is necessary to record large minimum bias samples of data. The plan is to record 10 nb^{-1} of Pb–Pb collisions together with 6 pb^{-1} of pp and 50 nb^{-1} of p–Pb collision at the same energy as reference until the end of Run 4 (2029). This is a factor of 100 more than the amount of data recorded by the end of Run 2 (2018). To collect this amount of data, the data-taking rate of ALICE has to be significantly increased, which requires the readout electronics of many detectors to be upgraded. The studies of heavy-flavor hadrons rely on the detection of secondary vertices, therefore the vertex reconstruction and the pointing resolution of tracks have to be improved significantly as well. To achieve these improvements in both data-taking rate and tracking, the following upgrades will take place during the Second Long Shutdown:

- A new smaller beampipe will be installed, which will allow the first layer of the ITS to be moved closer to the interaction point.
- The ITS will be replaced by a new detector with high resolution and low material budget, resulting in higher tracking efficiency and better resolution for the distance of closest approach of tracks to the primary vertex at low p_T . The upgrade of the ITS will be described in detail in Part II.
- The TPC will be upgraded by having GEM detectors instead of multi-wire chambers. This allows the detector to be operated without a gating grid by avoiding excessive charge accumulation in the drift volume. The new technology therefore allows for a faster data taking.
- A new Muon Forward Tracker (MFT) will be installed, which will allow better extrapolation of the muon tracks to the primary vertex.
- The readout electronics of the TPC, the Muon spectrometer, the TRD, the TOF and the PHOS detectors will be upgraded to cope with the required data taking rate.
- The trigger system and the forward trigger detectors will be upgraded also to cope with the required data taking rate.
- The Online and Offline Systems (O² project), including the High-Level Trigger and the data acquisition, will be upgraded to be able to cope with the planned amount of data.

Part II

INNER TRACKING SYSTEM UPGRADE

3. Motivation and technology

In this part, the upgrade of the Inner Tracking System is described in detail with emphasis on my contribution to this project.

3.1 Motivation and requirements of the upgrade

The current Inner Tracking System would not be able to fulfill the physics requirements of ALICE for Run 3 of the LHC, especially on the readout rate and the resolution of the distance between the tracks and the primary vertex at their closest point [45]. The current resolution in the transverse momentum range relevant for the daughter particles of the Λ_c is around $60\ \mu\text{m}$, which is close to the proper decay length of the Λ_c itself. To study beauty mesons and baryons, and hadrons with more than one heavy quark, the precise description of the background originating from the decay of charm is needed, which is not possible with the current detector [46]. To make these measurements possible the current ITS will be replaced during the Second Long Shutdown of the LHC.

The readout of the current ITS is limited to 1 kHz, independent of the occupancy of the detector, which is far below the requirements of the upgrade to readout Pb–Pb collisions at 50 kHz. Another limitation of the current detector is that it is not accessible without moving the TPC. This takes longer than the yearly shutdown of the LHC, therefore making it impossible to access the ITS during this time. This makes it difficult to maintain high detector performance throughout the years. For this reason, it is required of the upgraded detector that it is easily removable and reinsertable during the yearly shutdown, which puts strict requirements on the support structures of the detector [45].

The layout of the current and the upgraded detector can be seen in Fig. 3.1. The current ITS consists of six concentric layers, the two innermost are equipped with pixel detectors (SPD) with a pixel size of $50\ \mu\text{m} \times 425\ \mu\text{m}$, the middle two layers with silicon drift detectors (SDD), with a cell size of $294\ \mu\text{m} \times 202\ \mu\text{m}$, while the outer two with silicon strip detectors (SSD), with a strip pitch of $95\ \mu\text{m}$. The innermost layer is

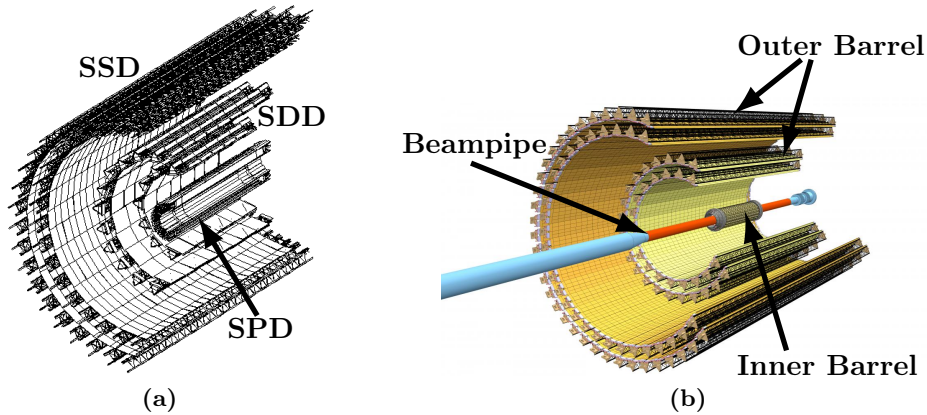


Figure 3.1: Panel (a) shows the layout of the current ITS [47], while (b) shows the layout of the upgraded ITS [45].

39 mm away from the center of the beampipe, and the layers have a total material budget of around 7.66% of the radiation length.

The resolution of the distance of closest approach of the tracks to the primary vertex is influenced by the resolution of the primary vertex and the pointing resolution of the tracks. These two parameters are influenced by the amount of material the particles traverse and by the spatial resolution, the placement and the granularity of the sensors of the ITS. To improve the resolution of the distance of closest approach of ALICE, the beampipe will be replaced by a new one with a smaller diameter. This will allow to move the new ITS closer to the nominal interaction point, with the closest layer being as close as 23 mm. This new beampipe will have a wall thickness of 0.8 mm, which contributes around 0.2% of the radiation length to the material budget. All layers of the upgraded detector will be equipped with pixel chips, increasing the granularity and the intrinsic spatial resolution significantly. The layers will also have a much lower material budget as the current detector, which will be achieved by having thinner detectors (factor of seven) with lower power consumption (factor of two at least). The lower power consumption will be reached by an optimization of the readout architecture and of the timing specifications of the analog front-end of the sensor [45].

The different layers of the ITS will have different distances from the beampipe, therefore they will have to fulfill different requirements. They will be grouped into the Outer Barrel (outermost four layers) and the Inner Barrel (innermost three layers), and their requirements will be determined based on to which barrel they belong to. The requirements for both barrels can be seen in Table 3.1. Since all the layers will be equipped with the same chip, for each parameter, the final chip will have to fulfill the stronger

requirement of the two. This leads to a chip which is radiation hard up to 2700 krad total ionizing dose, 1.7×10^{13} 1 MeV $n_{\text{eq}}/\text{cm}^2$ non-ionizing irradiation and has a detection efficiency higher than 99%, a fake hit rate lower than 10^{-6} hits/event/pixel and a position resolution of about 5 μm . Furthermore, it is required that the sensors can be read out in Pb–Pb collisions with a frequency of around 100 kHz and in pp collisions of a few 100 kHz. There is no sensor readily available which fulfills all these requirements, and which also meets the requirements of the material budget, therefore R&D had to be carried out specifically for the upgrade of the Inner Tracking System of ALICE [45].

Parameter	Inner Barrel	Outer Barrel
Silicon thickness	50 μm	100 μm
Chip size	15 mm \times 30 mm (r - φ \times z)	
Spatial resolution	5 μm	10 μm
Power density	< 300 mW/cm ²	< 100 mW/cm ²
Integration time	< 30 μs	
Detection efficiency	> 99%	
Fake hit rate	< 10^{-6} hits/event/pixel	
Average hit density *	14.9 – 30.4 hits/cm ²	0.3 – 1 hits/cm ²
Material budget per layer	0.3% X_0	1.0% X_0
TID radiation **	2700 krad	100 krad
NIEL radiation **	1.7×10^{13} 1 MeV $n_{\text{eq}}/\text{cm}^2$	10^{12} 1 MeV $n_{\text{eq}}/\text{cm}^2$

* Maximum hit densities in central Pb–Pb collisions, including secondaries produced in the material.

** Including a safety factor of 10.

Table 3.1: Requirements for the Inner Barrel and Outer Barrel of the upgraded ITS. Values are from Ref. [45], with updated values for the radiation levels from the latest simulations, for the noise occupancy values and for the material budget [48, 49].

The seven layers of the detector have different length in the z -direction and are equipped with different number of sensors per layer. The number of sensors for each layer can be found in Table 3.2, and it amounts to around 25 000 sensors in total. Each layer is subdivided into staves in the azimuthal direction, and each stave extends over the full length of the layer in the z -direction. The staves of the Inner and Outer Barrels have a different design, because of the different length of the layers [45]. In each stave, the sensors are soldered to a Flexible Printed Circuit board (FPC), which provides the transmission of the data, the control signals and the clock. In the case of the Inner Barrel the power of the chips is also provided by the FPC, while in the Outer Barrel, a separate power bus is used to limit the voltage drop along the stave. The sensors on their other side are glued to a so-called cold-plate, which provides the cooling of the detector. The detector will be operated at room temperature, and the maximum allowed power consumption will be 300 mW/cm² (100 mW/cm²) for the Inner (Outer) Barrel layers respectively. This power consumption allows

to have the detectors water-cooled. In the case of the Outer Barrel, the cold plate, the sensors and the FPC are attached to a carbon fiber support structure, which provides the mechanical support of the sensors with low contribution to the material budget. The design is similar in the case of the Inner Barrel as well; however, for these layers, the cold plate is integrated within the support structure. The schematic drawing of the staves of the Inner and Outer Barrel layers can be seen in Fig. 3.2.

Layer	Distance from the center of the beampipe (mm)	Number of sensors
1	22.4	108
2	31.0	144
3	37.8	180
4	194.4	2688
5	243.9	3360
6	342.3	8232
7	391.8	9408

Table 3.2: The radial distance of the layers from the interaction point and the number of sensors needed to equip each layer of the detector [45].

3.2 Monolithic Active Pixel Sensors

In many of the pixel detectors currently used in high-energy physics, the sensitive layer and the readout electronics are fabricated using separate wafers, which are then bump-bonded to one-another. This is the case for the current Inner Tracking System of ALICE [47] and also for the inner detector layers of the ATLAS, CMS and LHCb detectors [50–52]. The requirement on the material budget in the case of the upgraded ITS, however, makes this hybrid technique not well suited for the upgrade. Instead, CMOS Monolithic Active Pixel Sensors were chosen, which integrate the sensitive layer and the readout electronics on the same wafer, allowing for detectors with much lower material budgets. The material budget, however, has another contribution arising from the support structure of the detector. This contribution can be reduced by a sensor with low power consumption, because it allows to minimize the material needed for the cooling.

MAPS have attractive features for high energy application (e.g. the low material budget); however, their limited radiation tolerance and moderate read-out time did not make them suitable for these applications until recently. The first implementation of MAPS for heavy-ion physics is the STAR PXL detector [53], which has been installed in 2014. The

ULTIMATE chip of the STAR experiment is using the AMS 0.35 μm OPTO process and has a pixel pitch of 20.7 μm [54]. It has a rolling-shutter readout with an integration time of 190 μs . This is much longer than the required 30 μs for the ITS, therefore further development was needed for ALICE.

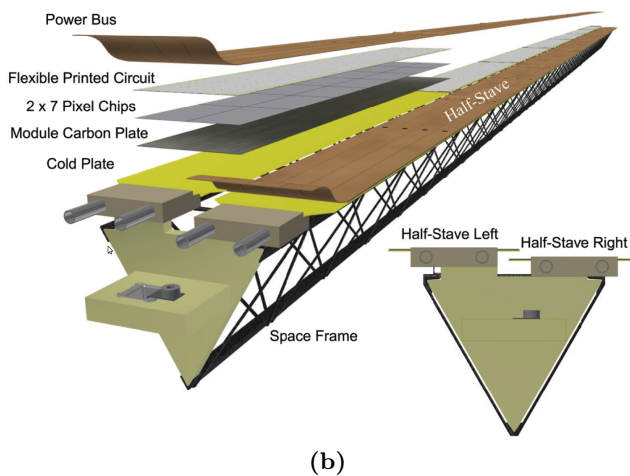
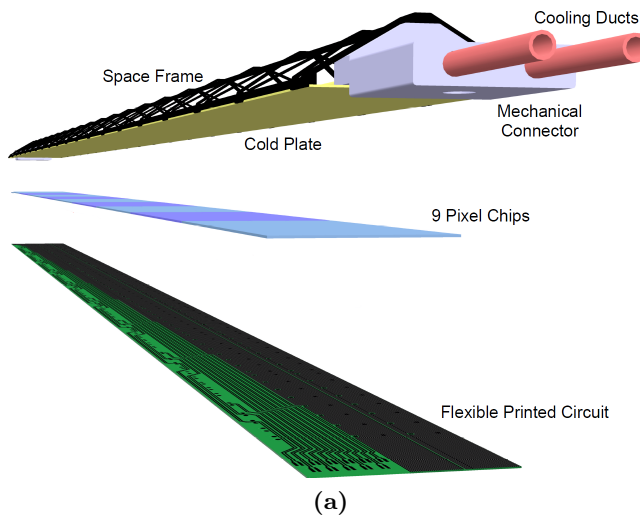


Figure 3.2: Schematic drawing of (a) the Inner Barrel stave and (b) the Outer Barrel stave, adopted from Ref. [45].

3.2.1 Technology aspects

The technology chosen for the upgrade of the ITS is the TowerJazz 0.18 μm CMOS imaging process, where the sensitive epitaxial layer is a weakly doped p-type material with an n-type implant for the collection of charge (Fig. 3.3). The traversing charged particle generates electron-hole pairs in the high-resistivity epitaxial layer, and the detection of this generated charge is based on the pn-junction of the collection diode and the epitaxial layer. Since, in contrast to hybrid silicon sensors, the sensor is not fully depleted, the electrons move by diffusion until they reach the depleted region (indicated by white in Fig. 3.3) [55]. Once the electrons reach the depleted region, they drift towards the collection diode, where they are collected and read out.

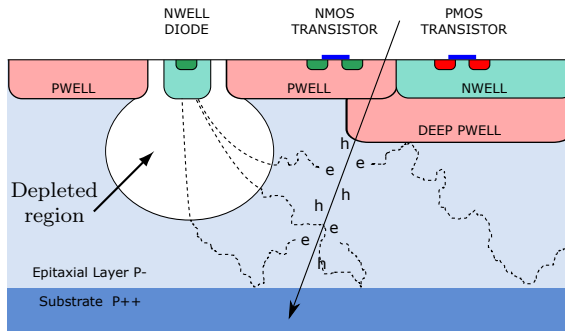


Figure 3.3: Schematic drawing of a pixel in the TowerJazz technology [45].

In the TowerJazz technology, the so called deep p-well, enables the use of full CMOS circuitry within the active area of the pixel, allowing the integration of the readout electronics into the sensitive area. This is done by shielding the n-wells of the PMOS transistors from the epitaxial layer by a p-well underneath these n-wells. Without this deep p-well, the n-wells of the PMOS transistors would be competing with the n-well of the collection diode in the charge collection process. This would result in a loss of signal, therefore full CMOS circuitry, could not be used within the active area of the pixel without accepting lower charge-collection efficiency.

Since MAPS are operated normally not fully depleted, the size and shape of the depleted region at the pn-junction have a large influence on the efficiency and the speed of the charge collection. The size and shape of the depleted region depend on many parameters, for example the size and shape of the collection diode and the thickness and resistivity of the epitaxial layer. The size of the depletion region can also be changed by applying a moderate reverse substrate bias, up to around -6 V in the case of the sensors for the ITS upgrade.

A larger depleted region is beneficial for the speed of the charge collection; however, it can lead to larger noise through a higher leakage current. This current is present even when no charge is generated in the sensor by an external source, i.e. when there are no particles passing through it. The origin of this so-called leakage current or dark current is free charge carriers entering from the non-depleted volume and thermal generation of electron-hole pairs in the depleted volume. The thermal component grows with the size of the depletion region, and therefore with the level of applied reverse substrate bias. As a consequence, the reverse substrate bias can have an influence on the magnitude of the leakage current, and therefore on the noise of the sensor as well [55]. However, even if the enlarged leakage current can be tolerated in the sensor, the reverse substrate bias cannot be enlarged arbitrarily. At a certain voltage electric breakdown occurs, at which point the sensor is not operational anymore. This might also damage the chip permanently, therefore the applied reverse substrate bias has to be always lower than this limit.

3.2.2 Radiation effects

In the experiment, the ITS will be exposed to ionizing and non-ionizing radiation, which both can damage the sensor. Non-ionizing radiation is the interaction of particles (e.g. electrons, protons and neutrons) with the nuclei of the silicon atoms. It can cause nuclei to be misplaced from their original place in the crystal, and therefore it is referred to as a bulk effect. It leads to the increase of the leakage current and to the trapping of the charge carriers in the epitaxial layer [55], which refers to the process that in the silicon of the epitaxial layer, the defects caused by radiation can result in the appearance of new energy levels, where the available carriers can get trapped. Most of the defects caused by non-ionizing radiation are not stable and can anneal over time. The time needed for annealing depends on the movement of the defects through the crystal, therefore it depends strongly on the temperature of the sensor. Stable defects, however, might also form, and these can change the characteristics of the sensors. Charge trapping results in lower detection efficiency, while higher leakage currents lead to higher noise, and both effects can worsen the position resolution. Charge trapping might be compensated by faster charge collection, which can be achieved by enlarging the depletion volume (e.g. by applying larger reverse substrate bias) and thus collecting the charge by drift from a larger area.

Ionizing irradiation causes damage in the silicon oxide layer on the surface of the sensor, therefore these effects are referred to as surface effects. The defects created by the ionization have low mobility in the oxide layer, therefore they are easily trapped. These defects can also be annealed, but

for these temperatures well above room temperature are needed (around 150°C) [55].

The TowerJazz 0.18 μm technology is expected to be radiation tolerant against ionizing radiation because it has a gate oxide thickness below 3 nm. This allows a fast recombination of the trapped holes with electrons from silicon, therefore making the sensor radiation tolerant. The radiation hardness against non-ionizing radiation can be improved by producing the sensors on a high resistivity epitaxial layer, since higher resistivity leads to a larger depleted volume. In the TowerJazz CMOS Imaging Sensor process this is possible: the chip can be produced with an epitaxial layer resistivity between 1 $\text{k}\Omega\text{cm}$ and 6 $\text{k}\Omega\text{cm}$.

3.3 The ALPIDE family

The sensor developed for the ALICE ITS upgrade is called ALPIDE, which stands for ALICE Pixel DEtector. The first prototype of this chip was fabricated in 2012. In Fig. 3.4, the development timeline of the ALPIDE chip can be seen with the main characteristics and the main purpose of each chip. These prototypes will be discussed in detail in the following.

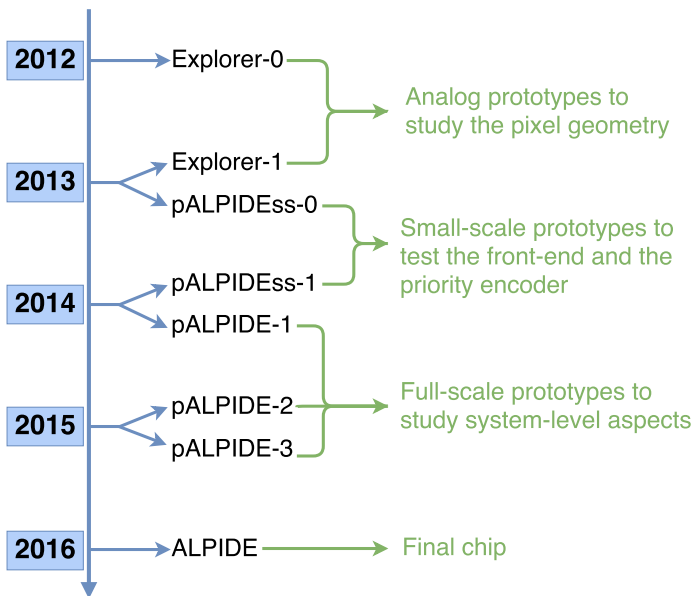


Figure 3.4: Development timeline of the ALPIDE prototypes.

3.3.1 Small-scale prototypes

There are two types of small-scale prototypes of the ALPIDE family: the Explorer and the pALPIDEss. The Explorer has analog output, while the pALPIDEss has a digital readout. In the following these will be discussed in detail.

Explorer

The Explorer was the first prototype of the ALPIDE family with the aim to optimize the sensor and the collection diode of the pixel [56]. It has two variants Explorer-0 and Explorer-1, which both contain two matrices, one with pixels of the size of $20\ \mu\text{m} \times 20\ \mu\text{m}$ and one with the size of $30\ \mu\text{m} \times 30\ \mu\text{m}$. Each of these matrices is subdivided into nine sectors with different collection diode geometries and different spacings between the collection diode and the surrounding p-well. This spacing is an area between the n-type collection diode and the surrounding p-well (p-type), which is not doped, and it plays an important role in the shaping of the depleted volume (see Fig. 3.5).

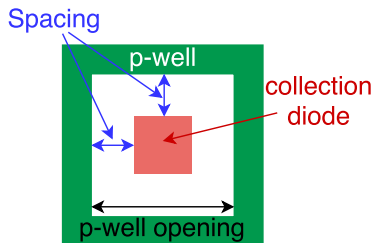


Figure 3.5: Illustration of the spacing between the collection diode and the surrounding p-well.

The Explorer chips were fabricated on wafers with different epitaxial-layer thicknesses and different resistivities, and some sensors were irradiated to test the radiation hardness of the technology. The difference between the two variants of the Explorer chip is that the circuit input capacitance, which is the capacitance of the junction between the collection diode and the following transistor, was reduced in the case of the Explorer-1. This results in a larger voltage signal for the same collected charge.

From the characterization of the Explorer, it was learned that larger spacing is beneficial between the collection n-well and the surrounding p-well, and it was also found that the optimal epitaxial layer thickness

depends on the reverse-substrate-bias value and the pixel geometry. A detailed description of the characterization results can be found in Ref. [57].

pALPIDEss

The pALPIDEss was the first ALPIDE prototype which had a digital readout [56]. The chip has 64×512 pixels of the size $22 \mu\text{m} \times 22 \mu\text{m}$ and is divided into four sectors which either differ in the pixel geometries or in the possibility to inject signals into the pixels. The discrimination of the hits is done by the front-end of each pixel, and the chip is read out by an Address Encoder Reset Decoder logic (AERD). This logic is built as a tree structure, where each element of a level represents four elements of the level underneath it, with the lowest level being the level of pixels. Each column has its own AERD, and the readout of hit pixels is done in the following way: the address of the first hit pixel is generated by the AERD based on their position in the matrix, and it is propagated to the periphery. The same pixel, which is being read out, is also reset, and once the pixel is reset the logic moves on to reading out the next hit pixel [58]. The schematic drawing of the address generation in the case of 16 pixels can be seen in Fig. 3.6. In this case four pixels belong to one group, and for 16 pixels four groups of four pixels exist. In Fig. 3.6a, a situation is shown, where two pixels fire. First, the address of the pixel on the top is generated and propagated to the periphery, and this pixel is reset. The situation at this

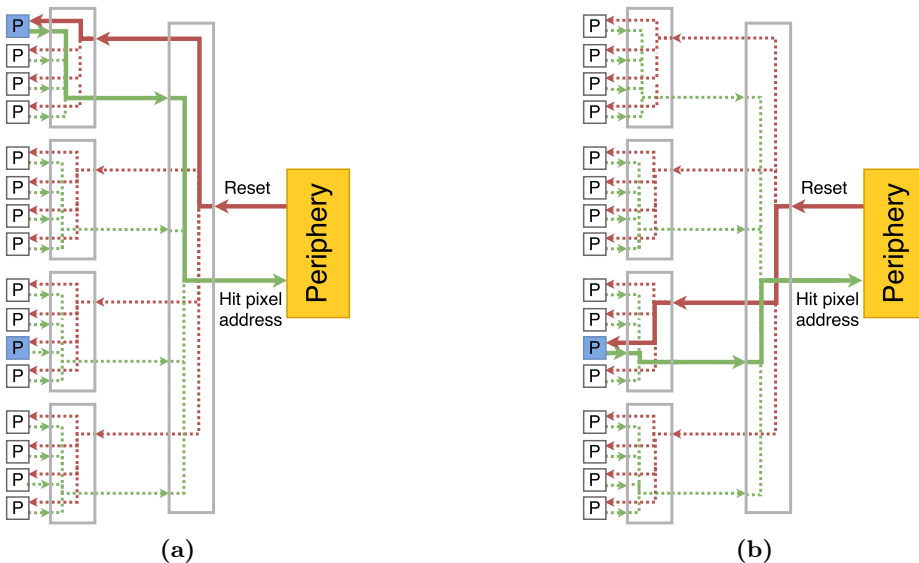


Figure 3.6: Schematic drawing of the principle of operation of the readout and reset of the pixels by the AERD.

point can be seen in Fig. 3.6b. At that moment the logic moves to the next hit pixel, which in the example is situated in the third block of four pixels. The address of this pixel is generated and propagated, and this pixel is also reset. Since in each level four elements of the previous level are grouped together, to read out 16 pixels, only two levels are required. In the final chip, one AERD will read out 1024 pixels, therefore five such levels will be present. The working principle of this AERD logic has been successfully validated by the measurements done with the pALPIDEss prototype [59].

3.3.2 The pALPIDE-1 sensor

The pALPIDE-1 is the first large-scale prototype of the ALPIDE family, and the schematic drawing of its building blocks can be seen in Fig. 3.7. The amplification and the discrimination of the analog signal are done within each pixel, and the address of the hit pixels is encoded in the AERD as was discussed for the pALPIDEss. These addresses are propagated to the periphery, where they are stored, and a data-compression can be performed before transmitting the hit information off the chip. The recorded hits can be from real particles passing through the sensor, from noise, or analog and digital signals can be injected into selected pixels to test the response of the pixels.

The control and trigger signals are provided to the periphery, and the control logic in the periphery manages the AERD and the pixels. The bias currents and bias voltages are also generated in the periphery by digital to analog conversion (DAC) and are then propagated to all the pixels from there.

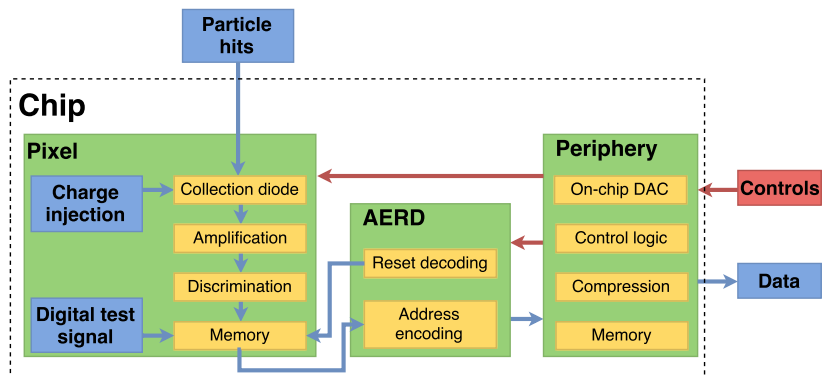


Figure 3.7: Schematic drawing of the building blocks of the digital prototypes of the ALPIDE family.

The pALPIDE-1 has a size of $15.3 \text{ mm} \times 30 \text{ mm}$, and it consists of 512×1024 pixels, which are $28 \text{ }\mu\text{m} \times 28 \text{ }\mu\text{m}$ large. It has digital input and output signals and a similar AERD as in the pALPIDEss, which provides the readout of any hit pixel and the reset of the pixels. In the case of the pALPIDE-1, columns are grouped into pairs, and each double column has an AERD, which is built as a full-custom logic [60]. The chip is organized into 32 regions with 16 AERDs belonging to each region. The regions are read out in parallel, while within the region the fired pixels are read out sequentially. The AERD always reads out the hit pixels in the order of their priority, which only depends on their placement in the matrix. Therefore if a pixel cannot be reset, the AERD will keep on trying to read out and reset that one pixel, since that is the one with the highest priority. It has to be prevented that this stops the read out of the chip completely, therefore a mechanism is implemented in the chip that if a pixel cannot be reset, the full double column in which this pixel is situated is turned off.

Fig. 3.8 shows how the signal is processed before the AERD logic. Charge is collected on the collection diode or injected through a capacitance (C_{inj}), both resulting in a voltage drop on the PIX_IN node. In the analog front-end of the chip, the signal is amplified and discriminated by comparing it to a certain threshold level. After that the binary signal is propagated to the in-pixel memory.

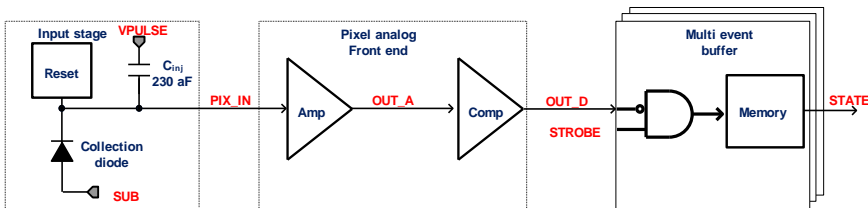


Figure 3.8: Schematic drawing of the in-pixel signal processing in case of the digital prototypes of the ALPIDE family, adopted from Ref. [61].

The working principle and the schematic drawing of the analog front-end of the pALPIDE-1 can be seen in Fig. 3.9 [61]. In Fig. 3.9a, it is shown how charge is collected on the PIX_IN node of the pixel and how, with M_1 acting as a source follower, the $SOURCE$ node follows the PIX_IN node. Therefore a voltage drop at the PIX_IN node results in the transfer of charge from the large capacitance of C_{SOURCE} to a small capacitance at C_{OUT_A} , resulting in a voltage gain. The concept of the analog front-end of the pALPIDE-1 is shown in Fig. 3.9b. At rest, the currents I_{thr} and I_{bias} flow through M_3 , and the baseline at the OUT_A node is defined by the voltage needed to let I_{thr} flow through M_5 at a

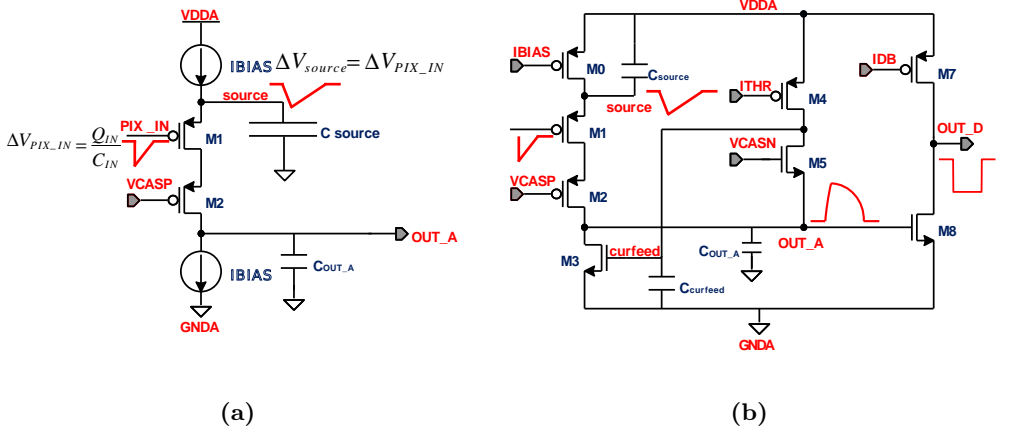


Figure 3.9: Schematic drawing of the input branch the analog front-end (a) and of the concept of the analog front-end (b). Adapted from Ref. [61].

fixed V_{CASN} value. When there is a hit, the voltage at the OUT_A node increases, and an increased voltage at the gate of M_8 increases the current through it. When the current through M_8 becomes larger than I_{db} , the discriminated signal (active low) appears at the OUT_D node. From there the discriminated signal is propagated to the in-pixel memory. The voltage increase at the OUT_A node from a hit results in the redirection of I_{thr} from M_5 towards $C_{CURFEED}$. This causes I_{thr} to charge up $C_{CURFEED}$, which results in a larger conductance of M_3 , and therefore the discharging of the OUT_A node.

The amount of charge needed for a discriminated hit to appear on the OUT_D node depends on the parameters of the analog front-end. The baseline at the OUT_A node is defined by V_{CASN} and the current through M_5 such that at the same current a higher V_{CASN} causes a higher voltage at the OUT_A node. A higher baseline at the OUT_A node results in less charge needed for a signal to appear at the OUT_D node, i.e. a higher V_{CASN} setting leads to a lower charge threshold. A higher setting of I_{thr} , on the other hand, leads to a lower baseline at the OUT_A node, i.e. a higher charge threshold. A higher I_{thr} setting also leads to the faster discharge of the OUT_A node by making $C_{CURFEED}$ charge up faster. Since the two parameters (I_{thr} and V_{CASN}) have opposite effects on the charge threshold, the same charge threshold can be achieved by different combinations of the two. They, however, influence the other parameters of the circuit differently (e.g. the length of the pulse), therefore it is important to study whether any of the measurements are sensitive separately to the two parameters.

In Fig. 3.10, the implementation of the full analog front-end of the pALPIDE-1 chip is shown. To make the front-end more compact the transistors C_{SOURCE} and $C_{CURFEED}$ are combined into one transistor (C_S), which also results in a faster charge up of the OUT_A node. The C_S transistor introduces a capacitive coupling between the $SOURCE$ and the $CURFEED$ nodes, therefore a hit directly changes the conductivity of M_3 , allowing less current to flow through it, which results in the faster charge up of the OUT_A node. A clipping mechanism is also implemented, which is needed to limit the pulse length of hits with large charge deposit. This is done by the M_6 transistor, which is in diode connection between the $CURFEED$ and the OUT_A node, meaning that its source and gate are connected to the same potential. It is reverse biased in its rest state, therefore no current is flowing through it. When, however, the signal at OUT_A becomes higher than $V_{CURFEED}$, it gets forward biased, allowing a current to flow through it. This results in a much faster discharge of the OUT_A node after hits which deposited a large amount of charge in the pixel.

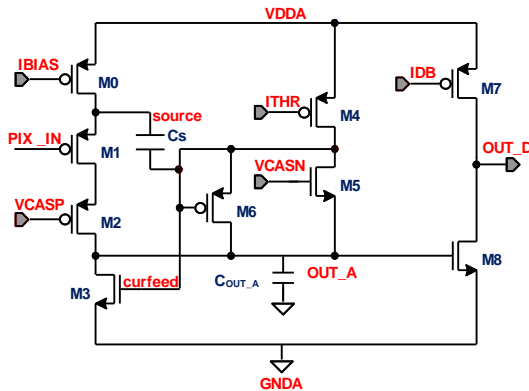


Figure 3.10: Schematic drawing of the practical implementation of the analog front-end in the pALPIDE-1, adapted from Ref. [61].

The charge threshold can be measured by injecting a known amount of charge into the input node, which is possible by applying a voltage step in the front-end circuit to a capacitance of $C_{inj} = 230$ aF. This capacitance is connected to the PIX_IN node, and a voltage step (ΔV) applied to it results in an injected charge of $Q_{inj} = \Delta V C_{inj}$. By varying the applied voltage and thus the amount of injected charge, it can be studied at which level the pixel starts to fire. The level where the pixel fires with

50% probability is then called the charge threshold. The details of such a measurement will be discussed in Section 5.1.

To improve the charge collection, it is possible to apply a moderate reverse substrate bias (up to around $V_{BB} = -6$ V) also in the case of the pALPIDE-1 chip. The body of the NMOS transistors in the front-end are on the reverse-substrate-bias voltage, therefore changing it results in a change of the operating point of the sensor. This changes the charge threshold and is compensated by adjusting V_{CASN} for each level of reverse substrate bias.

As shown in Fig. 3.11, the pixel matrix of the pALPIDE-1 sensor is divided into four sectors along its longer side with different pixel geometries and with different reset mechanisms. Three of the four sectors differ in the spacing between the collection n-well and the surrounding p-well (ranging from $1\ \mu\text{m}$ to $4\ \mu\text{m}$) (see Fig. 3.5), while the fourth sector has a different reset mechanism implemented. The details of the sectors are shown in Table 3.3.

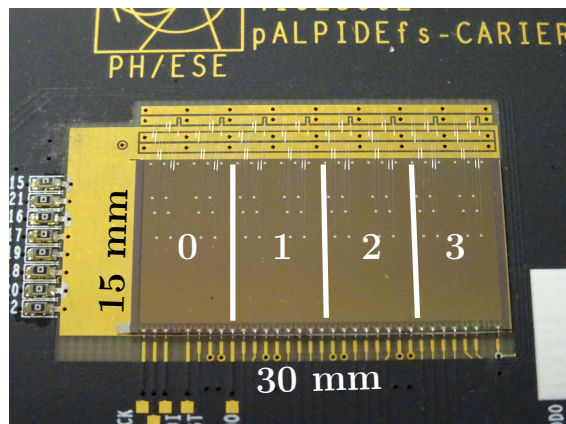


Figure 3.11: Picture of the pALPIDE-1 chip with the four sectors indicated.

Sector	N-well diameter	Spacing	P-well opening	Reset
0	$2\ \mu\text{m}$	$1\ \mu\text{m}$	$4\ \mu\text{m}$	PMOS
1	$2\ \mu\text{m}$	$2\ \mu\text{m}$	$6\ \mu\text{m}$	PMOS
2	$2\ \mu\text{m}$	$2\ \mu\text{m}$	$6\ \mu\text{m}$	Diode
3	$2\ \mu\text{m}$	$4\ \mu\text{m}$	$10\ \mu\text{m}$	PMOS

Table 3.3: Details of the four sectors of the pALPIDE-1 chip.

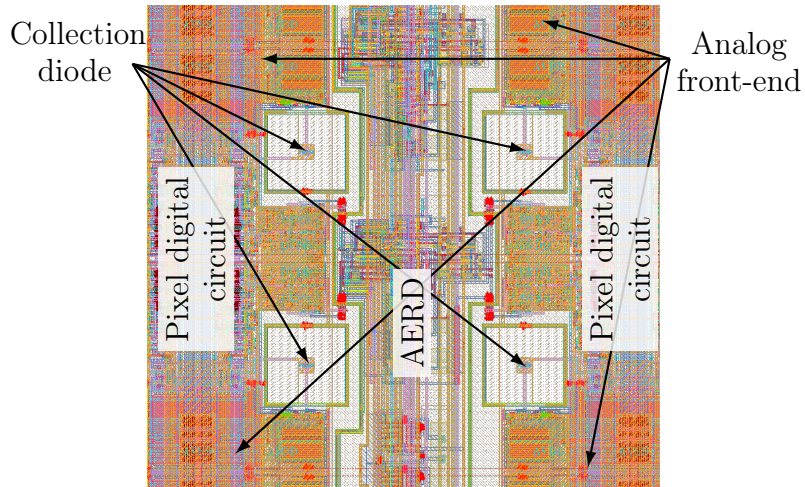


Figure 3.13: The routing plan of the smallest repeated unit of two times two pixels ($56 \mu\text{m} \times 56 \mu\text{m}$) with the different areas indicated [62].

3.3.3 The pALPIDE-2 and pALPIDE-3 sensors

The pALPIDE-2 and pALPIDE-3 chips are final-size ($15 \text{ mm} \times 30 \text{ mm}$) prototypes of the ALPIDE family. The pALPIDE-2 has the same pixel size as the pALPIDE-1, while the pALPIDE-3 has a slightly modified pixel pitch of $29.24 \mu\text{m} \times 26.88 \mu\text{m}$. Just as the pALPIDE-1, these chips also have binary output signals and an AERD. The AERD of the pALPIDE-2 is the same as of the pALPIDE-1, while the logic of the pALPIDE-3 is built from standard cells in contrary to the full custom logic of the pALPIDE-1 and the pALPIDE-2. These prototypes are also segmented into sectors with different pixel geometries: the pALPIDE-2 has four sectors, while the pALPIDE-3 has eight different sectors. Their characteristics can be found in Tables 3.4 and 3.5, respectively. The main goal for the sectors in the pALPIDE-2 is to test the effect of the reset mechanism and of the spacing

Sector	Spacing	Reset	Input transistor size
0	$2 \mu\text{m}$	PMOS	small
1	$2 \mu\text{m}$	PMOS	large
2	$4 \mu\text{m}$	PMOS	small
3	$4 \mu\text{m}$	Diode	small

Table 3.4: Details of the four sectors of the pALPIDE-2 chip [59].

Sector	Transistor size (M_3, M_4, M_5, M_8)	Introduction of V_{CASN2}	Connection of M_6 gate	Connection of M_1 bulk	Reset	Spacing
0	optimized	Yes	diode connection	AVDD	Diode	2 μm
1	optimized	No	diode connection	AVDD	Diode	2 μm
2	as in pALPIDE-1/2	No	diode connection	AVDD	Diode	2 μm
3	optimized	Yes	V_{CLIP}	AVDD	Diode	2 μm
4	optimized	Yes	V_{CLIP}	Source	Diode	2 μm
5	optimized	Yes	V_{CLIP}	Source	Diode	3 μm
6	as in pALPIDE-1/2	No	diode connection	AVDD	PMOS	2 μm
7	optimized	Yes	V_{CLIP}	AVDD	PMOS	2 μm

Table 3.5: Details of the eight sectors of the pALPIDE-3 chip [63].

between the collection n-well and the surrounding p-well, but there is also a sector where the change is the size of the input transistor. This sector was expected to have a lower fake hit rate, but a higher charge threshold. The lower fake hit rate was confirmed by the measurements, but no significant change in the threshold was seen.

In the pALPIDE-3, the analog front-end was further optimized to reduce the length of the pulse and the spread in the charge threshold values between pixels (Fig. 3.14). The fully optimized pixels with a diode reset are in sectors 4 and 5 for two different values of the spacing between the collection diode and the surrounding p-well. Sector 7 is the fully optimized circuit in the case of a PMOS reset. The other sectors correspond to the optimization steps of the analog front-end. Sectors 2 and 6 are non-optimized, and they are included to allow the direct assessment of the effects of the optimization. The steps of the optimization are the following: in sector 1, the size of several transistors were optimized. In sector 0, V_{CASN2} is introduced to reduce the parasitic coupling of OUT_A and OUT_D (indicated by C_{P1} in Fig. 3.14). In sector 3, V_{CLIP} is introduced, which allows to set the clipping threshold where M_6 gets forward biased. The final step of the optimization, in sectors 4 and 5, is the change in the connection of the bulk of the M_1 transistor, which results in larger gain.

Other new features were also introduced in the pALPIDE-2 and the pALPIDE-3, which were missing from the pALPIDE-1. The pALPIDE-2 is the first prototype, where all the functionality to build detector modules from it are included. In the pALPIDE-3, three in-pixel memories were introduced, which derandomize the readout of a pixel. This is needed to cope with the expected data-taking rate of ALICE [63].

While the pALPIDE-1 was produced on wafers with 18 μm thick epitaxial layers only, the pALPIDE-2 and pALPIDE-3 prototypes were produced on wafers with different thicknesses (18 μm , 25 μm and 30 μm). A thicker epitaxial layer means the sensitive volume traversed by the charged

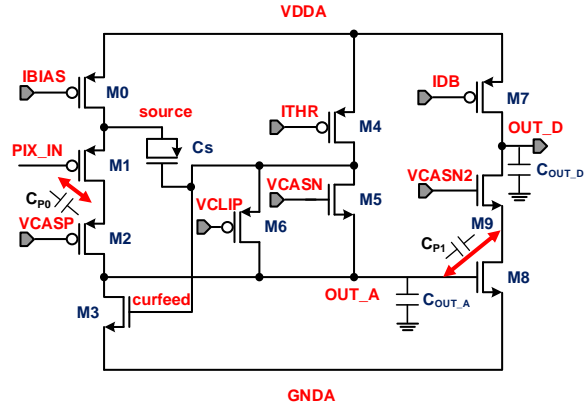


Figure 3.14: The schematic drawing of the analog front-end of the pALPIDE-3 chip [61].

particles is larger, therefore larger signal is expected. If the size of the depletion region, however, is the same, the volume where the signal travels by diffusion is larger, therefore charge collection can become slower or less effective, or the charge can spread over many pixels. It is therefore expected that the advantages of a thicker epitaxial layer become more pronounced if higher reverse substrate bias is applied, if the spacing between the collection n-well and the surrounding p-well is enlarged or with an epitaxial layer with higher resistivity. These effects were confirmed by measurements [59].

3.3.4 The ALPIDE sensor

ALPIDE is the final chip developed for the ALICE ITS upgrade. It is $15 \times 30 \text{ mm}^2$ as the earlier prototypes with 512×1024 pixels of $29.24 \mu\text{m} \times 26.88 \mu\text{m}$ [64]. It has only one pixel flavor, which corresponds to sector 5 of the pALPIDE-3, which had the fully optimized analog front-end with a diode reset and a spacing of $3 \mu\text{m}$ between the collection n-well and the surrounding p-well. The large input transistor, which was found to be beneficial for the noise occupancy in the pALPIDE-2 and pALPIDE-3 was kept for the ALPIDE as well. The chip is produced with $25 \mu\text{m}$ thick epitaxial layer, and minor modifications were introduced in the periphery to further optimize the power consumption and the tolerance to single event upsets.

4. Sensor prototype characterization tools

The prototypes of the upgrade have to be thoroughly characterized to test whether they fulfill the requirements of the upgrade or whether further optimization is needed towards the final sensor. Several functionalities of the sensor have to be tested, and different environments are required for the different measurements. Many measurements can be done without external sources, for example measuring the charge threshold and the noise occupancy of the chip. Some test, however, require external sources, for example the measurement of the charge collection efficiency requires an ^{55}Fe source, while the detection efficiency can be determined in test-beam measurements. In this chapter, the setups used for the different tests will be discussed, with emphasis on the measurements done at the test-beam facilities.

4.1 Measurement methods

The tests of the sensors of the ALPIDE family start with verifying the read and write options to all registers of the chip and with validating the analog and digital circuitry of the chip. After the chip passes these tests, the charge threshold and the temporal noise of the chip can be measured. This is done by injecting charge into the pixels and measuring at which level of charge the pixels fire (for details see Section 5.1). This measurement is used also to establish the proper working range for each parameter of the chip, which might vary depending on the biasing conditions or on the irradiation level and the temperature of the chip. Once the proper settings are established, the noise occupancy values with these settings are measured. This can further limit the working range of the parameters, since the noise occupancy has to stay below 10^{-6} hits/event/pixel for the upgrade.

Once the working conditions from the previously described measurements are established for the chip, it can be tested in test-beam measurements. This is done by using a setup, called a telescope, of seven

pALPIDE-1 chips which is described in detail in Section 4.3. The central layer is being tested and is referred to as the Device Under Test (DUT), while the other six are used for tracking. The tracks are interpolated to the DUT, and the detection efficiency, the spatial resolution and the shape and size distribution of the clusters of this chip is measured.

There were several measurements at test-beam facilities to test the performance of the ALPIDE prototypes. These were done at the Proton Synchrotron (PS) and the Super Proton Synchrotron (SPS) at CERN, at the DESY II synchrotron at the Deutsches Elektronen-Synchrotron (DESY) and at the beam-line called Beam Test Facility (BTF) at the National Laboratory of Frascati. The main settings, parameters and goals of each measurement campaign of the pALPIDE-1 chip are summarized in Appendix A.

All of these measurements, in the case of the full-scale ALPIDE prototypes, are done in a setup where the sensor is wire-bonded to a carrier card, which is connected to a DAQ board via an edge connector. The DAQ board is read out by a computer via a USB-3 connection. The picture of this setup can be seen in Fig. 4.1.

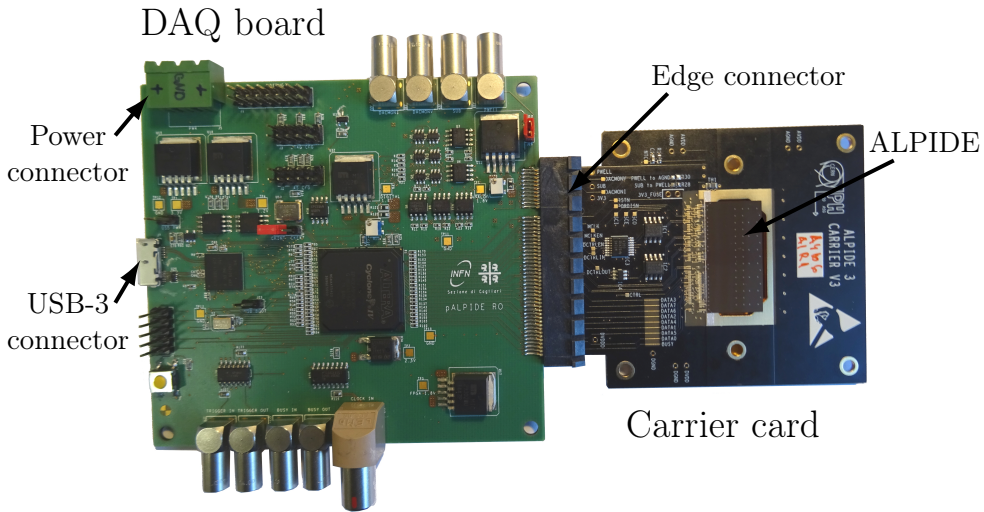


Figure 4.1: Picture of the setup used for the tests of the full-scale ALPIDE prototypes.

4.2 The EUTelescope framework

In the case of the measurements at test-beam facilities, the data taking is done by the EUDAQ framework¹, and the analysis of the collected data is performed by the EUTelescope framework [66,67]². Both of these software packages are written for general usage, and therefore have to be adapted to be used with the ALPIDE prototypes. This is done by including in the framework a sensor specific *Producer* which reads the data of the chip during data-taking, a *Converter* which accesses the data saved during data-taking, and processors for any further analysis of the data that is specific to the ALPIDE. In this way, the full data analysis can be done within the framework, from processing of the raw data to the calculation of the detection efficiency and the spatial resolution.

To be able to perform any analysis of the data, it first has to go through a few stages of preparation. First, the data has to be converted to the internal format of the software, then it has to be prepared for the analysis by identifying noisy pixels and inactive double columns. The fired pixels can then be grouped into clusters, and these clusters can be used for aligning the planes and for tracking. Once the tracks are identified, the final analysis, including the calculation of the detection efficiency and spatial resolution, can be performed. The structure of the framework is such, that it has separate steps for all these different stages of the analysis. These steps can be seen in Fig. 4.2 and are discussed in detail in the following:

- **converter**

The data recorded during data-taking is converted during this step to the internal format of the framework called *lcio*, which stands for Linear Collider Input Output. In this step the chip specific *Converter* is needed to access the recorded data.

- **deadColumn**

As was discussed in Section 3.3.2, the logic of the AERD is such that it loops through all pixels which were hit, it generates and propagates the address of these pixel to the periphery, and it resets them. If the pixel is faulty and cannot be reset, it can cause the AERD to keep reading out the same pixel over and over again, stopping the full readout of the chip. In the case of the full-scale ALPIDE prototypes, if this happens, the full double column gets deactivated, therefore the affected AERD is not used anymore. If this is not taken into account during the analysis, the detection efficiency of the chip will be artificially lower than the real value, since hits, which would have

¹Documentation and source code can be found at Ref. [65]

²Documentation and source code can be found at Ref. [68]

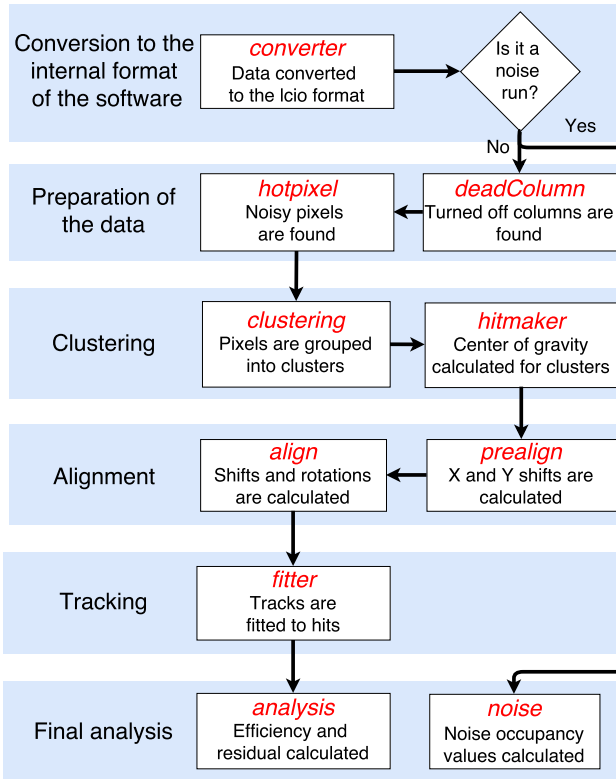


Figure 4.2: Flowchart of the analysis steps. The red headers indicate the names of the steps in the framework.

been in the deactivated double column, were not saved during data-taking. This situation can be avoided with two methods: the first method is that the faulty pixels are masked during data taking, so that they do not need to be reset, therefore they do not cause the double column to be switched off. If this was not done, deactivated double columns have to be taken care of at the stage of the analysis. If a pixel cannot be reset, it appears in the data twice in the same event. This step therefore saves all pixels of double columns, in which the same pixel appeared twice in one event. It also compares the average number of hits per event in each double column to the surrounding double columns, and if a double column has 30% less hits than the surrounding double columns, the pixels of the double column are saved. The saved pixels can be ignored by later steps, thus masking the faulty double columns.

- **hotpixel**

If a pixel is too noisy or faulty, it can fire frequently, up to firing in every event. These hot pixels can cause problems in aligning the planes or in fitting tracks to the hits. In this step hot pixels are identified and removed from the further analysis. To speed up the analysis process, only the first 10 000 events are analyzed, and if a pixel fires more than a certain frequency, it is treated as a hot pixel. In the data analysis of the pALPIDE-1, this step is repeated twice with two different cuts: there is a tight cut used for the alignment and a looser cut used for the calculation of the efficiency and the resolution values. This is needed because the alignment is much more sensitive to the presence of hot pixels than all the other steps.

- **clustering**

A charged particle can generate charge in more than one pixel or the generated charge can diffuse to more than one pixel. This results in a cluster of pixels firing for one passing particle. In this step, these clusters are identified by grouping pixels which fired in the same event together. It can be set how far two pixel can be for considering them as belonging to one cluster. The algorithm loops through all fired pixels, and to each of them it groups the other fired pixels which are closer than the maximum allowed distance (in the current Thesis only first neighbors are considered). It then repeats the same search in the case of the pixels, which fulfilled the distance criteria, therefore finding all pixels belonging to a cluster.

- **hitmaker**

In this step, the center of gravity is calculated for each cluster identified in the previous step, and from this step on each cluster is represented by the x , y , z coordinates of its center of gravity. These calculated hits then undergo a coordinate system transformation, which transforms them from the local coordinate system of each chip to a global coordinate system. The $(0, 0, 0)$ point of this coordinate system is the center of the first chip. The positions and sizes of all the chips needed for this transformation are taken from a so-called gear file containing the geometry description of the setup. This is specific to the chips used and to the mechanical setup. These differ from test-beam campaign to test-beam campaign, thus a separate file is needed for all test-beam setups. The z -axis of the global coordinate system is pointing along the beam, in the direction of the beam, the x -axis is horizontal and the y -axis is vertical. The global coordinate system is needed for the alignment of the planes and to perform the track fitting.

- **prealign**

The alignment of the planes is done in two steps: *prealign* and *align*. These two steps try to correct for the fact that our description of the positions of the planes is not perfect, therefore the real global hit position might not be the position that is measured within the chip. This step calculates the distance in x and y between the position of hits in the first plane and the position of hits in all other planes. For each plane, it then calculates and saves how much the mean of this distribution is shifted from 0. In this step, no correction is done on the rotation of the planes, therefore this is a rough estimate of the alignment and can treat planes misaligned up to 3 – 4 mm.

- **align**

Once the rough estimate of the alignment is obtained in the previous step, the precise alignment can be calculated. This is done in this step, where straight tracks are fitted through the hits in the planes. The hits in the first and the last planes are treated fixed and the best parameters for the alignment constants are calculated by a χ^2 minimization. In this step three alignment constants per layer are fitted: the shifts in x and y and a rotation in the x - y -plane. The data is not very sensitive to the shift in z and the other two rotations, thus their corrections are not calculated from the data. The obtained alignment parameters are saved in both this and the *pre-align* step, and they must be applied to the data in any later steps. This means a transformation of the hit positions according to the calculated alignment constants.

- **fitter**

In this step, broken-line tracks are fitted to the hits in the tracking planes. The DUT is not included in the fitting to be able to study its detection efficiency and spatial resolution unbiased; however, the impinging point of the track at the DUT is calculated. The details of the tracking model will be discussed below.

- **analysis**

In the previous step, the impinging point of the track at the DUT was calculated, but since the hits of the DUT were not included in the tracking, they are not yet associated to tracks. This association is performed in this step, and the detection efficiency and spatial resolution is calculated. The size and shape of clusters is also studied in this step, which is specific to the ALPIDE prototypes.

- **noise**

This step is also specific to the ALPIDE prototypes, and it is used only for data which was taken with the setup outside of the beam to study the noise occupancy of the chip. It integrates over all events taken and calculates the average noise occupancy.

4.2.1 Tracking models

Different models can be used for tracking depending on the data taking conditions and on the requirements on the precision of the tracking. The outer layers of the setup are used for fitting the track, which is then interpolated to the DUT whose hits were not used in the fitting. The concept is illustrated in Fig. 4.3, where the central plane is indicated as the DUT. In most of the cases only the central plane was treated as the DUT; however, in some cases the settings of all three central planes were changed and all of them were treated as DUTs. This data was analyzed such that the tracking was repeated three times, always omitting the hits of one of the DUTs, but using the hits of the other two DUTs in the fitting.

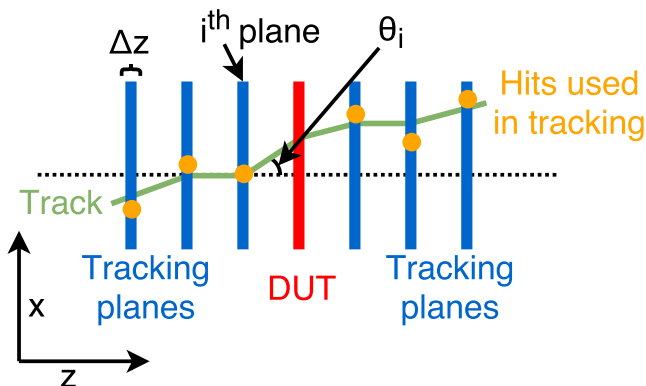


Figure 4.3: The drawing illustrates the concept of the tracking.

Straight-line tracks are the simplest model, but they are accurate only if the multiple scattering in the tracking layers can be neglected. On the other hand, if there is significant multiple scattering, so-called broken-line tracks, tracks which are allowed to change direction at the layers, give a more accurate description of the path of the particles. These models can account for the material of each detector layer by the change of the direction of the track at these layers. The tracking model used for the analysis of the data from the ALPIDE prototypes is discussed in detail in Ref. [69], and it is summarized below.

The model needs a few conditions to be fulfilled, which are all reason-

able to assume in the case of the setup of the full-scale ALPIDE chips. The conditions are the following:

- The angle between the particle track and the nominal beam direction is small.
- The beam is perpendicular to the planes, therefore the amount of material traversed and the traveled distance between the planes are the same for all tracks.
- The thickness of the planes (Δz) can be neglected compared to the distance of the layers.
- There is no correlation between the horizontal and vertical position-measurements.
- The distribution of the scattering angle is Gaussian, and its width can be described by the following formula [35]:

$$\Delta\theta = \frac{13.6 \text{ MeV}}{\beta c p} Z \sqrt{\frac{\Delta z}{X_0}} \left[1 + 0.0038 \ln \left(\frac{\Delta z}{X_0} \right) \right] \quad (4.1)$$

where p is the momentum, βc is the velocity and Z is the charge of the particle, Δz is the thickness of the material traversed, and X_0 is the radiation length of the material.

- The distribution of the distance between the hits and the tracks is Gaussian in all planes.

If all these conditions are met, the tracking can be done in only one-dimension and be repeated for the x and the y direction separately. The fitting is done by a χ^2 -minimization, where the χ^2 has two contributions: one from the distance of the track and the measured hits and one from the scattering in the material of the planes:

$$\chi^2 = \sum_{i=1}^N \left(\frac{y_i - p_i}{\sigma_i} \right)^2 \Big|_{i \neq i_{DUT}} + \sum_{i=2}^{N-1} \left(\frac{\Theta_i - \Theta_{i-1}}{\Delta\Theta_i} \right)^2 \quad (4.2)$$

where the index i denotes the planes starting from 1, y_i is the hit position, p_i is the track position, σ_i is the resolution, $\Delta\Theta_i$ is the average scattering angle, and Θ_i is the angle between the nominal beam direction and the track. The first term in this equation is missing for the DUT, because the DUT is treated as a so-called passive layer, which means that its hits are not used for the calculation of the χ^2 . The track, however, is allowed to break at the DUT, therefore the second term is present for also the DUT.

4.3 Optimization of the telescope setup

One of the parameters to be measured at the test-beam facilities is the spatial resolution of the sensor. This, however, cannot be measured directly, only the residual distribution, which includes the resolution of the plane (σ_{DUT}), but also has a contribution from the uncertainty of the tracking (σ_{track}). The residual (σ) can be written as the following:

$$\sigma^2 = \sigma_{DUT}^2 + \sigma_{track}^2. \quad (4.3)$$

The requirement of the upgrade is that the resolution has to be around 5 μm , therefore an interpolation uncertainty below 5 μm is needed to calculate a precise estimate of the resolution. Before assembling the telescope for the measurements, studies were performed to find the best geometry with which the lowest possible interpolation uncertainty can be achieved using the given sensors. The studied parameters effecting the uncertainty were the following:

- Distance between the layers
- Which layer is the DUT
- Number of the layers
- Effect of having air or vacuum between the layers
- Momentum of the particles
- Material budget
- Resolution of the tracking planes

The last two points were studied, because the pALPIDE-1 chip was not yet available when the planning of the telescope started, therefore its resolution was not yet known. It was also not yet clear whether chips thinned to 50 μm will be available, and how they will be bonded, which both can change the material budget significantly. In the following, the effect of all these parameters will be shown.

The simulation used for the study of the interpolation uncertainty uses the same track model as the reconstruction algorithm in EU Telescope, therefore it can also be used directly to calculate σ_{track} , which is needed to determine the resolution (σ_{DUT}) from the residuals (σ) in data. It assumes that in each plane there is a hit, and it scatters these hits according to a Gaussian distribution around the place where the particle passed through the sensor to account for the finite resolution of the planes. It also assumes scattering according to Eq. (4.1) in each plane and on the air between the

layers if the setup is not simulated in vacuum. In this case, the air is treated as an extra layer in the center between each plane.

In Ref. [69], it is shown that in the case of the tracking model used in the EUTelescope framework, the uncertainty of the track positions in each plane can be calculated analytically. This means that if a perfect resolution is assumed for the DUT, the width of the residual distribution at the DUT should be equal to the analytically calculated uncertainty of the position of the fitted tracks at the DUT. This was thoroughly checked by comparing the two, and it was found that for a large enough number of tracks (around 10 000), the two values are in good agreement, therefore the calculations in Ref. [69] are confirmed. This means that it is not necessary to simulate thousands of tracks, but the pointing resolution of the track can be taken from the analytically calculated uncertainty of the fit parameters.

4.3.1 Default parameters of the simulations

In the following, one parameter of the simulation at a time will be changed to study its effect, while all the other parameters will be kept at their default values. The default values try to describe a reasonable setup, but they do not correspond to the best-case scenario. In the default case, a test at the PS with pions with momenta of 6 GeV/ c will be considered. Seven planes will be used, which will be placed symmetrically with the central one being the DUT, and there will be air between the layers. It is assumed that the chips are not thinned, therefore they will be treated as 450 μm thick, and they will be soldered to a FPC. This corresponds to an equivalent thickness of 0.566 mm of silicon for each layer. The contribution to the scattering material from the different layers will be described in Section 4.3.2.

For the resolution, the scenario when for all crossing particles only one pixel fires will be assumed. If a uniform density of the incoming particles is assumed, and if only particles crossing a certain pixel cause that pixel to fire, the resolution can be calculated and is found to be [55]:

$$\sigma_{DUT}^2 = \frac{d^2}{12} \quad (4.4)$$

where d is the pixel pitch ($d = 28 \mu\text{m}$ for the pALPIDE-1). This results in a resolution of $\sigma_{DUT} = 8.1 \mu\text{m}$ for the pALPIDE-1, which will be used as the default value in the simulation. All the default parameters are summarized in Table 4.1.

Parameter	Default value
Momentum	6 GeV/ c
Particle type	pions
In vacuum	No
Number of planes	7
Symmetric setup	Yes
DUT	Central plane
Equivalent thickness of layers in Si	0.566 mm
Resolution	8.1 μm

Table 4.1: Default parameters of the simulation.

4.3.2 Study of the effect of the parameters

Arrangement of layers

The effect of the distance of the layers, and whether an asymmetric setup is preferred over a symmetric one were studied. It is expected that varying the distance between the layers has a large effect, since the further apart the layers surrounding the DUT are, the more pronounced the effect of multiple scattering becomes. This would mean that it is better to keep the layers as close as possible; however, if they would be moved infinitely close, the best uncertainty, which can be achieved, would be the resolution of the tracking planes themselves. There are also limitations on how close the layers can be moved, for example they cannot easily be moved closer than the thickness of the DAQ boards. Therefore it has to be confirmed whether moving them as close as possible is beneficial, and if yes, whether they can be moved close enough to have a smaller interpolation uncertainty than 5 μm .

The sensors have to be shielded from light to avoid dependencies in the operating point of the sensor on the lighting conditions. For this reason, the layers have to be placed in light-tight boxes, where one possibility is to place the full telescope in one box, but another option would be to place groups of chips into boxes. This can be beneficial for example if the DUT needs to be changed often, because then only the box of the DUT has to be opened. It was therefore studied whether keeping the DUT separately in a box is a valid option, or whether grouping it with one other plane would help in the interpolation, which would still make the exchange of the DUT easier.

In Fig. 4.4, the effect of the distance of the planes can be seen. It can be concluded that the distance has a large influence on the pointing resolution, and that keeping the planes as close as possible is crucial. It can also be seen that if the DUT is kept close to one of the neighboring tracking planes, the effect of increasing all the other distances is much smaller, therefore if it is necessary to move the planes further, it would be important to keep at least the distance of the DUT and the surrounding planes small. It can also be seen from Fig. 4.4b that if the planes are sufficiently close, placing the DUT asymmetrically does not result in a better interpolation; however, if the planes are 20 cm apart, placing the DUT asymmetrically (close to one plane and far from the next) is better. The DAQ boards are around 2 cm wide, therefore the smallest distance allowed by the DAQ board seems to be enough to measure a resolution of around $5 \mu\text{m}$.

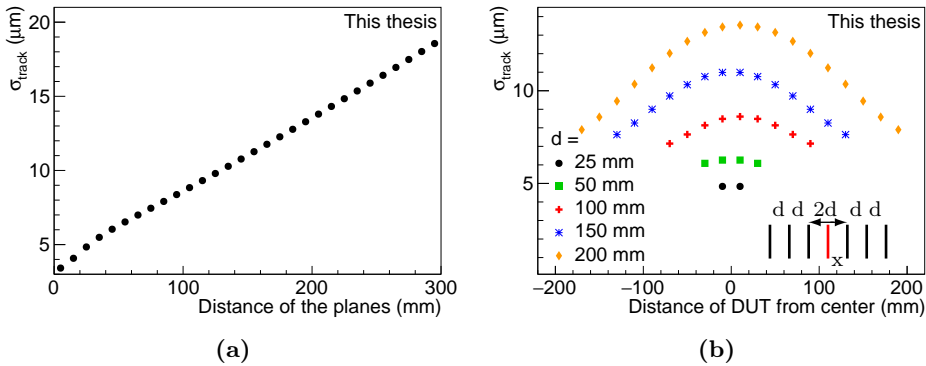


Figure 4.4: The pointing resolution at the DUT is shown in two different ways. In panel (a), the distances between the layers are equal and are shown on the x-axis. In panel (b), all the distances are kept at the indicated values (shown by d on the cartoon), but the DUT is moved between the two fixed neighboring planes as indicated on the x-axis, where 0 corresponds to the center between the two neighboring planes.

In Fig. 4.5, the effect having a symmetric or asymmetric setup and of grouping layers by two in boxes can be seen. Since an odd number of layers is considered one of the planes will be alone, therefore it was studied whether or not this layer should be the DUT. The study was done only to test the placement of the layers, therefore the additional material introduced by the boxes is neglected. From Fig. 4.5a and Fig. 4.5b, it can be seen that there is no real advantage of having an asymmetric setup, therefore a symmetric setup is preferred. It can also be seen that, as expected, there is no direction preference in the setup, therefore grouping planes as 4 planes + DUT + 2 planes gives exactly the same pointing resolution as 2 planes + DUT + 4 planes. In Fig. 4.5c, it is shown that if

the layers can be moved close enough the grouping does not have a large effect. However, if they are further apart, putting the layer next to the DUT within one box would be clearly beneficial.

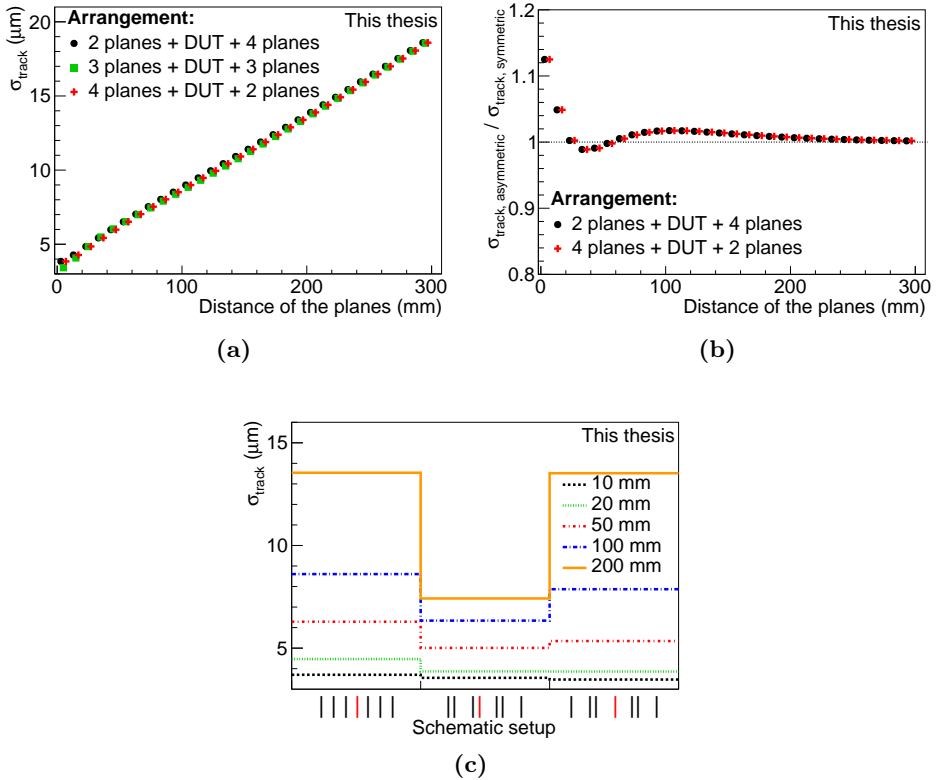


Figure 4.5: Panel (a) and (b) show the effect of placing the DUT symmetrically in the center or asymmetrically. Panel (a) shows the actual pointing resolution values, while panel (b) shows the values divided by the symmetric case. Panel (c) shows the effect of grouping the layers in such a way that pairs of layers are close. This mimics the effect of grouping pairs of layers within one box for light shielding. The distance between the two planes within a pair is always 0.5 cm, while the distance between the pairs is indicated on the figure. The cartoon on the plot shows schematically the placing of the layers, with the DUT indicated by red.

Number of the layers

It was studied how many telescope layers are needed to achieve an extrapolation uncertainty less than $5 \mu\text{m}$. The results can be seen in Fig. 4.6, where a significant effect of the number of planes is observed, if there are less than five planes. Between five, seven and nine planes, the pointing resolution agrees at large distances, but there is an effect at small distances. The effect, however, is much larger between five and seven planes than between seven and nine, where it is only visible for the smallest tested distance. It was therefore decided to build a telescope of six tracking planes plus the DUT in the center.

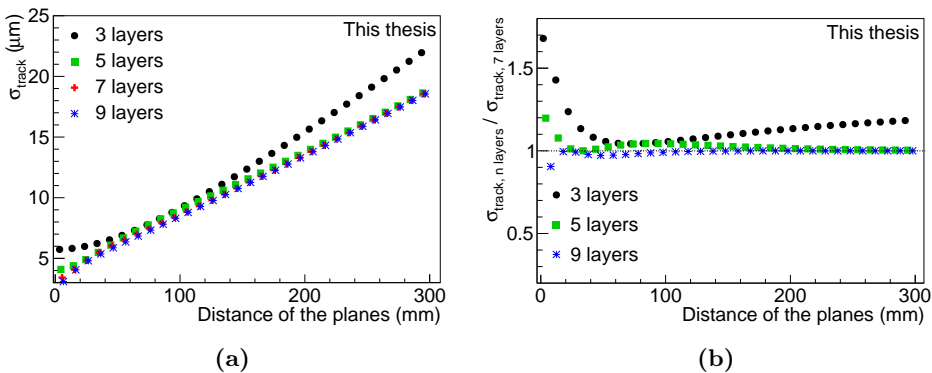


Figure 4.6: Effect of the number of layers on the pointing resolution of the tracks. Panel (a) shows the pointing resolution, while panel (b) shows the ratio to the case with 7 planes.

Effect of having air or vacuum between the layers

If vacuum is needed between the layers, it would complicate the setup greatly, therefore it should be done only if it gives a significant improvement in the pointing resolution. In Fig. 4.7, the comparison between having air or vacuum between the layers can be seen, and since the effect is less than 1%, it can be concluded that it is not necessary to put the setup in vacuum.

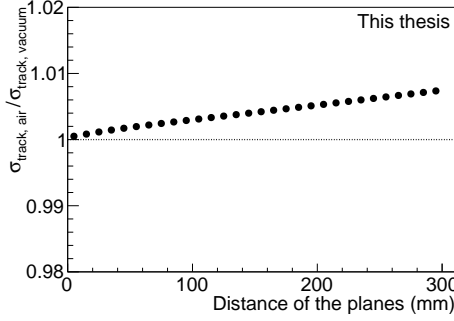


Figure 4.7: Ratio of the pointing resolution if there is air or vacuum between the layers.

Momentum of the particles

There are options to test the sensor in various accelerators, which have significantly different momentum ranges. The scattering of the particles depends on the momentum according to Eq. (4.1), therefore the interpolation error also changes with momentum. It needs to be studied whether the momentum range of the PS (up to 6 GeV/c) is enough for the resolution measurements or whether the momentum range of the SPS will be needed (up to 120 GeV/c). In Fig. 4.8, the comparison for 500 MeV/c, 6 GeV/c and 120 GeV/c is shown. It can be seen that the pointing resolution is the smallest at the SPS, so the measurement there will be the most precise. The momentum at the PS, however, is high enough to stay

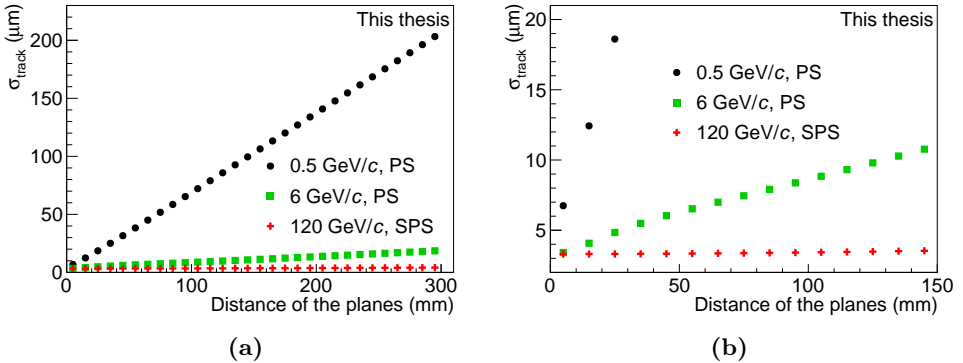


Figure 4.8: Panel (a) shows the comparison of the pointing resolution for different momenta, while (b) is a zoomed view showing the difference between the 6 GeV/c and the 120 GeV/c case.

below the $5\ \mu\text{m}$ limit, which is the expected value for the resolution, so a meaningful measurement can be done there as well. It is also clear from these measurements that $500\ \text{MeV}/c$ is not enough to study the resolution, because even if all the planes are as close as $2\ \text{cm}$, the pointing resolution is still around $7\ \mu\text{m}$, which is too high for a precise measurement.

Material budget

The contributions to the material budget of a plane can be categorized into three main layers: the chip, the Printed Circuit Board (PCB) and the FPC. A simplified material composition of each of these three layers can be seen in Fig. 4.9. In the worst-case scenario all these layers are present in each sensor of the telescope, but some of them might be omitted. The part labeled as *PCB* in Fig. 4.9 might be eliminated if it is possible to cut a hole in the PCB underneath (at least part of) the chip or if the FPC gives enough mechanical support to the chip. In the final detector, there will be an FPC underneath the chip, but for the test beam, the chips can be wire-bonded to the PCB instead of the FPC. This would mean that the part labeled as *FPC* would not be present in the layers. Three cases were investigated:

- Worst-case scenario: PCB is covering the full chip, the chip is $450\ \mu\text{m}$ thick, and it is soldered to the FPC.
- Default case: The PCB is not needed under the chip, but the chip is $450\ \mu\text{m}$ thick and it is soldered to the FPC. This is the option, which was treated as default in the previous chapters.
- Best-case scenario: There is a hole in the PCB under the chip, the chip is thinned to $50\ \mu\text{m}$, and it is wire-bonded to the PCB, therefore no FPC is needed.

The material budget of these three cases can be found in Table 4.2, and their effect on the pointing resolution is shown in Fig. 4.10. It can be concluded that if all the material of the worst-case scenario is present in all the layers, the layers have to be moved as close as possible, and the pointing resolution goes below the expected resolution of the sensor (around $5\ \mu\text{m}$) only at a distance below $5\ \text{mm}$. Therefore in this case, if the planes cannot be moved this close, it is necessary to do the measurements at higher momenta than what is available at the PS. If, however, the default case used in the simulation or the best-case scenario is feasible, the measurements are precise enough at $6\ \text{GeV}/c$ with even larger spacing between the planes.



Figure 4.9: Simplified schematic cross section of the materials of one plane. The drawing is not to scale.

Case	X/X_0	Corresponding thickness in Silicon (mm)
Worst	0.0256	2.399
Default	0.0058	0.544
Best	0.0005	0.050

Table 4.2: Material budget of three different scenarios. Please see the text for details.

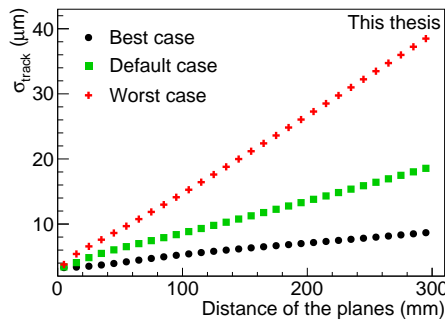


Figure 4.10: Effect of the material budget on the pointing resolution of the tracks. For details on the three cases please see the text.

Resolution of the tracking planes

If all particles would induce clusters of one pixel only in the sensor, the resolution would be $d/\sqrt{12}$, with d being the pixel pitch. This, in the case of the pALPIDE-1, would be equal to $8.1\ \mu\text{m}$. The requirement for the final chip, however, is to have a better resolution than $5\ \mu\text{m}$ by having clusters with more than one pixel. These two values ($8.1\ \mu\text{m}$ and $5\ \mu\text{m}$) were therefore tested in the simulation. The results can be seen in Fig. 4.11, where it is clear that with a better resolution in the tracking planes, the track interpolation to the DUT becomes much more precise; however, it can be seen that even with $8.1\ \mu\text{m}$ resolution, the interpolation error can stay below $5\ \mu\text{m}$ if the layers are sufficiently close.

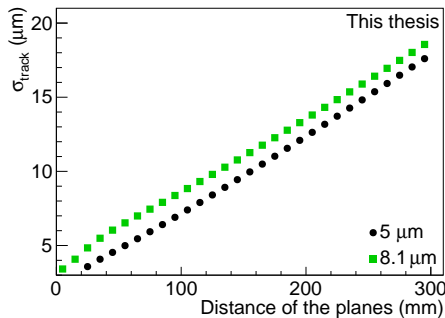


Figure 4.11: Effect of the resolution of the tracking planes on the pointing resolution of the track at the DUT.

4.3.3 The final telescope setup

The conclusions from the simulation of the telescope are the following:

- Six tracking layers are needed, but it is not necessary to have more.
- The layers have to be moved as close as possible, especially the layer right next to the DUT has to be kept as close as possible to the DUT.
- An asymmetric arrangement around the DUT does not have any benefits.
- Vacuum is not needed between the planes.
- The momentum at the SPS gives better precision; however, the momentum at the PS is sufficiently large to study the resolution of the chip, if the material budget is not the worst-case scenario or if the planes can be moved sufficiently close.

- It is important to have a hole in the PCB underneath the chip.
- Wire-bonding would be better for the testing than having the chip soldered to the FPC, but if the planes are sufficiently close it is not necessary.
- Thinning the chips would be needed if the planes could not be moved close enough.
- Even if all clusters are only one pixel large and therefore the resolution of the chip is $8.1\ \mu\text{m}$, this is good enough to measure the resolution of the DUT precisely.

Taking these results into account, a telescope was built of 6+1 parallel layers of pALPIDE-1 chips, with the DUT being symmetrically placed in the center of the setup. The layers were moved as close as possible, but a distance of 19.6 mm was needed between the layers to keep the DAQ boards from touching. All chips, except for the outermost two were thinned to $50\ \mu\text{m}$, and all of them were wire-bonded to the PCB. In each carrier card a hole was cut, which covered around third of the sensitive area, therefore this part will be used in the following for the resolution measurements. With this setup, with the assumption of $5\ \mu\text{m}$ for the resolution of the planes (which turned out to be realistic), around $2.3\ \mu\text{m}$ tracking uncertainty at the DUT can be reached with pions with a momentum of $6\ \text{GeV}/c$. This telescope can therefore be used to study the resolution of the DUT. It can also be used to do measurements as a function of the impinging point of the track within a pixel, since the tracking uncertainty ($2.3\ \mu\text{m}$) is much smaller than the size of a pixel ($28\ \mu\text{m} \times 28\ \mu\text{m}$). A picture of the setup, assembled in the laboratory before installation at the test-beam area, can be seen in Fig. 4.12, and the installed setup is shown in Fig. 4.13.

The chips in the telescope were placed in a box to shield them from light, and the full setup was adjustable in x and y to center it on the beam. The temperature of neither the boxes, nor the chips was regulated, and it changed throughout the measurements between around 20°C and 30°C . Outside the light cover four scintillators were placed parallel to the setup, which were used for triggering. Two of the scintillators were small and covered only part of the chip, therefore either only the two large scintillator were used, or the measurement had to be repeated after moving the setup to test the full chip. The trigger signal was the coincidence of the two or four scintillators and was accepted and propagated to the chips only when none of the chips were busy. The data-taking was done by a PC inside the test-beam area, and the monitoring was done on a PC outside the area, which was connected to the data-taking PC over the network.

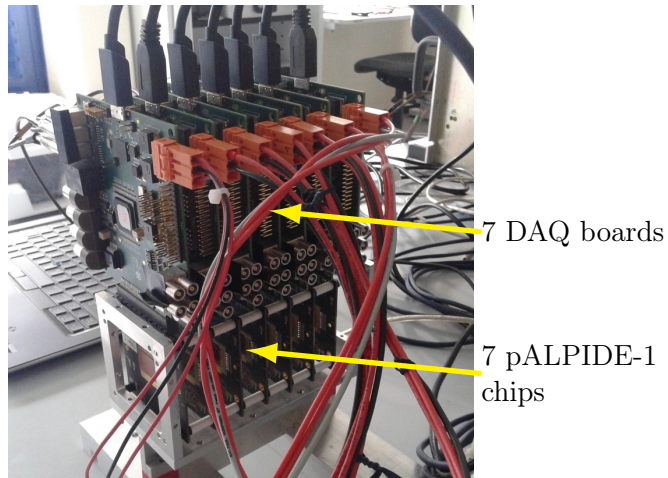


Figure 4.12: Picture of the data taking setup before installation.

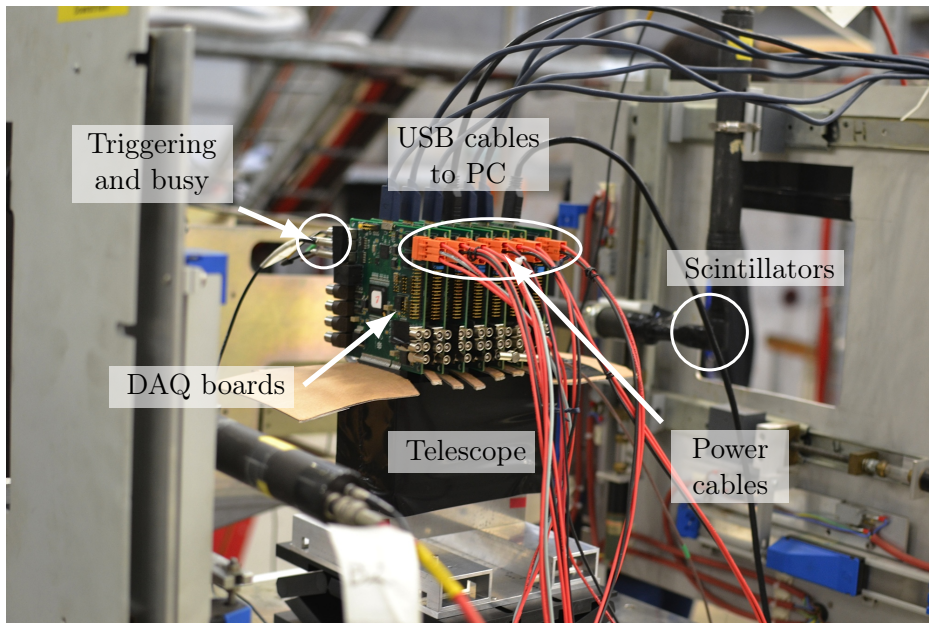


Figure 4.13: Picture of the data taking setup after installation, taken by Jongsik Eum.

5. Characterization of the pALPIDE-1 prototype

In this chapter, a description of the determination of the different properties of the pALPIDE-1 based on test-beam measurements will be given, and the results of these measurements will be discussed in detail. The test-beam measurements focused on the measurement of the detection efficiency and the spatial resolution, but the cluster size and shape distributions for clusters associated to tracks were also studied. Results on the charge threshold and noise occupancy will be presented as well.

In the following, the emphasis will be on studying how the properties of the chip depend on the charge threshold, which was changed by adjusting I_{thr} and V_{CASN} . It was also studied in the case of each parameter, whether there is a degradation of the performance after irradiation, and whether applying reverse substrate bias to the sensor has a positive effect. The dependence of the measured quantities on the momentum of the beam and the chip-to-chip fluctuations were also characterized for each measurement. The properties were studied separately for the four sectors of the sensor to investigate the effects of the reset mechanism and of the spacing between the collection n-well and the surrounding p-well.

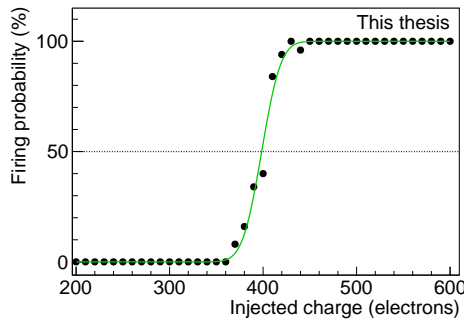
The measurements were done at several values of the reverse substrate bias. In the following sections, the different results will be shown for different reverse substrate bias values chosen such as to emphasize the effects being studied.

5.1 Charge threshold and temporal noise

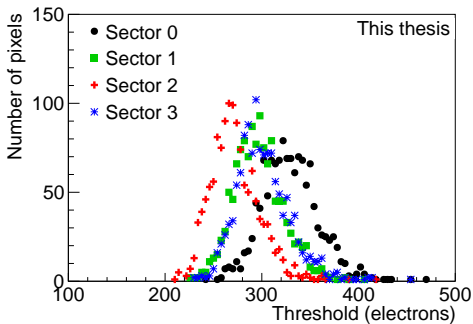
Charge threshold and temporal noise are measured by injecting the same amount of charge many times in the pixels and measuring the firing probability as a function of the injected charge. This injection is done by a dedicated capacitance in each pixel as described in Section 3.3.2. These measurements do not need the beam, but to keep the environment for the testing the same (especially the temperature), the threshold and noise measurement of a certain setting was taken right before the measurement

with beam for the same setting. For these measurement the telescope was taken out of the beam by around 20 cm by a remotely controlled linear stage.

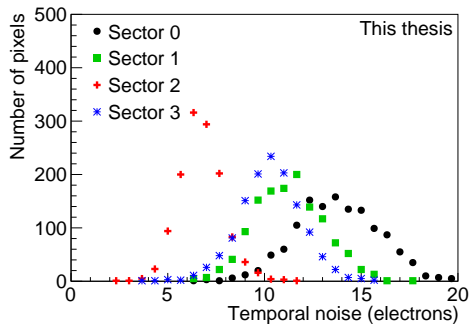
In Fig. 5.1a, an example charge threshold and temporal noise measurement is shown, where the firing probability is presented as a function of the injected charge. It can be seen that until a certain amount of charge (around 350 electrons in the example), the pixel never fires, since the injected charge is below its threshold. Above a certain amount (around 450 electrons in the example), the pixel always fires, and there is a transition region between the two. The threshold is defined as the charge, where the pixel fires 50% of the time, and the temporal noise represents the width of the transition region. This data is analyzed during the data analysis chain with the EU Telescope software [66–68] in the *converter* step (see Fig. 4.2) where an error function of the following format is fitted to the data of each



(a)



(b)



(c)

Figure 5.1: Panel (a) shows an example of the fit to the firing probability of one pixel of chip W2-31 at $V_{BB} = 0$ V, $I_{thr} = 60$ DAC units and $V_{CASN} = 57$ DAC units. Panels (b) and (c) show the threshold and noise distribution respectively of the different pixels of the sensor at the same settings.

pixel:

$$\frac{1}{2} + \frac{1}{2} \operatorname{erf} \left(\frac{x - t}{\sqrt{2}\sigma} \right) \quad (5.1)$$

In the function x is the amount of injected charge, t represents the threshold of the pixel and σ the temporal noise of the pixel. This fit function presumes that the noise of the pixel is Gaussian. In Fig. 5.1a, the fit is overlaid with the data.

The threshold and temporal noise of the full sensor are calculated as the average of the threshold and temporal noise of the separate pixels, and a typical distribution for each can be seen in Fig. 5.1.

As discussed in Section 3.3.2, the two main parameters that influence the threshold are I_{thr} and V_{CASN} . In Fig. 5.2, the effect of these two parameters on the threshold and temporal noise can be seen at -2 V reverse substrate bias for sector 2 of the pALPIDE-1. The error bars indicate the RMS of the distributions within the sensor. As discussed earlier, the two parameters have opposite effect on the threshold: increasing I_{thr} increases the threshold, while increasing V_{CASN} decreases it. This results in the fact that the same threshold can be set with different combinations of the parameters, therefore it has to be studied whether the different characteristics of the chip depend on the two parameters separately or only on the achieved threshold. To study this, in Fig. 5.2b, the temporal noise is plotted with indicating the V_{CASN} setting, which was used to set the threshold. This shows that the temporal noise does not depend solely on the threshold, but falls on different curves for the different V_{CASN} values. This indicates that for all measured quantities, it has to be tested whether

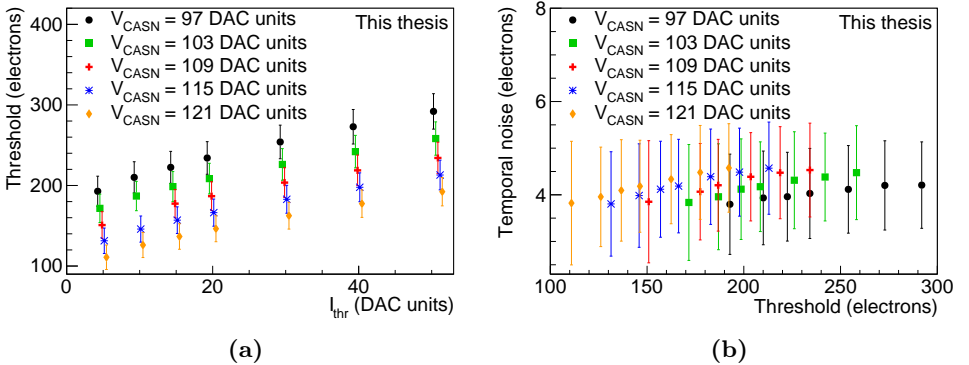


Figure 5.2: Measured threshold (a) and temporal noise (b) values for sector 2 of chip W9-16 at $V_{BB} = -2$ V. The error bars show the RMS of the distributions, indicating the pixel-to-pixel fluctuations. The points in (a) are slightly shifted on the horizontal axis for better visibility.

they depend solely on the threshold or separately on I_{thr} and V_{CASN} . If the latter is the case, the optimization for the working point of the chip has to be done separately for the two parameters.

5.2 Detection efficiency

The upgrade requirement is to have a detection efficiency higher than 99%, therefore it has to be studied which settings of the chip and which pixel geometries can fulfill that. The measurement is done such that the hits of the DUT, the chip for which the detection efficiency is being measured, are not included in the fitting of the tracks. Tracks, however, are interpolated to position of the DUT to calculate where they crossed it. Hits in the DUT are associated to these tracks, and the detection efficiency is calculated as the ratio of tracks, which have an associated hit to all tracks. The statistical uncertainty of the detection efficiency is calculated following the method described in Ref. [70]. This paper uses the Bayesian theorem to calculate the uncertainty on efficiencies from the following probability density function:

$$P(\epsilon; k, n) = \frac{(n+1)!}{k!(n-k)!} \epsilon^k (1-\epsilon)^{n-k} \quad (5.2)$$

where ϵ is the efficiency, which is the mode of the distribution, k is the number of observed events and n is the number of events in the sample. The calculation results in an asymmetric uncertainty of $\sqrt{V} \mp (\epsilon - \langle \epsilon \rangle)$, where V is the variance of the distribution and $\langle \epsilon \rangle$ is the mean of the distribution.

In Fig. 5.3, the efficiency at $V_{BB} = -1$ V for sector 2 of chip W6-14 can be seen as a function of the threshold. It can be seen that, as expected, the efficiency drops towards higher threshold values, since the charge collected in a single pixel is less likely to exceed the threshold at high threshold values. Up to around 250 electrons, the sensor fulfills the requirement of having a higher efficiency than 99%. The dependency on I_{thr} and V_{CASN} separately is negligible, since all points with different V_{CASN} settings fall on the same curve. Consequently, in the following the efficiency will be reported as a function of the threshold only, without indicating the I_{thr} and V_{CASN} values.

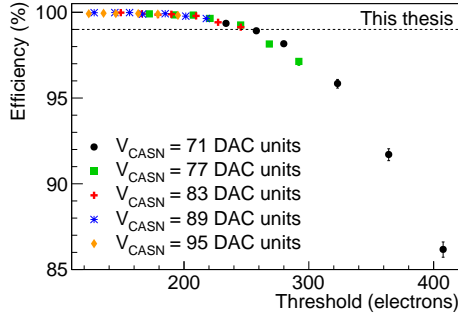


Figure 5.3: Detection efficiency as a function of the threshold for different V_{CASN} values for sector 2 of chip W6-14 at $V_{BB} = -1$ V. The dotted line at 99% represent the minimum requirement for the upgrade.

Dependence on the pixel geometry

In Fig. 5.4, the effect of the pixel geometry is studied. The comparison of sectors 0, 1 and 3 allows to draw conclusions on the effect of the spacing between the collection n-well and the surrounding p-well, while comparing sectors 1 and 2, the effect of the reset mechanism can be studied. The spacing has a strong effect on the detection efficiency, with the sector, which has 1 μm spacing (sector 0) showing the lowest efficiency, and the sectors with a larger spacing (sectors 2 and 3) showing much higher efficiency values. This can be understood by considering the change in the size of the depleted region for the different spacings. A large spacing results in a larger depletion volume around the collection diode, which results in more

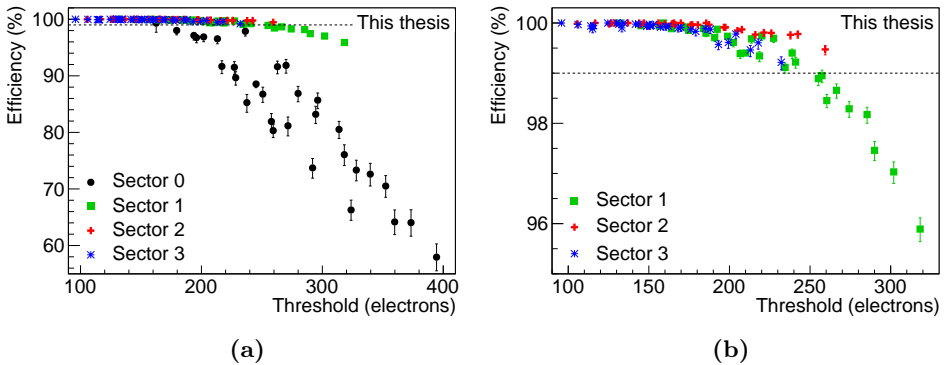


Figure 5.4: Comparison of the detection efficiency between the different sectors for chip W9-16 as a function of the threshold at $V_{BB} = -3$ V. Panel (a) shows all four sectors, while (b) is a zoom without sector 0 to show the difference between sectors 1 to 3.

efficient charge collection. In Fig. 5.4, it can be also seen that sector 0, which is the sector with the smallest spacing between the collection diode and the surrounding p-well (1 μm), shows a much larger spread in the efficiency values at the same threshold than the sectors with larger spacings. The threshold values in the case of all sectors were set changing both I_{thr} and V_{CASN} , and in the case of sector 0, this large spread comes from a dependence of the efficiency separately on I_{thr} and V_{CASN} and not just on the threshold.

The effect of the reset mechanism is much smaller than the effect of the spacing; however, the sector with a diode reset mechanism (sector 2) shows higher detection efficiency values at the same threshold than the sector with the same spacing, but with a PMOS reset (sector 1). In the following the results will be presented for sector 2, which has a diode reset and 2 μm spacing, and which shows the best performance in terms of detection efficiency. All the corresponding plots for the other sectors can be found in Ref. [71].

Chip-to-chip fluctuations

The chip-to-chip fluctuation of a quantity can be studied testing several chips with the same specifications under the same conditions. In Fig. 5.5, the chip-to-chip fluctuation of the efficiency is shown both as a function of I_{thr} and as a function of the threshold. In the figure, the naming convention of the chips is that the name contains the number of the wafer they are from, and a number, which represents their placement on the wafer, so for example W1-9 is the ninth chip from the first wafer. The chip-to-chip fluctuation is negligible if the measured efficiency is close to 100%, but it becomes larger at high I_{thr} , where the efficiency starts to drop. At the highest measured I_{thr} values it is around 4%. It can be seen also that the fluctuation is smaller as a function of the threshold than as a function of I_{thr} . This means that the chip-to-chip fluctuation of the efficiency is actually a result of the chip-to-chip fluctuation of the threshold of the sensors. In the experiment, this can be corrected for, since the parameters of the different sensors can be set separately.

In Fig. 5.5a, there are eight chips with exactly the same specifications, while one is slightly different. Chip W1-25 was not thinned to 50 μm as the others, but was kept at the original 450 μm , therefore comparing the results from this chip and the others one can draw conclusions on the effect of the thinning. There is no visible degradation arising from thinning the sensors to the required 50 μm thickness.

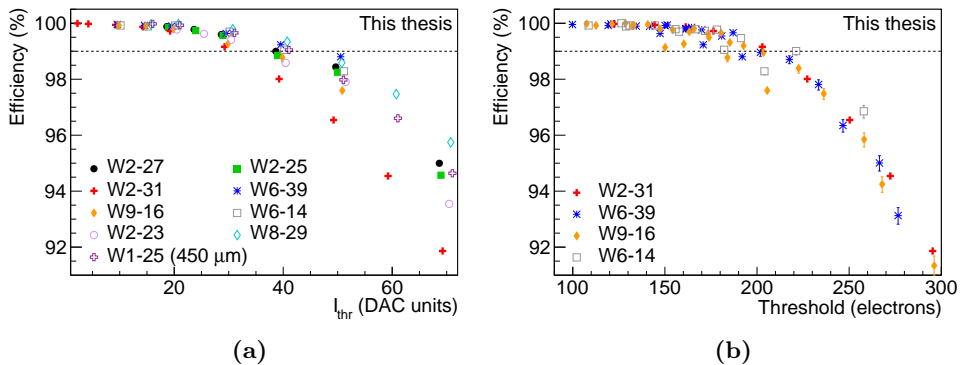


Figure 5.5: Detection efficiency values for different chips at $V_{BB} = 0$ V. In panel (a), the detection efficiency values are shown for the measured chips at $V_{CASN} = 57$ DAC units as a function of I_{thr} , while in panel (b), the results are shown as a function of the threshold for all measured V_{CASN} values for those sensors where the threshold has been determined.

Dependence on the momentum and particle type

In ALICE, different types of charged particles covering a large range in momentum are created. They have to be measurable by the ITS independent of their type down to very low momenta, therefore it is important to test whether the detection efficiency has a particle type or momentum dependence. This test has to be performed on the same sensor or on a large sample of sensors to exclude effects arising from chip-to-chip fluctuations, and it can be done by comparing measurements at different accelerators. Sensor W2-31 was tested using different particle species and different particle momenta, including tests with pions and positrons, and ranging in momentum from 500 MeV/ c to 120 GeV/ c . Results of these measurements can be seen in Fig. 5.6, where the largest difference between the measured curves is around 1%. It can therefore be concluded that the efficiency does not depend strongly on the momentum of the particles in the measured range, and there is no difference between measuring pions or positrons. The momentum dependence of the measured quantities will be further discussed in Section 5.3.

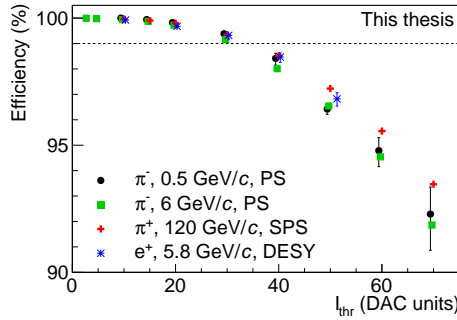


Figure 5.6: Detection efficiency values at $V_{BB} = 0$ V and $V_{CASN} = 57$ DAC units for the same chip (W2-31) at different momenta and for different particle species.

Influence of the reverse substrate bias

As discussed in Section 3.3.2, it is possible to apply a moderate reverse substrate bias to the pALPIDE-1 chip, which results in an enlarged depletion volume around the collection diode. This enlarged depletion volume results in more charge being collected in one pixel. Applying reverse substrate bias also reduces the input capacitance of the pixel, therefore a larger voltage drop is expected on the input node. These effects are beneficial for the detection efficiency; however, the enlarged depletion volume can also lead to larger leakage currents, therefore it has to be tested at which reverse-substrate-bias level the chip shows the best performance. In Fig. 5.7, the effect of applying reverse substrate bias to the chip can be seen. In the studied range (from 0 V to -4 V) applying reverse substrate bias has a positive effect on the detection efficiency, and no degradation

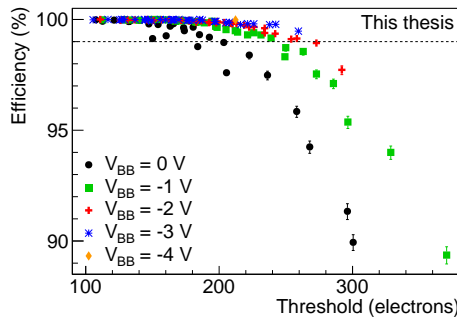


Figure 5.7: Comparison of the detection efficiency with different reverse-substrate-bias voltages for chip W9-16.

due to a possibly increased leakage current is seen even at the largest negative voltage.

Radiation hardness

The characteristics of the prototypes can change after being irradiated with ionizing or non-ionizing radiation. It has to be therefore tested whether their performance is still sufficient after irradiation with the expected radiation doses. From simulations, 1.7×10^{13} 1 MeV $n_{\text{eq}}/\text{cm}^2$ and 2700 krad is expected in the innermost layer during the lifetime of the detector (around seven years) including a safety factor of 10 [48]. However, these values are from a more recent simulation than the time of the tests of the pALPIDE-1 chip, when the focus was to test the chip irradiated to the values presented in the Technical Design Report [45]: 700 krad and 10^{13} 1 MeV $n_{\text{eq}}/\text{cm}^2$. Some prototypes, however, were irradiated up to 4×10^{13} 1 MeV $n_{\text{eq}}/\text{cm}^2$ to test the upper limit of the operating range of the sensor.

The non-ionizing irradiation of the prototypes was done at the TRIGA Mark II Reactor at the Jozef Stefan Institute (JSI) in Ljubljana [72] prior to bonding them on the carrier cards. This is done by putting a few sensors at a time into aluminum tubes, which are then exposed to the neutron flux of the reactor. The ionizing radiation of the sensors up to 700 krad was done by an X-ray machine at CERN. This machine uses a 3 kW X-ray tube with a tungsten target with a peak energy of around 10 keV and a maximum energy of 50 keV. Some prototypes were also exposed to both ionizing and non-ionizing irradiation to test the combined effect on the sensor.

The detection efficiency values after irradiation are presented in Fig. 5.8. It has to be noted that the different irradiation levels were measured with

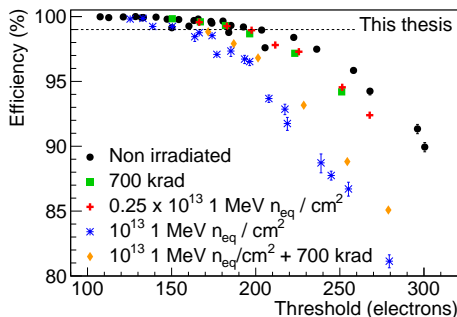


Figure 5.8: Comparison of the detection efficiency with different irradiation levels for five sensors at $V_{BB} = 0$ V.

different sensors, therefore chip-to-chip fluctuations cannot be excluded a priori. It was shown, however, in Fig. 5.5, that the chip-to-chip fluctuation of the efficiency as a function of the threshold is maximum around 1%, so a larger difference than that can be interpreted as the effect of irradiation. Ionizing radiation does not degrade the efficiency significantly, but a drop in efficiency can be seen after irradiating the sensors up to 10^{13} 1 MeV $n_{\text{eq}}/\text{cm}^2$. The sensor, however, stays functional, and fully efficient at low threshold, therefore the slight degradation of the efficiency results only in a reduced operational margin, but the sensor still fulfills the requirement of the upgrade in terms of detection efficiency.

Dependence on the impinging point of the track

The uniformity of the response over the surface of the pixel is studied in this section. This can be done if the tracking precision at the DUT is significantly better than the size of the pixel, allowing the characteristics of the chip to be studied as a function of the impinging point of the track within a pixel. In the case of the pALPIDE-1 telescope with 7 planes, the uncertainty of the track position at the DUT is around 2–3 μm , which is much smaller than the size of the pixels (28 $\mu\text{m} \times 28 \mu\text{m}$). The uniformity of the detection efficiency was studied for different threshold levels, and the results are shown for two threshold cases in Fig. 5.9. It can be seen that at low threshold (Fig. 5.9a) and high detection efficiency, the response of the pixel is uniform. When the threshold is high (Fig. 5.9b); however, the drop of efficiency first happens at the corner of the pixels, while the center is still fully efficient. This can be understood by the concept of charge sharing between pixels: at the center of the pixel it is more likely that all the charge is collected in one pixel, therefore the collected charge is still above the threshold even at high threshold values. At the corners, however, it is more likely to share the charge between the neighboring pixels, and as a consequence the collected charge in the separate pixels can fall below the threshold. This will be further discussed in Section 5.3, where a similar study for the cluster size is shown. In Fig. 5.10, a cross section of the two dimensional plot is presented, where it can be studied quantitatively how the effect changes from low to high threshold.

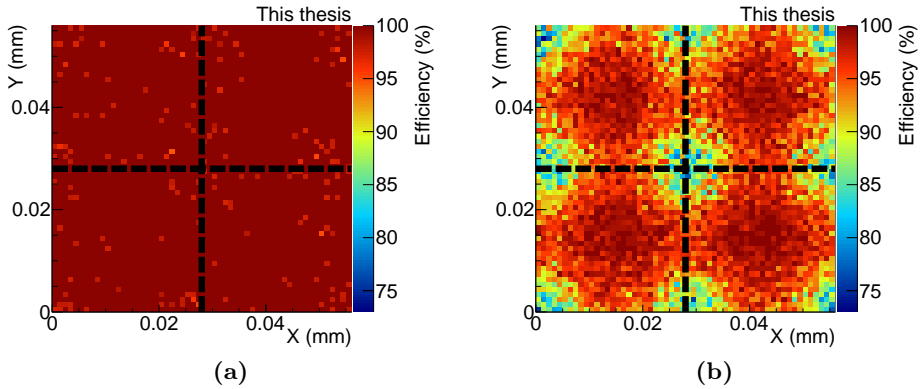


Figure 5.9: Detection efficiency as a function of the impinging point of the track within the smallest repeated unit of the chip (two times two pixels) at $V_{BB} = 0$ V and $V_{CASN} = 57$ DAC units for chip W2-25. Panel (a) shows the efficiency in the case of a low threshold ($I_{thr} = 20$ DAC units), while (b) shows the same in the case of a high threshold value ($I_{thr} = 70$ DAC units).

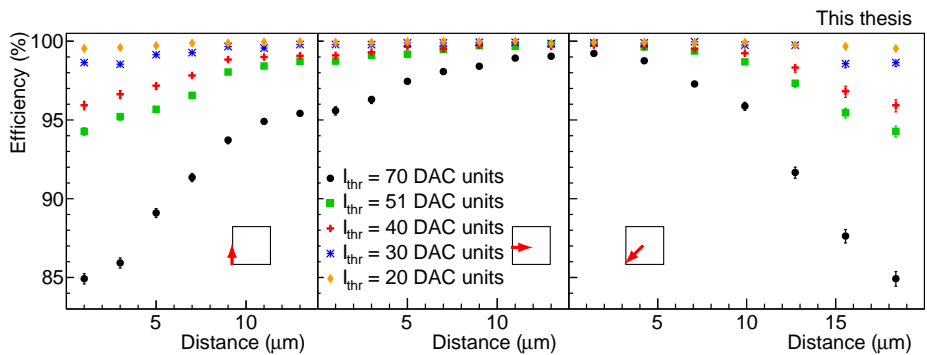


Figure 5.10: Detection efficiency as a function of the impinging point of the track along three different paths within one pixel indicated by the drawings. The data are from chip W2-25 at $V_{BB} = 0$ V and $V_{CASN} = 57$ DAC units.

5.3 Cluster size

The average cluster size has a significant effect on the amount of data to be transferred from the chip and on the resolution of the detector. The cluster size distribution can change depending on the settings of the different parameters of the chip, but also on the operating environment and the momentum of the measured particles. A typical distribution of the cluster size for different settings of I_{thr} is shown in Fig. 5.11. It can be seen from this plot that the average of the distribution shifts to larger values at lower I_{thr} settings. This is expected, since with lower I_{thr} and therefore lower threshold settings, the charge shared with the neighboring pixels can become sufficient to make those pixels fire as well resulting in larger clusters.

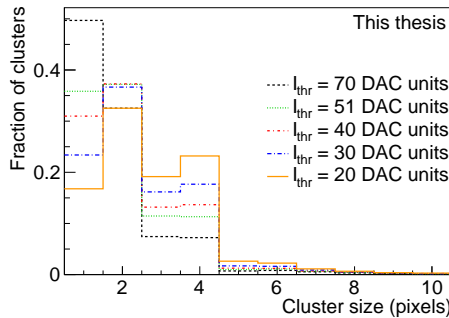


Figure 5.11: Example of the cluster size distribution at $V_{BB} = 0$ V and $V_{CASN} = 57$ DAC units for chip W2-25.

The cluster size distribution can be studied for all measured clusters of the DUT, independent of the tracks which were reconstructed in the analysis. This set of clusters includes both the clusters originating from the crossing particle and also from the noise of the chip. The clusters originating from noise consist usually of only one pixel, therefore they bias the average cluster size towards small values. If the interest is in the response of the sensor to the particles passing through it, the average cluster size has to be calculated from only those clusters, which were associated to tracks. For this reason in the following, the average cluster size from clusters associated to tracks will be shown.

Dependence on the pixel geometry

The cluster size depends strongly on the size of the depletion volume, which changes depending on the spacing between the collection n-well and the surrounding p-well. In Fig. 5.12, the comparison of the average cluster size can be seen for the different sectors of the chip. By comparing the three sectors with a PMOS reset (sectors 0, 1 and 3), it can be seen that larger spacing between the collection n-well and the surrounding p-well results in smaller cluster sizes, as it was expected from the reduced charge sharing due to the larger depletion volume. The reset mechanism (sectors 1 and 2) does not have a strong effect on the cluster size, but the values are slightly higher in the case of the sector with a diode reset. In the following, the results for sector 2 (diode reset, 2 μm spacing) will be shown.

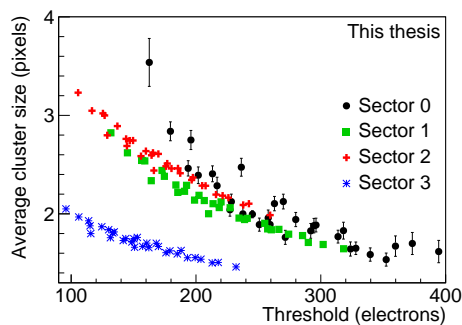


Figure 5.12: Comparison of the average cluster size for the different sectors for chip W9-16 at $V_{BB} = -3$ V.

Chip-to-chip fluctuations

In Figs. 5.13 and 5.14, the chip-to-chip fluctuation of the average cluster size and of the RMS of the average cluster size are shown, respectively. It can be seen that the fluctuation is maximum one pixel for the average and maximum 0.2 pixel for the RMS, and becomes even smaller at large threshold values. Comparing chip W1-25 with the others, it can be concluded that there is no significant difference in the distribution of the cluster size depending on the thickness of the chip.

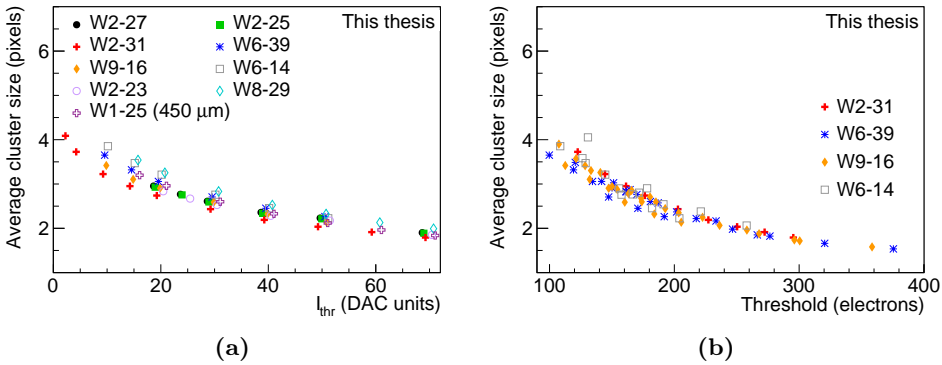


Figure 5.13: Panel (a) shows the chip-to-chip fluctuation of the average cluster size as a function of I_{thr} at $V_{BB} = 0$ V and $V_{CASN} = 57$ DAC units, while panel (b) shows it as a function of the threshold at $V_{BB} = 0$ V for all measured V_{CASN} values for those sensors where the threshold has been determined.

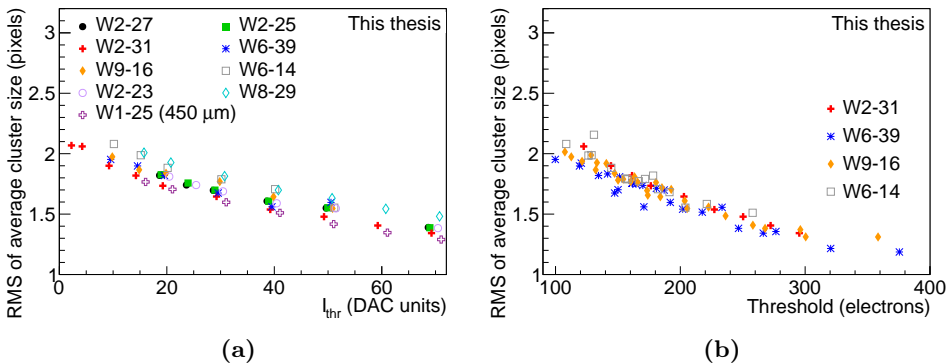


Figure 5.14: Panel (a) shows the chip-to-chip fluctuation of the RMS of the average cluster size as a function of I_{thr} at $V_{BB} = 0$ V and $V_{CASN} = 57$ DAC units, while panel (b) shows it as a function of the threshold at $V_{BB} = 0$ V for all measured V_{CASN} values for those sensors where the threshold has been determined.

Dependence on the momentum and particle type

At the studied pion momenta (from 500 MeV/ c to 120 GeV/ c), the energy loss of the pions in silicon changes by around 10% [35], which is relatively small; however, it is interesting to study whether this change is reflected in the cluster size. In Fig. 5.15, the average cluster size can be seen for four different momenta and two different particle types. From this plot, it can be concluded that the average cluster size does not depend on the momentum of the incident particle in the studied momentum range. Measurements have been done at much lower momenta with protons (30–35 MeV/ c) [73], which show that this finding is only true in a certain momentum range (from 500 MeV/ c to 120 GeV/ c), and if much lower momentum values are considered the average cluster size becomes significantly larger. This is expected, since the studied momentum range corresponds to close to minimum ionizing particles, with only a 10% change in the energy loss. In the case of the protons with momentum around 30–35 MeV/ c , the energy loss is much higher, therefore the generated charge is higher, resulting in larger clusters.

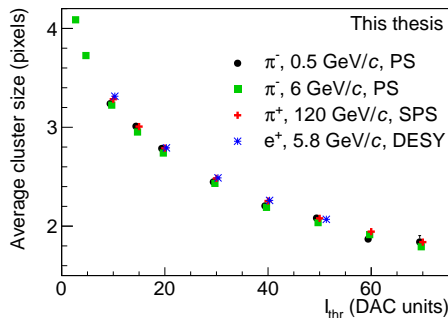


Figure 5.15: Average cluster size values at $V_{BB} = 0$ V and $V_{CASN} = 57$ DAC units for the same chip (W2-31) at different momenta and for different particle species.

Influence of the reverse substrate bias

Applying reverse substrate bias changes the size of the depleted region significantly, with larger negative bias values resulting in a larger depleted region. If a larger part of the epitaxial layer is depleted, the electrons can reach it easier, therefore it results in less diffusion, which means less pixels firing for one passing particle. The effect of this is shown in Fig. 5.16, where it is confirmed that larger negative bias values result in smaller clusters; however, the difference is within one pixel for the measured threshold values.

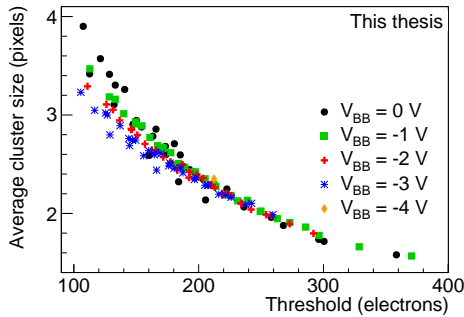


Figure 5.16: Comparison of the average cluster size with different reverse-substrate-bias values for chip W9-16.

Radiation hardness

The effects of irradiating the chips was studied in the case of the average cluster as well, and the comparison of the results with different irradiation levels is presented in Fig. 5.17. As can be expected from the efficiency measurements, ionizing radiation has no effect on the performance, while the cluster size becomes slightly smaller after irradiating the sensor with 10^{13} 1 MeV n_{eq}/cm^2 . It is a small change of maximum around 0.5 pixel, but it has to be studied, whether the effect causes some change in the position resolution of the chips, which is described further below.

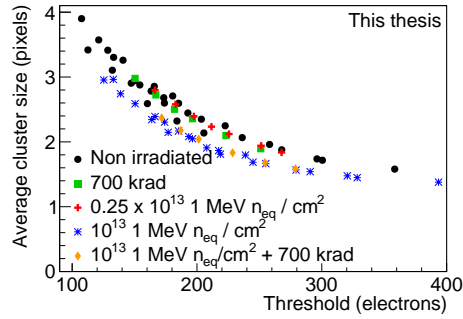


Figure 5.17: Comparison of the average cluster size with different irradiation levels for five sensors at $V_{BB} = 0$ V.

Dependence on the impinging point of the track

It is interesting to study the dependence of the average cluster size on the impinging point of the track, because this can shed light on the charge sharing between the neighboring pixels. In Fig. 5.18, the average cluster size as a function of the impinging point of the tracks for two times two pixels can be seen for two threshold values. It can be concluded that the tracks passing through the center of the pixel cause less pixels to fire on average than the tracks passing through at the corners. This can be explained by charge sharing, because the charge has a larger path to travel to the neighboring pixels, if a track passed through the center of the pixel,

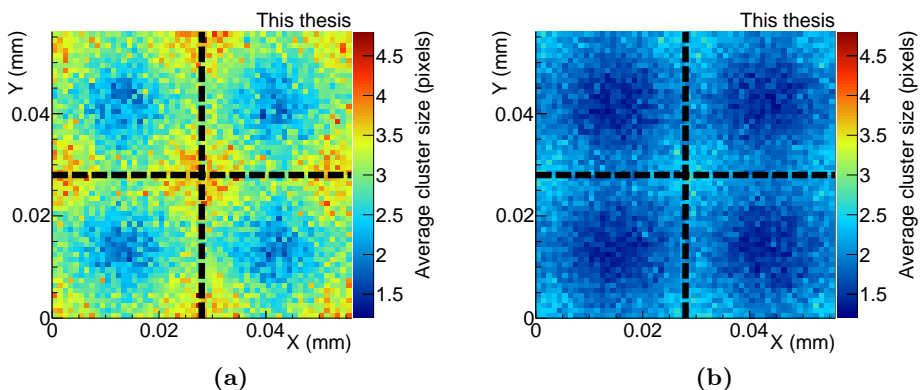


Figure 5.18: Average cluster size as a function of the impinging point of the track within two times two pixels at $V_{BB} = 0$ V and $V_{CASN} = 57$ DAC units for chip W2-25. Panel (a) shows the cluster size in the case of a low threshold ($I_{thr} = 20$ DAC units), while (b) shows the same in the case of a high threshold value ($I_{thr} = 70$ DAC units).

than if it went through the corner. Also, if a particle went through the center of the pixel, most of the charge was generated inside or close to the depleted region. The electrons within the depleted region drift towards the collection diode, therefore they are less likely to be collected in a different pixel than where they were generated. However, if the particle crossed the sensor at the border of two pixels, the generated charge first has to reach a depleted region by diffusion, which can be the one in the neighboring pixel. This results in charge being more likely to be collected by only one pixel in the former case and by more than one pixel in the latter. The effect is similar for the high and the low threshold case, but the overall value of the average cluster size changes, which can be seen better in Fig. 5.19, where a cross section of the two-dimensional plot is shown.

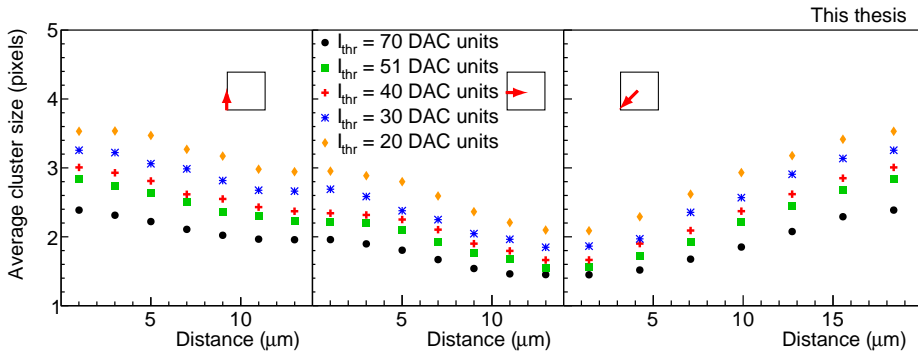


Figure 5.19: Average cluster size as a function of the impinging point of the track along three different paths within one pixel indicated by the drawings. The data from chip W2-25 at $V_{BB} = 0$ V and $V_{CASN} = 57$ DAC units were used.

5.4 Position resolution

As mentioned in Section 4.3, the resolution of the chip cannot be measured directly, only its residual, which contains a contribution originating from the uncertainty of the interpolation of the track to the DUT. This interpolation uncertainty comes from two sources: the scattering of the particles in the material of the telescope layers and the resolution of the tracking planes. If the resolution of the tracking planes and their material is known, the interpolation uncertainty can be calculated with the same simulation tool, which was used for optimizing the telescope setup. However, since the same sensors are used as tracking devices as the one being tested, the resolution of the telescope layers is not known a priori. The resolution can still be calculated with an iterative procedure from runs where all chips were kept at the same settings. This iterative procedure is

the following: an initial guess is made on the resolution of the planes, and that is used as the resolution of the tracking planes in the simulation. The tracking uncertainty is calculated in the simulation, and by quadratically subtracting this value from the residual, a new value can be obtained for the resolution. The whole procedure is then repeated with this value as the resolution of the tracking planes, and the iteration is stopped when the difference of the assumed resolution and the measured resolution is sufficiently small ($\lesssim 0.05 \mu\text{m}$). In practice this was achieved after 2–3 iterations, and since the settings of the reference planes were not changed during the data-taking, the value achieved this way can be used for all the data measured in this setup.

The residual is measured by calculating the distance of the impinging point of the track to the associated hit in both the x and y direction for all the detected tracks. Therefore tracks which are not detected in the DUT are ignored for the analysis of the position resolution in the cases where the detection efficiency is not 100%. The typical distributions can be seen in Fig. 5.20, which is then fitted with a Gaussian function in both directions. Since the pixels have the same size in x and y , and the arrangement of the pixels is not staggered, no difference is expected in the resolution in the two directions. The residual is therefore calculated as the average of the width of the Gaussian functions in the two directions. The resolution is determined from the measured residual and the tracking uncertainty calculated from the simulations, where the tracking plane resolution is calculated from the iterative procedure described above. Since the tracking planes have four sectors, and the different sectors can have different resolution, the iterative procedure to determine the resolution of the reference planes has to be repeated for each sector.

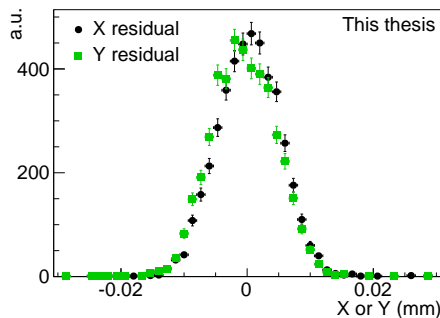


Figure 5.20: Example of the residual distribution for sector 2 of chip W2-31 at $V_{BB} = -3 \text{ V}$, $I_{thr} = 30 \text{ DAC units}$ and $V_{CASN} = 135 \text{ DAC units}$.

The telescope settings used for the determination of the tracking uncertainty were $V_{BB} = 0$ V, $I_{thr} = 30$ DAC units and $V_{CASN} = 57$ DAC units, and only tracks passing through the hole in the carrier card of the DUT were considered for resolution measurements. The estimation of the resolution of the tracking planes was done from the data taken at the PS with π^- particles with a momentum of 6 GeV/ c . An example comparing the residual values before the subtraction of the tracking uncertainty and the resolution values after the subtraction can be seen in Fig. 5.21 with a line at 5 μm indicating the requirement for the resolution of the final chip. In this figure, the typical dependence of the resolution on the threshold can be seen: the threshold is in close connection with the average cluster size, and as the average cluster size gets smaller towards large threshold values, the resolution values become higher. However, it does not continue to decrease towards very low threshold values, but has a minimum at a certain threshold. The place of the minimum depends on the pixel geometry and the biasing of the chip, but can be seen clearly, for example, in Fig. 5.21. This is because at low thresholds the noise of the chip starts to play a role. There are more noisy pixels which might be included in the clusters and pixels on the periphery of the cluster, in which the collected charge would not reach the threshold normally, might fire due to their noise. This then results in a worse resolution at low threshold values than at higher values. In Fig. 5.21, the theoretical resolution when only one pixel fires for each particle is also shown, and for any of the tested I_{thr} values, the measured resolution is at least 2 μm less than this limit. This is achieved by the charge sharing between the pixels, which results in more than one pixel firing for the passing particle.

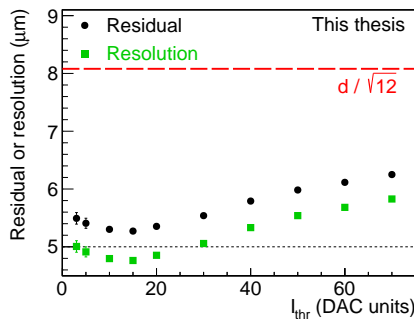


Figure 5.21: Example of the residual before the subtraction of the tracking uncertainty and the resolution after subtraction for sector 2 of chip W2-31 at $V_{BB} = 0$ V and $V_{CASN} = 57$ DAC units. The dotted line at 5 μm represents the upper limit acceptable for the upgrade, while the dashed line around 8 μm is the theoretical resolution in the case when only one pixel fires for each crossing particle ($d/\sqrt{12}$, where $d = 28$ μm is the pixel pitch).

Dependence on the momentum

The momentum dependence of the resolution is interesting to test, because the track interpolation uncertainties are momentum dependent, therefore this can be considered as a test of the validity of the simulations. In Fig. 5.22, the resolution can be seen for three different momenta, measured at the PS and at the SPS. The results agree well for the three studied momenta, with a maximum difference of around $0.2 \mu\text{m}$ at the higher two momenta ($6 \text{ GeV}/c$ and $120 \text{ GeV}/c$) and a maximum difference of around $0.6 \mu\text{m}$ for the lower two momenta ($0.5 \text{ GeV}/c$ and $6 \text{ GeV}/c$). At $500 \text{ MeV}/c$, the measurements have large statistical uncertainties, because of the few tracks that can be reconstructed due to the large scattering of the particles. From the small difference seen at the three momenta, it can be concluded that the tracking model and the simulations are well suited for the studied momentum range.

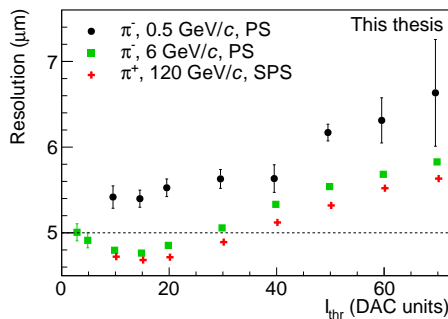


Figure 5.22: Resolution values for sector 2 of chip W2-31 with different momenta at $V_{BB} = 0 \text{ V}$ and $V_{CASN} = 57 \text{ DAC units}$.

Dependence on the pixel geometry

For the precise estimation of the tracking uncertainty larger statistics is needed than for the efficiency measurements, and in the case of sector 0 due to its low efficiency, the statistics was not enough. Because of this in Fig. 5.23, the resolution values are show only for sectors 1 to 3. It can be seen that there is no significant difference arising from the reset mechanism (sectors 1 and 2), while the spacing between the collection n-well and the surrounding p-well has a significant influence (sectors 1 and 3). Larger spacing results in worse resolution values, because in this case the average cluster size is smaller as was shown in Section 5.3. However, there is a threshold range in the case of all sectors, where the resolution is below the requirement of the ITS ($5 \mu\text{m}$). In the following the results for sector 2 will be presented, just as for the efficiency and the average cluster size.

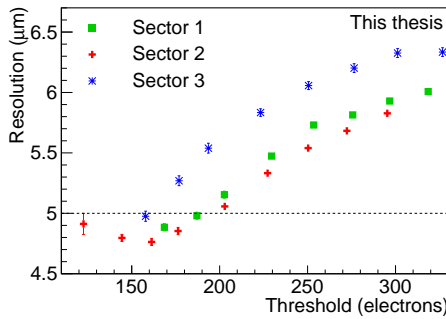


Figure 5.23: Comparison of the resolution of the different sectors of chip W2-31 at $V_{BB} = 0 \text{ V}$.

Chip-to-chip fluctuations

To be able to use the same estimation of the tracking uncertainty for multiple runs, it is needed that the settings of the tracking planes are kept the same. In some of the measurement campaigns, the settings of the central three planes were changed simultaneously to limit the time needed for the measurement of the chip-to-chip fluctuation of the efficiency. Since these planes are also used as tracking planes, this data cannot be used for the calculation of the resolution. With the proper setup for the resolution measurements, there were only three chips with the same specifications measured, therefore the chip-to-chip fluctuations can be studied only on these three chips. The results for these chips can be seen in Fig. 5.24a as a function of I_{thr} , and the difference is around $0.5 \mu\text{m}$ between the measured resolution values. In Fig. 5.24b, the results are shown as a function of the

threshold, which shows that at low threshold values, the difference becomes negligible when the resolution is plotted against the threshold, and it grows to around $0.2 \mu\text{m}$ at higher values. This means that most of the chip-to-chip fluctuation of the resolution arises from the chip to chip fluctuation of the threshold of the sensors.

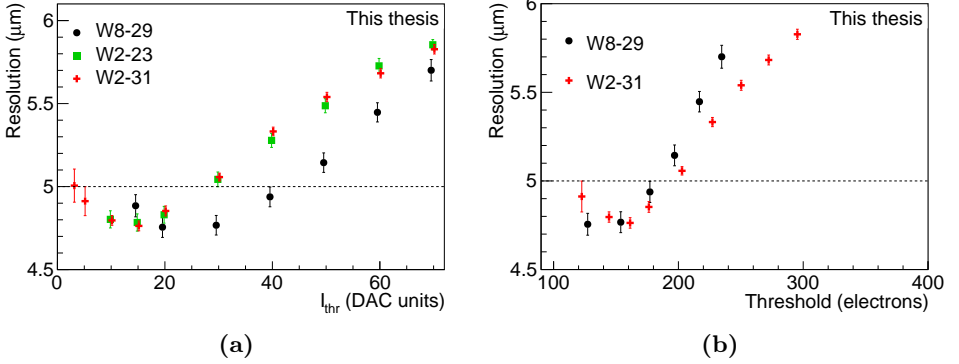


Figure 5.24: Resolution values for the different chips at $V_{BB} = 0 \text{ V}$ and $V_{CASN} = 57 \text{ DAC units}$ as a function of I_{thr} (a) and the threshold (b) for those sensors where the threshold has been determined.

Influence of the reverse substrate bias

The dependence of the resolution as a function of the reverse substrate bias can be seen in Fig. 5.25. The resolution becomes smaller with applying reverse substrate bias to the chip, but is similar for $V_{BB} = -3 \text{ V}$ and $V_{BB} = -6 \text{ V}$. A clear separate I_{thr} and V_{CASN} dependency in the case of $V_{BB} = -3 \text{ V}$ can also be seen, with lower V_{CASN} values showing better

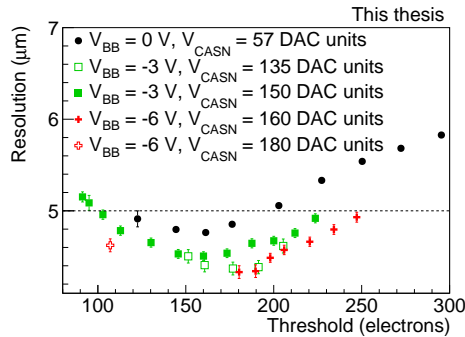


Figure 5.25: Resolution values for chip W2-31 comparing different reverse-substrate-bias values.

resolution. Possible explanations for the better resolution with reverse substrate bias are a lower noise occupancy at $V_{BB} = -3$ V or a different dependence of the cluster size on the impinging point of the track within a pixel.

Radiation hardness

The effect of irradiation has been studied also in the case of the resolution, and the results are presented in Fig. 5.26. It can be seen that, just as in the case of the detection efficiency and the average cluster size, ionizing radiation does not have a significant impact on the resolution, but non-ionizing radiation worsens the resolution. The change, however, is within 0.5 μm , therefore the resolution still fulfills the requirement of the ITS upgrade.

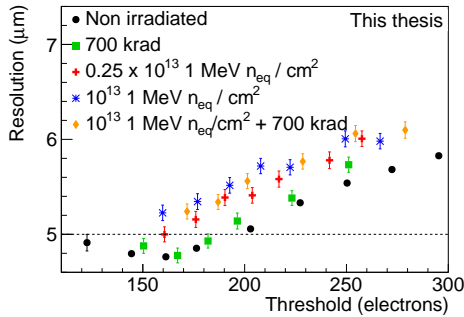


Figure 5.26: Comparison of resolution values for different levels of irradiation for five sensors at $V_{BB} = 0$ V.

Dependence on the impinging point of the track

Fig. 5.27 shows how the average residual values change depending on the impinging point of the track within two times two pixels in both the x and the y direction. In the case of a low threshold value (lower row), the residual values are small both at the center of the pixels and at the edges. This comes from the fact that if there is a cluster with only one pixel and there is no additional information available about the pixels, the best guess is that the hit was in the center of the pixel. It is also likely to have a one-pixel cluster if the track went through the center (see Section 5.3), therefore it is likely that the track and the reconstructed hit were close resulting in a small residual at the center. The same logic is true for the edge of the pixel: if a track crossed the sensor here it is likely that two pixels fired. That results in the hit being placed exactly at the edge,

therefore the distance between the impinging point of the track and the measured hit position is small. If there would be only clusters with one or two pixels this would also explain why the residual is larger between the center and the edge, since with one or two pixels the estimation of the position of the hit will never fall in this area. The approximation of having only one- and two-pixel clusters in one direction can be considered valid, as will be shown in Section 5.7. In the case of the high threshold (upper row), the minimum at the edge of the pixel is much less pronounced, but the minimum at the center did not change significantly. This can be explained

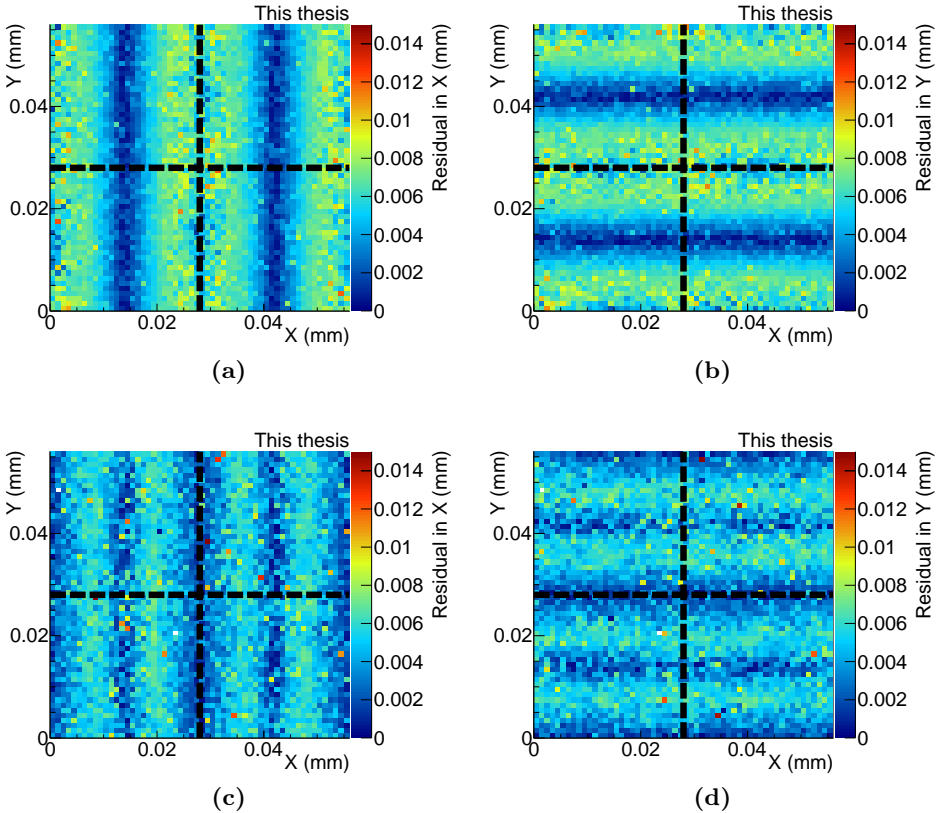


Figure 5.27: Average residual values as a function of the impinging point of the track inside two times two pixels for chip W2-25 at $V_{BB} = 0$ V and $V_{CASN} = 57$ DAC units. The upper row shows the results with a high threshold setting ($I_{thr} = 70$ DAC units) and the lower row shows the situation for a low threshold setting ($I_{thr} = 20$ DAC units). The left column shows the residual values in the x -direction and the right column in the y -direction. The tracking uncertainty can be slightly different for the two threshold settings, because the settings of the tracking planes were different; however, this would not change the seen structure, it would only cause an overall shift in the magnitude, when calculating the resolution values.

from the same principle: in this case, because of the lower efficiency, it is much more likely to have one-pixel clusters also at the edge of the pixels. The approximation of the hit position therefore becomes worse at the edge, but stays similar at the center to the low threshold case.

5.5 Noise occupancy

For noise occupancy measurements, the beam is not needed; however, to keep the data-taking environment as close to the environment for the other measurements as possible, noise data was also taken at the test-beam area. It was done in such a way that the telescope was moved out of the beam by around 20 cm each time a new setting was measured, and noise data was collected in this position for all the settings. This was, however, not done during all of the test-beam campaigns, therefore noise data is not available for all measured chips and settings. For triggering the data-taking, the scintillators were used, therefore the data-taking rate was exactly the same as in the case of the data used for the other measurements. This is important if the noise occupancy depends on the data-taking rate, and some effects on the data-taking rate were seen in the pALPIDE-1 chip. Details on these effects can be found in Ref. [71].

The noise occupancy is measured by measuring the average number of pixels, which fire without an external stimulus in an event, and dividing it by the number of pixels in the chip:

$$\text{Noise occupancy} = \frac{\text{Fired pixels}}{\text{Number of events} \times \text{Number of pixels}} \quad (5.3)$$

A typical hit map from a run without an external stimulus is shown in Fig. 5.28. It can be seen that there are some pixels, which fire a few times in a few 10 000 events, while there are also some pixels, which fire in almost all events. If the major part of the noise occupancy originates from a few pixels only, these can be masked during data-taking without lowering the efficiency. It therefore has to be studied, how much the noise occupancy of the chip changes by masking the noisiest few pixels.

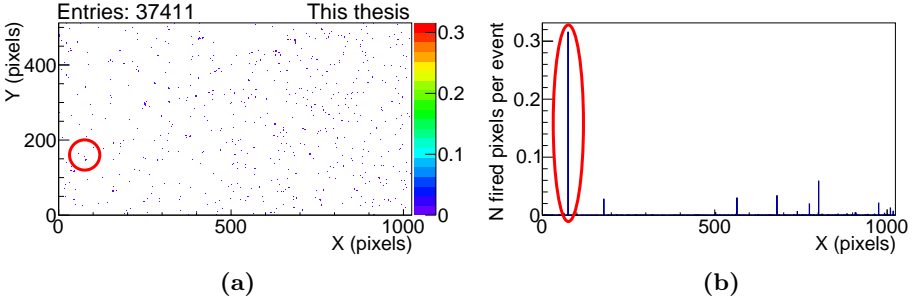


Figure 5.28: Panel (a) shows a typical hit map of a run without an external source at $V_{BB} = -3$ V with $I_{thr} = 30$ DAC units and $V_{CASN} = 135$ DAC units from the chip W9-16 with the firing frequency of the pixels indicated by the color code. Panel (b) shows the projection of the same hit map to the x -axis. In this case the y -axis corresponds to the average number of pixels firing in each column. The same very noisy pixel is highlighted in both plots.

The noise occupancy values after masking the 20 noisiest pixels in each sector can be seen in Fig. 5.29 as a function of the threshold, which was changed by changing I_{thr} and V_{CASN} , and the different I_{thr} values are highlighted in the plot. If the noise occupancy depends only on the measured threshold, the curves for the different I_{thr} values should lay on top of each other, but that is not the case, therefore it can be concluded that the noise occupancy depends separately on I_{thr} and V_{CASN} . To understand

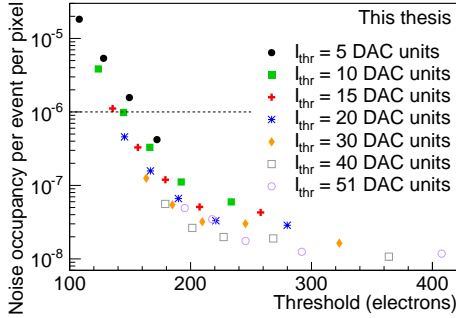


Figure 5.29: Dependency of the noise occupancy on I_{thr} at $V_{BB} = -1$ V for sector 2 of chip W6-14 after masking the 20 noisiest pixels. The dotted line at 10^{-6} hits/event/pixel represents the upper limit acceptable for the upgrade.

what is the difference between the dependency on I_{thr} and on V_{CASN} , extreme settings of the two parameters have been studied. In Fig. 5.30, the hit map of two such cases can be seen, where the number of events taken was similar. This shows that in the case of a low I_{thr} , there are many pixels firing, while in the case of a high V_{CASN} , less pixels fire, but those fire very often. The same effect can be seen in Fig. 5.31, where the number of fired pixels is plotted against their firing frequency per event. The two cases shown have similar noise occupancy values; however, the number of pixels causing this noise occupancy is very different. In the high V_{CASN} case (green points), a significant number of pixels fire in all or almost all events (around a few hundred), while in the low I_{thr} case (black points), there are hardly any pixels firing in all events, but there are around ten times more pixels firing in only a few events. Because of this separate dependence on I_{thr} and V_{CASN} noise occupancy values will be shown only for one selected V_{CASN} value in each plot.

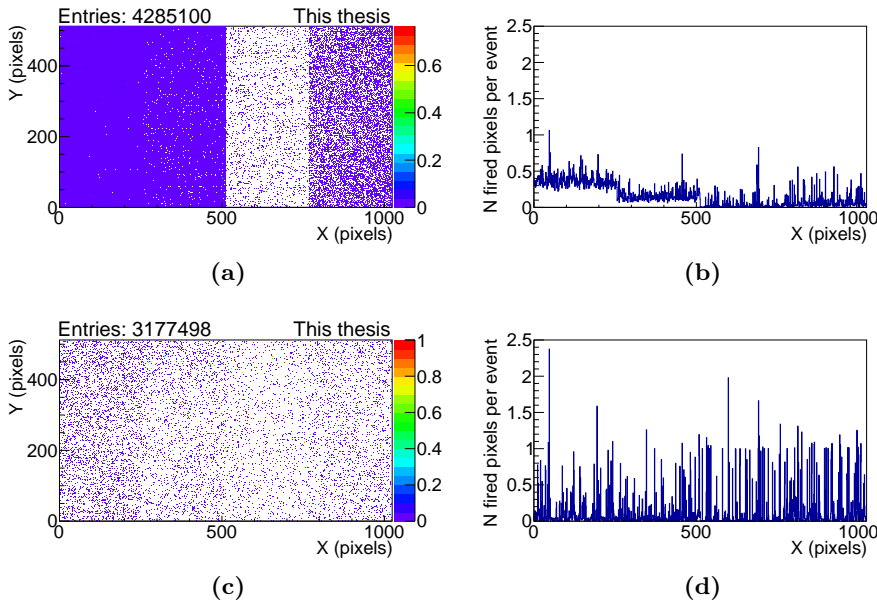


Figure 5.30: In the left column the noise map of the chip normalized by the number of events is shown at extreme threshold values for chip W9-16, while in the right column the projection of these histograms to the x-axis can be seen. In this case the y-axis corresponds to the average number of pixels firing in each column. In the upper row, the situation can be seen at $I_{thr} = 5$ DAC units and $V_{CASN} = 57$ DAC units, while in the lower row, for $I_{thr} = 20$ DAC units and $V_{CASN} = 69$ DAC units.

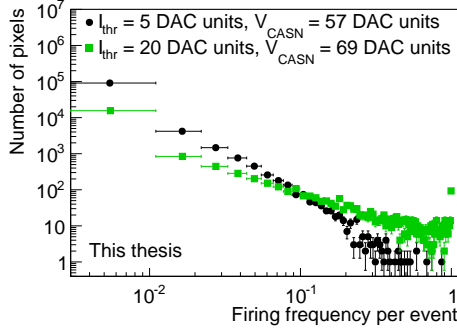


Figure 5.31: Distribution of the number of pixels with a certain firing frequency for two extremely low threshold cases at $V_{BB} = 0$ V for sector 1 of the chip W6-39. In the case with $I_{thr} = 5$ DAC units and $V_{CASN} = 57$ DAC units the overall noise occupancy is 3.1×10^{-3} hits/event/pixel, and in the case with $I_{thr} = 20$ DAC units and $V_{CASN} = 69$ DAC units, it is 5.1×10^{-3} hits/event/pixel.

The operating range of the chip in terms of the charge threshold is limited by the rising noise occupancy values towards low threshold values. Both the low I_{thr} case and the high V_{CASN} case results in a low charge threshold, therefore both extreme cases should be avoided. If, however, it is needed to extend the operating range to lower thresholds, it is possible by setting V_{CASN} high, since the few pixels that start firing in all or in almost all events can be masked. It is important, however, to confirm that this masking does not result in a loss of detection efficiency. It might also be beneficial in a non-extreme threshold case to set the threshold by a combination of high I_{thr} and high V_{CASN} . Apart from the possibility of masking the few noisy pixels arising from the high V_{CASN} setting, a high I_{thr} setting also results in a shorter pulse length in the front end [57]. This is beneficial if the time between consecutive events is comparable to the length of the pulse.

Dependence on the pixel geometry

The dependence of the noise occupancy on the pixel geometry can be seen in Fig. 5.32. Comparing sectors 0, 1 and 3, it can be seen that at the same threshold, sectors with larger spacing between the collection n-well and the surrounding p-well show a lower noise occupancy. Comparing sectors 1 and 2, it can be concluded that the diode reset is beneficial for the noise occupancy. In Fig. 5.30, it is also shown that the separate dependency of the noise occupancy on I_{thr} and V_{CASN} is smaller for the sector with the diode reset (sector 2) or with large spacing between the collection n-well and the surrounding p-well (sector 3). In the following, the results will be presented for sector 2.

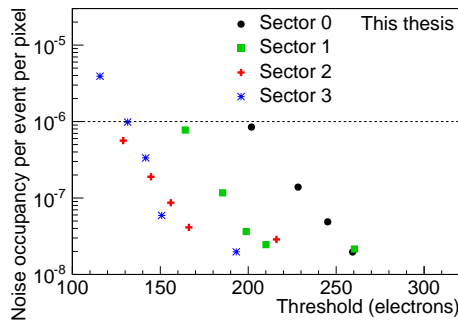


Figure 5.32: Comparison of the noise occupancy values for the different sectors of chip W9-16 after masking of the 20 noisiest pixels at $V_{BB} = -3$ V and $V_{CASN} = 135$ DAC units.

Chip-to-chip fluctuations

In Fig. 5.33, the chip-to-chip fluctuation of the noise occupancy values is studied. In Fig. 5.33a, the noise occupancy values are plotted as a function of I_{thr} for three different chips, while in Fig. 5.33b, the case with $I_{thr} = 40$ DAC units is studied in more detail by plotting the distribution of the firing frequency of the pixels. At this setting, there is a similar number of pixels firing with low frequency in the case of the three chips (around 150 pixels), and all three chips have a few pixels, which fire often, but there is a significant difference in the firing frequency of these pixels. This means that differences are expected in the noise occupancy values if no pixels are masked, while after masking the noisiest pixels similar values should be observed. This is confirmed in Fig. 5.33a, where the difference of the noise occupancy can be up to almost two orders of magnitude before

masking any pixels at $I_{thr} = 40$ DAC units, while it drops to around a factor 2 after masking the 20 noisiest pixels.

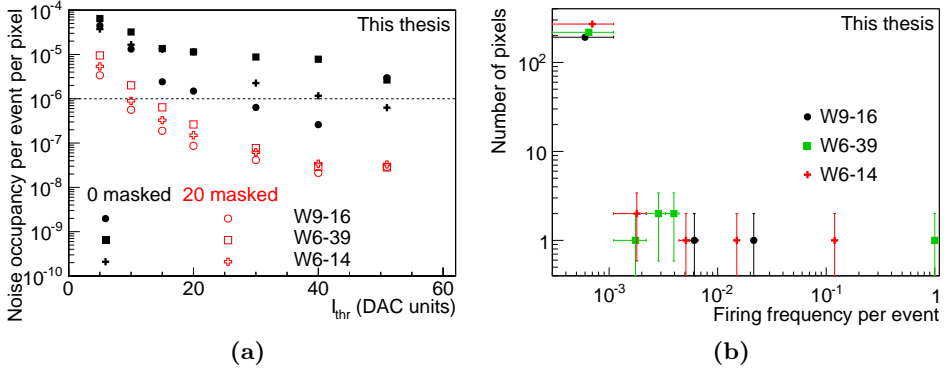


Figure 5.33: In panel (a) the noise occupancy values of three chips at $V_{BB} = -3$ V and $V_{CASN} = 135$ DAC units is plotted as a function I_{thr} without masking any pixels and after masking the 20 noisiest pixels. Panel (b) shows the number of pixels firing with a certain firing frequency per event for the same three chips at $V_{BB} = -3$ V, $I_{thr} = 40$ DAC units and $V_{CASN} = 135$ DAC units without masking any pixels.

Radiation hardness

In Fig. 5.34, the change of the noise occupancy is shown after irradiating the chips with non-ionizing irradiation. The measurement of the noise occupancy of the TID irradiated chips was unfortunately not done due to time limitations at the test-beam facilities. The chips become slightly more noisy after irradiating them with 10^{13} 1 MeV n_{eq}/cm^2 ; however, the

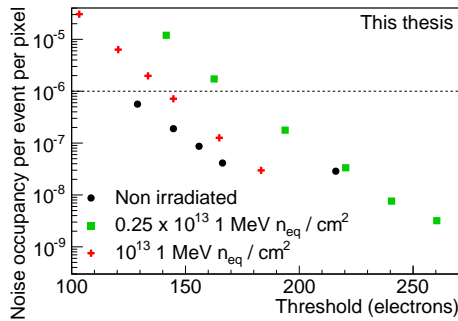


Figure 5.34: Comparison of the noise occupancy values after masking the noisiest 20 pixels with different irradiation levels for three sensors at $V_{BB} = -3$ V and $V_{CASN} = 135$ DAC units.

chips show a large operational margin also after irradiation. The chip irradiated to only 0.25×10^{13} 1 MeV $n_{\text{eq}}/\text{cm}^2$ shows the highest noise, which can be attributed to the fact that for this chip V_{AUX} was not adjusted, while for the chip with 10^{13} 1 MeV $n_{\text{eq}}/\text{cm}^2$, it was adjusted to $V_{\text{AUX}} = 125$ DAC units, instead of the default $V_{\text{AUX}} = 117$ DAC units.

5.6 The operating range

The operating range of the chip is mainly determined by the requirements on the noise occupancy ($< 10^{-6}$ hits/event/pixel), on the detection efficiency ($> 99\%$) and on the spatial resolution ($< 5 \mu\text{m}$). These requirements have to be fulfilled simultaneously, which give both an upper and a lower limit on the charge threshold range where the chip can be operated. The efficiency limits the operating range from large threshold values, the noise occupancy from low threshold values, and the resolution can give a limit from both directions. In Fig. 5.35, these parameters and the average cluster size are plotted as a function of the charge threshold for a non-irradiated and an irradiated sensor. It can be seen that the chip fulfills all the upgrade requirements between a charge threshold of around 130 and 230 electrons in the non-irradiated case. This range is slightly reduced after irradiation to around 140–210 electrons. This means that the small degradation in the performance of the detector seen after irradiation can be compensated by adjusting the threshold slightly, therefore the sensors are fully functional for the full planned lifetime of the detector.

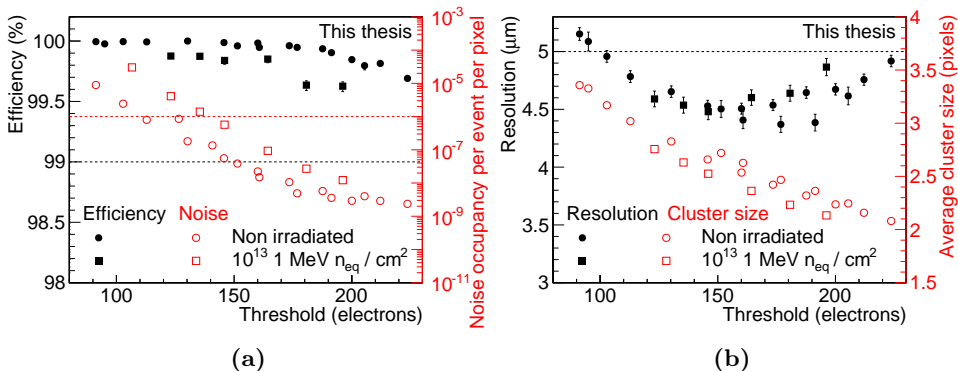


Figure 5.35: Panel (a) shows the detection efficiency and the noise occupancy as a function of the threshold, while panel (b) shows the average cluster size and the resolution as a function of the threshold for a non-irradiated chip (W2-31) and a chip irradiated to 10^{13} 1 MeV $n_{\text{eq}}/\text{cm}^2$ (W2-12) at $V_{\text{BB}} = -3$ V. The dotted lines at 99%, at 10^{-6} hits/event/pixel and at $5 \mu\text{m}$ are the requirements for the minimal efficiency, the maximal noise occupancy and the maximal resolution, respectively.

5.7 Cluster shape

The study of the shape of clusters was done integrating over all sectors to have higher statistics for the less frequent cluster shapes. During the analysis each cluster shape receives an ID, which is unique for each shape and for each rotation of the shape. In Fig. 5.36a, the probability of each cluster shape can be seen for different settings of I_{thr} as a function of this ID with the shapes indicated by drawings. In Fig. 5.36b, the probability is shown when the clusters with the same shape but different orientation are grouped together. Since the pixels of the pALPIDE-1 are squares, and the placement of the pixels is not staggered, it is expected that the probability of the different rotations is the same, which is confirmed within statistical fluctuations from these measurements. It can also be seen that at high I_{thr} , the most frequently appearing cluster type is the one containing only one pixel, while at lower I_{thr} values, larger clusters are favored. However, not even at the lowest I_{thr} values, do clusters longer than two pixels in one direction become frequent. This situation would change if the sensors were not placed perpendicular to the beam, which will be the case in the final detector.

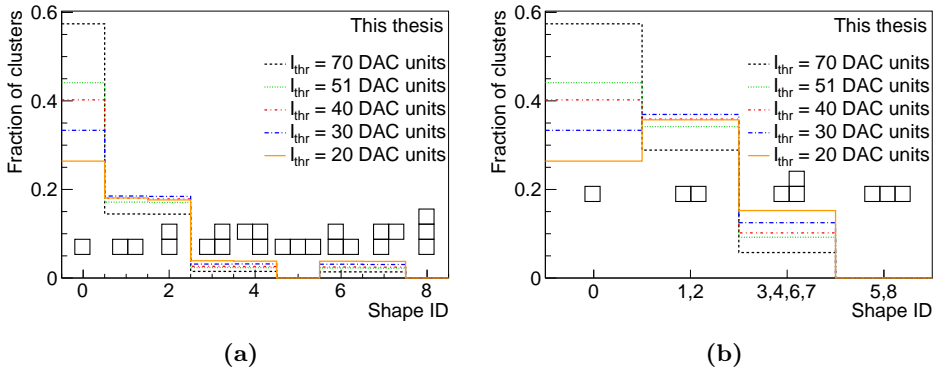


Figure 5.36: Both plots show the fraction of clusters with certain shapes at $V_{BB} = 0$ V and $V_{CASN} = 57$ DAC units for chip W2-25. In (a) each bin corresponds to a rotation of a shape, while in (b) each bin correspond to a shape with all rotation included. The shapes are indicated by drawings for each ID.

Figs. 5.37 to 5.39 show how frequently some cluster shapes appear depending on the impinging point of the track within two times two pixels. Single pixel clusters are presented in Fig. 5.37, which shows that they are most likely to appear when a track passes through the center of the pixels. Two-pixel clusters are shown in Fig. 5.38 both separately for the two possible rotations and summed. They are most likely to happen if the track goes through the border between two pixels and much less likely when the track goes through the center or the corner. The four rotations of the L-shaped three-pixel cluster can be seen in Fig. 5.39 together with the four rotations summed up. These shapes appear most frequently when a track passes through one corner of a pixel. From the summed histograms it can be also concluded that, as expected, the response of the pixels is symmetric under rotations and mirroring. The corresponding plot for the clusters with three pixels in a row is not included, because it does not have enough statistics.

From these results, it can be concluded that no asymmetry in the x - and y -direction of the pixel is present and that the dependence of the shape of the clusters on the impinging point of the track can be qualitatively understood based on charge sharing. These results can be used in the future for constructing the simulation of the pixel response.

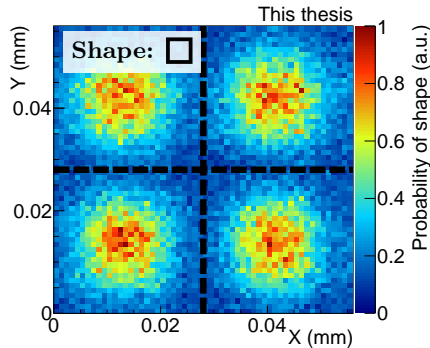


Figure 5.37: Probability of the appearance of one-pixel clusters within two times two pixels as a function of the impinging point of the track at $V_{BB} = 0$ V, $I_{thr} = 20$ DAC units and $V_{CASN} = 57$ DAC units for chip W2-25.

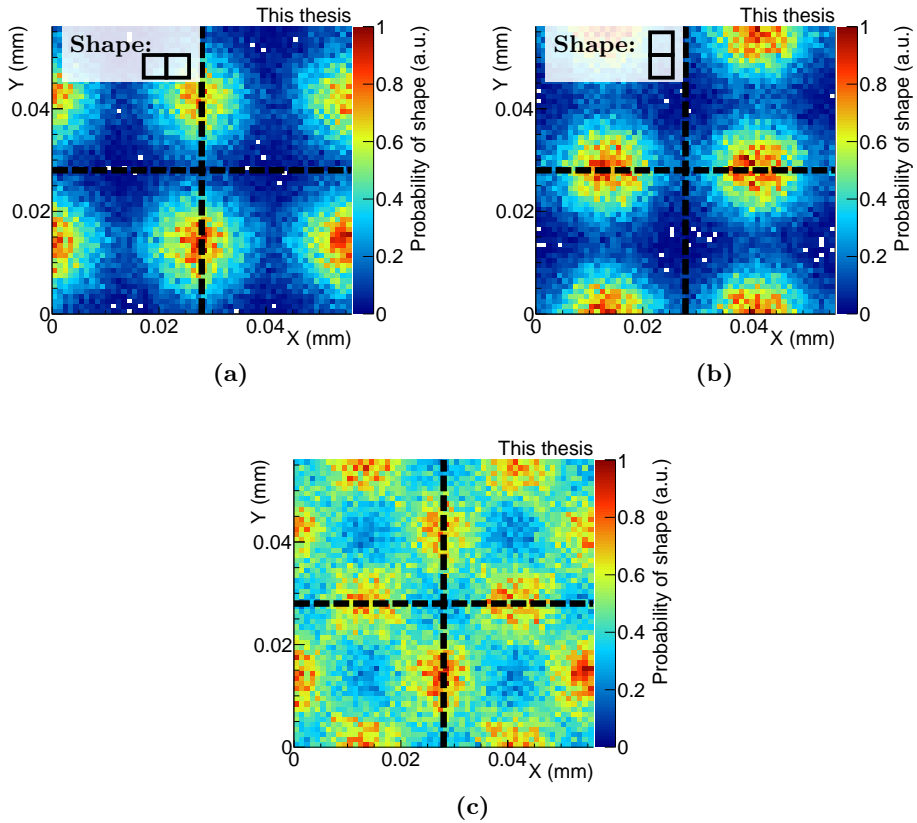


Figure 5.38: Probability of the appearance of two-pixel clusters within two times two pixels as a function of the impinging point of the track at $V_{BB} = 0$ V, $I_{thr} = 20$ DAC units and $V_{CASN} = 57$ DAC units for chip W2-25. Panels (a) and (b) show separately the two different rotations indicated on the plot, while (c) shows the two rotations summed up.

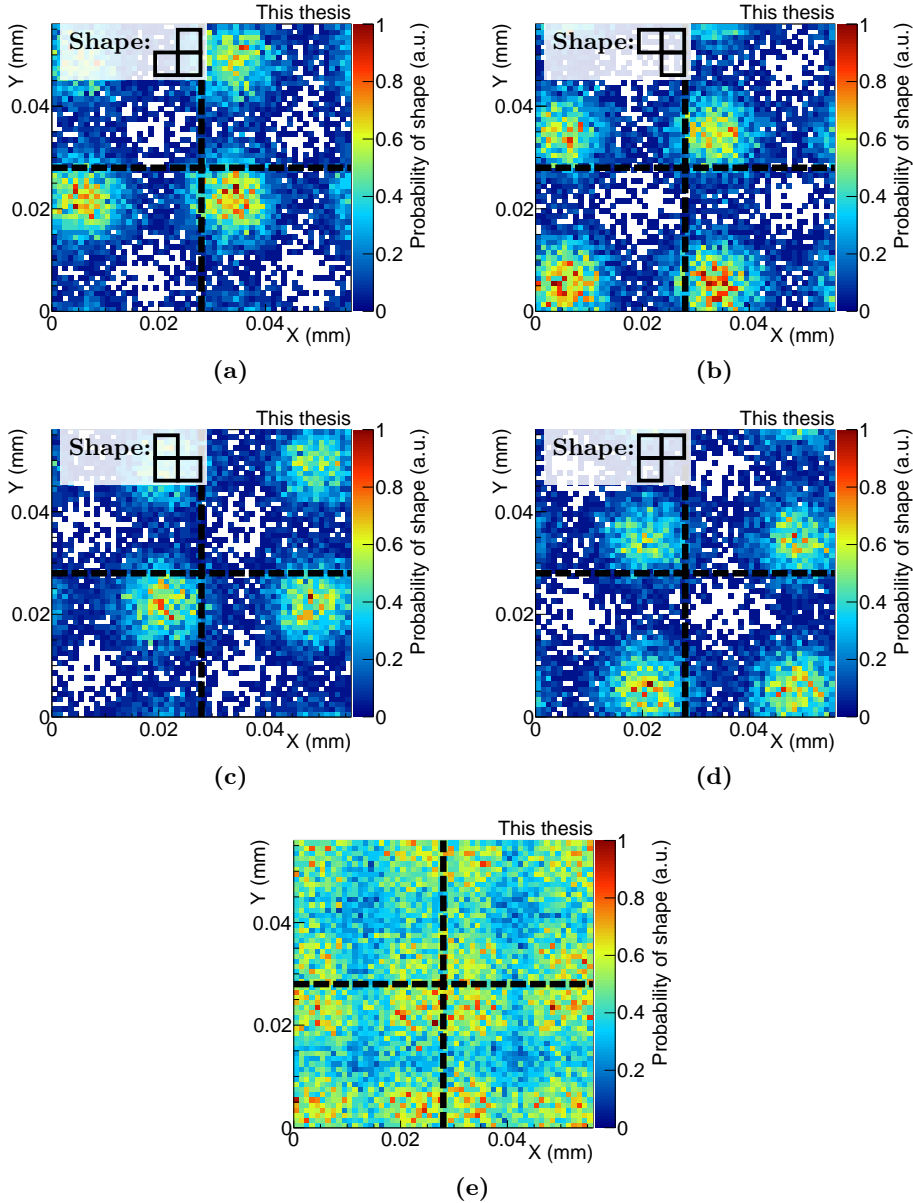


Figure 5.39: Probability of the appearance of three-pixel clusters with the shape of the letter **L** within two times two pixels as a function of the impinging point of the track at $V_{BB} = 0$ V, $I_{thr} = 20$ DAC units and $V_{CASN} = 57$ DAC units for chip W2-25. Panels (a), (b), (c) and (d) show separately the four possible rotations indicated on the plot, while (e) shows the four rotations summed up.

5.8 Outlook on later prototypes

Since the production and testing of the pALPIDE-1, two new prototypes and the final chip, the ALPIDE, have been produced and tested. The tests of the later chips at the test-beam facilities use the same software as the one described in detail in Section 4.2 and a telescope, which is a further developed form of the telescope described in Section 4.3. In the following, the main test results of these chips from Refs. [59, 74–76] are discussed and compared to the results of the pALPIDE-1 presented in the current Thesis.

5.8.1 pALPIDE-2

As discussed in Section 3.3, the pALPIDE-2 has four sectors. Two of them (sectors 0 and 2) have the same specifications as two sectors of the pALPIDE-1 (sectors 1 and 3 respectively), therefore they are directly comparable. Sector 3 of the pALPIDE-2 can be compared to sector 2 of the pALPIDE-1 to study the effect of the spacing between the collection n-well and the surrounding p-well for the pixels with a diode reset. Figs. 5.40 to 5.42 show the comparison between the corresponding sectors of the pALPIDE-1 and pALPIDE-2 prototypes.

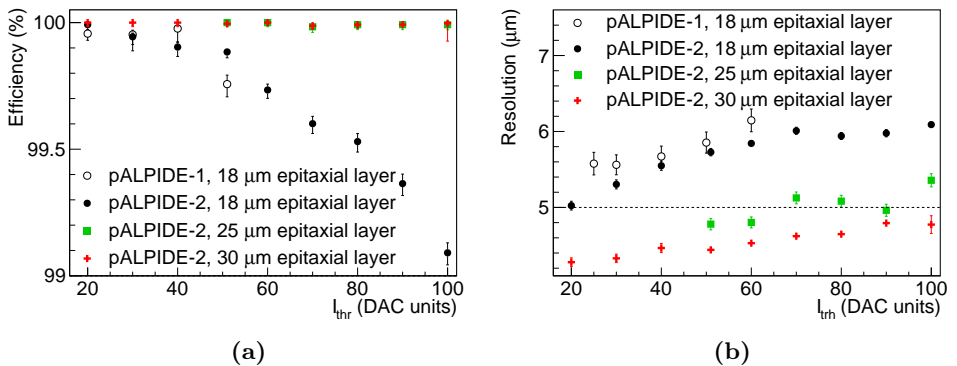


Figure 5.40: Comparison of the detection efficiency (a) and resolution (b) of the pALPIDE-1 and pALPIDE-2 for the sectors with a PMOS reset and 4 μm spacing between the collection n-well and the surrounding p-well at $V_{BB} = -6$ V and $V_{CASN} = 160$ DAC units. Points for the pALPIDE-2 are taken from Ref. [59].

Comparison of the sectors with a PMOS reset

Fig. 5.40 shows the comparison for the sectors with 4 μm spacing and a PMOS reset, where a good agreement can be seen between the pALPIDE-1 and pALPIDE-2 both in terms of efficiency and resolution. The pALPIDE-2, however, shows better performance with 2 μm spacing than the pALPIDE-1, which is shown in Fig. 5.41. This might be attributed to some changes in the routing, which was done to optimize the parasitic couplings within the sensor, and which could have a different effect on the sectors depending on the spacing.

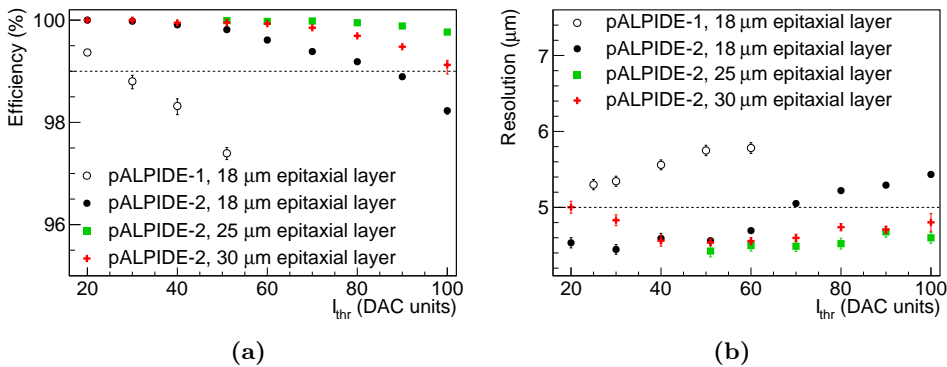


Figure 5.41: Comparison of the detection's efficiency (a) and resolution (b) of the pALPIDE-1 and pALPIDE-2 for the sectors with a PMOS reset and 2 μm spacing between the collection n -well and the surrounding p -well at $V_{BB} = -6$ V and $V_{CASN} = 160$ DAC units. Points for the pALPIDE-2 are taken from Ref. [59].

Comparison of the sectors with a diode reset

The comparison of the sectors with a diode reset (Fig. 5.42) show no positive effect from the larger spacing, which is in contradiction with the results from the sectors with a PMOS reset and also with the results obtained with the pALPIDE-3 as will be shown below. This might be explained by slightly different biasing settings for the pALPIDE-1 and the pALPIDE-2, since the parameter V_{AUX} was tuned differently for the two measurements. The pALPIDE-1 is relatively insensitive to this parameter; however, larger sensitivity was seen in the case of the pALPIDE-2, and most likely the setting used during the test-beam measurements was not optimal.

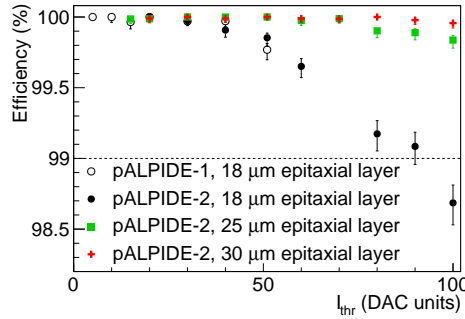


Figure 5.42: Comparison of the detection efficiency of sector 2 of the pALPIDE-1 (diode reset, 2 μm spacing) and sector 3 of the pALPIDE-2 (diode reset, 4 μm spacing) at $V_{BB} = -3$ V and $V_{CASN} = 135$ DAC units. Points for the pALPIDE-2 are taken from Ref. [74].

Further optimization in the pALPIDE-2

In the three comparison figures (Figs. 5.40 to 5.42), the results of the pALPIDE-2 are presented for three different thicknesses of the epitaxial layer. It can be concluded that a thicker epitaxial layer is beneficial for both the detection efficiency and the spatial resolution. The sector with 2 μm spacing between the collection n-well and the surrounding p-well performs best with a 25 μm thick epitaxial layer, while the sector with 4 μm spacing performs best with a 30 μm thick epitaxial layer. This can be explained by the size of the depletion region, which is smaller in the case of 2 μm spacing. Therefore with the 30 μm thick epitaxial layer, the generated charge travels a longer path by diffusion, and this worsens the charge collection efficiency. From these results and the results of the pALPIDE-3, the 25 μm thick epitaxial layer was chosen for the ALPIDE.

Sector 1 of the pALPIDE-2 has the same specifications in terms of spacing and reset mechanism as sector 0; however, the size of the input transistor has been optimized in this sector. This optimization lowers greatly the noise occupancy, which can be seen in Fig. 5.43. At low I_{thr} , which means low threshold, the optimization results in the noise occupancy being around a factor ten lower, while at higher I_{thr} values, the improvement is even larger. It reaches around four orders of magnitude at 500 pA, where it falls below the sensitivity limit of the measurement in the optimized sector.

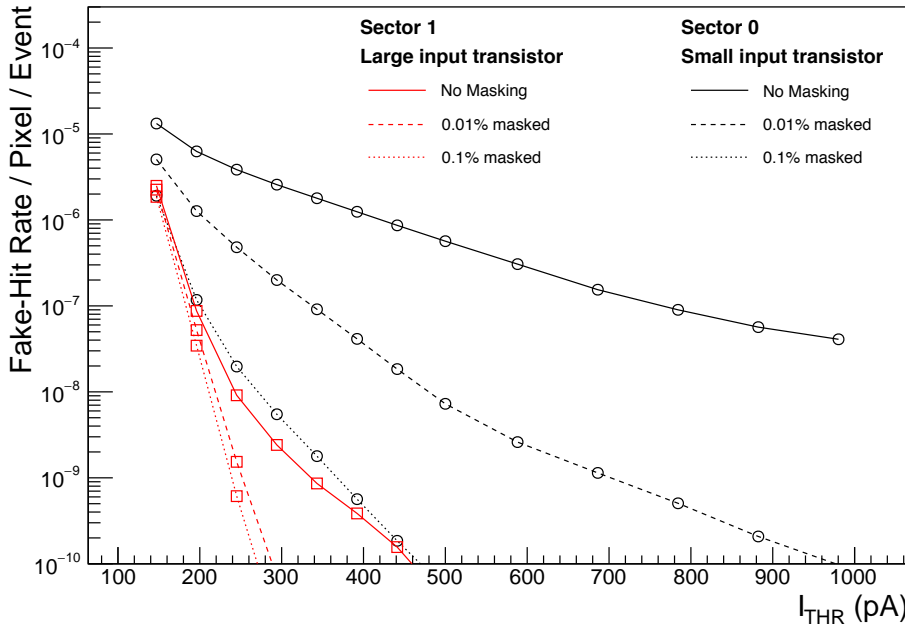


Figure 5.43: Comparison of the noise occupancy values for sector 0 (small input transistor) and sector 1 (optimized input transistor) of the pALPIDE-2 at $V_{BB} = -3$ V and $V_{CASN} = 135$ DAC units [59].

5.8.2 pALPIDE-3

The pALPIDE-3 chip has eight sectors, where the sectors correspond to the optimization steps of the analog front-end, as was described in Section 3.3. Sector 2 of the pALPIDE-3 corresponds to sector 2 of the pALPIDE-1, while sector 4 and 5 of the pALPIDE-3 has the fully optimized front-end with two different spacings between the collection n-well and the surrounding p-well. The comparison of the efficiency and the average cluster size values for these three sectors can be seen in Fig. 5.44 from data taken with electrons at a momentum of 450 MeV/ c . The plot shows that the efficiency becomes higher after the optimization, and that larger spacing has a beneficial effect. The cluster size stays similar after the optimization (sector 2 and 4), but becomes smaller with larger spacing between the collection n-well and the surrounding p-well. The difference is, however, within one pixel for the different sectors, therefore a large impact on the resolution is not expected. The resolution was also measured to confirm this, and values around 5 μm can be reached with a sufficient operational margin [77].

The pALPIDE-3 was produced in two versions: one with small input transistor size and one with the optimized size as in sector 1 of the pALPIDE-2. In the case of the version with the optimized size, the noise occupancy is always below the sensitivity limit of the measurements ($\sim 10^{-10}$ hits/event/pixel) [77]. Based on these results, for the final chip, the ALPIDE, the fully optimized sector of the pALPIDE-3 with the larger spacing between the collection n-well and the surrounding p-well (sector 5) with the optimized input transistor has been chosen.

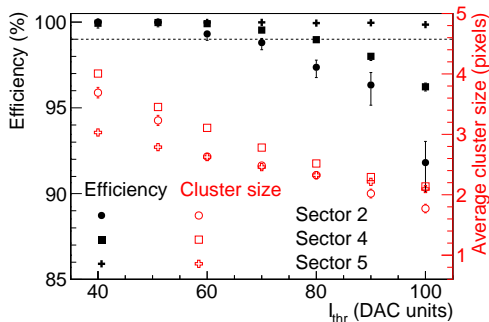


Figure 5.44: Comparison of the efficiency and average cluster size results for the different steps of the optimization of the pixels in the sectors of the pALPIDE-3 at $V_{BB} = -3$ V and $V_{CASN} = 105$ DAC units. The data are taken from Refs. [75, 76].

5.8.3 ALPIDE

The results for the final chip are presented in Fig. 5.45, which shows that it demonstrates similar behavior in all measured quantities to the prototypes. The noise occupancy stays below the sensitivity limit for the whole tested range of I_{thr} , while the efficiency stays above 99% below $I_{thr} = 100$ DAC units. In the same range the resolution is around $5 \mu\text{m}$, and then goes up to around $6.5 \mu\text{m}$, where it shows a plateau. The ALPIDE therefore fulfills all the requirements of the upgrade in terms of detection efficiency, noise occupancy and spatial resolution with a large operational margin.

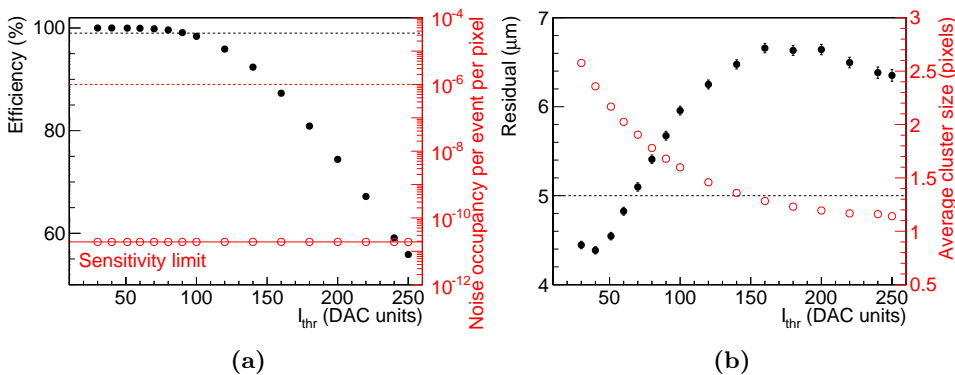


Figure 5.45: Panel (a) shows the efficiency and noise occupancy results of the ALPIDE at $V_{BB} = -3$ V and $V_{CASN} = 105$ DAC units. The noise occupancy is calculated after masking the ten noisiest pixels. Panel (b) shows the resolution and the average cluster size at the same settings. The data are taken from Refs. [78–80].

5.9 Summary

The Inner Tracking System of ALICE will be replaced during the Second Long Shutdown of the LHC in 2019–2020 to improve greatly the tracking capabilities and the data-taking rate of the detector. The new ITS will consist of seven layers, all of them equipped with Monolithic Active Pixel Sensors. In the previous chapters, the first large scale prototype of the ALPIDE has been introduced, and the characterization results have been discussed in detail. Furthermore, a detailed description of the setup and of the software used for the analysis of the data taken at test-beam measurements has been given. It has been shown by simulation and confirmed by the measurements that a telescope of seven equidistantly placed (with 1.9 cm distance) pALPIDE-1 chips has a pointing resolution of 2–3 μm at

the central chip, which makes such a telescope a suitable tool to measure a spatial resolution of around 5 μm .

The pALPIDE-1 has been shown to fulfill the requirements of the upgrade in terms of detection efficiency, spatial resolution and noise occupancy. It shows a high (above 99%) efficiency both before irradiation and after irradiating the sensors with 700 krad and 10^{13} 1 MeV $n_{\text{eq}}/\text{cm}^2$, with a slight degradation caused by the non-ionizing irradiation. It was shown that applying reverse substrate bias and a large spacing between the collection n-well and the surrounding p-well are clearly beneficial, and that the sectors with a diode reset have the highest efficiency.

The position resolution was calculated from the measured residuals, and it has been demonstrated that the reset mechanism has a negligible influence on the resolution. The spacing and the application of reverse substrate bias, however, have a significant influence, with smaller spacing and large negative reverse substrate bias being beneficial. A slight degradation of the resolution has been observed after irradiating the sensors with 10^{13} 1 MeV $n_{\text{eq}}/\text{cm}^2$, but the measured values are still compatible with the requirements of the upgrade.

The noise occupancy was also studied, and it was shown that it is lower than the required 10^{-6} hits/event/pixel above a threshold of around 120 electrons if the most noisy 0.1% of the pixels are masked. Pixels with a large spacing between the collection n-well and the surrounding p-well show a lower noise occupancy, and the diode reset is favored. It was shown also that the noise occupancy values become slightly higher after irradiating the chips to 10^{13} 1 MeV $n_{\text{eq}}/\text{cm}^2$, and that tuning other parameters of the chip (e.g. V_{AUX}) might be necessary. It was discussed also that in later prototypes much lower noise occupancy values have been achieved by optimizing the size of the input transistor.

Overall, the pALPIDE-1 chip shows very good performance, which is compatible with the requirements of the upgrade, and the later prototypes show an as good or even improved performance, while also integrating all the additional features needed for the detector, which were missing from the pALPIDE-1 (e.g. buffers within the pixels.). The ALPIDE is therefore well suited to equip the detector, which will replace the current Inner Tracking System of the ALICE experiment.

Part III

**NEAR-SIDE JET PEAK
SHAPE ANALYSIS**

6. Motivation and datasets

In this part, a two-particle angular correlation analysis of the Pb–Pb and pp data taken at $\sqrt{s_{\text{NN}}} = 2.76$ TeV by the ALICE experiment will be presented. First in this chapter, after giving a short motivation for the two-particle angular-correlation studies, the data and the Monte Carlo event generators used for the analysis will be introduced in detail.

6.1 Motivation

The interaction of partons with the Quark-Gluon Plasma (QGP) can be studied directly by full jet reconstruction. However, in heavy-ion collisions the magnitude of the combinatorial background makes it difficult to reconstruct jets below a certain energy [81, 82]. An alternative approach is to study the interactions of partons with the QGP statistically by integrating over many events. Measuring the angular correlation of particles is such a technique, which can be used for studying jets down to the energy regime where the perturbative approximations of QCD are not reliable. Jets in this energy regime are commonly referred to as mini-jets.

In two-particle angular correlation measurements, particles are correlated in their azimuthal angle (φ) and pseudorapidity (η), and the differences for particle pairs in these variables are calculated (indicated by $\Delta\varphi$ and $\Delta\eta$). Back-to-back jets manifest themselves as a peak above the combinatorial background around $\Delta\varphi = 0$, $\Delta\eta = 0$ and as a structure elongated in $\Delta\eta$ around $\Delta\varphi = \pi$. The structure at $\Delta\varphi = \pi$ is not collimated around $\Delta\eta = 0$, because the partons carry different momenta of the nucleon, therefore the two jets are not expected to be back-to-back exactly in η . Also the difference in η between back-to-back jets depends on their η and gives an approximately constant distribution when averaged over many events. Comparing the height or shape of the peak or of the structure at $\Delta\varphi = \pi$ to the same in pp collisions can give insight into the interactions of the jets with the medium produced in heavy-ion collisions.

The size of the interaction region, and therefore the area where the QGP is produced, greatly depends on centrality. Peripheral collisions are expected to be more similar to pp collisions than central collisions. This

has been observed in many analyses, for example in the measurement of the nuclear modification factor in Pb–Pb [17], where the measurements show about five times larger suppression in central collisions than in peripheral ones at $p_T = 6 - 7 \text{ GeV}/c$. Therefore it is interesting to study angular correlation measurements as a function of centrality. The effects of the medium will be strongest in central collisions, while in peripheral collisions a similar shape as in pp collisions is expected.

The yield in the peak around $(\Delta\varphi, \Delta\eta) = (0, 0)$ and in the elongated structure around $\Delta\varphi = \pi$, both originating from jets, has been studied and compared to pp collisions [83]. In Fig. 6.1, the ratio of the peak yield from Pb–Pb to the one from pp is shown for the near-side ($-\pi/2 < \Delta\varphi < \pi/2$) and the away-side ($\pi/2 < \Delta\varphi < 3\pi/2$), corresponding to the back-to-back jet pair. The yield on the away-side, which corresponds to the jet which traversed a longer pathlength in the QGP, is found to be suppressed in central collisions. This is expected, since this jet loses more energy while traversing the longer path. In Fig. 6.1, however, a modification of the yield (a moderate enhancement) is also seen on the near-side in central collisions. It is therefore expected that the shape of near-side jet peak is also modified by the medium. As expected no significant modification is seen in peripheral collisions on either the near- or the away-side.

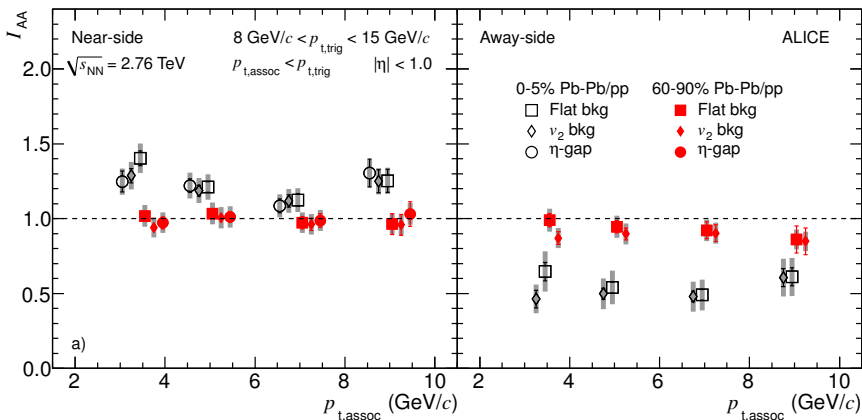


Figure 6.1: I_{AA} , the ratio of yield from Pb–Pb and from pp as a function of the momentum of the associated particles for the near- (left) and away-side (right) [83].

In Ref. [15], the CMS collaboration studies the correlation of high- p_T jets with hadrons. They select events with back-to-back jets, where for one of them, p_T is larger than $120 \text{ GeV}/c$, while for the other, larger than $50 \text{ GeV}/c$. In this sample, they find that in central collisions, the two back-to-back jets have imbalanced p_T . They then study whether this imbalance can be recovered by low p_T (below $8 \text{ GeV}/c$) tracks. They find that in

central events the imbalance can be recovered by tracks with $p_T < 2 \text{ GeV}/c$ at large angles from the jet axis ($\sqrt{\Delta\varphi^2 + \Delta\eta^2} > 0.8$). The analysis performed in this Thesis will study the interactions of partons with the medium in this regime further by measuring angular correlations of low- p_T particles. These particles are not directly accessible with jet reconstruction techniques, therefore this study complements the jet analysis of CMS.

The distribution of particles traveling through a static medium can already be modified; however, the medium created in heavy-ion collisions is not static, but shows longitudinal, radial and anisotropic flow (see e.g. Refs. [84, 85]). Therefore any modification of the peak in Pb–Pb collisions compared to pp collisions has to be interpreted as an interaction of the flowing medium and the traversing particles. In Ref. [86], the shape of the peak was modeled for the presence of longitudinal flow in the medium. The conclusions of the paper are that if there is a static medium produced, the peak becomes broader, whereas if longitudinal flow is present, the peak still becomes broader, but it also becomes asymmetric in $\Delta\eta$ and $\Delta\varphi$. They predict a 20% broadening in $\Delta\varphi$ and a 60% broadening in $\Delta\eta$ from peripheral to central events. This is illustrated in Fig. 6.2. In the same paper they find that the presence of collective flow can result in the energy distribution of a jet being asymmetric with respect to its calorimetric center. This in turn can manifest itself as a "double-hump shape" when looking at the energy distribution of a sample of such jets (Fig. 6.3).

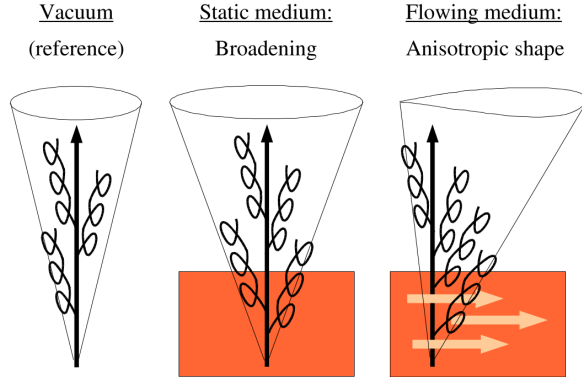


Figure 6.2: Illustration of how longitudinal flow deforms the near-side jet peak [86].

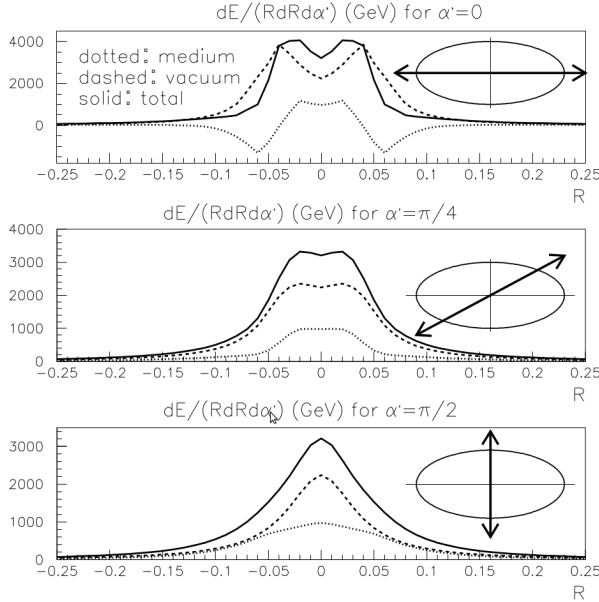


Figure 6.3: "Double-hump shape" in the correlation function as a result from the interplay of jets and collective flow [86].

6.2 Data sets and physics selection

To study the interplay of jets with the flowing medium, Pb–Pb and pp data at the center-of-mass-energy of $\sqrt{s_{\text{NN}}} = 2.76$ TeV taken with the ALICE detector were analyzed. The Pb–Pb data taken in both 2010 and 2011 is used in the current analysis. It consists of both minimum-bias data (around 16 million events taken in 2010 and around 2 million events taken in 2011) and data taken with a trigger enhancing the 0–50% centrality range taken in 2011 (around 21 million events). The pp sample was taken in 2011, and it corresponds to around 30 million minimum-bias events. In the case of the pp data, an energy deposition in the V0-A, the V0-C or in the SPD was required as trigger and it was requested to be in coincidence with the crossing of the proton bunches, which was determined from the filling scheme of the LHC. The beam background was reduced with cuts on the V0 timing signals and the number of clusters and tracklets in the SPD [87, 88].

For minimum-bias Pb–Pb collisions in 2010, events were recorded if two of the following three conditions were met in coincidence with the crossing of the Pb bunches determined from the filling scheme of the LHC [13, 89]:

- Two hits in the outer layer of the SPD

- Signal in V0-A
- Signal in V0-C

In the offline event selection, the information of the ZDC and the V0 was used to further reduce the number of events coming from beam background and electromagnetically induced interactions.

In 2011, the trigger required a coincidence of the two V0 detectors and the passage of two crossing Pb bunches according to the filling scheme of the LHC, for both the minimum-bias and the centrality enhanced data. For the centrality enhanced data an additional online selection criteria was applied on the amplitude of the V0 detector [88, 90]. Offline, similarly to 2010, the information from the timing of the ZDC was used to reduce background events. The details of these datasets used can be found in Appendix C.

If only minimum-bias triggers were used, the number of events in each centrality class should be the same; however, by merging the events from different triggers, the centrality classes used in this analysis contain different numbers of events. In Table 6.1, the number of accepted events can be seen for all five centrality classes. To accept an event, it has to have a centrality lower than 80% and the reconstructed vertex has to be within ± 7 cm of the center of the detector.

Collision system	Centrality class	Accepted events (10^6)
Pb–Pb	0–10%	7.7
	10–20%	2.9
	20–30%	2.9
	30–50%	5.9
	50–80%	3.9
pp	—	24.0

Table 6.1: Number of accepted events in *pp* and *Pb–Pb* collisions for each centrality class.

The width of the centrality bins are not the same throughout the full centrality range, because the number of tracks per event change with centrality. This means that the same number of events in a peripheral bin corresponds to smaller statistics in terms of number of tracks than in a central bin. Therefore to have similar statistics in all bins, the peripheral ones are wider. However, this is achieved by doing part of the analysis in smaller bins and merging them at a certain point in the analysis. The same kind of merging is also done for the high centrality bins, where the reason behind it is to be able to apply centrality dependent corrections to

the data in finer centrality bins than the ones used for the final analysis. The smaller bins, which are to be merged, have to have equal number of events to avoid a situation that a bin is dominated by a sub-sample of the events from a smaller bin. Therefore if the smaller bins have a different number of events, some of these events are randomly removed from the data analysis such that the number of the events becomes equal. In Fig. 6.4, the number of events before and after this removal is shown with the final bin sizes indicated by the dashed lines. The effect is clearly visible in the 0–10% centrality class, where first this flattening of the number of events is done in the first 5 bins (all 1% wide), then it is repeated for the bins of 0–5% and 5–10%. It is also visible for the 50–60% centrality bin, where the number of events is reduced such that it becomes the same as for the rest of the bins between 50% and 80%. An effect is also present in the 20–30% bin, which, however, is not merged later with any other bin. The number of events in this bin was reduced to have the possibility to merge the 20–30% bin with the 30–40% bin, if it is necessary due to small statistics. This was found not needed in the end.

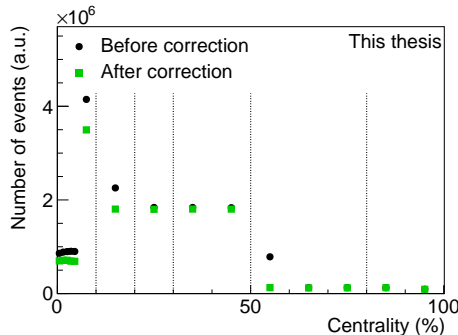


Figure 6.4: Illustration of the concept of the centrality flattening from Pb–Pb data taken in 2011. Each point corresponds to a centrality bin used when centrality dependent corrections are applied to the data, while the dashed lines show the bins used for the final analysis.

6.3 Track and collision vertex reconstruction

For the reconstruction of the vertex, the ITS and TPC detectors were used. The tracks used in the reconstruction are extrapolated to the point of their closest approach and the outliers are removed before the determination of the vertex. The vertex is then fitted after weighting the tracks to account for any remaining outliers. In high pileup events in addition, an iterative procedure is introduced for the fitting [91]. In the current

analysis events with a reconstructed primary vertex within ± 7 cm in the z -direction of the nominal collision point are accepted. This limitation is introduced because the η acceptance of the detector is changing with the z -position of the primary vertex, which can have a direct effect on the $\Delta\eta$ distribution of particle pairs.

For the current analysis, two types of track reconstruction algorithms were used to study the systematic uncertainties arising from the tracking algorithms. The default reconstruction algorithm is described in detail in Ref. [82], and can be summarized as the following. In the reconstruction of these tracks, the ITS and the TPC are used. The ITS, however, had inactive SPD modules during data-taking, which results in a highly non-uniform acceptance of the ITS as a function of φ . This would cause problems for an angular correlation measurement, since it would result in the appearance of non-trivial structures as a function of $\Delta\varphi$. To avoid this, a set of tracks which have a hit in the SPD is combined with a set which do not have a hit in the SPD. In the latter case, however, instead of the hit in the SPD, the primary vertex is used in constraining the tracks. In both cases a track is required to have at least 70 space points (out of 159) in the TPC and a $\chi^2/ndf < 2$ for the fit. The tracks are further required to have a distance of closest approach to the primary vertex of 2.4 cm in the transverse direction and 3.2 cm in the longitudinal direction. The φ and η distributions of this set of tracks are indicated as *Hybrid tracks* in Fig. 6.5.

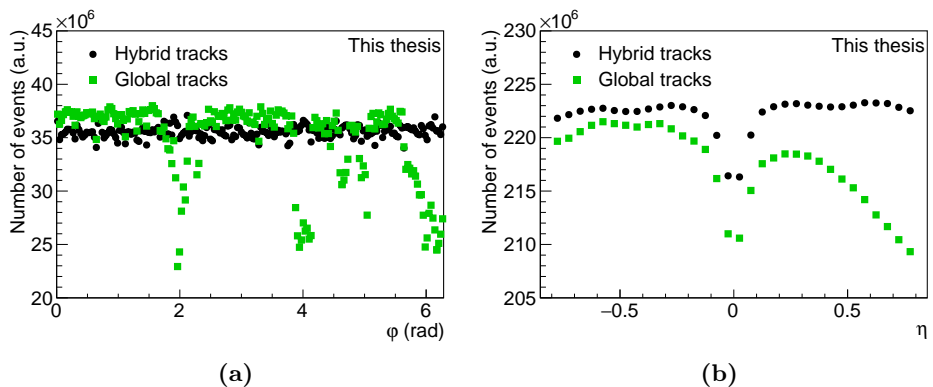


Figure 6.5: The φ (a) and η (b) distribution of the two types of tracks used for the analysis. The tracks called Hybrid are used for the default analysis, while the ones called Global are used for the studies of the systematic uncertainties.

The second type of track reconstruction algorithm, which is used in the analysis to estimate the systematic uncertainty arising from the tracking, is described in detail in Ref. [92]. The requirement on the number of minimum space points in the TPC is the same as in the first type of tracks

(70 out of 159), but three hits in the ITS are also required from which at least one must be in one of the first three layers of the ITS. The requirement on the quality of the tracks is also the same ($\chi^2/ndf < 2$), but there is a stricter criteria on the distance of closest approach to the primary vertex. In the z -direction, it has to be less than 2 cm, while in the transverse plane a p_T dependent cut is applied, where for each p_T bin, it has to be smaller than 7 standard deviations of the inclusive probability distribution of the distance of closest approach. These tracks have a less uniform φ distribution compared to the ones in the first group, as can be seen in Fig. 6.5, where this set of tracks is called *Global*. However, they contain less secondary tracks originating from weak decays and from interactions in the detector material.

6.4 Monte Carlo event generators

Monte Carlo (MC) generators are software packages which simulate high-energy particle collisions. These software packages are needed because many aspects of these collisions cannot be calculated from first principles, therefore phenomenological models have to be used. There are many MC generators available both for the description of pp collisions and heavy-ion collisions. These models incorporate different phenomenological approaches, but certain aspects are common in all of them (for a summary about generators of pp collisions see Refs. [93, 94]). Before the simulation of the collisions itself, the initial states of the partons within the proton have to be described. For this usually the Parton Distribution Functions (PDFs) are used, which give the probability of finding a quark or a gluon in the proton with a certain momentum fraction of the proton. The first step of simulating the collision itself is then the modeling of the initial hard scattering, which can be calculated from first principles by perturbation theory. After that, the parton shower has to be modeled, which describes the outgoing partons from the hard scattering by modeling the final state radiation. The same models can also be used to describe the initial state radiation of the incoming partons before the hard scattering. The next step is to describe the hadronization of the produced partons, which is not calculable from perturbative QCD (pQCD), therefore phenomenological models have to be applied. In the last step, the unstable hadrons have to be decayed. These processes would describe the collision completely if in one collision, only one hard scattering would take place. However, both for pp and for heavy-ion collisions, the rest of the partons of the nuclei can interact as well. These interactions cause the so-called underlying event, which gives an important contribution to the background of any process, therefore it has to be carefully modeled. It is also possible that within one

collisions multiple hard scatterings occur. This is referred to as Multiple Parton Interactions (MPI), and this also either contributes to the background of the measurements or it can distort the signals [95]. In heavy-ion collisions, it is not enough to model the interactions of the rest of the partons, also the dynamics of the produced QGP and the interactions of the partons with it have to be modeled. In the angular correlation analysis, three MC generators, PYTHIA, HIJING and AMPT, were used. These are discussed in detail in the following.

6.4.1 PYTHIA

Two different versions of PYTHIA were used to study pp collisions: PYTHIA 6.4 [96] with the Perugia-0 tune [97] and PYTHIA 8.1 [98, 99] with the Monash tune [100]. The two versions of PYTHIA (6.4 and 8.1) implement similar physics with some small modifications, but the main difference is that while PYTHIA 6.4 was written in FORTRAN 77, while from PYTHIA 8 on, the new versions were written in C++. Both versions start from parametrized PDFs and include hard scatterings of the types $2 \rightarrow 1$, $2 \rightarrow 2$ and $2 \rightarrow 3$. For the description of initial- and final-state radiation, both versions use both matrix elements from Feynman diagrams and parton showers. The difference between the two versions is that in PYTHIA 6.4, only the initial-state evolution and the multiple interactions were treated together, while in PYTHIA 8.1, the final state interactions are also treated together, which allows for the simulation of recoils. For the hadronization in PYTHIA 6.4, different models were available, while in PYTHIA 8.1, only the Lund string fragmentation model [101] is used. Finally, the decay of unstable particles is treated according to branching ratios and decay modes stored in the program for both versions.

The different tunes of PYTHIA are created because the phenomenological models in the MC generators have several parameters, which can be tuned to describe properly the data. For this, the important parameters have to be identified, and it is important to tune them such that the generator describes the broadest possible range of observables. For the Perugia-0 tune, data from LEP, the Tevatron, and the SPS were used and it was used to make predictions for the LHC before it started. The Monash tune reevaluates and optimizes the parameters based on the e^+e^- collider data and incorporates the results of the LHC, together with the results from the SPS and the Tevatron to tune the energy dependence in hadron-hadron collisions.

The two versions of PYTHIA were used for two different purposes in the analysis. PYTHIA 6.4 with the Perugia-0 tune was used to estimate the efficiency and the contamination from secondary and from fake particles, while the comparison of the results from pp data was done with

PYTHIA 8.1 with the Monash tune. The production called *LHC11b10a* was used for the Perugia-0 tune, while for the Monash tune, the on-the-fly production called *Pythia8_MB_2760GeV_Monash* was used.

6.4.2 HIJING

The HIJING 1.383 (Heavy Ion Jet INteraction Generator) simulation treats nucleus-nucleus collisions as a superposition of binary collisions. It combines pQCD inspired models for the high- p_T region and multiple string phenomenology for the low- p_T region [102]. In the high p_T region (above 2.3 GeV/ c), multiple mini-jets are produced, where the kinetic variables of these mini-jets are calculated by PYTHIA. At low p_T (below 2.3 GeV/ c), the multiple string phenomenology is inspired by a picture that soft gluon exchanges between the constituent quarks can lead to longitudinal string-like excitations of the hadrons. These strings are assumed to decay independently, resulting in quark-antiquark creation.

HIJING is also used in the current analysis for two purposes. First, it is used to estimate the reconstruction efficiency and the contamination in the case of Pb–Pb events, and second, it is used to validate the analysis method in a case without collective effects. A simple model of jet-quenching is available in HIJING; however, since it was used for the validation of the analysis without collective effects, this was turned off. For HIJING, the on-the-fly production referred to as *HIJING* was used.

6.4.3 AMPT

A Multi-Phase Transport model (AMPT) [103,104] is used to relate the results of the analysis of Pb–Pb events to the interplay of jets and mini-jets with the flowing QGP. Different configurations of AMPT are used in the analysis to study the effects of flow on angular correlations. AMPT is constructed of several stages: the initial stage, partonic interactions, hadronization and hadronic interactions. The initial conditions are taken from HIJING in the form of excited strings and mini-jet partons. Partonic interactions are done using Zhang’s Parton Cascade (ZPC) model, where the Boltzmann equation is solved for gluons and quark by a cascade model [105]. Hadronization is done by either a quark coalescence model or the Lund string fragmentation model, depending on the chosen settings of AMPT. Finally, the hadronic rescattering phase is modeled by the ART model [106,107]. These different stages are summarized in Fig. 6.6.

Three configurations of AMPT were used for the comparison with the results. Two of them differ in the version of AMPT. Versions v1.25t3 is the so-called string melting off version, where the mini-jet partons from HIJING go through the partonic rescattering phase, then they unite with

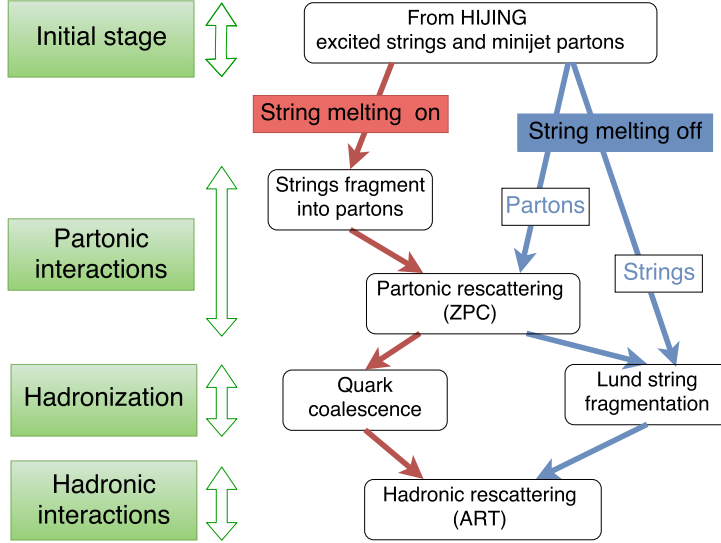


Figure 6.6: Summary of the stages of the different AMPT configurations. Adapted from Ref. [103].

their parent strings, and the strings are hadronized by the Lund string fragmentation model. Version v2.25t3 is the so-called string melting on version, where the excited strings from HIJING are fragmented into partons, and both these partons and the mini-jet partons from HIJING are included in the partonic rescattering phase. In this version the hadronization is done by a quark coalescence model. In both versions after hadronization, a hadronic rescattering phase is possible. Two configurations were used with the string melting on version, one where the hadronic rescattering phase was used and one where it was turned off. The parameters used for the three configurations can be found in Table 6.2, and further information is presented in Ref. [108]. The three productions of AMPT, corresponding to the three versions were *AMPT_LHC13f3a*, *AMPT_LHC13f3b* and *AMPT_LHC13f3b*.

Configurations	Version	isoft	ntmax
String melting off, hadronic rescattering on	v1.25t3	1	150
String melting on, hadronic rescattering off	v2.25t3	4	3
String melting on, hadronic rescattering on	v2.25t3	4	150

Table 6.2: Parameters of the three AMPT configurations.

7. Analysis technique

In this chapter, first the characterization of the near-side jet peak is described, then the studies of the systematic uncertainties are presented.

7.1 Two-particle correlations

The idea of two-particle correlation measurements is to study to which extent particles originating from the collision tend to appear spatially correlated. Correlations are, of course, expected, since collective flow and jets have been observed before, but further questions can also be answered from these measurements. In these measurements, the so-called per trigger yield is studied, which refers to the distribution of particle pairs as a function of $\Delta\varphi$ and $\Delta\eta$ normalized by the number of triggers. The details of how this observable is extracted from data will be discussed below, but to introduce the terminology an example is presented in Fig. 7.1. In Fig. 7.1a, it is presented with coloring according to the height of the distribution, while in Fig. 7.1b, it is shown with artificial coloring to indicate the different regions of the histogram. The histograms are divided into the near-

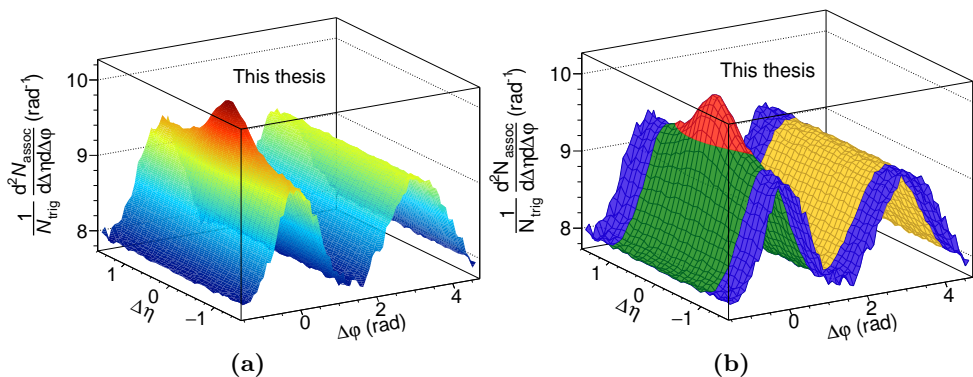


Figure 7.1: Example of the per trigger yield after all correction are applied which will be discussed below. The distribution is from the 30–50% centrality bin at $3 < p_{T,\text{trig}} < 4$ GeV/ c , $1 < p_{T,\text{assoc}} < 2$ GeV/ c .

and the away-side regions along $\Delta\varphi$. The near-side (indicated by green) spans from $-\pi/2$ to $\pi/2$ and the away-side (indicated by yellow) from $\pi/2$ to $3\pi/2$. The combinatorial and the flow modulated background can be seen in both the near- and the away-side, and it is indicated by blue. The dominant cosine-like $\Delta\eta$ -independent shape arises from the elliptic flow. The near-side jet-peak, the subject of the current analysis, is indicated by red, while the away-side jets appear as an elongated structure in $\Delta\eta$, therefore it is not easily distinguishable from the flow background.

7.1.1 Analysis method

To test the spatial correlation of particles, a trigger particle in a certain p_T window is chosen ($p_{T,\text{trig}}$), and all the particles from the same event, chosen also from a certain p_T window ($p_{T,\text{assoc}}$) are correlated to the trigger particle. The $p_{T,\text{assoc}}$ window can be lower than the $p_{T,\text{trig}}$ window or the same, in which case only those associated particles are considered, which have a lower p_T than the trigger particle to avoid double counting. The azimuthal and the pseudorapidity difference of the two particles are calculated, and a histogram showing the distribution of the particle pairs is filled. This is repeated for all trigger particles in the chosen p_T window from the event and also for all events in the same centrality and z -vertex bin. The histograms are filled separately for the different z -vertex bins to avoid biases arising from the the different pair acceptance and pair efficiency of the different bins. This distribution can be written as the following and an example can be seen in Fig. 7.2:

$$S(\Delta\varphi, \Delta\eta) = \frac{d^2N}{d\Delta\varphi d\Delta\eta} \quad (7.1)$$

where $S(\Delta\varphi, \Delta\eta)$ is the signal distribution and N is the number of particle pairs.

The detector response and the reconstruction procedure is not perfect, which can result in different inefficiencies in the analysis. A correction is therefore done for the detector acceptance, reconstruction efficiencies and contamination by secondary particles for each trigger and associated particle. This is achieved by applying a weight to each particle depending on their η , z -vertex, centrality and p_T while filling the histograms mentioned above. The weight is calculated from MC simulations, where the particles are propagated through the detector and are reconstructed in the same way as the real data. Comparing this reconstructed MC sample to the one containing the originally produced particles from the MC simulation (the MC truth), the weights can be calculated. The tracking efficiency and the contamination results for Pb–Pb collisions can be seen in Fig. 7.3 as a function of p_T or $\Delta\eta$, while the other axis and the z -vertex axis are

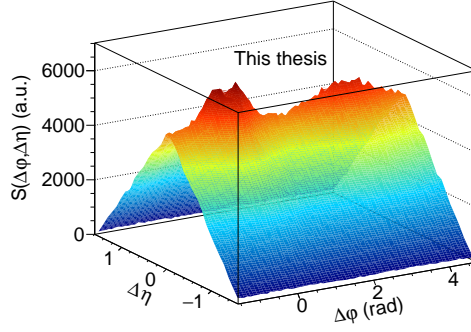


Figure 7.2: Example of the signal distribution at $3 < p_{T,\text{trig}} < 4$ GeV/c, $1 < p_{T,\text{assoc}} < 2$ GeV/c, for the 50–60% centrality class and for the vertex bin from -1 cm to 1 cm.

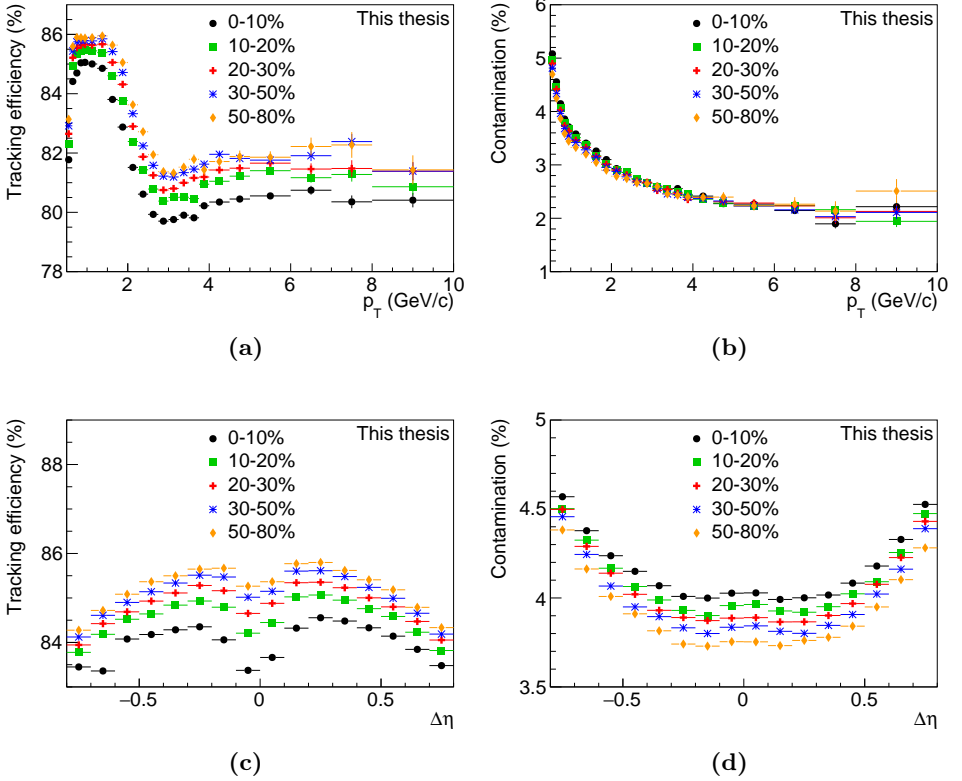


Figure 7.3: Tracking efficiency (left column) and contamination (right column) as a function of p_T (top row) and $\Delta\eta$ (bottom row) for the Pb–Pb data collected in 2010, calculated from HIJING simulations.

projected. There is a small dependence on the centrality (maximum 2% in the efficiency and below 0.5% in the contamination), with the most central collisions giving the lowest efficiency and the the highest contamination. This arises from the high multiplicity in these collisions, which makes the tracking more difficult. The contamination rises towards low p_T , while the tracking efficiency has a maximum around $p_T = 1 \text{ GeV}/c$. Towards lower p_T , the drop in the efficiency arises from the loss of tracks due to their energy loss in the material. The fraction of the clusters of a track falling into inefficient parts of the detector (e.g. sector borders of the TPC) changes with p_T [91], and this causes the drop in efficiency at higher p_T . As a function of $\Delta\eta$, the change in the efficiency and the contamination from secondaries is much smaller than as a function of p_T . The efficiency (contamination) is slightly lower (higher) at large $|\Delta\eta|$ due to measuring close to the outer limit of the detectors and around $\Delta\eta = 0$, due to track merging and track splitting effects.

The distribution presented in Fig. 7.2 contains the signal, but also contains some trivial structures originating from the finite acceptance of the detector. This can be corrected for by the so-called mixed event technique, which means that the the distribution of particles pairs as a function of $\Delta\varphi$ and $\Delta\eta$ is also constructed from pairs where the two particles originate from different events. This mixed distribution, by definition, does not contain any physical correlations; however, any structures originating from detector acceptance or pair inefficiencies are present. This is also created separately for the different p_T ranges, centralities and z-vertex bins, and an example can be seen in Fig. 7.4a. For these distributions, tracks originating from 5 to 20 events, depending on the centrality of the event were used. These distributions are normalized by α such that they are unity around $(\Delta\varphi, \Delta\eta) = (0, 0)$:

$$M(\Delta\varphi, \Delta\eta) = \alpha \frac{d^2 N_{mixed}}{d\Delta\varphi d\Delta\eta} \quad (7.2)$$

where $M(\Delta\varphi, \Delta\eta)$ is the mixed event distribution and N_{mixed} is the number of pairs where the two particles are taken from two events. The normalization α is calculated at $(\Delta\varphi, \Delta\eta) = (0, 0)$, because if the detector would be perfect, then two particles traveling in the same direction would by definition have the same reconstruction efficiency. Therefore if the trigger particle was found, the associated particle is also found, making the pair efficiency unity at $(\Delta\varphi, \Delta\eta) = (0, 0)$ and no correction necessary there. The mixed event distribution has a triangular shape as a function of $\Delta\eta$, which means that it has a maximum at $(\Delta\varphi, \Delta\eta) = (0, 0)$ and it is falling towards large $\Delta\eta$. The normalization should be 1 at exactly $(\Delta\varphi, \Delta\eta) = (0, 0)$, but because of the finite binning in $\Delta\eta$, a correction factor has to be calculated for the normalization. This correction factor

is based solely on the width of the bins in $\Delta\eta$ and the maximum η acceptance of the analysis. In practice, the normalization is calculated as the average of four bins around $(\Delta\varphi, \Delta\eta) = (0, 0)$ to minimize the statistical fluctuations, and then it is corrected for the above described finite bin effect.

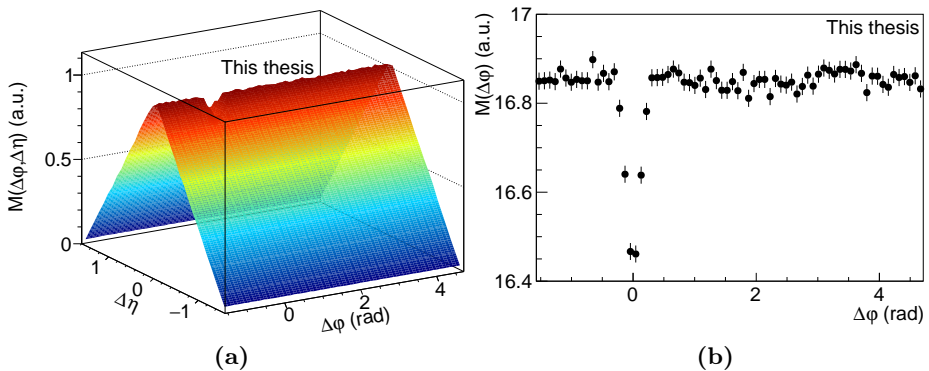


Figure 7.4: Panel (a) shows an example of the mixed distribution at $3 < p_{T,\text{trig}} < 4$ GeV/ c , $1 < p_{T,\text{assoc}} < 2$ GeV/ c , for the 50–60% centrality class and for the vertex bin from -1 cm to 1 cm. Panel (b) shows the projection of panel (a) to the $\Delta\varphi$ axis.

This calculation works if the detector is fully efficient for pairs with $(\Delta\varphi, \Delta\eta) = (0, 0)$, which, however, is not the case due to track merging and track splitting, which will be further discussed below. If the inefficiency at small $\Delta\varphi$ and $\Delta\eta$ cannot be neglected in the signal distribution, this has to be corrected for by the mixed event distribution. Due to this correction, which will be discussed further below, the mixed event distribution also shows an inefficiency around $(\Delta\varphi, \Delta\eta) = (0, 0)$ (Fig. 7.4b). Therefore a different approach has to be used for the calculation of the normalization, which takes into account this inefficiency. In this approach, it is assumed that apart from a small region around $\Delta\varphi = 0$, the detection efficiency is constant at $\Delta\eta = 0$ as a function of $\Delta\varphi$. Two bins around $\Delta\eta = 0$ are then averaged along the full $\Delta\varphi$ region except the bins effected by the inefficiency around $\Delta\varphi = 0$. This value is then also corrected for the effect of the finite bin width in $\Delta\eta$. The calculation of the normalization is done from a mixed distribution where all the z -vertex bins are summed, because this factor was found to be independent of the binning in the position of the vertex in the z -direction. The normalization for the bins is then calculated by weighting this factor with the number of trigger particles used for the mixed distributions in each z -vertex bin.

After properly normalizing the mixed distribution, the associated yield per trigger particle is calculated as the average of the contributions of the

different z -vertex bins:

$$\frac{1}{N_{trig}} \frac{d^2 N_{assoc}}{d\Delta\varphi d\Delta\eta} = \frac{1}{N_{trig}} \sum_i \frac{1}{\alpha_i} \frac{S_i(\Delta\varphi, \Delta\eta)}{M_i(\Delta\varphi, \Delta\eta)} \quad (7.3)$$

where N_{trig} is the number of triggers in the signal distribution, the summation is over the different z -vertex bins and α_i is the normalization factor weighted by ratio of the number of triggers from the mixed distribution of the i^{th} z -vertex bin ($N_{trig,M,i}$) and from all z -vertex bins ($N_{trig,M,all}$), $\alpha_i = \alpha N_{trig,M,i}/N_{trig,M,all}$.

As was mentioned above, the reconstruction of particle pairs can also have inefficiencies which have to be corrected for. Inefficiencies appear for example when two particles are too close. This is because shared clusters in the detector can appear in these cases resulting in the merging of the two tracks. The opposite effect is also possible, referred to as track splitting, when one track is falsely reconstructed as two close tracks. To account for these two effects, cuts are implemented to both the distribution from the same event and the mixed event. Particle pairs are not accepted if $|\Delta\eta| \leq 0.02$ and $|\Delta\varphi^*| \leq 0.02$, with $\Delta\varphi^*$ being the minimal φ distance of the two particles at the same radius within the volume of the TPC. It can be calculated from their φ distance ($\Delta\varphi$), the momentum of the particles ($p_{T,1}$ and $p_{T,2}$), the magnetic field (B_z), the elementary charge (e), the sign of the charge of the particles (z_1 , and z_2) and the radial position (r):

$$\Delta\varphi^* = \Delta\varphi + \arcsin \frac{z_1 e B_z r}{2p_{T,1}} - \arcsin \frac{z_2 e B_z r}{2p_{T,2}} \quad (7.4)$$

The effect of this cut is clearly visible in Fig. 7.4b around $\Delta\varphi = 0$.

Decay products of short lived neutral particles show a correlation in their $\Delta\eta$ and $\Delta\varphi$ distribution. These secondary particles are not the study of the current analysis, therefore they are eliminated from the data. The decay products of K_S^0 and Λ particles and the particles from γ -conversion are removed by applying a cut on the invariant mass of the particle pairs. The invariant mass is calculated for the K_S^0 by assuming the two particles are pions, for Λ particles assuming that one is a pion and one is a proton, while for γ -conversions the mass of the electrons is used. The pair is removed if the invariant mass of the pair is closer than $5 \text{ MeV}/c^2$ to the mass of the K_S^0 or Λ . To remove particles from γ -conversion all pairs are removed where $m_{inv} < 4 \text{ MeV}/c^2$. These cuts are also applied to both the same and the mixed distributions, therefore the inefficiency caused by removing the combinatorial pairs is corrected for.

As discussed earlier, on the away-side the contribution from the jet is roughly independent of $\Delta\eta$. An η -independent elliptic flow would also result in $\Delta\eta$ -independent structures; however, the elliptic flow shows a

small dependence on η , which was measured to be at most 10–15% from $\eta = 0$ to $|\eta| = 2.5$ [109, 110]. Particle production has also a small η dependence, at most 10% from $\eta = 0$ to $|\eta| = 1.5$ [111]. These can result in the appearance of $\Delta\eta$ -dependent structures on the away-side. A further cause of $\Delta\eta$ dependence of the away-side can arise from the mixed event technique. The correction would be perfect only, if it was done in infinitely small bins in $\Delta\varphi$, $\Delta\eta$, centrality and the position of the z -vertex which is not possible. The small $\Delta\eta$ dependence of the away-side is shown in Fig. 7.5, and it is taken into account in the analysis by multiplying the full per trigger yield distributions with a $\Delta\eta$ -dependent factor. This factor is calculated such that the away-side becomes independent of $\Delta\eta$. This is indicated in Fig. 7.6, where both the away- and the near-side are shown

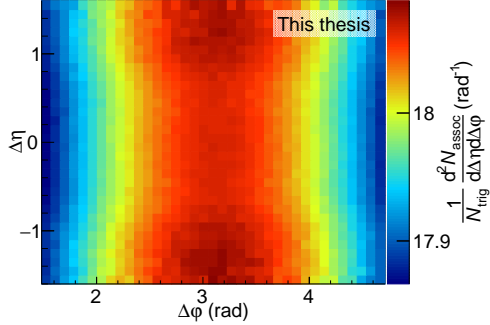


Figure 7.5: $\Delta\eta$ dependence of the away-side at $1 < p_{T,\text{trig}} < 2 \text{ GeV}/c$, $1 < p_{T,\text{assoc}} < 2 \text{ GeV}/c$ and for the most central 10% of the events.

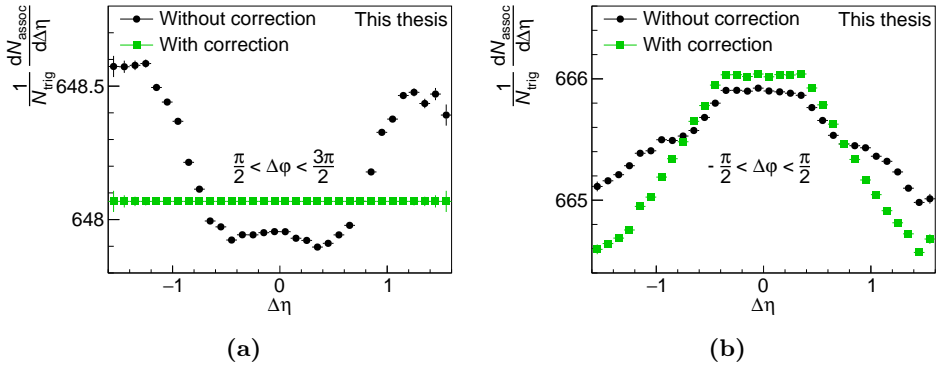


Figure 7.6: Projection to the $\Delta\eta$ -axis of the per trigger yield at $1 < p_{T,\text{trig}} < 2 \text{ GeV}/c$, $1 < p_{T,\text{assoc}} < 2 \text{ GeV}/c$ and for the most central 10% of the events. Panel (a) shows the away-side, while panel (b) shows the near-side. Both plots present the projections before and after the correction for the $\Delta\eta$ dependence of the away-side.

before and after this correction. As expected, the away-side becomes flat in $\Delta\eta$ after the correction, while the near-side also changes and is closer to a Gaussian shape than before the correction.

After all these corrections, the per trigger yield presented in Fig. 7.1 is obtained. In Fig. 7.7, the near-side of the per trigger yield is shown for two different p_T bins for the most central, the most peripheral and the pp case. There are several features of the distribution which change with p_T and centrality. Both the combinatorial and the flow backgrounds are most significant in the low p_T case due to the higher multiplicity in these bins. These backgrounds are most pronounced in the central bins, again due to the high multiplicity in these bins. The peak in the peripheral collisions is similar to the peak in pp collisions, while it gets broader in central events in the lower p_T case. At low p_T , the peak departs from the Gaussian-like shape, and a depletion develops around $(\Delta\varphi, \Delta\eta) = (0, 0)$. The broadening and the depletion can be a sign for the interplay of the jets with the collective medium, therefore in the following these changes, described here qualitatively, will be characterized quantitatively.

7.1.2 Fitting procedure of the near-side peak

To quantify the changes in the width and shape of the near-side peak, it is fitted together with the background. The background is represented by the sum of a constant (A), accounting for the combinatorial background, and the sum of cosine functions accounting for the anisotropic flow up to fourth order, which are represented by the parameters V_n :

$$A + \sum_{n=2}^4 2V_n \cos(n\Delta\varphi) \quad (7.5)$$

The shape of the peak is influenced by several physics mechanisms (e.g. the fragmentation of the jets, hadronization, rescattering in both the partonic and the hadronic phase or interactions with the medium), therefore there is no clear theory prediction on what shape the peak has. Because of this different functions were tried for the fitting of the peak:

- Two-dimensional Gaussian function:

$$\frac{N}{2\pi\sigma_\varphi\sigma_\eta} e^{-\frac{\Delta\varphi^2}{2\sigma_\varphi^2} - \frac{\Delta\eta^2}{2\sigma_\eta^2}} \quad (7.6)$$

where N is the normalization of the Gaussian and σ_φ and σ_η are the widths of the Gaussian functions in the $\Delta\varphi$ and $\Delta\eta$ directions, respectively.

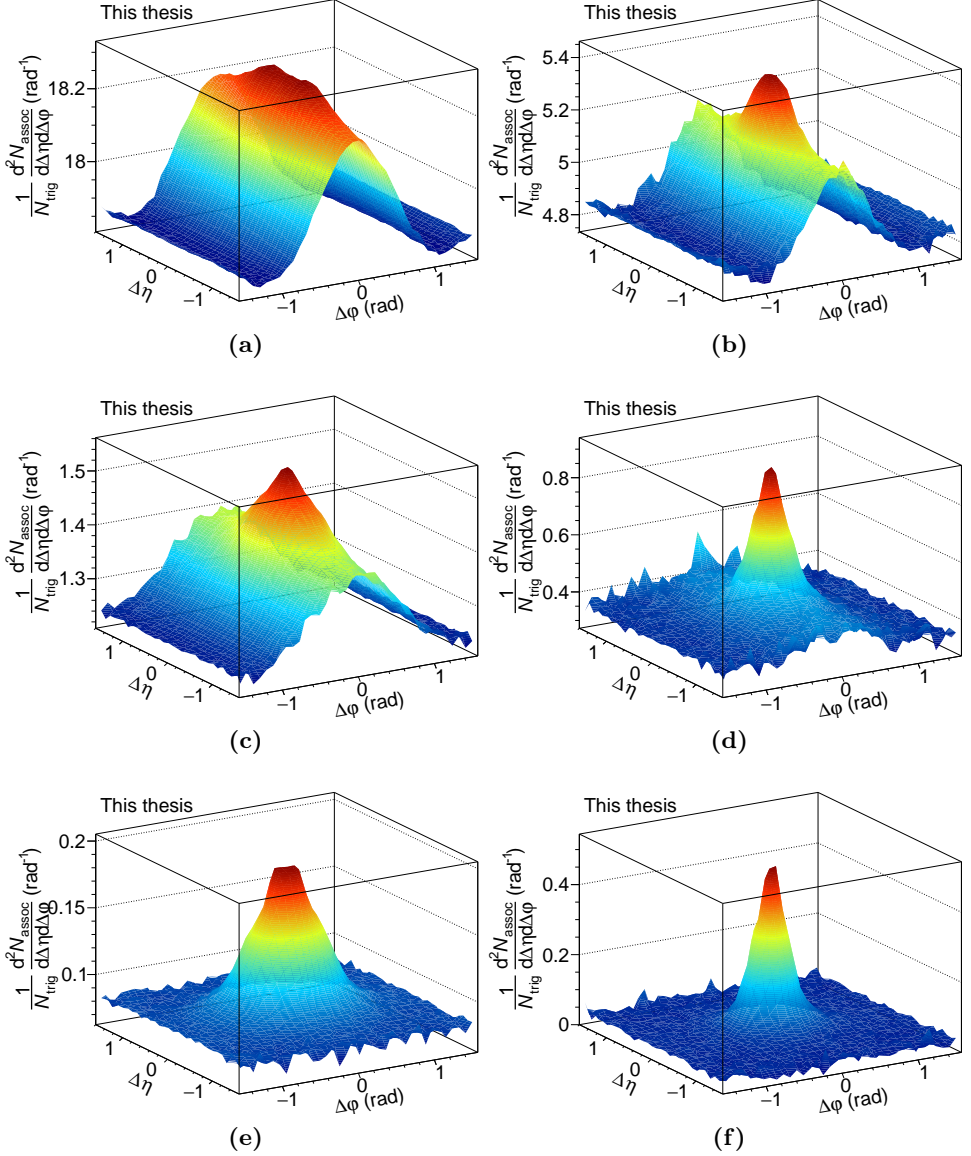


Figure 7.7: Per trigger yield for the lowest p_T bin ($1 < p_{T,\text{trig}} < 2$ GeV/c, $1 < p_{T,\text{assoc}} < 2$ GeV/c, left column) and for a higher p_T bin ($3 < p_{T,\text{trig}} < 4$ GeV/c, $2 < p_{T,\text{assoc}} < 3$ GeV/c, right column) for the most central (0-10%, top row), the most peripheral (50-80%, middle row) and the pp case (bottom row).

- Sum of two two-dimensional Gaussian functions:

$$N \times \left[\frac{\alpha}{2\pi\sigma_{\varphi_1}\sigma_{\eta_1}} e^{-\frac{\Delta\varphi^2}{2\sigma_{\varphi_1}^2} - \frac{\Delta\eta^2}{2\sigma_{\eta_1}^2}} + \frac{1-\alpha}{2\pi\sigma_{\varphi_2}\sigma_{\eta_2}} e^{-\frac{\Delta\varphi^2}{2\sigma_{\varphi_2}^2} - \frac{\Delta\eta^2}{2\sigma_{\eta_2}^2}} \right] \quad (7.7)$$

where N is the normalization of the Gaussian, α represents the ratio of the two Gaussian functions ($0 \leq \alpha \leq 1$), and the two Gaussian functions in the $\Delta\varphi$ direction and the two Gaussian functions in the $\Delta\eta$ directions have different widths (σ_{φ_1} , σ_{φ_2} , σ_{η_1} and σ_{η_2}).

- Generalized Gaussian function:

$$N \times \frac{\gamma_\varphi\gamma_\eta}{4w_\varphi w_\eta \Gamma\left(\frac{1}{\gamma_\varphi}\right) \Gamma\left(\frac{1}{\gamma_\eta}\right)} e^{-\left(\frac{|\Delta\varphi|}{w_\varphi}\right)^{\gamma_\varphi} - \left(\frac{|\Delta\eta|}{w_\eta}\right)^{\gamma_\eta}} \quad (7.8)$$

where N is the normalization of the function and w_φ and w_η are responsible for the width of the function. The generalized Gaussian also has an extra parameter in both directions (γ_φ and γ_η) compared to a Gaussian function. If $\gamma = 1$, the generalized Gaussian is an exponential function with $|x|$ as the variable (x being $\Delta\varphi$ or $\Delta\eta$), while at $\gamma = 2$, the generalized Gaussian function becomes a normal Gaussian. If γ is larger than 2, a flat top develops around $x = 0$. The generalized Gaussian has been used to fit different correlations (e.g. Bose–Einstein correlations) [112, 113], because under certain assumptions a Levy-stable function gives a good description of the source in these correlations [112, 114]. If a Levy-stable function is assumed for the source, the correlation function takes up the shape of a generalized Gaussian with the restriction of $0 < \gamma \leq 2$ [115]. In these analyses, the generalized Gaussian is also often referred to as a stretched exponential function. In the current analysis, however, no such assumption on a source function was made, therefore the restriction on γ is only that it has to be positive.

The generalized Gaussian for different values of γ , a normal Gaussian and the sum of two Gaussian functions in one dimension are shown in Fig. 7.8. The plot illustrates how both the shape of the peak and the shape of the tails change for the different functions.

In the case of the fit with a generalized Gaussian function, an example per trigger yield distribution and the fit to it is presented in Fig. 7.9. In the same figure, the two components of the fit: the near-side peak and the $\Delta\eta$ -independent background are also shown.

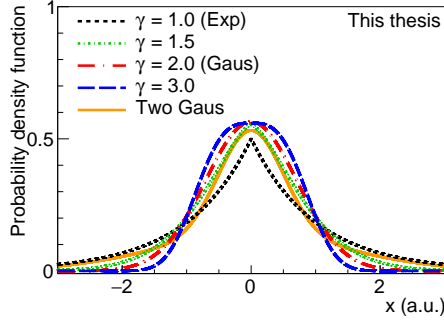


Figure 7.8: The figure shows the generalized Gaussian for different values of the parameter γ , where $\gamma = 1$ corresponds to an exponential function with the argument being $|x|$, while $\gamma = 2$ gives a normal Gaussian. The width parameter is set to $w = 1$ for all the generalized Gaussian functions. The plot shows also the sum of two Gaussian functions, where $\alpha = 0.5$, $\sigma_1 = 0.5$ and $\sigma_2 = 1.5$.

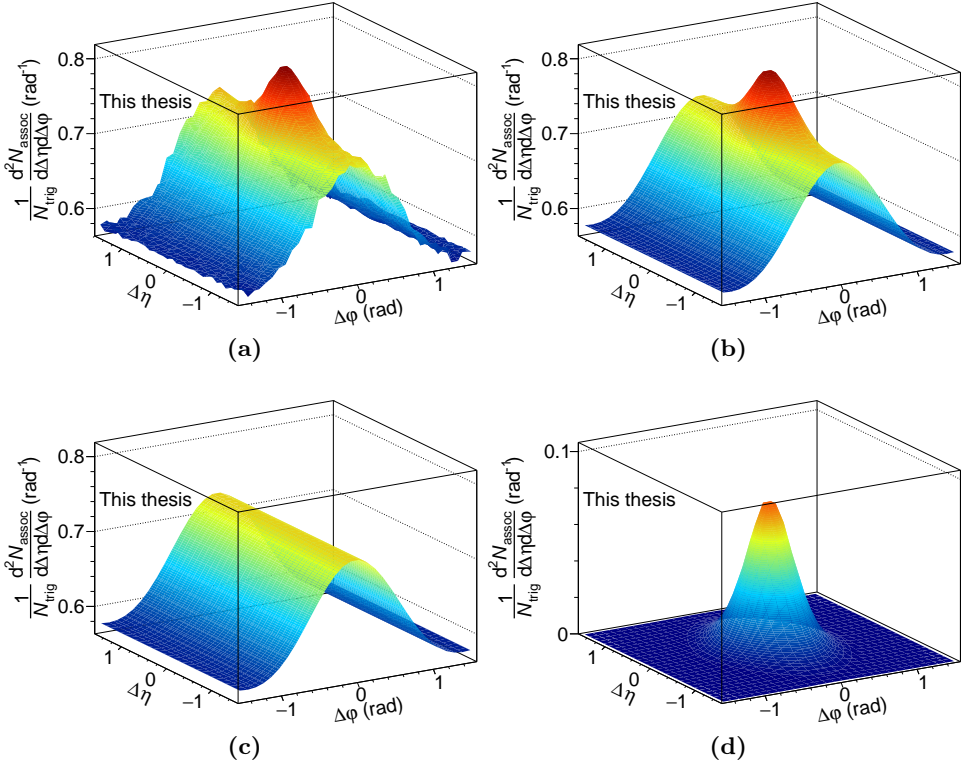


Figure 7.9: In panel (a) the per trigger yield is shown for $2 < p_{T,\text{trig}} < 3 \text{ GeV}/c$, $2 < p_{T,\text{assoc}} < 3 \text{ GeV}/c$ and for the 30–50% centrality class, while in panel (b), the fit to this distribution is presented in the case of a fit with a generalized Gaussian. In panel (c) and (d) the background and the peak component from the fit is shown, respectively.

Since the background is characterized by the same parameters independent of which function is used to describe the peak, it is possible to compare the fitted peaks directly. In Fig. 7.10, the peak part of the fit of the same distribution as in Fig. 7.9 is shown for the three fit functions. A small difference around $(\Delta\varphi, \Delta\eta) = (0, 0)$ is already visible from these plots, but it is much more pronounced if the difference of these distributions are calculated. In Fig. 7.11, the differences of the fit with one or two Gaussian functions with respect to the generalized Gaussian case are shown. It is clear from these plots that the difference has a structure, therefore the different functions describe to different extent the peak and the tails of the peak. Differences are visible in both the $\Delta\varphi$ and the $\Delta\eta$ directions; however, they extend to much further in the $\Delta\eta$ direction, which indicate that the different functions capture the tail of the distribution in the $\Delta\eta$ direction differently.

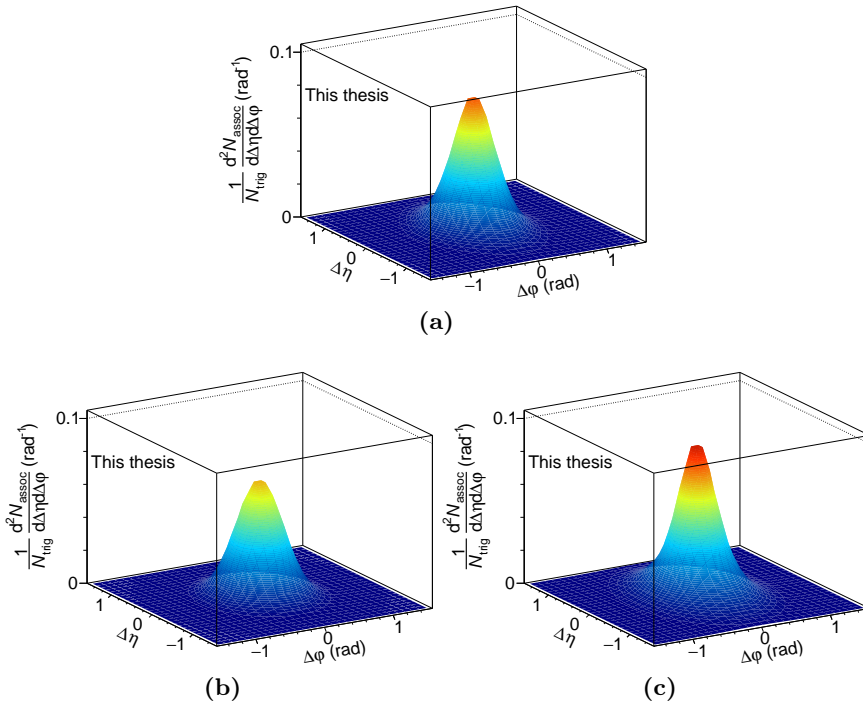


Figure 7.10: The three figures show the peak part of the fit for the three different fit functions for $2 < p_{T,\text{trig}} < 3 \text{ GeV}/c$, $2 < p_{T,\text{assoc}} < 3 \text{ GeV}/c$ for the 30–50% centrality class. Panel (a) shows the generalized Gaussian case, panel (b) the one Gaussian case and panel (c) the case with the sum of two Gaussian functions.

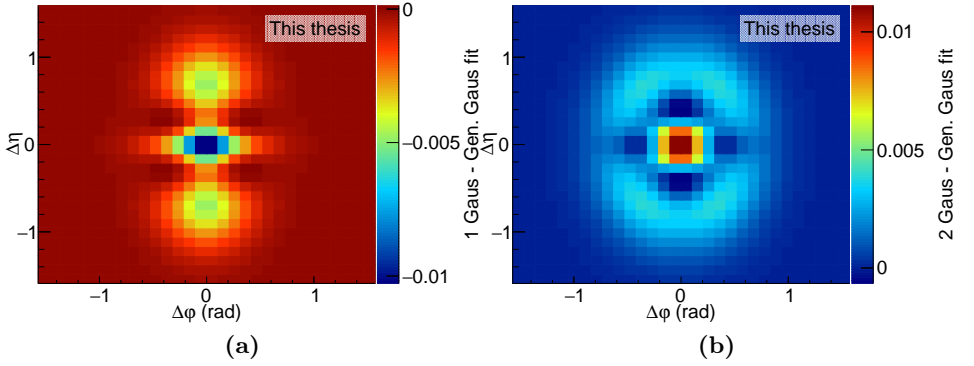


Figure 7.11: The two figures show the difference between the fit with the generalized Gaussian and the fit with one Gaussian function (a) or with two Gaussian functions (b). I.e. panel (a) is the difference of Fig. 7.10b and Fig. 7.10a, and panel (b) is the difference of Fig. 7.10c and Fig. 7.10a.

In Fig. 7.12, the projections of the three functions are overlaid with the data in both the $\Delta\varphi$ and the $\Delta\eta$ directions. In the $\Delta\varphi$ directions, all three functions give a good description of the data, while in the $\Delta\eta$ direction, the tails are captured differently by the three functions. In Fig. 7.13, the difference of the fit and the data is shown for all three cases in two dimensions. It can be seen that the difference is within $\pm 2\%$ in all three cases, with the biggest differences appearing around $(\Delta\varphi, \Delta\eta) = (0, 0)$.

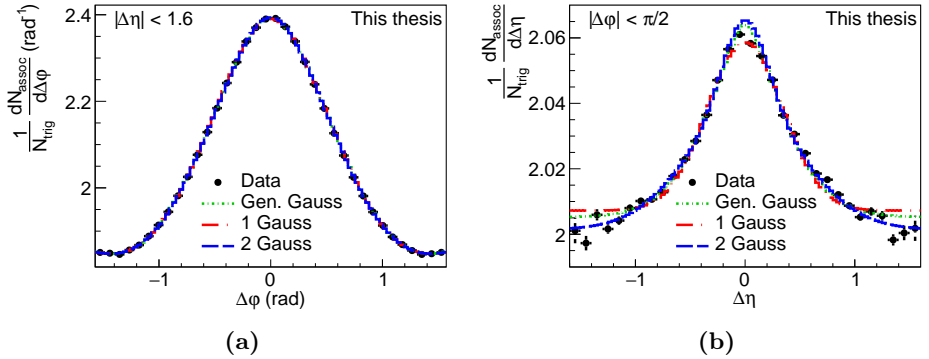


Figure 7.12: The $\Delta\varphi$ (a) and the $\Delta\eta$ (b) projections of the three fit functions overlaid with the data for $2 < p_{T,\text{trig}} < 3 \text{ GeV}/c$, $2 < p_{T,\text{assoc}} < 3 \text{ GeV}/c$ for the 30–50% centrality class.

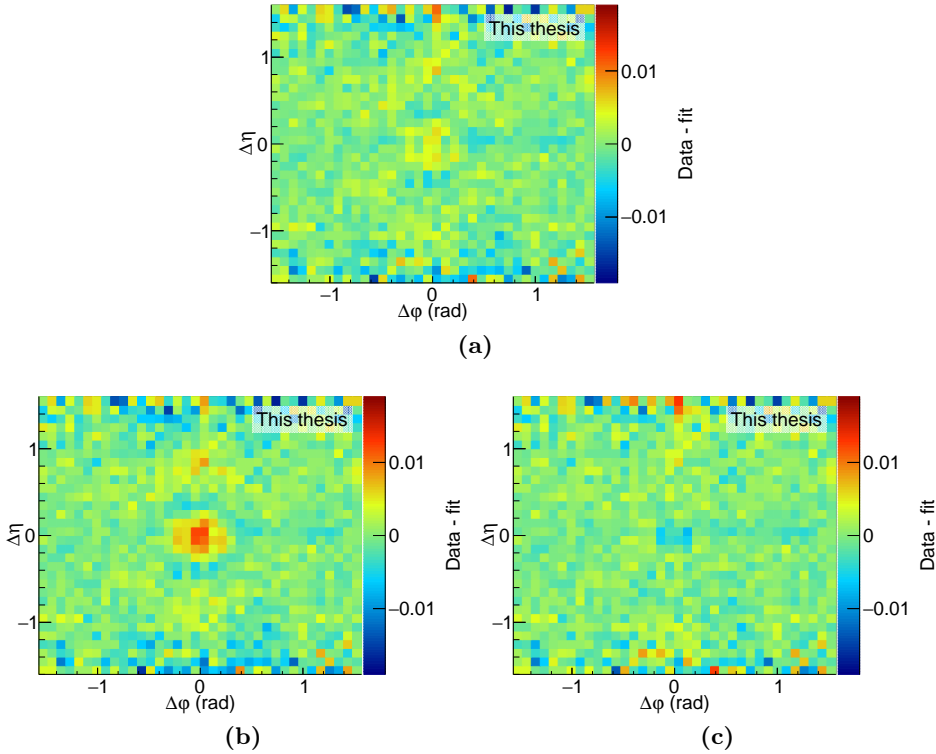


Figure 7.13: The three figures show the difference of the data and the fit function for the three different functions for $2 < p_{T,\text{trig}} < 3 \text{ GeV}/c$, $2 < p_{T,\text{assoc}} < 3 \text{ GeV}/c$ for the 30–50% centrality class. Panel (a) shows the generalized Gaussian case, panel (b) the one Gaussian case and panel (c) the case with the sum of two Gaussian functions.

In Fig. 7.14, the background parameters are presented for all p_T and centrality bins only for the case of the generalized Gaussian fit, since it is described by the same fit function in all three cases. Fig. 7.14a shows the parameter describing the combinatorial background (A from Eq. (7.5)), while the other three panels show the parameters describing the background arising from flow. The combinatorial background grows with centrality, with the most central events having the highest background, and decreases with increasing $p_{T,\text{assoc}}$. From this trend, the bins with symmetric p_T range are exceptions. It is easy to understand why the most central events have the highest combinatorial background, since the multiplicity of the events grow with centrality. The $p_{T,\text{assoc}}$ dependence is arising from the steeply falling p_T spectrum of particles in heavy-ion collisions [116], and the exception of the symmetric p_T bins are due to the avoidance of double counting of the pairs. This results in less pairs in these bins than in the asymmetric ones with the same $p_{T,\text{assoc}}$. The square roots of the other three parameters divided by \sqrt{A} correspond to the v_n parameters describ-

ing the anisotropic flow in the bins where the trigger and the associated p_T ranges are the same (see Eq. (1.2)). The v_n values calculated from these parameters follow well the trends seen for the published v_n values, and they agree quantitatively in the comparable bins [84]. A compari-

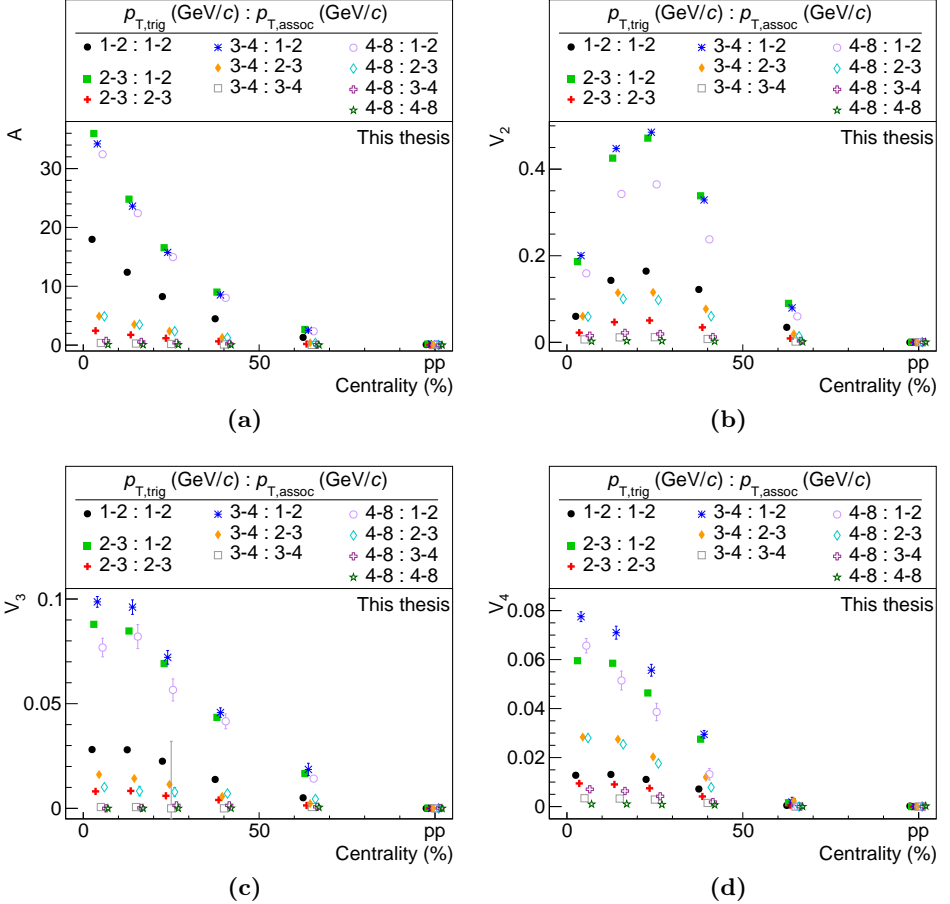


Figure 7.14: The figures show the parameters, which describe the background of the fit when for the description of the peak a generalized Gaussian function is used. The x-axis shows the collision centrality for the Pb–Pb case with the point at 100% indicating the results from pp collisions. The points are slightly shifted along this axis for better visibility. Please see Eq. (7.5) for the definition of the parameters.

son of the fit results of the background for the case with the generalized Gaussian, the case with one Gaussian and the case with the sum of two Gaussian functions used for the peak is presented in Fig. 7.15. The combinatorial background and V_2 agree within 5% for most bins, while V_3 and V_4 are more dependent on the choice of the fit function used for the peak.

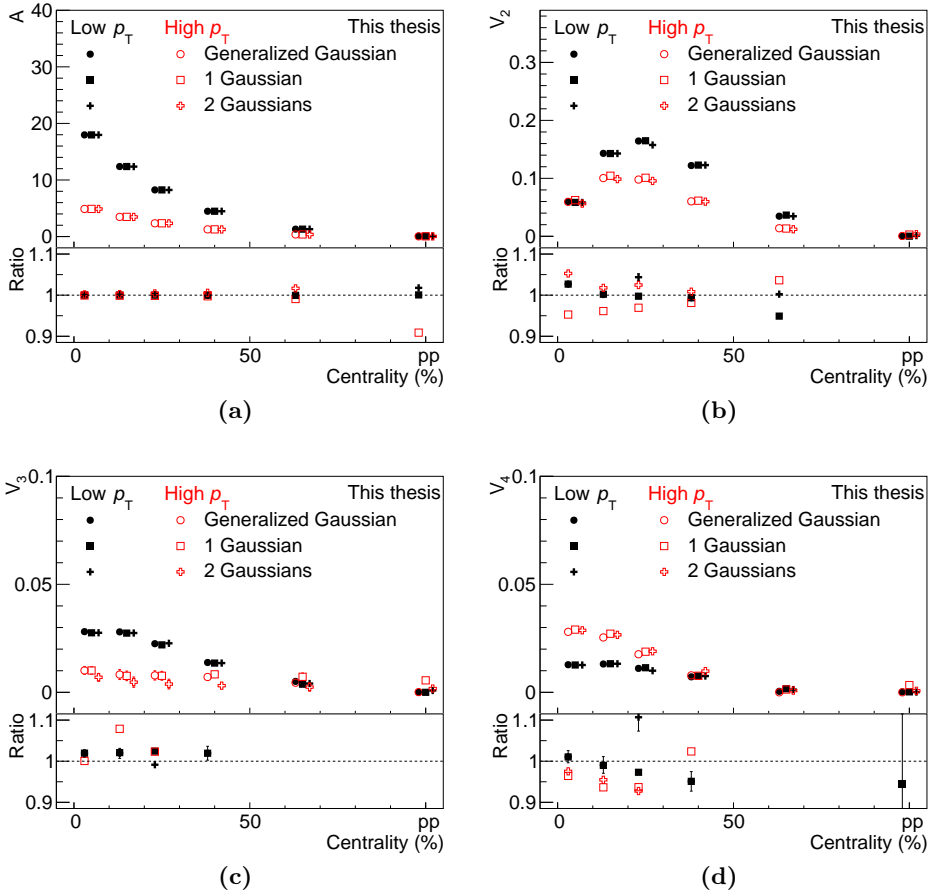


Figure 7.15: The figures compare the parameters, which describe the background of the fit when for the description of the peak a generalized Gaussian, one Gaussian or the sum of two Gaussian functions is used. The results are shown for a low p_T bin ($1 < p_{T,\text{trig}} < 2 \text{ GeV}/c$, $1 < p_{T,\text{assoc}} < 2 \text{ GeV}/c$) and a high p_T one ($4 < p_{T,\text{trig}} < 8 \text{ GeV}/c$, $2 < p_{T,\text{assoc}} < 3 \text{ GeV}/c$). Please see Eq. (7.5) for the definition of the parameters. Ratios are also shown after dividing by the generalized Gaussian case, and for this, the uncertainties are calculated by treating the statistical uncertainties on the two samples fully correlated.

The fit with one Gaussian function has three parameters to describe the peak (the widths in $\Delta\varphi$ and $\Delta\eta$ and the normalization). These are presented in Fig. 7.16. Both widths show a typical p_T dependence, with the peak at high p_T being narrower, which can be explained by the boost of the fragmenting parton. A broadening trend in both $\Delta\varphi$ and $\Delta\eta$ towards central events can also be seen, which disappears towards high p_T . There is no broadening above $p_{T,\text{trig}} > 4 \text{ GeV}/c$ or above $p_{T,\text{assoc}} > 3 \text{ GeV}/c$ in the $\Delta\varphi$ direction, while in the $\Delta\eta$ direction it disappears when both conditions are fulfilled ($p_{T,\text{trig}} > 4 \text{ GeV}/c$ and $p_{T,\text{assoc}} > 3 \text{ GeV}/c$). The integral of the Gaussian function (the parameter N), which is proportional to the yield is shown in Fig. 7.16c. It also shows a rising trend towards central events, but it has the highest values at moderate p_T values (around $2 < p_{T,\text{assoc}} < 4 \text{ GeV}/c$ and $1 < p_{T,\text{assoc}} < 2 \text{ GeV}/c$).

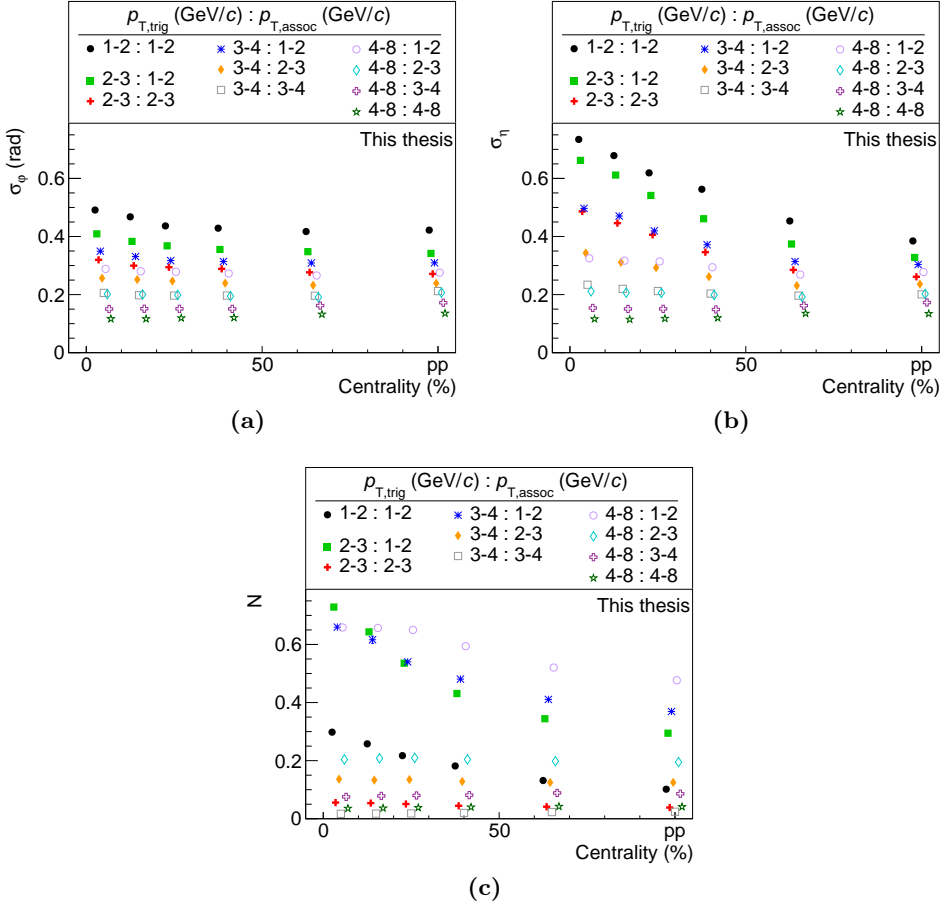


Figure 7.16: The figures show the centrality and p_T dependence of the three parameters of the peak in the case of fitting with one Gaussian function.

In Fig. 7.17, the fit parameters are shown as a function of the centrality for the studied p_T cases in the case of fitting with the sum of two Gaussian functions. In this case there are six parameters: two widths in $\Delta\eta$ and two in $\Delta\varphi$, one describing the relative contribution of the two Gaussian functions and one the normalization of the peak. The two widths are defined such that σ_1 is always the width of the narrower function, and α is the coefficient of the narrower function. As can be seen in Figs. 7.17a to 7.17d, the width of one of the two Gaussian functions is well defined; however, at low p_T , where one Gaussian is enough to properly describe the peak, the width of the other one is not well defined. This can be seen also in Fig. 7.17f, which shows that in these cases α is very close to one, which means that the second Gaussian is added with a weight of 0, therefore its width parameter is completely undefined from the fit. For some of these bins, the points are completely missing from the figures of the width, because of failing fits. In the bins, where the fit succeeds, the same trend as a function of p_T bins as in the case of the one Gaussian fit can be seen, and for the narrow width, the broadening at low p_T towards central events is also visible. In Fig. 7.17e, the normalization of the peak is plotted, and for the points, where the fit succeeded, the values are similar to the values from the fit with one Gaussian function.

Fig. 7.18 shows the fit parameters of the peak, when it is described by a generalized Gaussian function. This function has five parameters (widths in $\Delta\varphi$ and $\Delta\eta$, shape parameters in $\Delta\varphi$ and $\Delta\eta$ and a normalization parameter). The same p_T trend and broadening towards central events at low p_T can be seen as in the case of the fits with one or two Gaussian functions. The fit is more stable than in the case with two Gaussian functions, since the generalized Gaussian incorporates a normal Gaussian by setting the parameter γ to 2. So there are no undefined parameters even if the peak is well described by one Gaussian, which is in contrast to the case with the sum of two Gaussian functions. The shape parameters (γ) are between 1.5 and 2 in the $\Delta\varphi$ direction (Fig. 7.18c), which means that the peak shape varies between a Gaussian and a more peaked shape with larger tails, but does not reach the exponential function. The centrality dependence is small in the $\Delta\varphi$ direction, but it shows a clear p_T dependence with the lower p_T cases being more Gaussian-like. In the $\Delta\eta$ direction, the values range from 1.3 to 2.3 (Fig. 7.18d), which means the peak varies from almost exponential-like to Gaussian-like for most bins; however, in the lowest two p_T bins they start to develop a plateau at the top. The same p_T dependence can be seen here as in the $\Delta\varphi$ direction; however, at low p_T a centrality dependence is also visible. This shows that in the $\Delta\eta$ direction not only the width, but the shape is also changing as a function of centrality, which is not present in the $\Delta\varphi$ direction. In Fig. 7.18e,

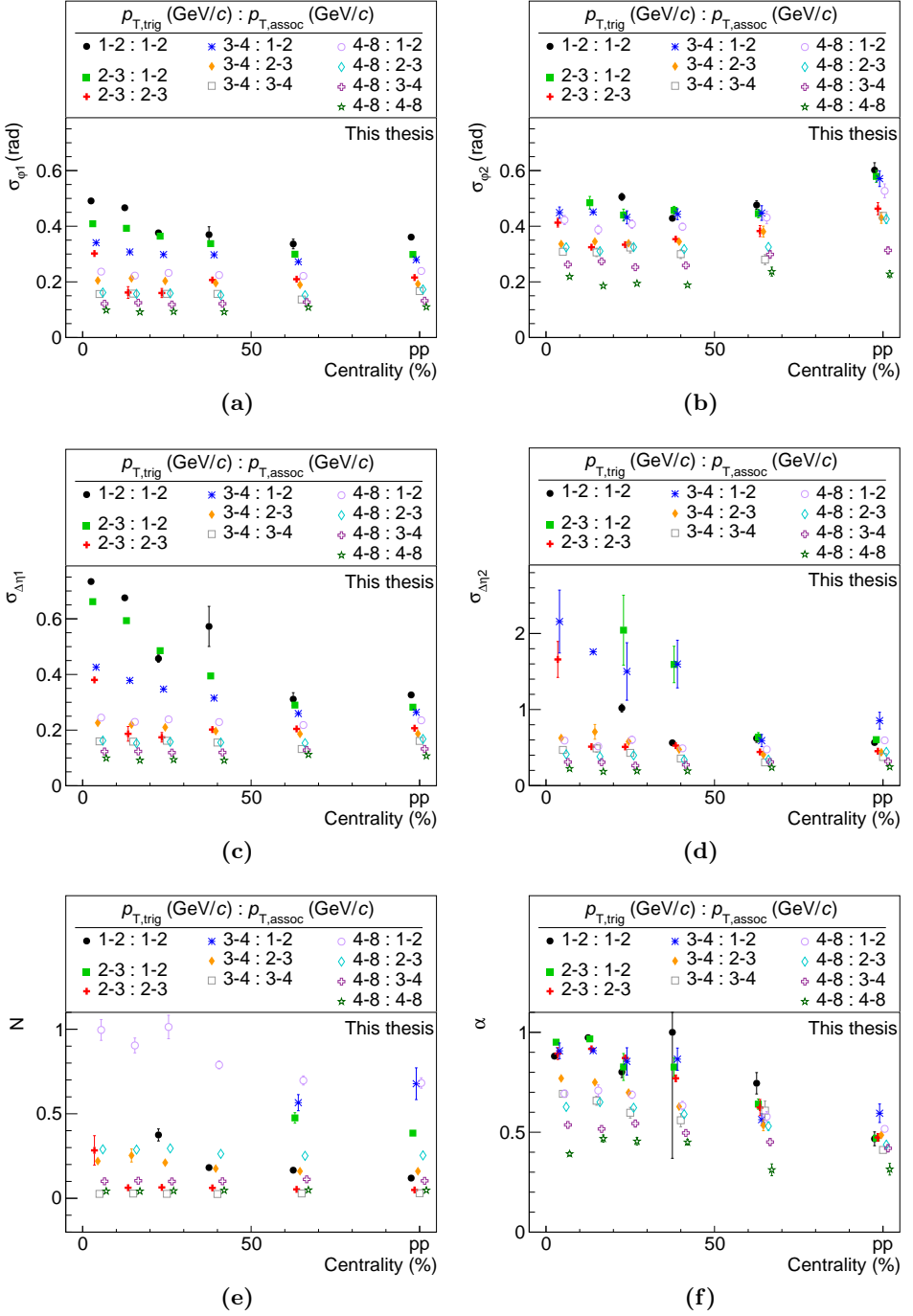


Figure 7.17: The figures show the centrality and p_T dependence of the six parameters of the peak in the case of fitting with the sum of two Gaussian functions. The definition of the parameters is such that σ_1 is always the smaller width and α is the coefficient of the narrower peak.

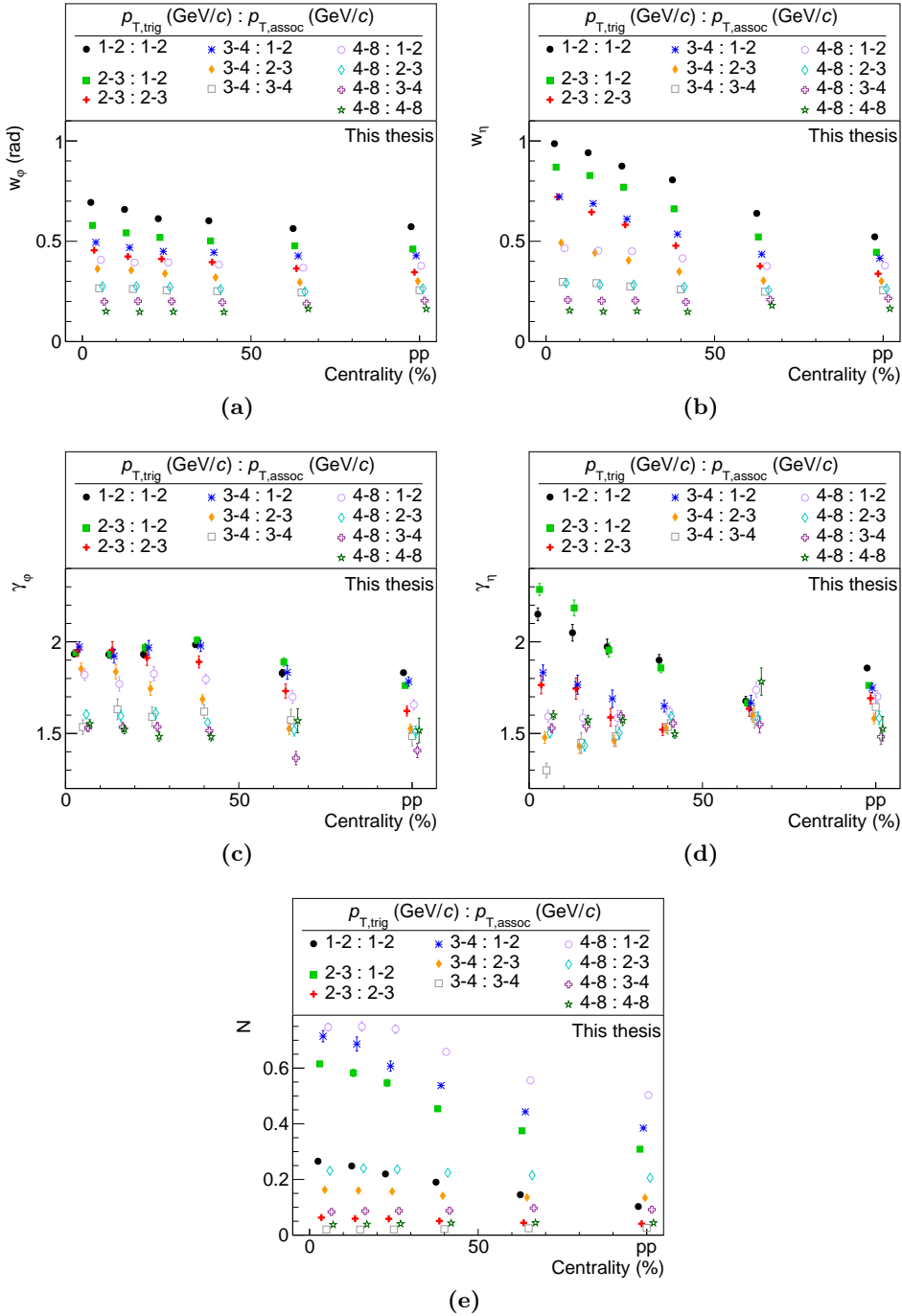


Figure 7.18: The figures show the centrality and p_T dependence of the five parameters of the peak in the case of fitting with a generalized Gaussian functions.

the normalization parameter of the peak can be seen, which shows similar values as in the other two cases.

To decide between the three fit functions, two aspects were considered. Firstly, the goodness of the fit was taken into account by calculating the χ^2 over the Number of Degrees of Freedom (ndf) of the fit in the peak region, and secondly, the stability of the fit was considered. The χ^2/ndf is calculated only in the region of the peak. The limit for the bins used for the calculation is $|\Delta\eta| < 0.8$ and it is changing in the $|\Delta\varphi|$ direction as a function of the p_T from 0.5 and 1.4. The values are presented in Fig. 7.19. The values are similar for the three fit functions at low p_T ; however, at high p_T , the fit with the sum of two Gaussian functions gives the lowest values. This fit, however, was shown to be less stable at low

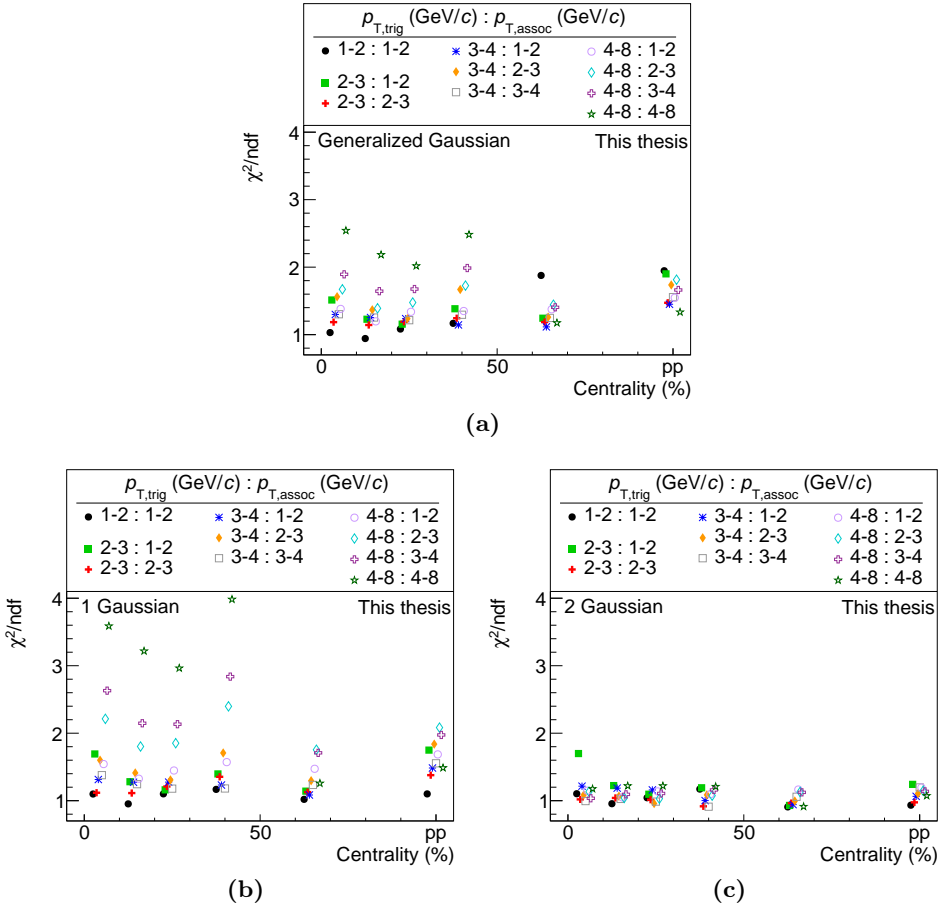


Figure 7.19: Comparison of the χ^2/ndf values for the three different fit function used for the description of the peak. Panel (a) shows the generalized Gaussian case, panel (b) the case with one Gaussian function and panel (c) the case with the sum of two Gaussian functions.

p_T than the other two. The fit with the generalized Gaussian gives better χ^2/ndf values than the fit with one Gaussian function and is more robust for all the studied p_T and centrality bins than the fit with the sum of two Gaussian functions. Therefore the generalized Gaussian function was chosen for the further analysis of the data. The χ^2/ndf values for two selected p_T bins for the three functions are shown in Fig. 7.20a for direct comparison.

The width of the three functions can be compared directly by calculating the variance of each function. It is given by the σ parameter in the case of one Gaussian and by $\sigma = \sqrt{\alpha \sigma_1^2 + (1 - \alpha) \sigma_2^2}$ for the sum of two Gaussian functions. For the generalized Gaussian function the variance is given by the following formula:

$$\sigma = \sqrt{\frac{w^2 \Gamma(3/\gamma)}{\Gamma(1/\gamma)}} \quad (7.9)$$

In Fig. 7.20, the width in both the $\Delta\varphi$ and the $\Delta\eta$ directions are shown. There is a small difference in the values for the three cases, with the one Gaussian case giving always the smallest width and the two Gaussian case the highest. Note, some of the points are missing for the two Gaussian case, because the fit failed in these bins due to the proper description of these bins by one Gaussian. In the following the width of the peak will be reported by the variance of the fit from the generalized Gaussian case.

The parameters are not limited to certain ranges during the fitting procedure. Because of this, the initial values of the parameters have to be set relatively precisely to achieve a good fit. This is achieved by an iterative procedure, which is described in the following.

- In the first step, only the parameters of the background are fitted. The parameters of the peak are fixed to some initial values, but these values have no influence on the fit, because the fit is restricted in $\Delta\eta$ to a region, where the background dominates. The region varies between $0.5 < \Delta\eta < 1.0$ and $1.4 < \Delta\eta < 1.6$, depending on the p_T to account for the different width of the peak at different transverse momentum values. The upper limit is changed to avoid including fluctuations from the background, which are largest close to the limit of the acceptance. The width is affected by this only at the largest p_T bin, where a maximum of 5% difference arises. Only the positive $\Delta\eta$ side of the distribution is used for this first step, which can be done since the fitted background is independent of $\Delta\eta$. The V_n parameters are limited to be above 0 and below 100, which range safely includes all possible values and serves only to keep the fit from failing by finding an unphysical minimum.

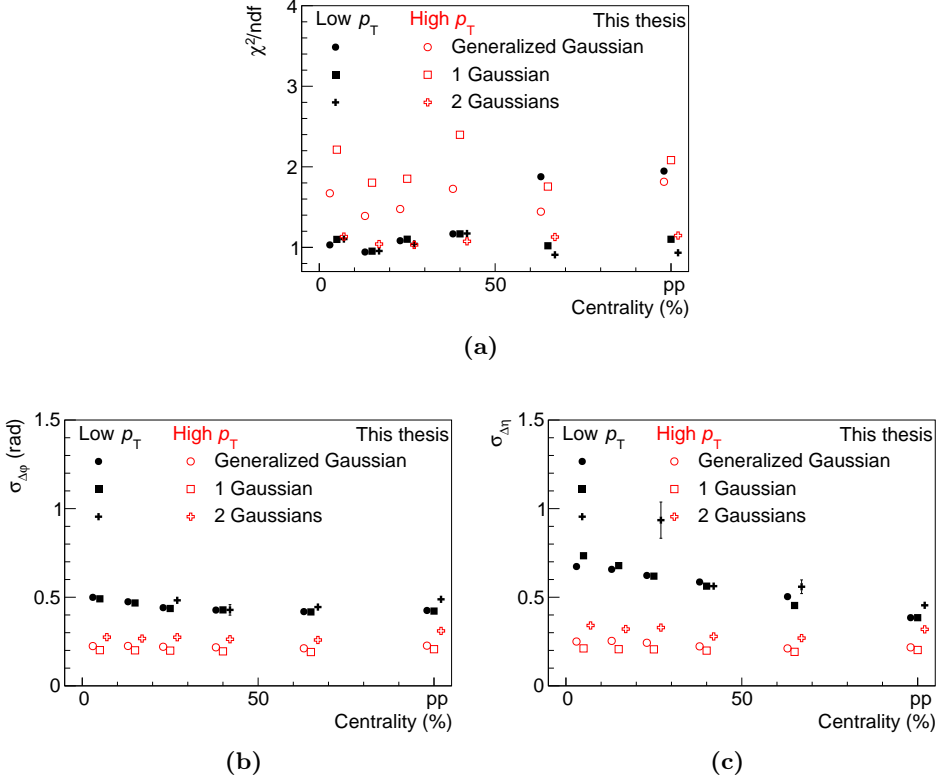


Figure 7.20: Comparison of the three types of fit functions used for fitting the peak at a low p_T value ($1 < p_{T,\text{trig}} < 2 \text{ GeV}/c$, $1 < p_{T,\text{assoc}} < 2 \text{ GeV}/c$) and a high p_T value ($4 < p_{T,\text{trig}} < 8 \text{ GeV}/c$, $2 < p_{T,\text{assoc}} < 3 \text{ GeV}/c$).

- In the second step, the background parameters are fixed to the values found in the first step, and the parameters of the peak are fitted. For this the fit region in $\Delta\eta$ is limited to a certain range, which, depending on p_T , varies from $|\Delta\eta| < 0.5$ to $|\Delta\eta| < 1.4$. In this step, the width parameters are limited to $0.15 < w < 2$ and the shape parameters to $0.1 < \gamma < 10$. Both of these limits are needed to stabilize the fit.
- In the next step, all parameters are fitted simultaneously, but their values are limited to $\pm 20\%$ of their value from the previous step. In this step, the outer limit in $|\Delta\eta|$ varies between 1.0 and 1.6 depending on p_T , as was done also in the first step. In the cases where the background from flow is negligible (at high p_T or in pp collisions), the fit can become under-constrained, since a constant background is being fitted with four parameters. There are several exceptions included in the fitting to avoid problems arising from this. If in the

first step all three V_n parameters were below 10^{-6} , the flow parameters in this step are set to 0 and they are not fitted. If only two of them were below this limit the flow parameters are not fitted, but they are kept at their previous values.

- In the last step, all parameters are fitted again without limits. The exceptions are the shape parameters, for which the limits are kept at $0.1 < \gamma < 10$; however, these values are never approached for any of the fit cases. The V_n parameters are also forced to be positive and below 100, where the lower limit is physical, while the upper limit is never approached.
- If the fit in the previous point succeeds, there are no more steps. If, however, the fit fails, the fitting is repeated with the same limits on γ and no limits on the other parameters, but excluding and setting to 0 any of the V_n parameters, which were below 10^{-8} in the previous step. This helps in the cases where the flow background is negligible and is needed only in a few bins when the systematic error studies are being done.

At low p_T in central collisions a depletion around $(\Delta\varphi, \Delta\eta) = (0, 0)$ was seen in the data (Fig. 7.7). This is not included in the fit function, therefore by definition, the fit cannot give a good description of this area. To avoid a bias on the extracted width arising from this improper description, the area of the depletion is excluded from the fit. The area of the depletion varies with p_T and centrality, and it is widest at the lowest p_T in the most central bin. To follow its trend, the area excluded from the fit changes with p_T and centrality from $(\Delta\varphi \times \Delta\eta) = (0.3 \text{ rad} \times 0.3)$ at the lowest p_T in the most central bin to no exclusion in peripheral bins or at high p_T . The exact values of the excluded region can be seen in Table 7.1.

Observables

As described above, the width of the near-side peak will be described by the variance of the fitted generalized Gaussian function. The centrality evolution of the width will be studied as a function of p_T , and to facilitate the comparison to models, the ratio of the width in the most central and in the most peripheral bins will be calculated:

$$\sigma_{\Delta\varphi}^{CP} = \frac{\sigma_{\Delta\varphi}(0 - 10\%)}{\sigma_{\Delta\varphi}(50 - 80\%)}; \quad \sigma_{\Delta\eta}^{CP} = \frac{\sigma_{\Delta\eta}(0 - 10\%)}{\sigma_{\Delta\eta}(50 - 80\%)} \quad (7.10)$$

	Pb–Pb 0-50%	Pb–Pb 50-80%, pp
$1 < p_{T,\text{trig}} < 2 \text{ GeV}/c$ $1 < p_{T,\text{assoc}} < 2 \text{ GeV}/c$	0.35×0.30	-
$2 < p_{T,\text{trig}} < 3 \text{ GeV}/c$ $1 < p_{T,\text{assoc}} < 2 \text{ GeV}/c$	0.17×0.20	-
$2 < p_{T,\text{trig}} < 3 \text{ GeV}/c$ $2 < p_{T,\text{assoc}} < 3 \text{ GeV}/c$	0.17×0.20	-
$3 < p_{T,\text{trig}} < 4 \text{ GeV}/c$ $1 < p_{T,\text{assoc}} < 2 \text{ GeV}/c$	0.09×0.10	-
$3 < p_{T,\text{trig}} < 4 \text{ GeV}/c$ $2 < p_{T,\text{assoc}} \text{ GeV}/c$	-	-
$4 < p_{T,\text{trig}} \text{ GeV}/c$ $1 < p_{T,\text{assoc}} \text{ GeV}/c$	-	-

Table 7.1: Areas of the excluded region for each p_T and centrality in the format $\Delta\varphi$ (rad) \times $\Delta\eta$. The different exclusion in the two directions arise from the different binning of the histograms.

The depletion observed around $(\Delta\varphi, \Delta\eta) = (0, 0)$ at low p_T in central events will be characterized as well. It will be done by taking the difference of the fit and the per trigger yield distribution in the region around $(\Delta\varphi, \Delta\eta) = (0, 0)$, which was excluded from the fit. This is then normalized by the total yield of the peak, and this normalized quantity will be referred to as the depletion yield.

7.1.3 Validation of the method with HIJING

To validate the construction and the fitting of the per trigger yield distributions, a model which does not incorporate collective behavior and where jets do not interact in the medium can be used. The main questions are whether the fit is influenced by the changing multiplicity and whether the width can be properly measured, independent of the multiplicity. HIJING with jet-quenching turned off was chosen for the current analysis.

In Fig. 7.21, the widths of the peak from HIJING in both the $\Delta\varphi$ and the $\Delta\eta$ direction are shown as a function of the centrality for all the p_T bins considered for the analysis. It can be concluded that no centrality dependence is present in either of the directions; however, the same dependence on the p_T as in the data can be observed.

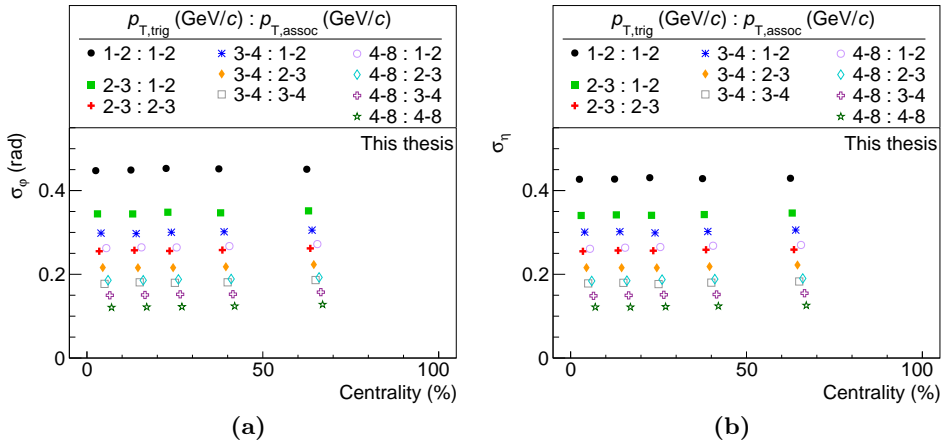


Figure 7.21: Width of the jet peak in HIJING at $\sqrt{s_{NN}} = 2.76$ TeV from Pb–Pb collisions as a function of centrality for different $p_{T,\text{trig}}$ and $p_{T,\text{assoc}}$ bins. Panel (a) shows the width in the $\Delta\varphi$ direction and panel (b) in the $\Delta\eta$ direction.

7.2 Systematic studies and uncertainties

Several studies have been carried out to see whether the results are robust against changes in the analysis procedure. These studies are detailed in the following, and the systematic uncertainty of the measurement is estimated from them. Further details on the systematic studies are available in Ref. [117].

Background characterization

First, it was studied whether the background is appropriately described by the flow harmonics up to fourth order or whether the inclusion of higher harmonics is needed. In Fig. 7.22, the χ^2/ndf , the depletion yield, and the widths in the $\Delta\varphi$ and $\Delta\eta$ directions are presented for the default case compared to when in addition V_5 and V_6 are included as fitting parameters. The change in the goodness of the fit, the depletion yield and the widths is below 5%, therefore it is concluded that it is enough to use the flow harmonics up to fourth order to describe the background. No systematic uncertainty was assigned to this change.

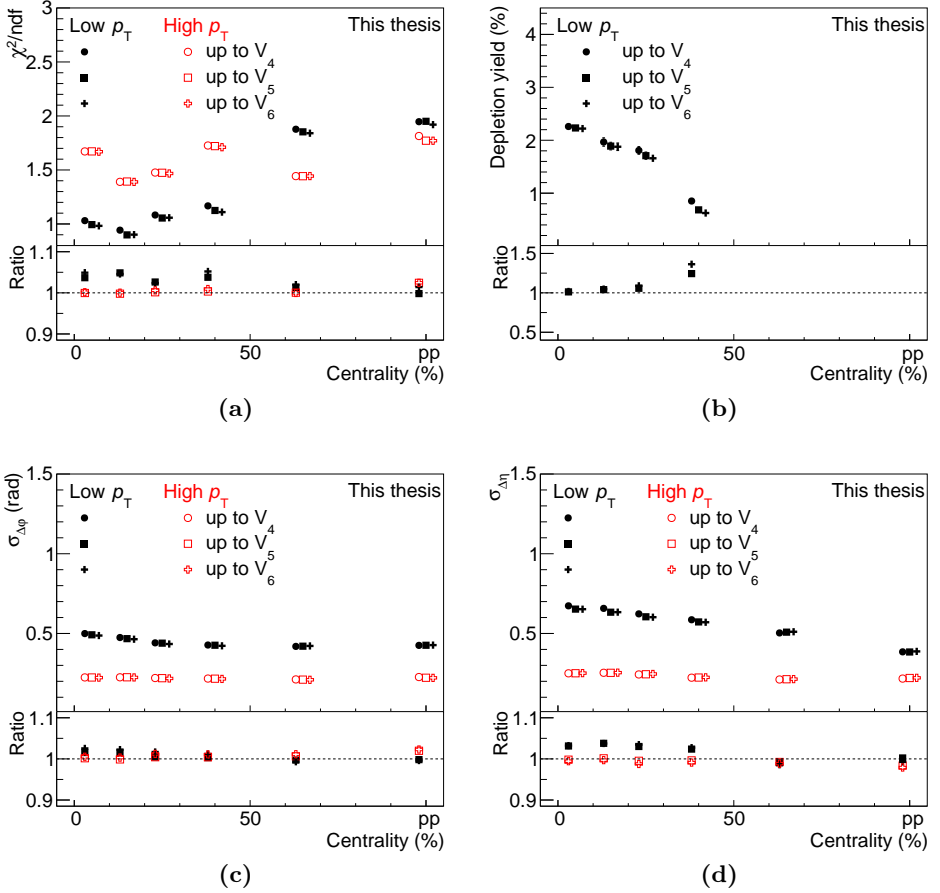


Figure 7.22: Comparison of the χ^2/ndf (a), the depletion yield (b), and the widths in the $\Delta\phi$ (c) and $\Delta\eta$ (d) directions of the default case with the case when the background is described with one or two additional flow parameters at low p_T ($1 < p_{T,\text{trig}} < 2 \text{ GeV}/c$, $1 < p_{T,\text{assoc}} < 2 \text{ GeV}/c$) and at high p_T ($4 < p_{T,\text{trig}} < 8 \text{ GeV}/c$, $2 < p_{T,\text{assoc}} < 3 \text{ GeV}/c$). Ratios to the default case are also shown, where the uncertainties are calculated by treating the statistical uncertainties on the two samples fully correlated.

Magnetic field

In ALICE, data with both positive and negative magnetic field configuration has been taken. Since the magnetic field changes the direction of the curvature of charged tracks, the different field configurations could effect the results, especially the cuts on the merging of close tracks. The default analysis is done such that events from positive and negative magnetic field settings are not mixed when creating the mixed event distribution; however, the same event and mixed event histograms from both field con-

figurations are merged before the division. As a systematic check, the data is processed separately for the two configurations, and it is merged only after the division. In Fig. 7.23, the comparisons of the widths and the depletion yield are shown with the two methods, and it can be seen that no significant effects are coming from the magnetic field, therefore it is not included as a systematic uncertainty.

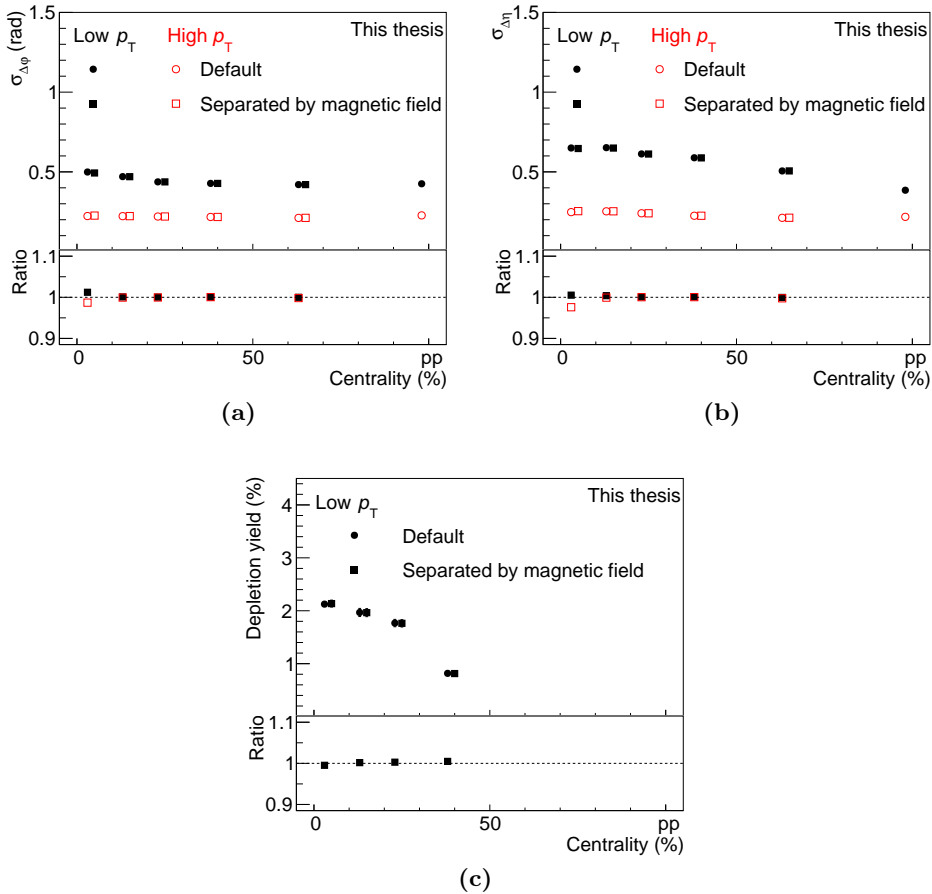


Figure 7.23: Comparison of the widths in the $\Delta\phi$ (a) and $\Delta\eta$ (b) directions and the depletion yield (c) of the default case with the case when the two magnetic field configurations are treated separately. The results are shown for a low p_T bin ($1 < p_{T,\text{trig}} < 2 \text{ GeV}/c$, $1 < p_{T,\text{assoc}} < 2 \text{ GeV}/c$) and a high p_T one ($4 < p_{T,\text{trig}} < 8 \text{ GeV}/c$, $2 < p_{T,\text{assoc}} < 3 \text{ GeV}/c$). Ratios to the default case are also shown, and for these the uncertainties are calculated by treating the statistical uncertainties on the two samples fully correlated.

Effect of resonances and Bose–Einstein correlations

The subject of the current study is the interaction of jets and mini-jets with the QGP; however, the near-side peak has contributions also from other sources. To test whether resonance decays or Bose–Einstein correlations are causing the observed broadening and depletion, the analysis was repeated separately for like- and unlike-sign pairs. If the effects originated from resonances, they would be stronger in the unlike-sign case, since neutral resonances decay into unlike-sign pairs. If, however, they originated solely from Bose–Einstein correlations, they would appear only in the like-sign case, since Bose–Einstein correlations affect only identical bosons. In Fig. 7.24, the width and the depletion yield are compared from the like- and unlike sign pairs with the default analysis. It can be seen that, while the numerical values are different in the two cases, the same broadening trend can be seen in both the like- and the unlike-sign case.

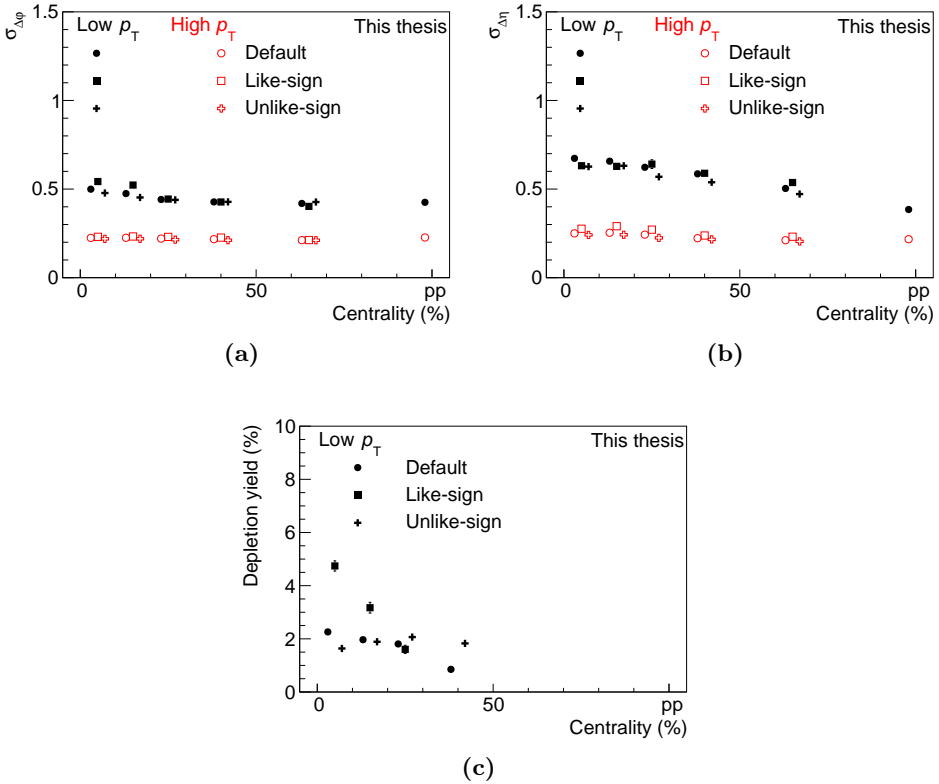


Figure 7.24: Comparison of the widths in the $\Delta\varphi$ (a) and $\Delta\eta$ (b) directions and the depletion yield (c) of the default case with the case when only like-sign or unlike-sign pairs are considered at low p_T ($1 < p_{T,\text{trig}} < 2 \text{ GeV}/c$, $1 < p_{T,\text{assoc}} < 2 \text{ GeV}/c$) and at high p_T ($4 < p_{T,\text{trig}} < 8 \text{ GeV}/c$, $2 < p_{T,\text{assoc}} < 3 \text{ GeV}/c$).

The depletion yield is smaller (larger) in the unlike-sign (like-sign) case than in the default analysis, but it is significant in all three cases. The like- and unlike-sign case are within the systematic uncertainty (see the end of the current chapter) in all bins, except in the most central one, where they differ by around two standard deviations. This comparison, however, assumes that each systematic effect has the same contribution in both cases. This is not necessarily true, for example track merging is more likely to happen in the like-sign case, therefore the systematic study on the small opening angle cut could give different results for the two cases. A full systematic study would therefore be necessary to quantify the difference, but this is outside of the scope of the current Thesis. Since both the broadening and the depletion are present in both the like-sign and the unlike-sign case, it can be excluded that these effects originate solely from the decay of resonances or solely from Bose–Einstein correlations.

Track selection and efficiencies

The effect of the selected tracking model can be studied by comparing the results obtained by using two different tracking models. For this, the analysis was repeated with two different sets of criteria on the track selection, which were described in Section 6.3. The full analysis chain is repeated with this selection and the width, σ^{CP} and the depletion yield is compared. Significant differences arise from the different track selections, therefore a systematic uncertainty is assigned. The differences are small in the case of the widths (1% of uncertainty is assigned) and bigger in the case of the depletion yield, where the assigned uncertainty is 20%.

Small opening angle cut

As described in Section 7.1.1, tracks that are closer than a certain distance in $\Delta\varphi^*$ and $\Delta\eta$ are removed from both the same and the mixed distributions. This corrects for track merging and splitting effects. For illustration in Fig. 7.25, the effect of the default correction is compared to the case when no correction is applied. As shown in the figure, this cut influences only the central few bins (two times two in $\Delta\varphi \times \Delta\eta$). There is a visible loss of tracks without the cut in these bins, which is corrected for by applying the cut. The default cut is at 0.02, which is doubled for the systematic studies. The point of closest approach for the two tracks is searched for, in 1 cm steps, between 3.9 cm and 251 cm radially from the center of the detector, which includes the volume of the ITS and the TPC. For the systematic studies the inner radius is changed to 80 cm, therefore only including the volume of the TPC. The analysis is repeated for the two systematic cases, and a 0.7% systematic uncertainty is assigned to the

widths. In the case of the depletion yield, 5–10% systematic uncertainty is assigned, where the lower value corresponds to the most central case and the higher value to the most peripheral one.

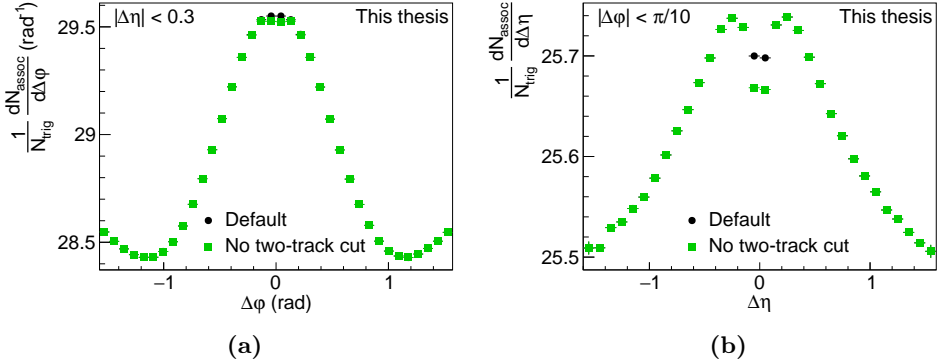


Figure 7.25: Projections to the $\Delta\varphi$ (a) and $\Delta\eta$ (b) axis around $(\Delta\varphi, \Delta\eta) = (0, 0)$ with and without the cut on the small opening angle of the particles for the bin $2 < p_{T,\text{trig}} < 3 \text{ GeV}/c$ and $1 < p_{T,\text{assoc}} < 2 \text{ GeV}/c$ for the most central 10% of the events.

Neutral-particle decay cut

Particles which are daughters of Λ and K_S^0 particles are removed by a cut on the invariant mass of the pairs to exclude trivial correlations arising from these particles. The default cut is $5 \text{ MeV}/c^2$ around the mass of the mother particle, which is changed to $10 \text{ MeV}/c^2$ and $2.5 \text{ MeV}/c^2$ for the systematic studies. The ratio of the per trigger yields in Fig. 7.26

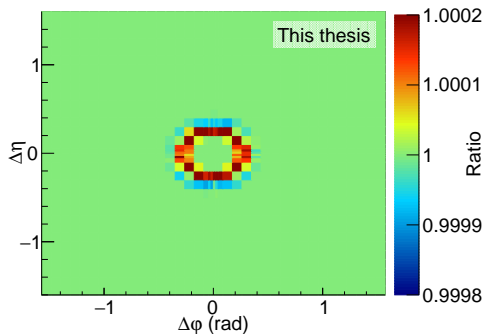


Figure 7.26: Ratio of the per trigger yield in the case when the cut on the decay products of neutral particles is halved ($2.5 \text{ MeV}/c^2$) and when it is doubled ($10 \text{ MeV}/c^2$) for the bin $1 < p_{T,\text{trig}} < 1 \text{ GeV}/c$, $1 < p_{T,\text{assoc}} < 2 \text{ GeV}/c$ and for the 10% most central collisions.

illustrates the trivial structure caused by the decay products of these particles. The analysis is repeated for the two systematic cases, and a 0.1% systematic uncertainty is assigned to the widths, while 8–20% is assigned to the depletion yield, depending on the centrality (being smallest for the most central case).

Vertex range

In the default analysis, only events where the reconstructed vertex is within ± 7 cm of the center of the detector in the z -direction are considered. The η and $\Delta\eta$ distribution of the tracks can change with the position of the vertex, therefore as a systematic check, the vertex range was limited to ± 3 cm. The analysis is repeated with the reduced vertex range, and the differences are assigned as systematic uncertainties, which results in 1% of systematic error for the widths and 5–10% for the depletion yield depending on the centrality (being smallest for the most central case).

Pseudorapidity dependence

For the study of the per trigger yield distributions, it is assumed that effects depend only on $\Delta\eta$ and not separately on the pseudorapidity of the two particles. The effect of the correction, which makes the away-side flat can be assessed by changing the considered η range. The default range of $|\eta| < 0.8$ is changed to $|\eta| < 0.7$ and to $|\eta| < 0.9$. The analysis is repeated for the two cases, and the differences are assigned as systematic uncertainties. In this case, a different value is assigned for the width in the $\Delta\varphi$ and the $\Delta\eta$ directions, 1.7% and 4.1%, respectively. This can be understood, since any effect which depends on the maximum η value is expected to cause a bigger effect in the $\Delta\eta$ direction than in the $\Delta\varphi$ direction. For the depletion yield, 5–15% is assigned, depending on the centrality (being smallest for the most central case).

Another check was done to exclude that there is a dependency on whether the trigger particle went in the positive or the negative η direction. A dependency is not expected; however, a difference could arise if there are unknown asymmetries in the detector. To study this, the per trigger yield distributions were created separately with trigger particles with positive and with negative η values, and there was no qualitative difference observed (an example is shown in Fig. 7.27). A quantitative study was not done, since the full $\Delta\eta$ range of the analysis is not available in these histograms, therefore the fitting of the distributions becomes problematic.

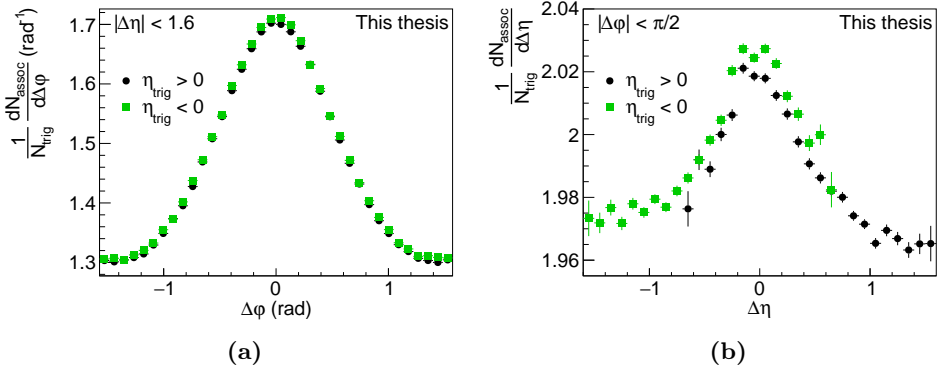


Figure 7.27: Projection of the per trigger yield distributions when the η of the trigger particle is positive or negative to the $\Delta\varphi$ direction (a) and the $\Delta\eta$ direction (b) for the bin $2 < p_{\text{T,trig}} < 3 \text{ GeV}/c$, $2 < p_{\text{T,assoc}} < 3 \text{ GeV}/c$ for the 30–50% centrality class.

Exclusion region

The size of the exclusion region plays a role at two points of the analysis. Firstly, it determines the size of the region around $(\Delta\varphi, \Delta\eta) = (0, 0)$ which is excluded from the fitting, so that the measurement of the width is not biased by the depletion seen at low p_{T} in the central collisions. The size of the exclusion region is enlarged for the systematic study by one bin. It is only enlarged, and not reduced, because if it would be reduced, it would not contain the full area of the depletion, therefore by definition the fit results would change. Enlarging it, however, should not change the fit results, because if the full area of the depletion was already contained in the smaller area, the fit should be describing properly the peak outside of this area in both cases. This enlargement is done for the bins where there was a region excluded originally. In all the other p_{T} and centrality bins in the systematic check, four bins in the center are excluded.

Secondly, the size of the exclusion region is also used for the determination of the depletion yield. In this case for the systematic studies, the region where the depletion yield is calculated is enlarged by one bin. It is not reduced for the same reasons as explained above. The two changes are done separately, therefore, by definition, this second study has an effect only on the depletion yield. The change is demonstrated in Fig. 7.28 for the most central bin in the lowest p_{T} case, which has the largest region excluded. The two changes give 0.1% systematic error for the width in the $\Delta\varphi$ direction, 1% for the width in the $\Delta\eta$ direction and 24–45% for the depletion yield. This is the largest contribution to the systematic un-

certainty of the depletion yield, and as was the case for the other effects as well, it gives a smaller uncertainty for the central case than for the peripheral case.

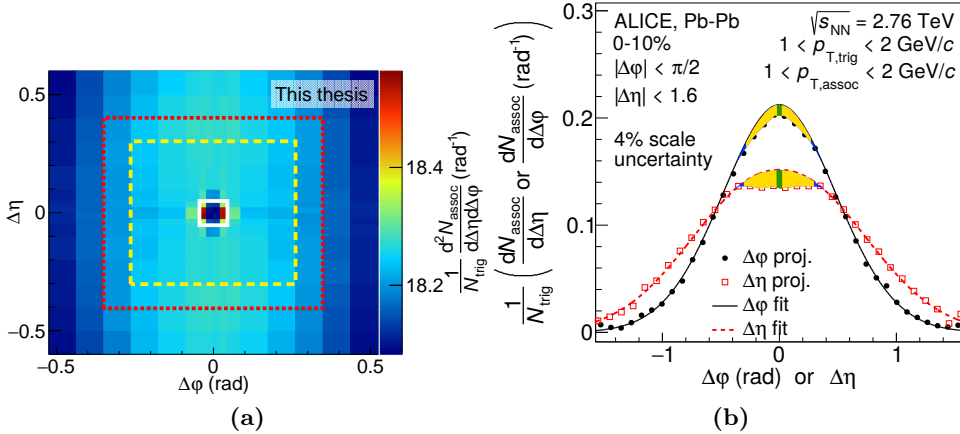


Figure 7.28: The two figures show the region used for the calculation of the depletion yield for the 10% most central events, in the bin $1 < p_{T,\text{trig}} < 2 \text{ GeV}/c$, $1 < p_{T,\text{assoc}} < 2 \text{ GeV}/c$. In panel (a), the default area for the calculation of the depletion yield is indicated by the area between the white line and the dashed yellow line, and the corresponding yield is indicated by yellow in panel (b). The area within the white line, and indicated by green in panel (b), is excluded from the calculation, because in this region the effects of track merging cannot be properly corrected for. The dotted red line indicates the enlargement of the area used for the calculation of the systematic uncertainty, and the additional yield is indicated by blue in panel (b).

Estimation of the systematic uncertainties

For all the previously described systematic cases, the widths, the σ^{CP} parameters and the depletion yield are calculated, and it is studied whether the changes cause a systematic difference in these quantities. In the cases where a systematic difference was found, a systematic uncertainty was calculated in the following way: The ratio of the measured quantities from the original and the changed analysis was calculated for all p_T and centrality bins. An example for all five measured quantities can be found in Fig. 7.29. The ratios were studied and no p_T or centrality dependence was found for the widths and for the σ^{CP} parameters, while a centrality dependence was found in some cases for the depletion yield. In the cases where there is no p_T and centrality dependence, the ratios were averaged and the average value is taken as the magnitude of the systematic uncertainty. In the case of the depletion yield, the averaging is only done for each p_T bin, but not for different centralities. The final systematic uncertainties are presented

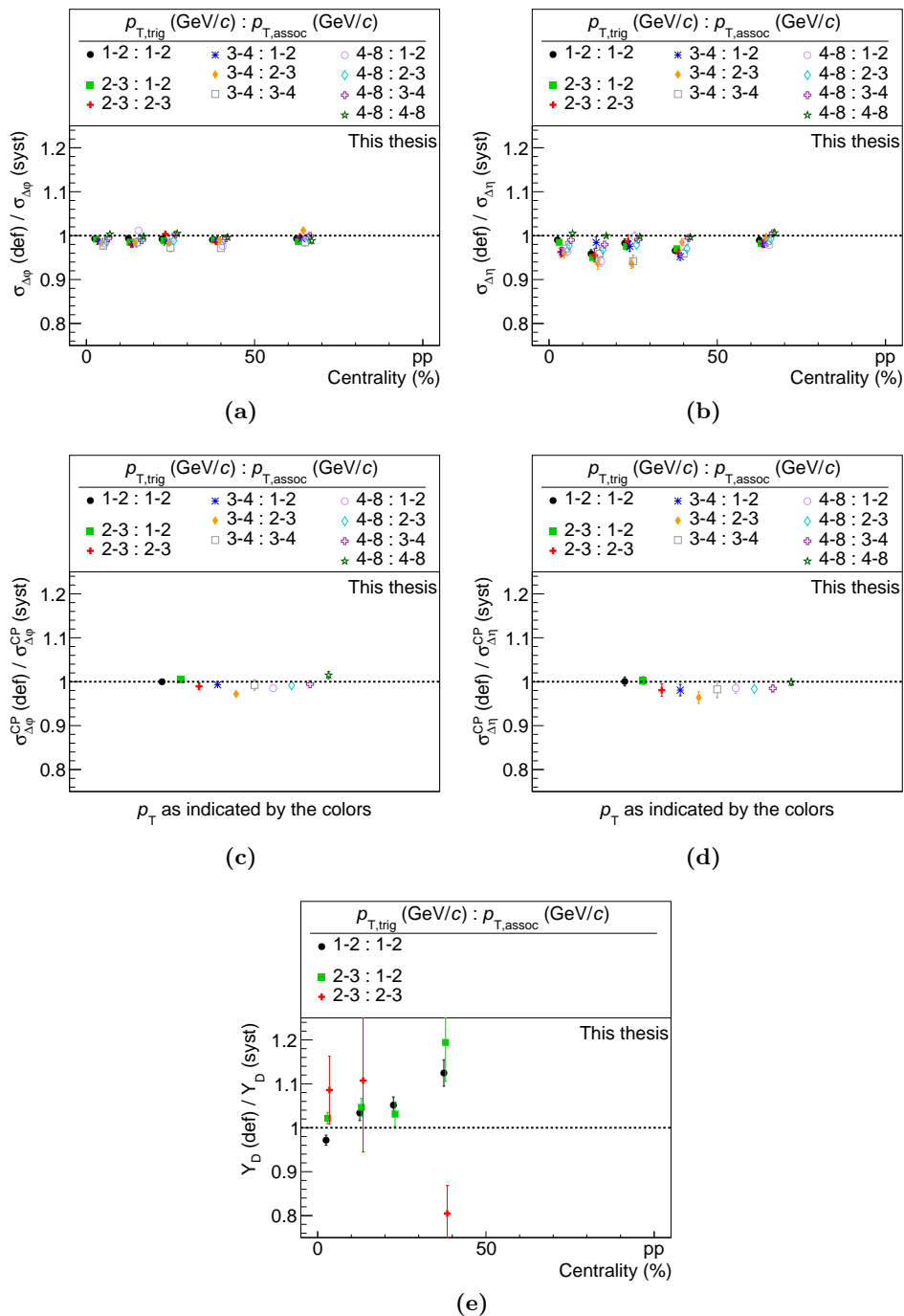


Figure 7.29: The figures show an example of the results compared between the default case and a case used for the systematic studies (change of the pseudorapidity range to $|\eta| < 0.9$). Panels (a) and (b) show the ratio for the widths of the peak in the $\Delta\phi$ and $\Delta\eta$ directions, respectively, panels (c) and (d) show the ratio for $\sigma_{\Delta\phi}^{\text{CP}}$ and $\sigma_{\Delta\eta}^{\text{CP}}$, respectively, while panel (e) shows the ratio for the depletion yield.

in Table 7.2. The widths and the σ^{CP} parameters are relatively insensitive to the changes, the systematic uncertainty is between 2.2% and 4.5%, while the depletion yield shows more sensitivity to the studied changes with a systematic uncertainty between 24% and 45%.

Source	$\sigma_{\Delta\varphi}$	$\sigma_{\Delta\eta}$	$\sigma_{\Delta\varphi}^{CP}$	$\sigma_{\Delta\eta}^{CP}$	Depletion yield
Track selection & efficiencies	1.0%		1.3%		20%
Small opening angle cut	0.7%		1.3%		5–10%
Neutral-particle decay cut	0.1%		0.2%		8–20%
Vertex range	1.0%		1.0%		5–10%
Pseudorapidity dependence	1.7%	4.1%	0.6%	2.5%	5–15%
Exclusion region	0.1%	1.0%	0.1%	1.5%	7–28%
Total	2.3%	4.5%	2.2%	3.6%	24–45%

Table 7.2: Summary of the systematic uncertainties of the analysis. Ranges indicate a dependence on the centrality.

8. Results

In this chapter, the results obtained from the fit with the generalized Gaussian are presented. These results are compared to results from the STAR [118] and the CMS [119] collaboration, as well as to PYTHIA and AMPT simulations.

8.1 Width of the near-side peak

In Fig. 8.1, the width of the near-side peak is shown for both the $\Delta\varphi$ and the $\Delta\eta$ directions. In both cases, the same dependence on p_T can be observed as in the case of the results from the HIJING simulations (Fig. 7.21). In both directions, in the highest two p_T bins, the width is independent of the centrality, and it is equal to the width in pp collisions.

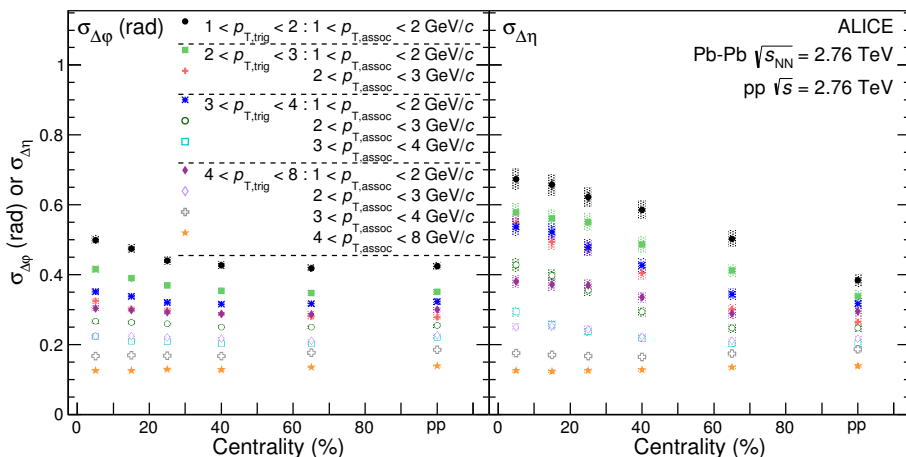


Figure 8.1: Width of the near-side peak in Pb–Pb and pp collisions (rightmost point for each p_T bin) at $\sqrt{s_{NN}} = 2.76$ TeV from a generalized Gaussian fit. The left panel shows the width in the $\Delta\varphi$ direction, while the right panel in the $\Delta\eta$ direction. Vertical lines (mostly smaller than the marker size) indicate the statistical uncertainties, while the filled areas represent the systematic ones.

In the $\Delta\varphi$ direction, the width in pp collisions and the width in the most peripheral (50-80%) bin is the same for all measured p_T bins; however, in the $\Delta\eta$ direction, the width in the peripheral bin is larger than the width in pp below $p_{T,\text{trig}} < 3 \text{ GeV}/c$ and $p_{T,\text{assoc}} < 3 \text{ GeV}/c$. The centrality bins presented in Fig. 8.1 represent the default binning used in this analysis; however, a finer binning was also tried to see whether the larger width in the peripheral case arises from having too wide bin as the most peripheral one. For this comparison 10% wide bins were used for all centralities, which, however, are too small at high p_T because of the limited statistics available. The results are presented in Fig. 8.2, where it can be seen that if finer bins are used the width in the most peripheral bin (80-90%) is equal to the width in pp in both directions for all studied p_T bins.

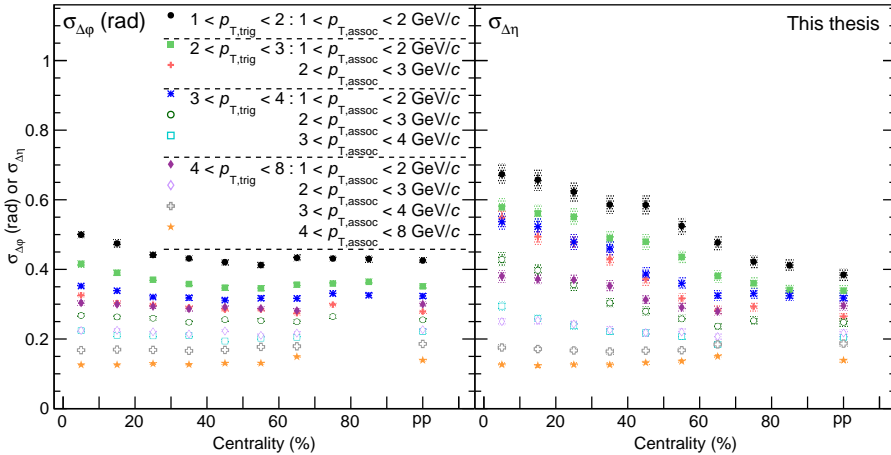


Figure 8.2: The same as Fig. 8.1, but with finer binning in centrality. Some of the points at high p_T are missing due to the limited statistics.

In Fig. 8.1 in the $\Delta\varphi$ direction, a slight broadening can be seen towards central events at low p_T ($p_{T,\text{trig}} < 3 \text{ GeV}/c$ or $p_{T,\text{assoc}} < 2 \text{ GeV}/c$). In the $\Delta\eta$ direction, the broadening is more significant and is visible in all p_T bins, except the highest two. This asymmetric broadening is even more visible in Fig. 8.3, where the ratio of the width in most central bin (0–10%) to the width in the most peripheral one (50–80%) is shown. The broadening is the largest in the $\Delta\eta$ direction in the intermediate p_T range ($2 < p_{T,\text{trig}} < 4 \text{ GeV}/c$ and $2 < p_{T,\text{assoc}} < 3 \text{ GeV}/c$), where the width in the central bin is around 1.8 times larger than the width in the peripheral bin.

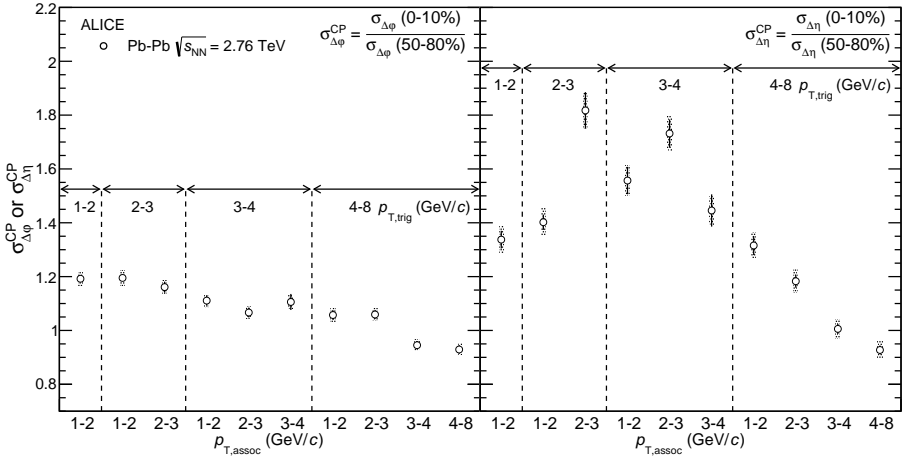


Figure 8.3: Ratio of the width in the most central (0–10%) and in the most peripheral (50–80%) collisions at $\sqrt{s_{\text{NN}}} = 2.76 \text{ TeV}$ as a function of p_T , where the x-axis combines the $p_{T,\text{trig}}$ and the $p_{T,\text{assoc}}$ axis. The error bars indicate the statistical uncertainty (mostly smaller than the symbol size), while the filled boxes denote the systematic ones. The left panel shows the σ^{CP} in the $\Delta\varphi$ direction, while the right panel in the $\Delta\eta$ direction.

8.2 Depletion yield

At low p_T and in central collisions, the peak departs from the Gaussian-like shape, and a depletion around $(\Delta\varphi, \Delta\eta) = (0, 0)$ appears. In Fig. 8.4, this is shown for a background subtracted per trigger yield distribution both in 2D and as projections to the $\Delta\varphi$ and $\Delta\eta$ directions. The depletion is described by the depletion yield, which is presented in Fig. 8.5. The depletion is statistically significant only for $p_{T,\text{trig}} < 3 \text{ GeV}/c$ and $p_{T,\text{assoc}} < 2 \text{ GeV}/c$, and even for these p_T bins, it disappears in the peripheral collisions. It does not appear for any of the p_T bins in pp collisions. The depletion is the largest in the most central 10% of the events, in the lowest p_T bin, where around 2.3% of the peak is missing around $(\Delta\varphi, \Delta\eta) = (0, 0)$.

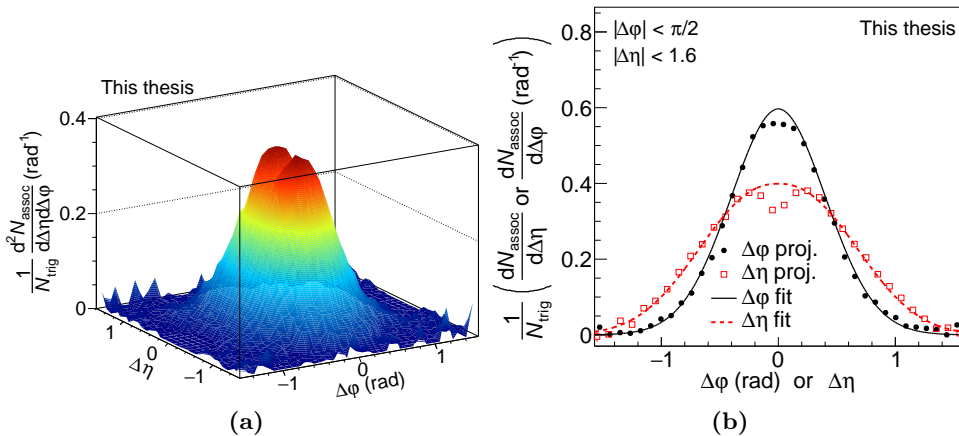


Figure 8.4: In panel (a), a background subtracted per trigger yield distribution is presented from Pb–Pb collisions at $\sqrt{s_{\text{NN}}} = 2.76 \text{ TeV}$ in the bin $2 < p_{T,\text{trig}} < 3 \text{ GeV}/c$ and $1 < p_{T,\text{assoc}} < 2 \text{ GeV}/c$ from the 10% most central collisions. In panel (b), the projections to the $\Delta\varphi$ and $\Delta\eta$ directions of the same histogram are shown overlaid with the fit functions.

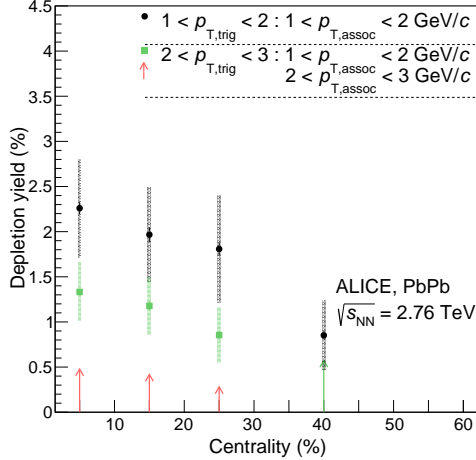


Figure 8.5: Depletion yield as a function of centrality for all the p_T ranges where a depletion is present. Vertical lines (mostly smaller than the marker size) indicate the statistical uncertainties, while the filled areas represent the systematic ones. The arrows represent an upper limit for the depletion yield in the cases where the band of the systematic uncertainty touches zero.

8.3 Comparison to results from other experiments

A similar measurement was done by the STAR collaboration in Cu–Cu, Au–Au and deuteron–Au collisions up to $\sqrt{s_{NN}} = 200$ GeV [118]. The construction of the per trigger yield was done in a similar way; however, there are some differences in the two analysis. The STAR experiment also corrected for the single particle reconstruction efficiency, but it was studied by embedding simulated particles into real events. They corrected for track merging and splitting effects also by a mixed event technique; however, they cut on the number of shared clusters between tracks and not on their $\Delta\varphi^*$ and $\Delta\eta$ difference, and they made the correction separately for the different helicity combinations. They also applied a correction to account for the limited acceptance of the detector. For this, instead of the mixed event technique used in the current analysis, they formed pairs by taking random φ and η values from their respective distributions and used the histogram built from these pairs to remove the effects arising from the limited acceptance.

The characterization of the near-side peak is also slightly different in the analysis done by the STAR collaboration. In their paper, the data is first projected to the $\Delta\varphi$ and $\Delta\eta$ directions, and the one-dimensional histograms are fitted to extract the widths. The background is treated in two different ways for the two directions. In the $\Delta\eta$ direction, the distribution is fitted with a constant to account for the background and a

Gaussian function for the signal. In the $\Delta\varphi$ direction, the two-dimensional histograms are projected in the range of $-0.78 < \eta < 0.78$, which contains both the background and the signal, and from these the backgrounds are subtracted by projecting the histogram in the range of $0.78 < |\eta| < 1.78$. The background-subtracted 1D per trigger yields are then fitted by a single Gaussian function in the $\Delta\varphi$ direction as well, and the variance of this Gaussian is extracted as the width of the peak. This width is shown in Fig. 8.6 as a function of the $p_{T,\text{assoc}}$ for a central and a peripheral bin, compared to the measurements from Pb–Pb collisions in the same $p_{T,\text{trig}}$ and $p_{T,\text{assoc}}$ range. The results are compatible in all bins, with a small (2σ) discrepancy in the central case in the $\Delta\varphi$ direction. This similarity will be further elaborated on in Section 8.5.

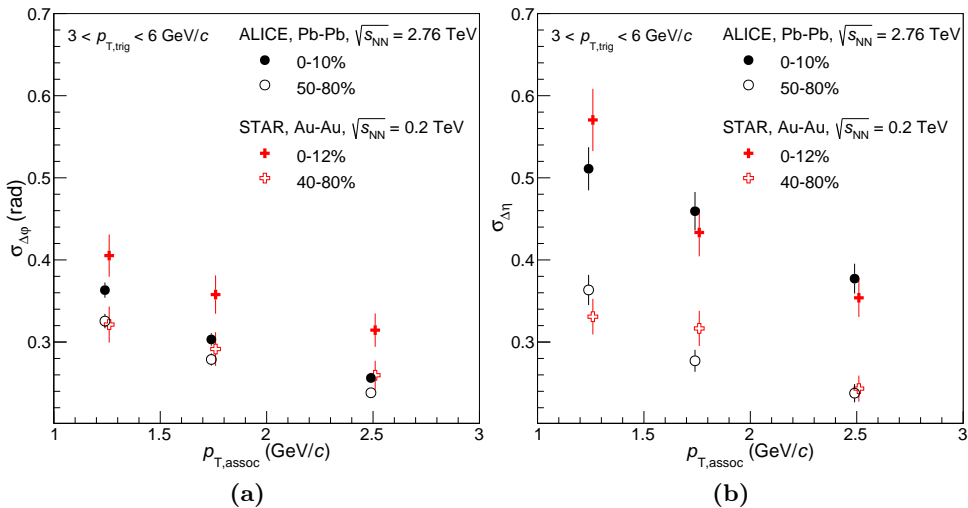


Figure 8.6: Comparison of the width measured by the STAR collaboration at $\sqrt{s_{\text{NN}}} = 200$ GeV in Au–Au collisions (red crosses) and by the ALICE collaboration in $\sqrt{s_{\text{NN}}} = 2.76$ TeV Pb–Pb collisions (black circles). The error bars contain the statistical and the systematic uncertainties added in quadrature.

The CMS collaboration has also done similar measurements [119]; however, they have used reconstructed jets as triggers instead of single particles. The jets have p_T larger than 120 GeV/ c , which is significantly higher than the highest p_T bin used in this analysis. This would mean that, to follow the p_T trend seen from the data, the width measured by the CMS collaboration should be lower than the width at the highest p_T bin in the current analysis. This was checked and it is indeed the case.

8.4 Comparison to models

The effect of the flowing medium on the near-side peak can be studied by comparing the data to model simulations. For this study the different configurations of AMPT, which were described in Section 6.4.3, were used. In the following these results will be presented, together with a comparison of the pp data with PYTHIA simulations. Both the AMPT and the PYTHIA simulations considered here are particle level simulations.

8.4.1 Width of the near-side peak

To extract the width of the near-side peak, the AMPT and PYTHIA per trigger yield distributions are created and fitted in the same way as it was described in the case of the data. In Figs. 8.7 to 8.9, the width in the $\Delta\varphi$ and $\Delta\eta$ directions are shown for the three studied AMPT configurations: string melting and hadronic rescattering turned on, only string melting turned on, and only hadronic rescattering turned on. If hadronic rescattering is turned on, there is a slight broadening in $\Delta\varphi$, while without it, the width is constant as a function of centrality and equal to the width from the PYTHIA simulations. In the $\Delta\eta$ direction, there is a broadening in all three AMPT cases at intermediate p_T , while at low p_T a broadening in mid-central events and a narrowing in the most central points can be seen.

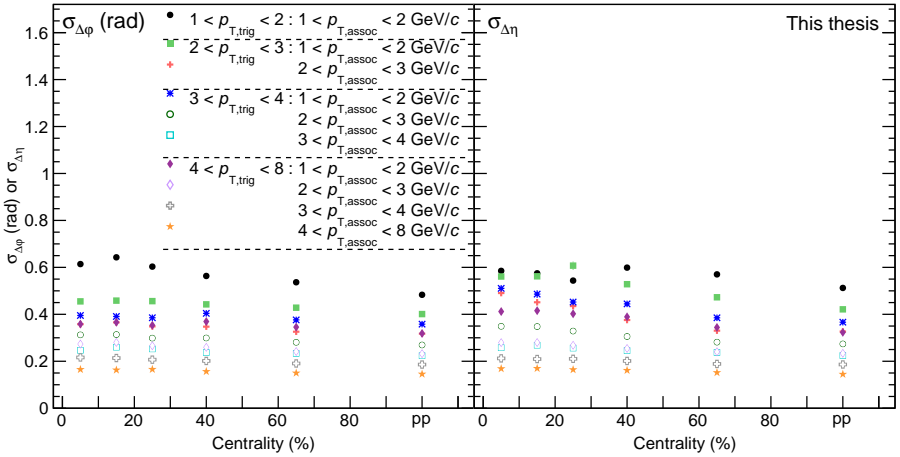


Figure 8.7: Width of the near-side peak from AMPT simulations with string melting and hadronic rescattering turned on from Pb-Pb collisions at $\sqrt{s_{\text{NN}}} = 2.76$ TeV and from PYTHIA simulations of pp collisions (rightmost point for each p_T bin) at the same energy. The left panel shows the width in the $\Delta\varphi$ direction, while the right panel in the $\Delta\eta$ direction. The error bars represent statistical uncertainties, which are mostly smaller than the marker size.

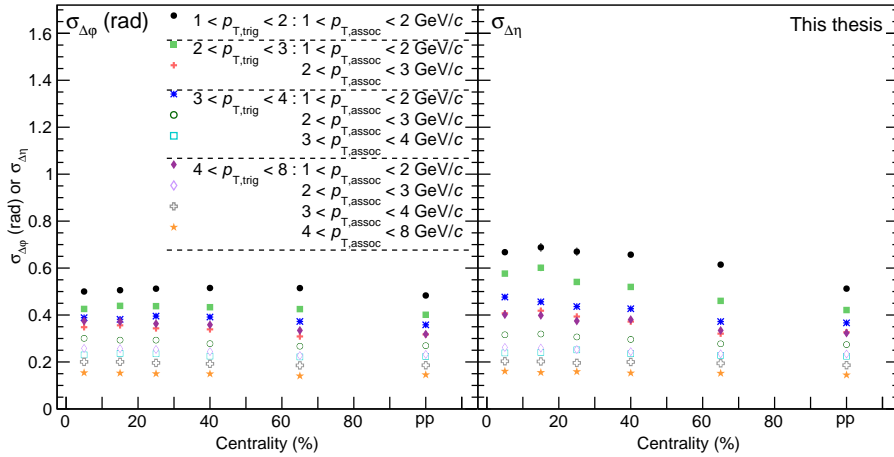


Figure 8.8: Same as Fig. 8.7, but for the AMPT configuration with string melting turned on and hadronic rescattering turned off.

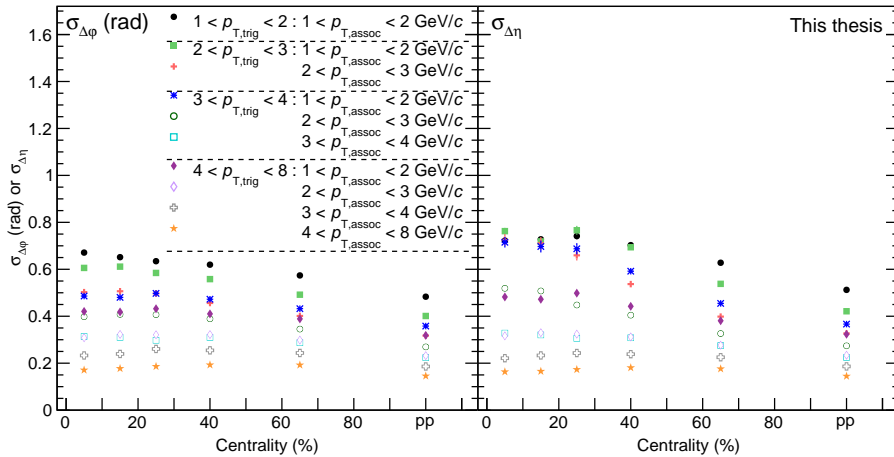


Figure 8.9: Same as Fig. 8.7, but for the AMPT configuration with string melting turned off and hadronic rescattering turned on.

The absolute width is not well reproduced by any of the AMPT configurations, as can be seen in Fig. 8.10, where the ratio of the width from AMPT and from data is presented for the most central (0-10%) and the most peripheral (50-80%) case. The configurations with string melting on give the best description, with a 10% difference to the data in the $\Delta\varphi$ direction and in the $\Delta\eta$ direction in peripheral collisions (50–80%) without a strong p_T dependence. The case when string melting is turned off is around 20% away from the data. In the $\Delta\eta$ direction in the most central

10% of the events, the two configurations with string melting on show a dependence on p_T , while the configuration with string melting turned off is almost constant as a function of p_T . This gives a hint that the configuration with string melting turned off follows the broadening trend of the data well, but misses the absolute value. The other configurations are better at reproducing the absolute value, but they do not follow the broadening trend seen in the data. In Fig. 8.10, the ratio of PYTHIA to the pp data is also presented, which shows a good agreement at high p_T , but at low p_T , PYTHIA over-predicts the data by 10–20%.

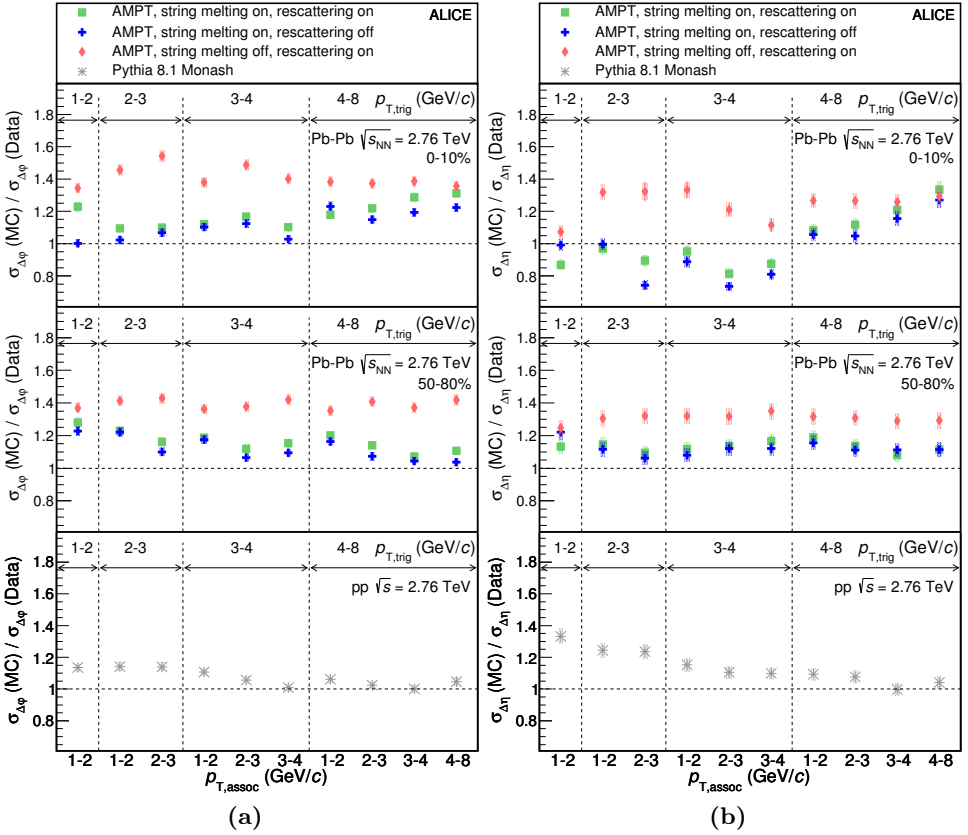


Figure 8.10: Ratio of the width from Monte Carlo generators and from data at $\sqrt{s_{\text{NN}}} = 2.76$ TeV for the most central 10% of Pb–Pb events (upper panels), the most peripheral bin (50–80%) in Pb–Pb events (middle panels) and for pp collisions (lower panels). The x-axis combines the $p_{T,\text{trig}}$ and the $p_{T,\text{assoc}}$ axis, and panel (a) shows the ratio in the $\Delta\phi$ direction, while panel (b) shows it in the $\Delta\eta$ direction. The error bars indicate the statistical uncertainty (mostly smaller than the symbol size), while the filled boxes denote the systematic ones.

The broadening trend is further studied in Fig. 8.11, where the ratio of the width in the most central bin (0–10%) to the most peripheral bin (50–80%) from AMPT is compared to data. It can be seen that the AMPT configuration with string melting turned off and hadronic rescattering turned on describes the data well in all p_T bins in both the $\Delta\varphi$ and the $\Delta\eta$ directions. The other configurations underestimate the data at high p_T in the $\Delta\varphi$ direction and fail to describe the large broadening in the intermediate p_T region in the $\Delta\eta$ direction.

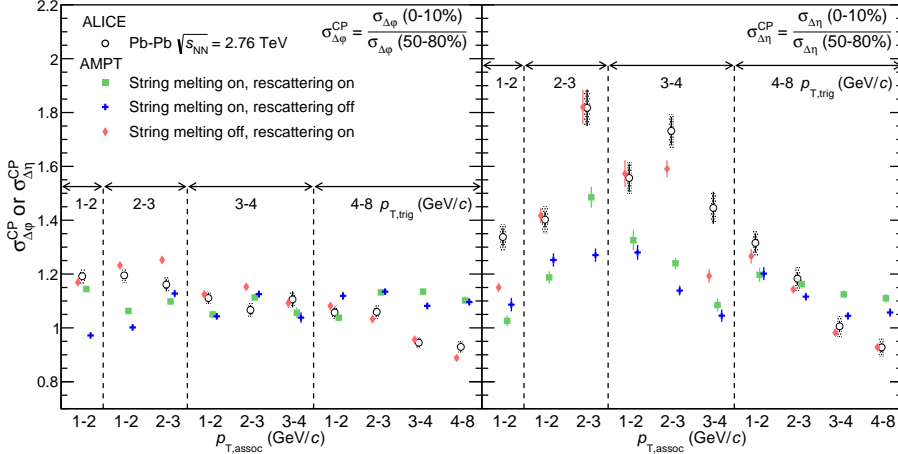


Figure 8.11: Ratio of the width in the most central (0–10%) and the most peripheral (50–80%) collisions as a function of p_T , where the x-axis combines the $p_{T,\text{trig}}$ and the $p_{T,\text{assoc}}$ axis. The three configurations of AMPT are compared to Pb–Pb data at $\sqrt{s_{\text{NN}}} = 2.76$ TeV. The error bars indicate the statistical uncertainty (mostly smaller than the symbol size), while the filled boxes denote the systematic ones (only for data). The left panel shows the ratio in the $\Delta\varphi$ direction, while the right panel shows it in the $\Delta\eta$ direction.

8.4.2 Depletion yield

The depletion seen in the data around $(\Delta\varphi, \Delta\eta) = (0, 0)$ can also be seen in certain configurations of AMPT. An example per trigger yield distribution at low p_T where the depletion is visible is shown for all three configurations in Fig. 8.12. The depletion is present if hadronic rescattering is turned on, independent of string melting. The depletion yield is calculated for these cases, in the same way as from the data, and it is overlaid with the results from data in Fig. 8.13. The depletion yield is compatible in the lowest p_T bin for the two cases with hadronic rescattering on, and it agrees with the data within the uncertainties of the analysis. In the higher p_T bins, no depletion is seen in any of the AMPT configurations.

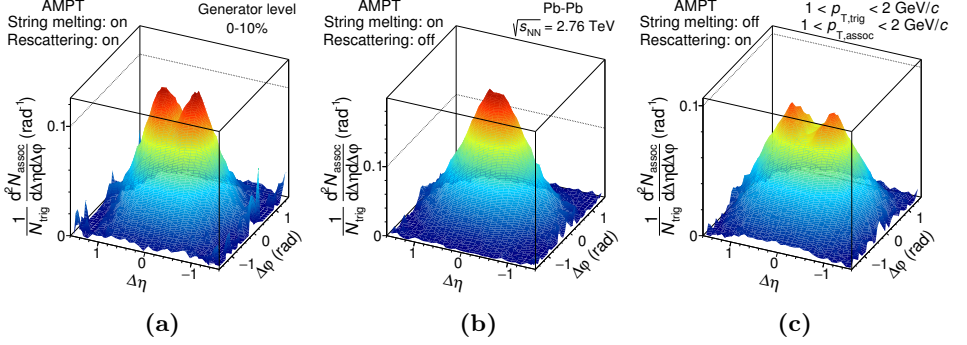


Figure 8.12: The three figures show the background subtracted per trigger yield distributions from AMPT simulations in Pb–Pb collisions at $\sqrt{s_{NN}} = 2.76$ TeV in the most central 10% of the events, from the bin $1 < p_{T,\text{trig}} < 2$ GeV/c and $1 < p_{T,\text{assoc}} < 2$ GeV/c. Panel (a) shows the case with both string melting and hadronic rescattering turned on, panel (b) the case with only string melting turned on and panel (c) the case with only hadronic rescattering turned on.

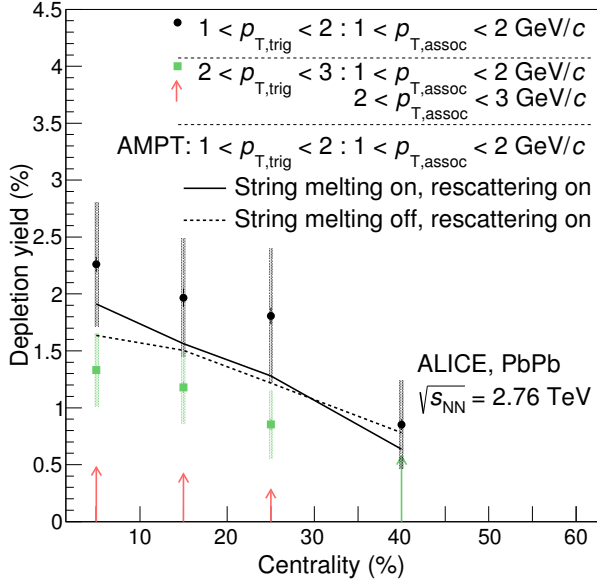


Figure 8.13: Depletion yield as a function of centrality. The data points are the same as in Fig. 8.5, and they are overlaid with the results from AMPT where a depletion is present.

8.4.3 Flow

To see whether the depletion and the broadening are caused by the interplay of the flowing medium and the propagating particles, the radial and elliptic flow of the three AMPT configurations are compared to data. The elliptic flow values in the case of the data are taken from Ref. [84], and the values for AMPT are extracted the same way as in the paper. The elliptic flow coefficient ($v_2\{2\}$) was extracted by the two-particle cumulant method [120] in the p_T range of $0.2 < p_T < 5.0$ GeV/ c . Particles with $|\eta| < 0.8$ were used, and the calculation was done for the 10% most central collisions. The results can be seen in Table 8.1. The AMPT configurations with either hadronic rescattering or string melting turned on describe the elliptic flow of the data within 10%, while the configuration where both effects are activated overestimates the data by around 15%.

Sample	β_T	$v_2\{2\}$
AMPT string melting & hadronic rescattering	0.442	0.0412 ± 0.0002
AMPT string melting	0.202	0.0389 ± 0.0002
AMPT hadronic rescattering	0.540	0.0330 ± 0.0002
Data	0.649 ± 0.022	0.0364 ± 0.0003

Table 8.1: Radial expansion velocity (β_T) and elliptic flow parameter ($v_2\{2\}$) from data [84, 85] and from the three studied AMPT cases. The uncertainties are combined statistical and systematic ones from data and only statistical for AMPT. The statistical uncertainties for β_T in AMPT are negligible.

The radial flow expansion velocity (β_T) was also estimated for both data and the three AMPT configurations. This is done by fitting a Blast wave function simultaneously to the spectrum of pions, kaons and protons [20]. The 10% most central events and particles with $|y| < 0.5$ are used. The method is described in detail in Ref. [85], and the results from data are also taken from there. The Blast wave function has the following form:

$$\frac{1}{p_T} \frac{dN}{dp_T} \propto \int_0^R r dr m_T I_0 \left(\frac{p_T \sinh \rho}{T_{kin}} \right) K_1 \left(\frac{m_T \cosh \rho}{T_{kin}} \right) \quad (8.1)$$

where I_0 and K_1 are the modified Bessel functions, r is the radial distance in the transverse plane, R is the radius of the fireball, T_{kin} is the freeze-out temperature and $\rho = \tanh^{-1}(\beta_T) = \tanh^{-1} \left[\left(\frac{r}{R} \right)^n \beta_S \right]$ with β_s being the transverse expansion velocity at the surface, β_T the transverse expansion velocity and n the velocity profile. From these parameters only β_T , T_{kin} and n are free parameters, while all the others have to be fixed from models. The three particle species are fitted simultaneously, but different p_T ranges are used for the three species ($0.5 < p_T < 1$ GeV/ c ,

$0.2 < p_T < 1.5 \text{ GeV}/c$ and $0.3 < p_T < 2 \text{ GeV}/c$ for pion, kaons and protons, respectively). From this fit, the expansion velocity and the kinetic freeze-out temperature are obtained. As an example, the AMPT case where both string melting and hadronic rescattering is turned on can be seen in Fig. 8.14. The function describes this configuration up to around 10%. If, however, the species are fitted separately a slightly better description can be achieved (see Fig. 8.15), but this way a common expansion velocity cannot be extracted. In Table 8.1, the β_T values from the simultaneous fits are presented for both data and the three AMPT cases.

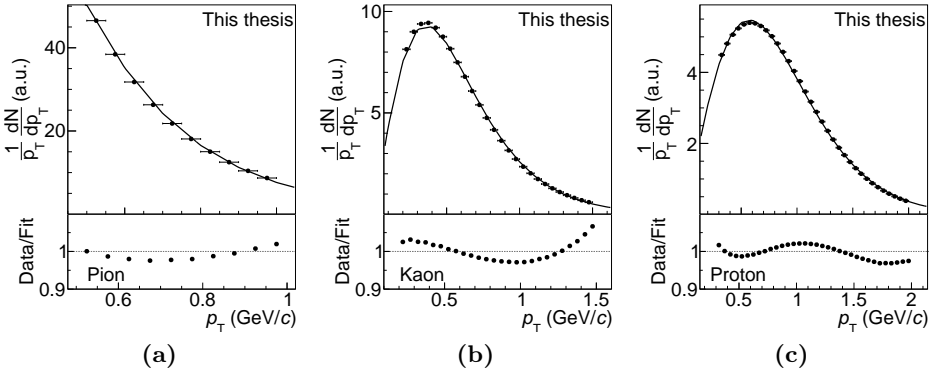


Figure 8.14: Simultaneous blast-wave fit to the p_T spectra of pions (a), kaons (b) and protons (c) with the ratio of the data and the fit indicated in the bottom panels, for the AMPT case with string melting and hadronic rescattering both turned on.

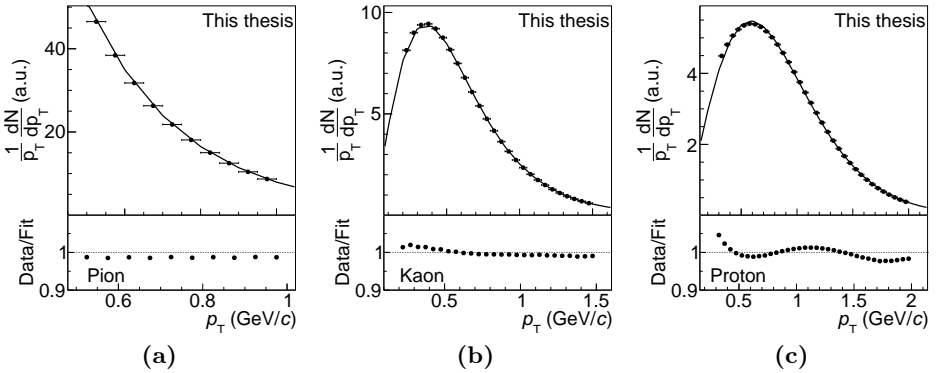


Figure 8.15: Separate blast-wave fits to the p_T spectra of pions (a), kaons (b) and protons (c) with the ratio of the data and the fit indicated in the bottom panels, for the AMPT case with string melting and hadronic rescattering both turned on.

All three AMPT versions underestimate the radial flow compared to the data. The version where string melting is turned off is the highest and the one closest to the data, but there is still around 17% difference.

8.5 Interplay of jets and flow

Three aspects were studied while comparing the data to the AMPT simulations: the absolute width of the peak (Fig. 8.10), the relative evolution of the width with centrality (Fig. 8.11) and the depletion yield (Fig. 8.13). The absolute width of the peak is not described properly by any of the AMPT configurations. The best description (up to around 10%) is given by the case when both string melting and hadronic rescattering are turned on. The relative evolution of the width is described only by the case when string melting is turned off, but hadronic rescattering is on, while the depletion yield is properly described if hadronic rescattering is turned on, independent of string melting. Table 8.2 gives a summary on how well these three aspects are described by the different configurations of AMPT.

AMPT configurations Measurements	String melting & hadronic rescattering	String melting	Hadronic rescattering
Absolute width	10%	10 – 15%	20 – 30%
Evolution of width	×	×	✓
Depletion	✓	×	✓

Table 8.2: Summary of the description of the different phenomena by the three configurations of AMPT.

AMPT gives a good description of $v_2\{2\}$ with either string melting or hadronic rescattering turned on; however, out of these two only the one with hadronic rescattering turned on shows a depletion and describes the evolution of the relative width. The same configuration is the one that has the closest β_T to the data, while the other two configurations show a much lower value. This shows that a good description of β_T is needed to describe the presented phenomena, while a good description of $v_2\{2\}$ alone is not sufficient to describe them. This suggests that the depletion and the broadening are driven by radial flow rather than elliptic flow.

In Ref. [121], the authors have studied the effect of longitudinal flow on the shape of the near-side peak in AMPT. They have found that strong longitudinal flow in AMPT is accompanied by a longitudinally broadened near-side peak. This coincides with the results of this analysis, and therefore reinforces the findings that the changes in the shape come from an interplay of jets with the flowing medium. Ref. [121] together with the

study discussed above indicate that the results are more likely caused by radial and longitudinal flow than by elliptic flow.

Radial flow in central events changes by about 15% from the energy at RHIC ($\sqrt{s_{\text{NN}}} = 200$ GeV) to the one at the LHC ($\sqrt{s_{\text{NN}}} = 2.76$ TeV) [85]. In Fig. 8.6, it was shown that the width and the broadening does not change significantly between the two energies, which can be explained by this relatively small dependence of the radial flow on the center of mass energy. It would be interesting to study this further by measuring both the radial flow and the peak shapes from the data taken by the ALICE detector in 2015 at $\sqrt{s_{\text{NN}}} = 5.02$ TeV.

8.6 Summary

A two-particle angular correlation measurement has been presented from data taken by the ALICE detector at $\sqrt{s_{\text{NN}}} = 2.76$ TeV for both Pb–Pb and pp collisions [1,2]. A broadening of the near-side peak towards low p_{T} is present in both the pp and Pb–Pb samples, which is explained by the boost of the fragmenting parton. An additional broadening is seen in central Pb–Pb collisions in both the $\Delta\varphi$ and $\Delta\eta$ directions. The broadening was quantified by the σ^{CP} quantities. This broadening is found to be more significant in the $\Delta\eta$ direction and it is persistent until larger p_{T} , resulting in an asymmetry in the shape of the peak. In the p_{T} bin, where it is most pronounced ($2 < p_{\text{T},\text{trig}} < 3$ GeV/ c , $2 < p_{\text{T},\text{assoc}} < 3$ GeV/ c), it is 1.6 times higher in the $\Delta\eta$ direction than in the $\Delta\varphi$ direction. At high p_{T} ($p_{\text{T},\text{trig}} > 4$ GeV/ c and $p_{\text{T},\text{assoc}} > 3$ GeV/ c) in Pb–Pb collisions, the broadening disappears and the peak is found to be symmetric. There is no asymmetry found in the case of pp collisions at any of the measured p_{T} bins.

Furthermore, a novel feature, a depletion around $(\Delta\varphi, \Delta\eta) = (0, 0)$, was observed in Pb–Pb collisions. This depletion is largest at low p_{T} in central collisions and disappears completely above $p_{\text{T}} > 3$ GeV/ c and in peripheral collisions. It is not present in pp collisions at any of the measured p_{T} values. It was characterized by the missing yield from the peak, which was found to be $2.26\% \pm 0.06\% \pm 0.24\%$ of the total yield of the peak in the lowest p_{T} bin ($1 < p_{\text{T},\text{trig}}, p_{\text{T},\text{assoc}} < 2$ GeV/ c) and the most central 10% of the collisions.

The results were compared to Monte Carlo simulations. PYTHIA 8.1 with the Monash tune describes the width of the peak in pp collisions well at high $p_{\text{T},\text{trig}}$; however, it overestimates the width at low $p_{\text{T},\text{trig}}$. Results from Pb–Pb collisions were compared to different configurations of AMPT. The configuration with string melting turned off but hadronic rescattering turned on describes properly the evolution of the width, but

has a 20–30% discrepancy in the absolute width. The two configurations with string melting turned on give a better description of the absolute width, but they do not reproduce properly the broadening trend seen in the data. The depletion yield is well described in the lowest p_T bin by both AMPT configurations with hadronic rescattering turned on.

To interpret the observations in context with the interaction of jets with the flowing medium created in heavy-ion collisions, the radial flow velocity and the elliptic flow parameter were calculated from both data and AMPT. From this comparison, it was found that a large radial flow velocity is needed to reproduce the effects, and that it is more likely the cause of both the broadening and the depletion than elliptic flow. These studies suggest that both the broadening and the depletion can be interpreted as an interaction of the expanding Quark-Gluon Plasma and the jets traversing through it.

8.7 Physics outlook

The current study suggests that the observed effects are caused by the interplay of jets with the flowing medium created in heavy-ion collisions. This conclusion was reached by comparing the results only to AMPT, therefore it would be important to verify them by comparing the results to other MC generators. For this comparison, MC generators which include both soft and hard p_T physics and their interplay would be needed. Unfortunately, the number of available generators which include all the needed ingredients is limited right now. A new version of EPOS (EPOS3 [122,123]) will become available for heavy-ion collisions in 2018 and HIJING++ [124] is also under development. These are promising candidates for such comparisons.

Another important aspect, which would require further studies, is the energy dependence of the results. It was shown that there is no energy dependence of the broadening from $\sqrt{s_{NN}} = 200$ GeV to $\sqrt{s_{NN}} = 2.76$ TeV; however, the depletion was not present in the measurements of the STAR collaboration at the lower energy. To continue this study, the Pb–Pb data taken in 2015 by the ALICE detector at $\sqrt{s_{NN}} = 5.02$ TeV can be used. It was shown that the radial flow changes by 5–10% at the same multiplicity between the two energies [125], therefore the sensitivity of the peak shape to the change in radial flow can be further tested by comparing these two.

It was shown that the depletion yield differs in the like-sign and the unlike-sign case; however, the full study of the systematic uncertainties was outside the scope of the current Thesis. It would therefore be interesting to investigate in detail whether their difference is significant, and if it is found significant, to pursue the underlying physics mechanism.

To exclude the possibility that the presented phenomena are arising from cold nuclear effects, such as the modification of the nuclear parton distribution function in a Pb nucleus, the data of p–Pb collisions can be studied. The data should be analyzed as a function of the collision multiplicity and they have to be compared to pp collisions at the same center of mass energy. If either a change compared to pp collisions or as a function of multiplicity is seen, it is important to verify that the presented effects do not arise from solely cold nuclear effects.

In conclusion, there are still open questions before we have a complete understanding of how the interaction of jets with the flowing medium modify two-particle angular correlations; however, this Thesis gives a first comprehensive study of the modifications at $\sqrt{s_{\text{NN}}} = 2.76$ TeV in Pb–Pb collisions and also provides a useful starting point for future measurements on this topic.

A. Test-beam measurement campaigns

The measurements of the pALPIDE-1 were done in measurement campaigns, which means usually beam time for one week, but sometimes beam was available continuously for up to a few weeks. These campaigns focused on one or a few aspects of the testing (e.g. setup optimized for efficiency or testing chips with different irradiation levels). The details of the campaigns are given below and the main settings of each campaign are summarized in Table A.1.

A.1 Measurements at the PS

A.1.1 July 2014

This was the first test-beam campaign at the PS to test the pALPIDE-1, and negative pions with a momentum of 5–6 GeV/ c were used for the measurements. At the beginning the telescope consisted of six pALPIDE-1 planes, but later a seventh one was added. One or all of planes 2, 3 and 4 (counted from 0) were treated as DUTs, which means the settings of these chips were changed run by run, while the settings of the other planes were kept the same throughout the whole campaign ($I_{thr} = 51$ DAC units, $V_{CASN} = 57$ DAC units and $V_{BB} = 0$ V). The chips used for tracking were W1-22 and W2-24 before the DUTs and W1-18 and W1-17 behind the DUTs. The distance between the planes varied between runs from 19.6 mm to 31.6 mm. There were four non irradiated planes tested (W2-23, W2-25, W2-27 and W1-25) and one irradiated one (W1-9). The goal during this campaign was to take more than 1 000 000 events for each setting. Unfortunately, the data-taking software was not yet fully stable, so this goal was not achieved for all settings. Noise data was also taken for most of the settings with the stack of chips moved outside of the beam, and data with and without masking pixels during data-taking was also collected to test the masking functionality of the chip. The rate of the data-taking was low, because with higher rate the data-taking software became more unstable.

Place, time, momentum, type	Settings of the tracking planes	Tracking planes	DUTs	Main goals of the campaign
BTF 2014 June 500 MeV/c, e^- ,	$I_{thr} = 51$ DAC units $V_{CASN} = 57 - 64$ DAC units $V_{BB} = 0$ V	First a telescope of 3 planes was used, later it was changed to a telescope of 5 planes with the central 3 being the DUTs		First validation of the setup
BTF 2014 November 450 MeV/c, e^-	$I_{thr} = 51$ DAC units $V_{CASN} = 57$ DAC units $V_{BB} = 0$ V	W1-17, W2-23, W2-24, W2-25, W2-27, W1-18	W2-31	Hit multiplicity dependence of efficiency
PS 2014 July 5-6 GeV/c, π^-	$I_{thr} = 51$ DAC units $V_{CASN} = 57$ DAC units $V_{BB} = 0$ V	W1-22, W2-24, W1-18, W1-17	W2-23, W2-25, W2-27, W1-25, W1-9	First validation of the 7-plane setup and efficiency measurements
PS 2014 Sept.-Nov. 500 MeV/c, 5-6 GeV/c, π^-	$I_{thr} = 30$ DAC units $V_{CASN} = 57$ DAC units $V_{BB} = 0$ V	W1-17, W2-23, W2-24, W2-25, W2-27, W1-18	W2-12, W2-8, W2-14, W2-32, W2-15, W2-9, W2-10, W2-31, W2-23, W8-29	Efficiency, resolution and noise occupancy for different irradiation levels
PS 2014 December 5-6 GeV/c, π^-	$I_{thr} = 20$ DAC units $V_{CASN} = 57$ DAC units $V_{BB} = 0$ V	W1-18, W2-27, W2-23, W1-17	W6-39, W9-16, W6-14 W6-6, W5-21, W5-25	Chip-to-chip fluctuations of efficiency and noise occupancy
SPS 2014 October 120 GeV/c, π^+	$I_{thr} = 30$ DAC units $V_{CASN} = 57$ DAC units $V_{BB} = 0$ V	W1-17, W2-23, W2-24, W2-25 W2-27, W1-18	W2-31	Efficiency and resolution at higher momentum
DESY 2015 February 5.8 GeV/c, e^+	$I_{thr} = 51$ DAC units $V_{CASN} = 65$ DAC units $V_{BB} = 0$ V $I_{DB} = 128$ DAC units	W2-23, W5-39, W9-38, W1-18	W6-39, W9-16, W2-31	Noise occupancy, pulse length and efficiency with optimized tracking plane settings

Table A.1: Summary of the main settings of each test-beam campaign. Where certain settings are not listed it means that they were kept at the default values of the chip, which are listed in Table A.2.

Parameter name	Default setting
I_{thr}	51 DAC units
V_{CASN}	57 DAC units
I_{db}	64 DAC units
V_{AUX}	117 DAC units
V_{CASP}	86 DAC units
V_{RESET}	117 DAC units
V_{BB}	0 V

Table A.2: The default settings of the parameters of the pALPIDE-1.

The rate was, however, not well controlled, because we were not main user most of the time, which means that another group was controlling the parameters of the beam.

The results of this measurement campaign were included in Figs. 5.5, 5.9 to 5.11, 5.13, 5.14, 5.18, 5.19, 5.24, 5.27 and 5.36 to 5.39.

A.1.2 September-November 2014

During this campaign, we were main users for most of the time, so the rate was relatively constant. Since the problems experienced during the July campaign were solved, it was possible to use high beam intensity, and therefore the limitation of the rate was the readout speed of the chip. Negatively charged pions were used for the measurements with three different momenta: 0.5 GeV/ c , 5 GeV/ c and 6 GeV/ c . There were seven pALPIDE-1 chips in the beam, and the settings were changed only for the middle one, while the others were kept at $I_{thr} = 30$ DAC units, $V_{CASN} = 57$ DAC units and $V_{BB} = 0$ V. All the distances between the planes were 19.6 mm. More than 1 000 000 events for each setting were collected, and 11 different chips with 5 different irradiation levels were tested. Noise data was also taken for some of the tested chips. The tracking planes were always in the same conditions, so the data can be compared easily, and the data can be used for resolution calculation, since the tracking uncertainty is the same for all runs. The tracking planes were W1-17, W2-23, W2-24, W2-25, W2-27 and W1-18, and the DUTs were the following: W2-12, W2-8, W2-14, W2-32, W2-15, W2-9, W2-10, W2-31, W2-23 (with W2-31 as the tracking plane) and W8-29.

The results of this measurement campaign were included in Figs. 5.1, 5.5, 5.6, 5.8, 5.13 to 5.15, 5.17, 5.20 to 5.26, 5.34, 5.35 and 5.40 to 5.42.

A.1.3 December 2014

In the December test-beam campaign, seven pALPIDE-1 chips were in the setup, and negative pions with a momentum of 5–6 GeV/ c were used. The middle three were used as DUTs, which means that the settings of the outer four were kept the same ($I_{thr} = 20$ DAC units, $V_{CASN} = 57$ DAC units and $V_{BB} = 0$ V), and the settings of the middle three were changed between each run. The chips used for tracking were W1-18, W2-27, W2-23 and W1-17, and all the distances between the planes were 19.6 mm. Around 60 000 events were taken with each setting with a relatively low rate. Since for most of the week of data-taking we were not main users, the rate was not well controlled. Around 60 000 events of noise data was also taken for each setting, which means that the chips were moved outside of the beam on a linear stage in the horizontal direction by 22 cm. There were three non irradiated (W6-39, W9-16 and W6-14) and three irradiated chips (W6-6, W5-21 and W5-25) measured in a way that the three chips with the same irradiation level were in the setup at the same time.

The results of this measurement campaign were included in Figs. 5.2 to 5.5, 5.7, 5.8, 5.12 to 5.14, 5.16, 5.17 and 5.28 to 5.34.

A.2 Measurements at the SPS

In October 2014, a measurement campaign took place at the SPS. The settings were the same as in the September–November 2014 PS test-beam campaign, with the only difference being that the rate was not well controlled, since we were not running as main users. During this campaign there was only one chip tested (W2-31), and there was no noise data taken. Positive pions were used with a momentum of 120 GeV/ c , and 1 000 000 events for each setting was taken.

The results of this measurement campaign were included in Figs. 5.6, 5.15 and 5.22.

A.3 Measurements at DESY

In February 2015, at DESY there were seven pALPIDE-1 planes used, out of which the middle three were treated as DUTs. The other planes were kept with $V_{CASN} = 65$ DAC units, $I_{thr} = 51$ DAC units and $V_{BB} = 0$ V. In this campaign I_{DB} was also adjusted ($I_{DB} = 128$ DAC units), together with the other default settings of the tracking planes compared to the other test-beam campaigns to keep the pulse length in the tracking planes shorter than in the DUT. A positron beam with a momentum of 5.8 GeV/ c was

used, and around 120 000 events were taken for each setting. Noise data was taken for all settings with the setup placed outside of the beam. The planes were 19.6 mm apart with the tracking planes being W2-23, W5-39, W9-38 and W1-18 and the DUTs being W6-39, W9-16 and W2-31.

The results of this measurement campaign were included in Figs. 5.6, 5.15 and 5.22.

B. Technical details of the analysis of the pALPIDE-1

B.1 Integration of the chip in the EUTelescope framework

As outlined in Section 4.2, a few steps have to be taken to include a new chip in the EUTelescope framework. First of all, a chip specific *Producer* has to be written, which takes care of the integration of the chip in the readout during data-taking. Afterwards, for the data analysis, a chip specific *Converter* is needed, which is responsible for the conversion of the recorded data to the internal format (lcio) of the framework. For each different measurement setup a gear file also has to be written, which contains the geometric description of the setup and of the chips used. Once these three are available, the default analysis can be performed, which provides the fitted tracks. Further analysis is needed, however, for the determination of the characteristics of the sensor. This can be either done by a separate program or it can be integrated into the EUTelescope framework, which was the chosen option in the case of the ALPIDE prototypes. The last step, called *analysis* (see Fig. 4.2), is specific to the ALPIDE prototypes and is responsible for the calculation of detection efficiency, residual and for the characterization of clusters. Noise data with the setup outside of the beam has also been taken, and the analysis of this has been also integrated into the EUTelescope framework. This requires a separate step, which is executed right after the conversion of the data to the lcio format (*noise* step). One more additional step has been introduced for the ALPIDE prototypes to treat the cases when one or more double columns were switched off during data taking. The *deadColumn* step finds these double columns and saves them into a file for later masking.

B.2 Default parameters of the analysis

In this section, important parameters and their values used as default in the analysis will be discussed. In the analysis of the pALPIDE-1, hits are grouped together in a cluster if they are touching by a side and not if they are only touching by a corner. If pixels fire more than a certain firing frequency without any external stipulation, they are considered noisy, and they are removed from the analysis. There are two different cuts on the firing frequency in the analysis: a tight cut is used for the alignment and a looser cut is used for the calculation of the efficiency and the resolution values. This is needed because the alignment is much more sensitive to the presence of hot pixels than all the other steps. To speed up the processing of the data, the noisy pixels are looked for in only the first 10 000 events. This check is done to exclude pixels, which fire much more frequently than once per 10 000 events, therefore the noisy pixels can already be identified by looking only at this subset of the events. For the analysis a pixel is excluded if it fires more often than 0.1% of the analyzed events. Not using all the events of a run, however, allows the use of an even stricter cut for the alignment, which is set to 0.01%. In the case of the data used for the results presented in this Thesis, the beam intensity was set such that there are one or two tracks per event, which means if a pixel was hit in the first 10 000 events, it would have a minimum firing frequency of around 0.01%. Therefore the stricter cut already removes hits originating from particles, which in practice means that any pixels firing in the first 10 000 events are removed from the alignment. With maximum two particles per event and assuming that the particles leave only one-pixel clusters, this would result in removing up to 20 000 pixels, which is around 4% of the full chip. If this was done for the full analysis, it would cause problems, but since this is done only for the alignment step, this does not harm the calculation of the efficiency, the resolution or the cluster size.

Hits in the DUT are associated to tracks if they were closer to the track in both the x and the y direction than $100\ \mu\text{m}$. This value is much larger than the uncertainty of the tracking ($2\text{--}3\ \mu\text{m}$) and the resolution of the sensor ($\sim 5\ \mu\text{m}$), but it is necessary to include some safety margin on the association for the case that the *prealign* and *align* steps were not able to correct completely the misalignment of the setup. This could be a problem if more than one hit falls into the search window, which could come from noise or from a high track multiplicity. To detect a hit originating from noise in each $100\ \mu\text{m} \times 100\ \mu\text{m}$ large area of the chip, a noise occupancy of around 0.08 hits/pixel/event is needed, which is much larger than the noise occupancy of the sensor (around 10^{-6} hits/pixel/event). To detect an additional hit from a second track in the same area, around 45 000 particles have to pass through the sensor in each event. In the measurements used

for the result in this Thesis, the beam intensity was set such that 1–2 tracks were passing through the detector in each event.

For measurements of the detection efficiency, it is important that only those tracks are considered that would have a corresponding hit in the detector if the detector would be fully efficient. For example if a track was closer to the sensor edge than the tracking precision, it is possible that the actual particle passed outside the sensor, and the track is only within the sensor because of the finite precision of the tracking. Several cuts were implemented in the analysis to avoid artificially lowering the efficiency because of such effects. Tracks are not considered if they are closer than 100 μm to the edge of the sensor. If there were noisy pixels masked offline or online, or double columns switched off, tracks closer than 100 μm in both x and y to these are also not considered.

Particles which could have left charge in two sectors at the same time are also not considered. This is done for two reasons: firstly, the characteristics of each geometry should be studied separately, and particles, which left charge in two sectors could bias these studies. Secondly, the electric-field configuration could be different in the pixels at the sector borders, e.g. if the size of the depletion region is different between the sectors. For these reasons, tracks which are closer to the sector borders than two times the pixel pitch plus 100 μm ($2 \times 28 + 100 \mu\text{m} = 156 \mu\text{m}$) are dropped from the analysis.

Only events with one reconstructed track and only events where there are maximum three reference planes with more than one hit are used. The second cut is to ensure that there was no other track in the event that was not reconstructed properly. The requirement to study only those events which have only one track was introduced because of a measured efficiency loss connected to the strong dependence of the pulse length on I_{thr} . If the length of the signal is longer than the time between two consecutive events, it is possible that the same track is recorded in both of the events. If then the length of the pulse is shorter in the DUT than in the tracking planes due to the different settings of I_{thr} , it is possible that the hit is not present anymore in the DUT in the second event. This results in an artificial loss of efficiency, which can be avoided if events with more than one reconstructed track are not used for the calculation of the efficiency (for more details see [71]). If the reference planes are too noisy during data-taking, the analysis can become statistically limited because of this cut, since many events could have more than three tracking planes with multiple hits. This gives a lower limit on the charge threshold of the tracking planes, while an upper limit is given from the requirement to have as high detection efficiency in the tracking planes as possible. Another cut on the spacing of events in time was also introduced to avoid problems arising from the same I_{thr} dependence of the pulse length. The cut filters events which are closer

than 30 μs plus the busy time of the setup, which is on average around 93 μs , but has a large spread (85-375 μs), depending on the settings of the chip.

When the central three planes were treated as DUTs and at extreme charge threshold settings, it is possible that all three chips have very low detection efficiencies. This causes a problem, if all tracking planes have to contribute a hit to each track, since two out of the three DUTs are always included in these cases in the tracking. To avoid this, a maximum of two hits, to account for the two DUTs with low efficiencies, are allowed to be missing from the track. The only case where a hit was required in all tracking planes were the runs, which are used for resolution measurements; however, in these runs, the settings of only one chip were varied at a time, therefore no problem arises from tracking planes with low efficiency. To have a hit in all tracking planes is useful for resolution measurements. If hits are allowed to be missing from a track, it results in a varying interpolation uncertainty to the DUT track by track, and that causes a problem in the calculation of the resolution from the residual values. If, however, this cut cannot be used, (e.g because of an inefficient tracking plane), the interpolation error can be calculated on a case-by-case basis depending on which hit was missing from the track. The change in the extrapolation uncertainty is small compared to the search window for tracks (100 μm), therefore this change does not effect the efficiency and cluster size results.

All the above mentioned default cuts of the analysis are summarized in Table B.1.

Cut	Default value
Hit associations in DUT	100 μm
Width of excluded area at the edge of the sensor	100 μm
Excluded area around hot or masked pixel	100 $\mu\text{m} \times 100 \mu\text{m}$
Width of excluded area around dead double column	100 μm
Width of excluded area at the border of sectors	156 μm
Only a single track per event	Yes
Maximum number of tracking planes with multiple hits	3
Maximum number of hits missing from a track	2
Maximum firing frequency for hot pixels (alignment)	0.01% in first 10 000 events
Maximum firing frequency for hot pixels (analysis)	0.1% in first 10 000 events
Minimum time between events	Busy time + 30 μs

Table B.1: Default cut values for the most important parameters of the data-processing.

C. Datasets of the $\Delta\varphi$ - $\Delta\eta$ analysis

C.1 2010 Pb–Pb

For the 2010 Pb–Pb data, the data-taking period called *LHC10h* and the dataset called *FILTER_PbPb_160_LHC10h_7input* was used. This consists of the following runs:

139510, 139507, 139505, 139503, 139465, 139438, 139437, 139360, 139329, 139328, 139314, 139310, 139309, 139173, 139107, 139105, 139038, 139037, 139036, 139029, 139028, 138872, 138871, 138870, 138837, 138732, 138730, 138666, 138662, 138653, 138652, 138638, 138624, 138621, 138583, 138582, 138578, 138534, 138469, 138442, 138439, 138438, 138396, 138364, 138275, 138225, 138201, 138197, 138192, 138190, 137848, 137844, 137752, 137751, 137724, 137722, 137718, 137704, 137693, 137692, 137691, 137686, 137685, 137639, 137638, 137608, 137595, 137549, 137546, 137544, 137541, 137539, 137531, 137530, 137443, 137441, 137440, 137439, 137434, 137432, 137431, 137430, 137366, 137243, 137236, 137235, 137232, 137231, 137230, 137162, 137161.

C.2 2011 Pb–Pb

For the 2011 Pb–Pb data, the data-taking period called *LHC11h* and the dataset called *LHC11h_AOD145_7input* was used. This consists of the following runs:

167915, 168115, 168460, 169035, 169238, 169859, 170228, 167920, 168310, 168464, 169091, 169411, 169923, 170230, 167985, 168311, 168467, 169094, 169415, 170027, 170268, 167987, 168322, 168511, 169138, 169417, 170081, 170269, 167988, 168325, 168512, 169144, 169835, 170155, 170270, 168069, 168341, 168514, 169145, 169837, 170159, 170306, 168076, 168342, 168777, 169148, 169838, 170163, 170308, 168105, 168361, 168826, 169156, 169846, 170193, 170309, 168107, 168362, 168988, 169160, 169855, 170203, 168108, 168458, 168992, 169167, 169858, 170204.

C.3 2011 pp

For the pp data, the data-taking period called *LHC11a* and the dataset called *LHC11a_p2_wSDD* was used. This consists of the following runs: 146860, 146859, 146858, 146856, 146824, 146817, 146806, 146805, 146804, 146803, 146802, 146801, 146748, 146747, 146746.

Acronyms

ACORDE ALICE COsmic Ray DEtector.

AERD Address Encoder Reset Decoder.

AGS Alternating Gradient Synchrotron.

ALICE A Large Ion Collider Experiment.

ALPIDE ALICE PIxel DEtector.

AMPT A Multi-Phase Transport.

ART A Relativistic Transport model.

ATLAS A Toroidal LHC ApparatuS.

BTF Beam Test Facility.

CERN Conseil Européen pour la Recherche Nucléaire.

CMOS Complementary Metal–Oxide–Semiconductor.

CMS Compact Muon Solenoid.

CPV Charged-Particle Veto.

DAC Digital to Analog Conversion.

DAQ Data AcQuisition.

DCAL Di-Jet Calorimeter.

DESY Deutsches Elektronen-Synchrotron.

DUT Device Under Test.

EMCal ElectroMagnetic CALorimeter.

FMD Forward Multiplicity Detector.

- FPC** Flexible Printed Circuit board.
- FR4** Flame Retardant 4: Classification of materials of PCBs made of composite material..
- HIJING** Heavy Ion Jet INteraction Generator.
- HMPID** High-Momentum Particle Identification Detector.
- ITS** Inner Tracking System.
- JSI** Jozef Stefan Institute.
- lcio** Linear Collider Input Output.
- LEP** Large Electron Positron collider.
- LHC** Large Hadron Collider.
- LHCb** Large Hadron Collider beauty.
- LS2** Second Long Shutdown.
- MAPS** Monolithic Active Pixel Sensor.
- MC** Monte Carlo.
- MFT** Muon Forward Tracker.
- MPI** Multiple Parton Interactions.
- ndf** Number of Degrees of Freedom.
- NIEL** Non Ionizing Energy Loss.
- pALPIDE-1** Prototype ALPIDE-1.
- pALPIDE-2** Prototype ALPIDE-2.
- pALPIDE-3** Prototype ALPIDE-3.
- pALPIDEss** Prototype ALPIDE Small Scale.
- PCB** Printed Circuit Board.
- PDF** Parton Distribution Function.
- PHOS** PHOton Spectrometer.
- PID** particle identification.
- PMD** Photon Multiplicity Detector.

- PMOS** p-channel MOSFET (Metal-Oxide-Semiconductor Field-Effect Transistor).
- pQCD** perturbative QCD.
- PS** Proton Synchrotron.
- QCD** Quantum Chromodynamics.
- QGP** Quark-Gluon Plasma.
- RHIC** Relativistic Heavy Ion Collider.
- RMS** Root Mean Square.
- SDD** Silicon Drift Detector.
- SPD** Silicon Pixel Detector.
- SPS** Super Proton Synchrotron.
- SSD** Silicon Strip Detector.
- STAR** Solenoid Tracker at RHIC.
- STAR PXL** STAR PiXeL detector.
- T0** Time 0.
- TDR** Technical Design Report.
- TID** Total Ionizing Dose.
- TOF** Time Of Flight.
- TPC** Time-Projection Chamber.
- TRD** Transition Radiation Detector.
- V0** Vertex 0.
- V0-A** Vertex 0 detector on the $z>0$ side of ALICE.
- V0-C** Vertex 0 detector on the $z<0$ side of ALICE.
- ZDC** Zero Degree Calorimeter.
- ZPC** Zhang's Parton Cascade.

Bibliography

- [1] **ALICE** Collaboration, “Anomalous evolution of the near-side jet peak shape in Pb–Pb collisions at $\sqrt{s_{\text{NN}}} = 2.76$ TeV”, *Phys. Rev. Lett.* **119** no. 10, (2017) 102301, [arXiv:1609.06643 \[nucl-ex\]](#).
- [2] **ALICE** Collaboration, “Evolution of the longitudinal and azimuthal structure of the near-side jet peak in Pb–Pb collisions at $\sqrt{s_{\text{NN}}} = 2.76$ TeV”, *Phys. Rev.* **C96** no. 3, (2017) 034904, [arXiv:1609.06667 \[nucl-ex\]](#).
- [3] C. L. Bennett *et al.*, “Nine-year Wilkinson Microwave Anisotropy Probe (WMAP) observations: final maps and results”, *The Astrophysical Journal Supplement Series* **208** (2013) 2, [arXiv:1212.5225 \[astro-ph.CO\]](#).
- [4] D. J. Schwarz, “The first second of the universe”, *Annalen Phys.* **12** (2003) 220–270, [arXiv:astro-ph/0303574 \[astro-ph\]](#).
- [5] E. V. Shuryak, “Quantum Chromodynamics and the Theory of Superdense Matter”, *Phys. Rept.* **61** (1980) 71–158.
- [6] I. Montvay and J. Zimanyi, “Hadron Chemistry in Heavy Ion Collisions”, *Nucl. Phys.* **A316** (1979) 490. [,360(1978)].
- [7] T. Biro and J. Zimanyi, “Quarkochemistry in Relativistic Heavy Ion Collisions”, *Phys. Lett.* **113B** (1982) 6.
- [8] J. Schükraft, “Heavy-ion physics at the LHC”,
<https://cds.cern.ch/record/935632>.
- [9] European Organization for Nuclear Research (CERN).
<https://home.cern/topics/large-hadron-collider>.
- [10] Relativistic Heavy Ion Collider at the Brookhaven National Laboratory. <https://www.bnl.gov/rhic>.
- [11] **PHENIX, PHOBOS, STAR, BRAHMS** Collaboration, “Hunting the quark gluon plasma.” BNL-73847-2005, 2005.

- [12] M. L. Miller, K. Reygers, S. J. Sanders, and P. Steinberg, “Glauber modeling in high energy nuclear collisions”, *Ann. Rev. Nucl. Part. Sci.* **57** (2007) 205–243, [arXiv:nucl-ex/0701025](#) [nucl-ex].
- [13] **ALICE** Collaboration, “Centrality determination of Pb–Pb collisions at $\sqrt{s_{\text{NN}}} = 2.76$ TeV with ALICE”, *Phys. Rev.* **C88** no. 4, (2013) 044909, [arXiv:1301.4361](#) [nucl-ex].
- [14] **ATLAS** Collaboration, “Observation of a Centrality-Dependent Dijet Asymmetry in Lead-Lead Collisions at $\sqrt{s_{\text{NN}}} = 2.76$ TeV with the ATLAS Detector at the LHC”, *Phys. Rev. Lett.* **105** (2010) 252303, [arXiv:1011.6182](#) [hep-ex].
- [15] **CMS** Collaboration, “Observation and studies of jet quenching in PbPb collisions at nucleon-nucleon center-of-mass energy = 2.76 TeV”, *Phys. Rev.* **C84** (2011) 024906, [arXiv:1102.1957](#) [nucl-ex].
- [16] **STAR** Collaboration, “Disappearance of back-to-back high p_T hadron correlations in central Au+Au collisions at $\sqrt{s_{\text{NN}}} = 200$ GeV”, *Phys. Rev. Lett.* **90** (2003) 082302, [arXiv:nucl-ex/0210033](#) [nucl-ex].
- [17] **ALICE** Collaboration, “Suppression of Charged Particle Production at Large Transverse Momentum in Central Pb–Pb Collisions at $\sqrt{s_{\text{NN}}} = 2.76$ TeV”, *Phys. Lett.* **B696** (2011) 30–39, [arXiv:1012.1004](#) [nucl-ex].
- [18] **PHENIX** Collaboration, “High p_T charged hadron suppression in Au + Au collisions at $\sqrt{s_{\text{NN}}} = 200$ GeV”, *Phys. Rev.* **C69** (2004) 034910, [arXiv:nucl-ex/0308006](#) [nucl-ex].
- [19] **STAR** Collaboration, “Transverse momentum and collision energy dependence of high $p(T)$ hadron suppression in Au+Au collisions at ultrarelativistic energies”, *Phys. Rev. Lett.* **91** (2003) 172302, [arXiv:nucl-ex/0305015](#) [nucl-ex].
- [20] E. Schnedermann, J. Sollfrank, and U. W. Heinz, “Thermal phenomenology of hadrons from 200 A/GeV S+S collisions”, *Phys. Rev.* **C48** (1993) 2462–2475, [arXiv:nucl-th/9307020](#) [nucl-th].
- [21] C. M. Hung and E. V. Shuryak, “Equation of state, radial flow and freezeout in high-energy heavy ion collisions”, *Phys. Rev.* **C57** (1998) 1891–1906, [arXiv:hep-ph/9709264](#) [hep-ph].
- [22] J. D. Bjorken, “Highly Relativistic Nucleus-Nucleus Collisions: The Central Rapidity Region”, *Phys. Rev.* **D27** (1983) 140–151.

- [23] A. Saini and S. Bhardwaj, “Elliptic Flow in Heavy Ion Collisions”, *Journal of Nuclear and Particle Physics* **4** no. 6, (2014) .
- [24] R. Snellings, “Elliptic Flow: A Brief Review”, *New J. Phys.* **13** (2011) 055008, [arXiv:1102.3010 \[nucl-ex\]](#).
- [25] **E877** Collaboration, “Energy and charged particle flow in a 10.8 A/GeV/c Au + Au collisions”, *Phys. Rev.* **C55** (1997) 1420–1430, [arXiv:nucl-ex/9610006 \[nucl-ex\]](#). [Erratum: *Phys. Rev.* **C56**, 2336(1997)].
- [26] **E895** Collaboration, “Elliptic flow: Transition from out-of-plane to in-plane emission in Au + Au collisions”, *Phys. Rev. Lett.* **83** (1999) 1295–1298, [arXiv:nucl-ex/9903010 \[nucl-ex\]](#).
- [27] **NA49** Collaboration, “Directed and elliptic flow in 158 GeV / nucleon Pb + Pb collisions”, *Phys. Rev. Lett.* **80** (1998) 4136–4140, [arXiv:nucl-ex/9711001 \[nucl-ex\]](#).
- [28] **NA49** Collaboration, “Centrality dependence of directed and elliptic flow at the SPS”, *Nucl. Phys.* **A661** (1999) 341–344, [arXiv:nucl-ex/9906013 \[nucl-ex\]](#).
- [29] **WA98** Collaboration, “Collective flow in 158 A GeV Pb + Pb collisions”, *Nucl. Phys.* **A638** (1998) 459–462.
- [30] **WA93** Collaboration, “Azimuthal anisotropy in S + Au reactions at 200 A/GeV”, *Phys. Lett.* **B403** (1997) 390–396.
- [31] **STAR** Collaboration, “Elliptic flow in Au + Au collisions at $\sqrt{s_{NN}} = 130$ GeV”, *Phys. Rev. Lett.* **86** (2001) 402–407, [arXiv:nucl-ex/0009011 \[nucl-ex\]](#).
- [32] B. Alver and G. Roland, “Collision geometry fluctuations and triangular flow in heavy-ion collisions”, *Phys. Rev.* **C81** (2010) 054905, [arXiv:1003.0194 \[nucl-th\]](#). [Erratum: *Phys. Rev.* **C82**, 039903(2010)].
- [33] **ALICE** Collaboration, “Higher harmonic anisotropic flow measurements of charged particles in Pb–Pb collisions at $\sqrt{s_{NN}} = 2.76$ TeV”, *Phys. Rev. Lett.* **107** (2011) 032301, [arXiv:1105.3865 \[nucl-ex\]](#).
- [34] **ALICE** Collaboration, “Azimuthal anisotropy of charged jet production in $\sqrt{s_{NN}} = 2.76$ TeV Pb–Pb collisions”, *Nucl. Phys.* **A956** (2016) 629–632, [arXiv:1511.05352 \[nucl-ex\]](#).

- [35] **Particle Data Group** Collaboration, “Review of Particle Physics”, *Chin. Phys.* **C38** (2014) 090001.
- [36] Y. L. Dokshitzer and D. E. Kharzeev, “Heavy quark colorimetry of QCD matter”, *Phys. Lett.* **B519** (2001) 199–206, [arXiv:hep-ph/0106202](#) [hep-ph].
- [37] **ALICE** Collaboration, “Upgrade of the ALICE Experiment: Letter of Intent”, Tech. Rep. CERN-LHCC-2012-012. LHCC-I-022. ALICE-UG-002, CERN, Geneva, Aug, 2012. <https://cds.cern.ch/record/1475243>.
- [38] **ALICE** Collaboration, “Elliptic flow of electrons from heavy-flavour hadron decays at mid-rapidity in Pb–Pb collisions at $\sqrt{s_{NN}} = 2.76$ TeV”, *JHEP* **09** (2016) 028, [arXiv:1606.00321](#) [nucl-ex].
- [39] **ALICE** Collaboration, “Elliptic flow of muons from heavy-flavour hadron decays at forward rapidity in Pb–Pb collisions at $\sqrt{s_{NN}} = 2.76$ TeV”, *Phys. Lett.* **B753** (2016) 41–56, [arXiv:1507.03134](#) [nucl-ex].
- [40] **ALICE** Collaboration, “D meson elliptic flow in non-central Pb–Pb collisions at $\sqrt{s_{NN}} = 2.76$ TeV”, *Phys. Rev. Lett.* **111** (2013) 102301, [arXiv:1305.2707](#) [nucl-ex].
- [41] **ALICE** Collaboration, “J/Ψ Elliptic Flow in Pb–Pb Collisions at $\sqrt{s_{NN}} = 2.76$ TeV”, *Phys. Rev. Lett.* **111** (2013) 162301, [arXiv:1303.5880](#) [nucl-ex].
- [42] **ALICE** Collaboration, “Transverse momentum dependence of D-meson production in Pb–Pb collisions at $\sqrt{s_{NN}} = 2.76$ TeV”, *JHEP* **03** (2016) 081, [arXiv:1509.06888](#) [nucl-ex].
- [43] **ALICE** Collaboration, “The ALICE experiment at the CERN LHC”, *JINST* **3** (2008) S08002.
- [44] A. Tauro, “ALICE Schematics.” General Photo, May, 2017.
- [45] **ALICE** Collaboration, “Technical Design Report for the Upgrade of the ALICE Inner Tracking System”, Tech. Rep. CERN-LHCC-2013-024. ALICE-TDR-017, CERN, Geneva, Nov, 2013. <https://cds.cern.ch/record/1625842>.
- [46] **ALICE** Collaboration, “Upgrade of the Inner Tracking System Conceptual Design Report.”, Tech. Rep. CERN-LHCC-2012-013. LHCC-P-005, CERN, Geneva, Aug, 2012. <https://cds.cern.ch/record/1475244>.

-
- [47] **ALICE** Collaboration, “ALICE Inner Tracking System (ITS): Technical Design Report”, tech. rep., Geneva, 1999.
<https://edms.cern.ch/document/398932/1>.
- [48] L. Musa. Personal communication.
- [49] J. Belikov. Personal communication.
- [50] **ATLAS** Collaboration, “ATLAS inner detector: Technical Design Report, 2”, tech. rep., Geneva, 1997.
<https://cds.cern.ch/record/331064>.
- [51] **CMS** Collaboration, “The CMS tracker system project: Technical Design Report”, tech. rep., Geneva, 1997.
<http://cds.cern.ch/record/368412>.
- [52] **LHCb** Collaboration, “LHCb VELO (VERTex LOcator): Technical Design Report”, tech. rep., Geneva, 2001.
<https://cds.cern.ch/record/504321>.
- [53] **STAR** Collaboration, “A Heavy Flavor Tracker for STAR”, Tech. Rep. LBNL/PUB-5509-2008, 2008.
- [54] **STAR** Collaboration, “The STAR PXL detector”, *JINST* **11** no. 12, (2016) C12068.
- [55] L. Rossi, P. Fischer, T. Rohe, and N. Wermes, *Pixel detectors: from fundamentals to applications*. Particle Acceleration and Detection. Springer, Berlin, 2006. <http://cds.cern.ch/record/976471>.
- [56] G. Aglieri *et al.*, “Monolithic active pixel sensor development for the upgrade of the ALICE inner tracking system”, *JINST* **8** no. 12, (2013) C12041. <http://cds.cern.ch/record/1709950>.
- [57] J. W. van Hoorne, *Study and Development of a novel Silicon Pixel Detector for the Upgrade of the ALICE Inner Tracking System*. PhD thesis, TU Vienna, Oct, 2015.
<https://cds.cern.ch/record/2119197>. Presented 24 Nov 2015.
- [58] P. Yang *et al.*, “Low-power priority Address-Encoder and Reset-Decoder data-driven readout for Monolithic Active Pixel Sensors for tracker system”, *Nucl. Instrum. Meth.* **A785** (2015) 61–69.
- [59] F. Reidt, *Studies for the ALICE Inner Tracking System Upgrade*. PhD thesis, Heidelberg U., Feb, 2016.
<https://cds.cern.ch/record/2151986>. Presented 28 Apr 2016.

- [60] ALICE ITS ALPIDE development team, “pALPIDEfs datasheet.” Internal note, 2013.
- [61] D. Kim *et al.*, “Front end optimization for the monolithic active pixel sensor of the ALICE Inner Tracking System upgrade”, *JINST* **11** no. 02, (2016) C02042.
- [62] W. Snoeys. Personal communication.
- [63] ALICE ITS ALPIDE development team, “ALPIDE-3 Operations Manual.” Internal note, 2015.
- [64] ALICE ITS ALPIDE development team, “ALPIDE Operations Manual.” Internal note, 2016.
- [65] EUDAQ Documentation and Source Code.
<http://eudaq.github.io>.
- [66] I. Rubinskiy, “EUTelescope. Offline track reconstruction and DUT analysis software”, EUDET Memo 2010-12. <http://www.eudet.org/e26/e28/e86887/e107460/EUDET-Memo-2010-12.pdf>.
- [67] H. Perrey, “EUDAQ and EUTelescope: Software Frameworks for Test Beam Data Acquisition and Analysis”, *PoS TIPP2014* (2014) 353.
- [68] EUTelescope Documentation and Source Code.
<http://eutelescope.web.cern.ch/>.
- [69] A. F. Zarnecki and P. Niezurawski, “EUDET Telescope Geometry and Resolution Studies”, [arXiv:physics/0703058](https://arxiv.org/abs/physics/0703058) [PHYSICS].
- [70] Z. X. T. Ullrich, “Treatment of Errors in Efficiency Calculations”, [arXiv:physics/0701199](https://arxiv.org/abs/physics/0701199) [PHYSICS].
- [71] M. Kofarago, “Summary of the test beam results of the pALPIDE-1”, <https://cds.cern.ch/record/2242504>. Internal note.
- [72] Web page of the TRIGA Mark II Reactor.
<http://www.rcp.ijs.si/ric/index-a.htm>.
- [73] J. Ferencei, F. Krizek, and T. Vanat. Personal communication.
- [74] C. Bedda, *The ALICE experiment: D⁺-meson production in heavy-ion collisions and silicon low noise sensors characterization for the ITS Upgrade*. PhD thesis, Politecnico di Torino, 2016.

- [75] M. Šuljić, “ALPIDE: the Monolithic Active Pixel Sensor for the ALICE ITS upgrade”, *JINST* **11** no. 11, (2016) C11025.
<http://stacks.iop.org/1748-0221/11/i=11/a=C11025>.
- [76] F. Reidt, “The ALICE pixel detector upgrade”, *JINST* **11** no. 12, (2016) C12038.
<http://stacks.iop.org/1748-0221/11/i=12/a=C12038>.
- [77] T. Kugathasan, “Pixels for ALICE tracker upgrade”, in *Proceedings, 10th International Meeting on Front-End Electronics, 2016*.
- [78] M. Mager, “The upgrade of the ALICE Inner Tracking System with the Monolithic Active Pixel Sensor ALPIDE.” Presented at the IEEE NSS/MIC in Strasbourg, France, 2016.
- [79] S. Beole, “The upgrade of the ALICE ITS.” Presented at the International Workshop on Vertex Detectors in La Biodola, Isola d’Elba, Italy, 2016.
- [80] P. Camerini, “The ALICE ITS upgrade.” Presented at the European Physical Society Conference on High Energy Physics in Venice, Italy, 2017.
- [81] D. d’Enterria, “Jet quenching”, *Landolt-Bornstein* **23** (2010) 471, [arXiv:0902.2011](https://arxiv.org/abs/0902.2011) [nucl-ex].
- [82] **ALICE** Collaboration, “Measurement of Event Background Fluctuations for Charged Particle Jet Reconstruction in Pb–Pb collisions at $\sqrt{s_{NN}} = 2.76$ TeV”, *JHEP* **03** (2012) 053, [arXiv:1201.2423](https://arxiv.org/abs/1201.2423) [hep-ex].
- [83] **ALICE** Collaboration, “Particle-yield modification in jet-like azimuthal di-hadron correlations in Pb–Pb collisions at $\sqrt{s_{NN}} = 2.76$ TeV”, *Phys. Rev. Lett.* **108** (2012) 092301, [arXiv:1110.0121](https://arxiv.org/abs/1110.0121) [nucl-ex].
- [84] **ALICE** Collaboration, “Elliptic flow of charged particles in Pb+Pb collisions at 2.76 TeV”, *Phys. Rev. Lett.* **105** (2010) 252302, [arXiv:1011.3914](https://arxiv.org/abs/1011.3914) [nucl-ex].
- [85] **ALICE** Collaboration, “Centrality dependence of π , K, p production in Pb–Pb collisions at $\sqrt{s_{NN}} = 2.76$ TeV”, *Phys. Rev.* **C88** (2013) 044910, [arXiv:1303.0737](https://arxiv.org/abs/1303.0737) [hep-ex].
- [86] N. Armesto, C. A. Salgado, and U. A. Wiedemann, “Measuring the collective flow with jets”, *Phys.Rev.Lett.* **93** (2004) 242301, [arXiv:hep-ph/0405301](https://arxiv.org/abs/hep-ph/0405301).

- [87] **ALICE** Collaboration, “Measurement of inelastic, single- and double-diffraction cross sections in proton–proton collisions at the LHC with ALICE”, *Eur. Phys. J.* **C73** no. 6, (2013) 2456, arXiv:1208.4968 [hep-ex].
- [88] **ALICE** Collaboration, “Performance of the ALICE VZERO system”, *JINST* **8** (2013) P10016, arXiv:1306.3130 [nucl-ex].
- [89] **ALICE** Collaboration, “Centrality dependence of the charged-particle multiplicity density at mid-rapidity in Pb–Pb collisions at $\sqrt{s_{\text{NN}}} = 2.76$ TeV”, *Phys. Rev. Lett.* **106** (2011) 032301, arXiv:1012.1657 [nucl-ex].
- [90] **ALICE** Collaboration, “Centrality, rapidity and transverse momentum dependence of J/ψ suppression in Pb–Pb collisions at $\sqrt{s_{\text{NN}}} = 2.76$ TeV”, *Phys. Lett.* **B734** (2014) 314–327, arXiv:1311.0214 [nucl-ex].
- [91] **ALICE** Collaboration, B. B. Abelev *et al.*, “Performance of the ALICE Experiment at the CERN LHC”, *Int. J. Mod. Phys.* **A29** (2014) 1430044, arXiv:1402.4476 [nucl-ex].
- [92] **ALICE** Collaboration, “Underlying Event measurements in pp collisions at $\sqrt{s} = 0.9$ and 7 TeV with the ALICE experiment at the LHC”, *JHEP* **07** (2012) 116, arXiv:1112.2082 [hep-ex].
- [93] M. H. Seymour and M. Marx, “Monte Carlo Event Generators”, in *Proceedings, 69th Scottish Universities Summer School in Physics : LHC Phenomenology (SUSSP69): St. Andrews, Scotland, August 19-September 1, 2012*, pp. 287–319. 2013. arXiv:1304.6677 [hep-ph].
- [94] T. Sjostrand, “Monte Carlo Generators”, in *High-energy physics. Proceedings, European School, Aronsborg, Sweden, June 18-July 1, 2006*, pp. 51–74. 2006. arXiv:hep-ph/0611247 [hep-ph]. <http://weblib.cern.ch/abstract?CERN-LCGAPP-2006-06>.
- [95] P. Bartalini *et al.*, “Multi-Parton Interactions at the LHC”, 2011. arXiv:1111.0469 [hep-ph]. <https://inspirehep.net/record/944170/files/arXiv:1111.0469.pdf>.
- [96] T. Sjostrand, S. Mrenna, and P. Z. Skands, “PYTHIA 6.4 Physics and Manual”, *JHEP* **05** (2006) 026, arXiv:hep-ph/0603175 [hep-ph].

- [97] P. Z. Skands, “Tuning Monte Carlo Generators: The Perugia Tunes”, *Phys. Rev.* **D82** (2010) 074018, [arXiv:1005.3457](#) [hep-ph].
- [98] T. Sjostrand, S. Mrenna, and P. Z. Skands, “A Brief Introduction to PYTHIA 8.1”, *Comput. Phys. Commun.* **178** (2008) 852–867, [arXiv:0710.3820](#) [hep-ph].
- [99] T. Sjostrand, “PYTHIA 8 Status Report”, in *Proceedings, workshop: HERA and the LHC workshop series on the implications of HERA for LHC physics*, pp. 726–732. 2008. [arXiv:0809.0303](#) [hep-ph]. <http://inspirehep.net/record/794180/files/arXiv:0809.0303.pdf>.
- [100] P. Skands, S. Carrazza, and J. Rojo, “Tuning PYTHIA 8.1: the Monash 2013 Tune”, *Eur. Phys. J.* **C74** no. 8, (2014) 3024, [arXiv:1404.5630](#) [hep-ph].
- [101] B. Andersson, G. Gustafson, G. Ingelman, and T. Sjostrand, “Parton Fragmentation and String Dynamics”, *Phys. Rept.* **97** (1983) 31–145.
- [102] X.-N. Wang and M. Gyulassy, “HIJING: A Monte Carlo model for multiple jet production in p p, p A and A A collisions”, *Phys. Rev.* **D44** (1991) 3501–3516.
- [103] Z.-W. Lin, C. M. Ko, B.-A. Li, B. Zhang, and S. Pal, “A Multi-phase transport model for relativistic heavy ion collisions”, *Phys. Rev.* **C72** (2005) 064901, [arXiv:nucl-th/0411110](#) [nucl-th].
- [104] J. Xu and C. M. Ko, “Pb–Pb collisions at $\sqrt{s_{NN}} = 2.76$ TeV in a multiphase transport model”, *Phys. Rev.* **C83** (2011) 034904, [arXiv:1101.2231](#) [nucl-th].
- [105] B. Zhang, “ZPC 1.0.1: A Parton cascade for ultrarelativistic heavy ion collisions”, *Comput. Phys. Commun.* **109** (1998) 193–206, [arXiv:nucl-th/9709009](#) [nucl-th].
- [106] B.-A. Li, A. T. Sustich, B. Zhang, and C. M. Ko, “Studies of superdense hadronic matter in a relativistic transport model”, *International Journal of Modern Physics E* **10** no. 04n05, (2001) 267–352, <http://www.worldscientific.com/doi/pdf/10.1142/S0218301301000575>.

- [107] B.-A. Li and C. M. Ko, “Formation of superdense hadronic matter in high-energy heavy ion collisions”, *Phys. Rev.* **C52** (1995) 2037–2063, [arXiv:nucl-th/9505016](#) [nucl-th].
- [108] **ALICE** Collaboration, “Higher harmonic flow coefficients of identified hadrons in Pb–Pb collisions at $\sqrt{s_{\text{NN}}} = 2.76$ TeV”, *JHEP* **09** (2016) 164, [arXiv:1606.06057](#) [nucl-ex].
- [109] **ATLAS** Collaboration, “Measurement of the centrality and pseudorapidity dependence of the integrated elliptic flow in lead-lead collisions at $\sqrt{s_{\text{NN}}} = 2.76$ TeV with the ATLAS detector”, *Eur. Phys. J.* **C74** no. 8, (2014) 2982, [arXiv:1405.3936](#) [hep-ex].
- [110] **CMS** Collaboration, “Measurement of the elliptic anisotropy of charged particles produced in PbPb collisions at $\sqrt{s_{\text{NN}}} = 2.76$ TeV”, *Phys. Rev.* **C87** no. 1, (2013) 014902, [arXiv:1204.1409](#) [nucl-ex].
- [111] **ALICE** Collaboration, “Centrality dependence of the pseudorapidity density distribution for charged particles in Pb–Pb collisions at $\sqrt{s_{\text{NN}}} = 2.76$ TeV”, *Phys. Lett.* **B726** (2013) 610–622, [arXiv:1304.0347](#) [nucl-ex].
- [112] T. Csorgo, S. Hegyi, and W. A. Zajc, “Bose-Einstein correlations for Levy stable source distributions”, *Eur. Phys. J.* **C36** (2004) 67–78, [arXiv:nucl-th/0310042](#) [nucl-th].
- [113] E. A. De Wolf, I. M. Dremin, and W. Kittel, “Scaling laws for density correlations and fluctuations in multiparticle dynamics”, *Phys. Rept.* **270** (1996) 1–141, [arXiv:hep-ph/9508325](#) [hep-ph].
- [114] T. Csorgo, S. Hegyi, T. Novak, and W. A. Zajc, “Bose-Einstein or HBT correlations and the anomalous dimension of QCD”, *Acta Phys. Polon.* **B36** (2005) 329–337, [arXiv:hep-ph/0412243](#) [hep-ph].
- [115] J. P. Nolan, *Stable Distributions - Models for Heavy Tailed Data*. Birkhauser, Boston, 2017. In progress, Chapter 1 online at <http://fs2.american.edu/jpnolan/www/stable/stable.html>.
- [116] **ALICE** Collaboration, “Centrality Dependence of Charged Particle Production at Large Transverse Momentum in Pb–Pb Collisions at $\sqrt{s_{\text{NN}}} = 2.76$ TeV”, *Phys. Lett.* **B720** (2013) 52–62, [arXiv:1208.2711](#) [hep-ex].
- [117] J. F. Grosse-Oetringhaus, M. Kofarago and A. Morsch, “Jet-like near-side peak shapes.” Internal note, ANA-56, 2016.

-
- [118] **STAR** Collaboration, “System size and energy dependence of near-side di-hadron correlations”, *Phys. Rev.* **C85** (2012) 014903, [arXiv:1110.5800](#) [nucl-ex].
- [119] **CMS** Collaboration, “Correlations between jets and charged particles in PbPb and pp collisions at $\sqrt{s_{NN}} = 2.76$ TeV”, *JHEP* **02** (2016) 156, [arXiv:1601.00079](#) [nucl-ex].
- [120] N. Borghini, P. M. Dinh, and J.-Y. Ollitrault, “Flow analysis from multiparticle azimuthal correlations”, *Phys. Rev.* **C64** (2001) 054901, [arXiv:nucl-th/0105040](#) [nucl-th].
- [121] G. L. Ma *et al.*, “Longitudinal broadening of near side jets due to parton cascade”, *Eur. Phys. J.* **C57** (2008) 589–593, [arXiv:0807.3987](#) [nucl-th].
- [122] K. Werner, B. Guiot, I. Karpenko, and T. Pierog, “Analysing radial flow features in p-Pb and p-p collisions at several TeV by studying identified particle production in EPOS3”, *Phys. Rev.* **C89** no. 6, (2014) 064903, [arXiv:1312.1233](#) [nucl-th].
- [123] T. Pierog, “Saturation Scale, MPI and Underlying Events.” Presented at the Rencontres de Moriond QCD and High Energy Interactions in La Thuile, Italy, 2017.
- [124] G. G. Barnaföldi *et al.*, “First Results with HIJING++ in High-Energy Heavy-Ion Collisions”, [arXiv:1701.08496](#) [hep-ph].
- [125] N. Jacazio, “Production of Identified and Unidentified Charged Hadrons in Pb–Pb Collisions at $\sqrt{s_{NN}} = 5.02$ TeV.” Presented at Quark Matter 2017 in Chicago, USA, 2017.

Summary in English

In the first second after the Big Bang, the Universe was in a state which is currently only accessible in particle collisions. This state, the so-called Quark-Gluon Plasma (QGP), is being studied at the Large Hadron Collider (LHC) in collisions of lead (Pb) ions at unprecedented energies. The ALICE detector was built at the LHC to study these heavy-ion collisions. In the current Thesis, two topics were discussed in detail: firstly, the upgrade of the Inner Tracking System (ITS) of ALICE was presented and secondly, a two-particle angular correlation analysis carried out with the ALICE detector was shown.

In 2019–2020, ALICE will be upgraded to enhance its readout rate and tracking capabilities. The ITS will be completely replaced by a new detector, which will allow better transverse momentum resolution, especially at low transverse momentum, and more precise vertex determination. Dedicated R&D was carried out to develop a sensor for the ITS which fulfills all the requirements of the upgrade. The technology of Monolithic Active Pixel Sensors was chosen for the new detector, and several prototypes have been produced and tested. The pALPIDE-1 was the first full-scale prototype, and it was thoroughly tested in laboratory measurements and at test-beam facilities.

The detection efficiency, spatial resolution, average cluster size and noise occupancy were studied in test-beam measurements as a function of the charge threshold of the sensor and the reverse substrate bias. Different types of particles with different momenta were used to validate the sensor for the applications in the ALICE detector. The results were obtained for non-irradiated chips and also for sensors irradiated up to 10^{13} 1 MeV $n_{\text{eq}}/\text{cm}^2$ non-ionizing dose and 700 krad of ionizing radiation. It was found that the efficiency of the pALPIDE-1 is above the required 99% for a wide operating range both before and after irradiation for all the measured particle types. In terms of spatial resolution the requirement is to stay below 5 μm , which is also fulfilled by the pALPIDE-1. The noise occupancy was shown to be below the limit of 10^{-6} hits/event/pixel for a wide operating range, and it was also presented that the noise occupancy

was further lowered by orders of magnitude in the later prototypes. In conclusion, the pALPIDE-1 fulfills the requirements of the upgrade in terms of detection efficiency, spatial resolution and noise occupancy with a large operational margin both before and after irradiation.

The QGP is believed to be a strongly interacting almost ideal fluid. The properties of this liquid can be inferred from studying the interactions of the particles traversing through it. In initial hard scatterings of the collision, partons with high transverse momentum are produced. These partons fragment into jets and propagate through the medium, therefore making them good probes. The interaction of these jets with the medium can be studied by two-particle angular correlation measurements. In these measurements, a charged trigger particle with higher transverse momentum ($1 < p_{T,\text{trig}} < 8 \text{ GeV}/c$) is correlated with other charged particles with lower transverse momenta. Their difference in azimuthal angle ($\Delta\varphi$) and in pseudorapidity ($\Delta\eta$) is calculated, and from these differences the particle yield per trigger is determined. In this distribution, jets appear as a peak around $(\Delta\varphi, \Delta\eta) = (0, 0)$ and as an elongated structure in $\Delta\eta$ around $\Delta\varphi = \pi$. The peak at $(\Delta\varphi, \Delta\eta) = (0, 0)$ is characterized in pp and in Pb–Pb collisions as a function of transverse momentum and collision centrality. It was found that in Pb–Pb collisions the peak gets broader towards central collisions at low transverse momentum and that the broadening is more pronounced in the $\Delta\eta$ direction than in the $\Delta\varphi$ direction. It was also found that at low transverse momentum in the most central collisions, the peak shape departs from the generalized Gaussian shape and a depletion around $(\Delta\varphi, \Delta\eta) = (0, 0)$ develops. This depletion was characterized and it was found that $2.26\% \pm 0.06\% \pm 0.24\%$ of the yield of the peak is missing in this central region in the case of the lowest studied transverse momentum ($1 < p_{T,\text{trig}} < 2 \text{ GeV}/c$, $1 < p_{T,\text{assoc}} < 2 \text{ GeV}/c$) and the most central 10% of the collisions.

To study whether the broadening and the depletion can arise from the interaction of jets with the QGP, the results were compared to Monte Carlo generators. AMPT was used for the comparison for the Pb–Pb case, while PYTHIA was used for the pp case. It was found that AMPT with string melting turned off and hadronic rescattering turned on describes both the broadening and the depletion well. To further study the origin of these effects, the radial and the elliptic flow were determined both from data and from AMPT. It was found that the effects are accompanied by a large radial flow in AMPT. The comparison therefore suggests that the results can be interpreted as arising from the interaction of jets with the flowing medium.

Samenvatting in het Nederlands

In de eerste seconde na de Big-Bang was het Universum in een toestand die op dit moment alleen in deeltjesfysica bestudeerd kan worden. Deze toestand, het zogenaamde Quark-Gluon Plasma (QGP), wordt bestudeerd met de Large Hadron Collider (LHC) in botsingen van Lood ionen bij zeer hoge botsingsenergieën. De ALICE-detector (A Large Ion Collider Experiment) is gebouwd om hierbij in de LHC deze botsingen te bestuderen.

In dit proefschrift worden twee onderwerpen in detail beschreven: ten eerste, de verbeteringen aan het zogenaamde “Inner Tracking System” (ITS) van ALICE, en ten tweede de gemeten hoekcorrelatie tussen twee geproduceerde deeltjes in botsingen van de Lood ionen.

In 2019–2020 zal de ALICE-detector gemodificeerd worden om de uitleessnelheid en de herkenning van de deeltjessporen te verbeteren. De binnenste detectorlagen, van de ITS zullen volledig worden vervangen door een nieuwe detector met een sterk verbeterd momentum en plaatsresolutie. Uitgebreid onderzoek is gedaan om een sensor voor de ITS te ontwikkelen die aan al deze eisen voldoet. Een zogenaamde Monolithic Active Pixel Sensor, waarvan verschillende prototypes zijn gemaakt en getest is gekozen als technologie. De pALPIDE-1 was het eerste volledige prototype en deze sensor is zorgvuldig getest in het laboratorium en met verschillende testbundels.

De detector efficiëntie, de plaatsresolutie, de gemiddelde signaal verdeling en de ruis zijn bestudeerd in zgn “testbundel experimenten” als functie van snedes op de minimale lading en de bias spanning. Verschillende soorten deeltjes met variërende energieën zijn gebruikt om te kijken of de detector voor ALICE geschikt is. De metingen zijn gedaan aan sensoren die a priori bestraald waren met een niet ioniserende dosis tot 10^{13} 1 MeV n_{eq}/cm^2 en aan niet bestraalde sensoren. We hebben gevonden dat de efficiëntie van de pALPIDE-1 sensor boven 99% lag voor zowel de bestraalde als niet bestraalde sensoren. Voor de plaatresolutie waren de eisen dat deze beter moest zijn dan $5 \mu m$, en ook daar voldeed deze sensor aan. Het gemeten ruisniveau was onder de limiet van 10^{-6} signalen boven de snede, per event, en per pixel. Voor de prototypen die er na

geproduceerd zijn was het ruis-niveau zelfs nog lager. Onze conclusie in dit proefschrift is dan ook dat de pALPIDE-1 sensor aan alle eisen voor de ALICE-detector modificatie voldoet.

We hebben gevonden dat het QGP zich gedraagt als een bijna ideale vloeistof waarin de microscopische interacties sterk zijn. De eigenschappen van deze vloeistof kunnen worden afgeleid uit de interacties tussen de vloeistof en de deeltjes die erdoorheen gaan. In initiële harde botsingen van quarks en gluonen worden partonen met een hoog transversale momentum geproduceerd. Deze partonen hadroniseren in zogenaamde “jets”, welke zich daarna voortbewegen door het geproduceerde medium. Dit maakt deze jets goede observabelen om de eigenschappen van de QGP-vloeistof te bepalen.

De interacties tussen jets en de vloeistof kunnen worden bestudeerd door het meten van hoekcorrelaties tussen de geproduceerde deeltjes. In deze metingen worden geladen deeltjes geselecteerd met een transversaal momentum tussen de $1 < p_T < 8$ GeV/ c en gecorreleerd met alle andere geladen deeltjes. Het hoekverschil tussen deze deeltjes wordt bepaald en van daaruit kan de deeltjesopbrengst per geselecteerd deeltje worden bepaald. In deze hoekverdeling zit de jet-piek bij $(\Delta\varphi, \Delta\eta) = (0, 0)$ en als een brede verdeling bij $\Delta\eta$ bij $\Delta\varphi = \pi$. Deze jet-piek is gemeten in proton-proton botsingen en in Lood-Lood botsingen als functie van de centraliteit van de botsing. We hebben gevonden dat in Lood-Lood botsingen de piek breder wordt voor meer centrale botsingen bij een lager transversaal momentum en dat deze verbreding sterker is in $\Delta\eta$ vergeleken met $\Delta\varphi$. We zagen ook dat bij laag transversaal momentum, bij de meest centrale botsingen, deze piek niet meer Gaussisch is en lager bij $(\Delta\varphi, \Delta\eta) = (0, 0)$.

Om te bestuderen of deze verandering veroorzaakt wordt door interacties van de jets met het QGP, hebben we de resultaten vergeleken gebruik makende van een “Monte Carlo event-generator”. Voor de event-generatoren hebben we het AMPT-model (A Multi-Phase Transport) gebruikt voor de Lood-Lood botsingen en het PYTHIA computer-model voor de proton-proton botsingen. We hebben gevonden dat het AMPT-model waarbij de string-melting uit- en de hadronische interacties aangezet waren de metingen accuraat beschreef. Deze parameters zorgden voor een sterke radiale expansie van het geproduceerde systeem. De vergelijking van de metingen met het model suggereert dus dat onze resultaten in overeenstemming zijn met de interacties van de jets met een sterk radiaal expanderende systeem.

Acknowledgments

I would like to thank my supervisor Jan Fiete Grosse-Oetringhaus for the constant guidance and support during the four years of my PhD without whom this Thesis would not have been possible. I am also very grateful to my professor Raimond Snellings for his supervision and for welcoming me into the Utrecht ALICE group.

I would like to thank all members of both the CERN ALICE ITS group and the CERN ALICE Physics group for making me feel welcome at CERN and for all the fruitful discussions during my three-year-long stay at CERN. I am also grateful to the Hungarian ALICE group at the MTA Wigner RCP that they welcomed me into the group while still finalizing my PhD.

A special thank you goes to my group leaders Gergely Barnaföldi, Magnus Mager, Andreas Morsch, Luciano Musa and Alice Ohlson to whom I could always turn to with my questions.

I would like to show my gratitude to Gergely Barnaföldi, Jan Fiete Grosse-Oetringhaus, Thanushan Kugathasan, Magnus Mager, Andreas Morsch, Alice Ohlson, Felix Reidt, Raimond Snellings, Jacobus Van Hoorne, Róbert Vértesi and Walter Snoeys for helping me with valuable feedback on the drafts of this Thesis.

Last but not least, a huge thank you goes to my family, especially to my husband, Bence Varga, for their constant support and patience even in the moments when things were not easy.

The work presented in this Thesis was carried out and the Thesis was written within the CERN Doctoral Student Program. I am very grateful to all the organizers who make this program possible year after year. The work was also supported by the Hungarian National Funds "OTKA" with grant number K120660.

Curriculum Vitae

Mónika Varga-Kőfaragó

Email: monika.varga.kofarago@gmail.com

2016 – present:

MTA Wigner RCP (Budapest, Hungary)
Young Researcher Contract

2013 – 2018:

Utrecht University (Utrecht, Netherlands)
Graduate School of Natural Sciences
PhD in Physics

2013 – 2016:

CERN (Geneva, Switzerland)
Doctoral Student Program

2011 – 2013:

Eötvös Loránd University (Budapest, Hungary)
Faculty of Natural Science
Master of Science degree in physics with grade with honors
Specialization in Particle Physics

2008 – 2011:

Eötvös Loránd University (Budapest, Hungary)
Faculty of Natural Science
Bachelor of Science degree in physics with grade with honors